On the Necessary Degrees of Freedom for Helicopter and Wind Turbine Low-Frequency Mode Modeling

On the Necessary Degrees of Freedom for Helicopter and Wind Turbine Low-Frequency Mode Modeling

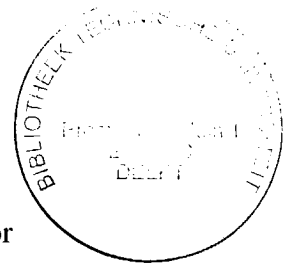

Proefschrift

ter verkrijging van de graad van doctor
aan de Technische Universiteit Delft,
op gezag van de Rector Magnificus prof. ir. K.F. Wakker,
voorzitter van het College voor Promoties,
in het openbaar te verdedigen op 12 maart 2001 te 10.30 uur

door

Marilena Domnica PAVEL

"inginer aeronave"
Faculty of Aerospace Engineering, "Politehnica" University of Bucharest

geboren te Braşov, Roemenië

Dit proefschrift is goedgekeurd door de promotor:

Prof. Dr. ir. Th. van Holten

Sammenstelling promotiecommissie:

Rector Magnificus, voorzitter	Technische Universiteit Delft
Prof. Dr. ir. Th. van Holten, promotor	Technische Universiteit Delft
Prof. Dr. G. A. M. van Kuik	Technische Universiteit Delft
Prof. Dr. G. D. Padfield	University of Liverpool
Prof. Dr. J. H. de Leeuw	University of Toronto
Prof. Dr. M. Radeş	"Politehnica" University of Bucharest
Dr. S. Dijkstra	Technische Universiteit Delft
Dr. A. Marinescu	National Institute for Aerospace Research "Elie Carafoli", Bucharest

ISBN 90 - 9014594 - X

CIP-DATA KONINKLIJKE BIBLIOTHEEK, DEN HAAG

Pavel, Marilena Domnica

On the Necessary Degrees of Freedom for Helicopter and Wind Turbine Low-Frequency Mode Modeling / Marilena Domnica Pavel
Delft: Delft University of Technology. -Ill.
Delft: Thesis Delft Univesity of Technology. -With ref. -With summary in Dutch and Romanian.
NUGI 841
Keywords: Necessary Degrees of Freedom / Helicopters / Wind Turbines / Flight Mechanics / Structural Modeling

Printed in The Netherlands by Doc Vision BV. Technische Universiteit Delft

To my parents

Acknowledgements

First I would like to thank my supervisor, prof. dr. Theo van Holten, for his interest and advices he gave me during my research.

I owe many thanks to Koen Jessurun for his enthusiasm and the help he gave me to find my way in the "jungle" of rotorcraft instabilities. His knowledge on the subject and the references he advised me to read made me realise how complex the subject of prediction of dynamic behaviour of rotary wing systems is.

My gratitude goes also to prof. dr. Gareth Padfield for the fruitful discussions we had on the subject of reducing the model order in helicopter dynamics. I am grateful that he found the time to read the manuscript and for his valuable suggestions.

Many thanks go also to dr. Alexe Marinescu for reading and judging my dissertation and for validating the results I presented for the Puma helicopter on the simulator. I am also very grateful that he accepted to join the examination committee.

I thank Michiel Haanschoten for assisting me in any computer matter. I wish to thank all my colleagues from the Department of Flight Mechanics and Propulsion for the pleasant working atmosphere. All my good friends from Romania and colleagues from the National Institute of Aviation in Bucharest I thank for the contact we kept through the years and distance. Finally, special thanks to my good friend Dolf Bos for helping me to adapt to this culture, from learning me to stay on my bike to making me understand the people here.

Marilena Pavel
Delft, 24 January 2001

Summary

During the design of helicopters or horizontal-axis wind turbines, simulation models are developed for different purposes, such as to ascertain the device's performance; to ensure aeroelastic stability; to determine the system's response to different external perturbations; to determine fatigue characteristics as well as extreme loads in critical components or to design control systems. One of the first questions which must be answered before commencing the actual derivation of a simulation model, is how much detail should be considered in terms of number and type of mechanical degrees of freedom and level of aerodynamic modeling. For rotary wing devices this question is not yet solved. Contradictory statements are found in the literature when it comes to the question of which modes have a substantial effect on the low frequency dynamic characteristics important for helicopter piloted simulation or wind turbine structural modeling. The aim of the present dissertation is to develop a general method which can be used by the design-analyst to determine the necessary degrees of freedom to be considered in a low-frequency simulation model for helicopters and horizontal-axis wind turbines, before deriving a complete model.

A new method -the so-called "critical pole distance method"- was developed which can be used both as a design and an evaluation tool capable of determining the significant degrees of freedom of the simulation model. The critical pole distance method consists in essence of representing the uncoupled modes' eigenvalues in the complex plane and defining "critical regions" where potential couplings between different modes of motion occur. A critical region is formed by eigenvalues which can be considered "sufficiently close" together in the complex plane. To quantify the relative position of the eigenvalues in the complex plane a criterion was developed to provide an estimation as to the meaning of "sufficiently close" for the dynamic system analyzed.

Using the critical pole distance method, guidelines for the necessary model structure were elaborated for three cases: 1) investigation of the significant rotor disc-tilt modes in piloted simulation modeling; 2) investigation of the mechanism of instability of the KEWT two-bladed horizontal-axis wind turbine; 3) investigation of the effects of blade kinematic pitch-flap and pitch-lag couplings on the blade flap-lag motion in an articulated rotor in hovering flight. Criteria and rules of thumb on how to judge whether eigenvalues should be considered as sufficiently remote, or in close proximity, were developed for the critical pole distance method in each of the problems analyzed.

Concerning the effects of disc-tilt dynamics on the body dynamics, studying the natural and piloted behaviour of the articulated Puma SA-330 and semi-rigid Bölkow Bö-105 using the critical pole distance method and simulating a deceleration and a side-step manoeuvre, two critical regions of coupling between the body and the rotor disc-tilt motion were discovered: first, a critical region in the longitudinal plane of motion, formed by the body short-period mode eigenvalue and the regressing flapping mode eigenvalue; and second a critical region in the lateral plane of motion formed by the body roll-subsidence mode eigenvalue and the regressing flapping mode eigenvalue. A criterion to quantify the coupling between the body modes and the regressing flapping mode was established. The body/rotor disc-tilt coupling, in the case of the articulated

Puma helicopter depends on the manoeuvre performed: for the deceleration manoeuvre the couplings could be neglected whereas for the side-step manoeuvre they could not. The body/rotor disc-tilt coupling in the semi-rigid Bö-105 is always strong, independent of the manoeuvre performed.

Concerning the *chassis** second bending mode/rotor lead-lag instability on the KEWT wind turbine, according to the critical pole distance method, the prime responsible for this instability is the coupling between the harmonic ω_{DIF+I} of the differential lead-lag mode and the chassis second bending mode. These two modes form the main path through which the gravity excitation is transmitted from the blade to the chassis and back. Varying the blade and chassis characteristics, a criterion was developed for the critical pole distance method. Using this criterion, it was found that the instability could be eliminated either by increasing the tower damping ratio, or by softening the tower or by stiffening the blades.

Concerning the strength of the coupling between the flap and lag motions in a rotor blade, a quantitative criterion for the critical pole distance method was established on the basis of different kinematic pitch-flap and pitch-lag couplings in the system.

The critical pole distance criterion needs to be quantified by investigating a multitude of cases, before conclusions can be drawn. Therefore, this method should actually be considered an engineering approach to the problem of simulation modeling. The validity of the critical pole distance method was evaluated by comparing it to similar methods (methods able to give an indication of the level of detail in a simulation model, such as the Campbell diagram, the Milne criterion and the Vector Shift Method or methods used to determine the mechanism of instability of a rotary wing system such as the Force-Phasing Matrix Technique or the Energy-Flow method). The strength of the critical pole distance method is that it may be applied before the actual derivation of the coupled dynamic equations is undertaken.

Examining the problem of helicopter and wind turbine modeling in parallel, it appeared that there is a misunderstanding in the definition of soft/stiff configurations in the two communities. At first sight, it appears that modern wind turbines are becoming softer but in terms of non-dimensional flapping and lead-lag natural frequencies, they are actually stiffening. This observation serves as a warning to wind turbine designers to be aware that current wind turbine configurations are heading towards a new area of rotor and rotor/tower aeroelastic instabilities characteristic for stiff systems, which may be difficult to control and eliminate.

Concluding, the present dissertation may be considered a first step in developing a general method which can be used by the design-analyst to determine the necessary degrees of freedom for helicopters and horizontal-axis wind turbines. To obtain general guidelines about the necessary model structure, the critical pole distance method will have to be applied to a database of problems specific to helicopter and wind turbine low-frequency simulation-modeling. These proposed guidelines should take into consideration the desired accuracy and the purpose for which the dynamical model will be used.

Table of contents

Notations

A	constant in response of the 1-dof vibration problem (equation 2.12) and in the motion-induced load problem; constant in the wind turbine motion defined by equation 6.5; matrix of motion derivatives in the 6-dof helicopter model; area of the rotor disc $A= \pi R^2$ [m^2]
$A_2^* ... A_5^*$	terms in the wind turbine response expressed by equation 6.7
A_{lat}	matrix of motion derivatives in the 6-dof helicopter model in the lateral plane (equation E.72)
A_{long}	matrix of motion derivatives in the 6-dof helicopter model in the longitudinal plane (equation E.71)
a_0	coning angle; collective lead-lag mode [rad] collective mode in Coleman transformation (equation D.1)
a_1	longitudinal disc-tilt angle; $a_1>0$ if the disc plane tilts backwards [rad]
$a_1, ...a_n$	cyclic modes in the Coleman transformation (equation (D.1)) [rad]
B	constant in response of the 1-dof vibration problem (equation 2.12) and in the motion-induced load problem; matrix of control derivatives in the 6-dof helicopter model; terms in the wind turbine response expressed by equation 6.5
$B_2^* ... B_5^*$	terms in the wind turbine response expressed by equation 6.7, 6.8, 6.9
B_{lat}	matrix of control derivatives in the 6-dof helicopter model in the lateral plane (equation E.72)
B_{long}	matrix of control derivatives in the 6-dof helicopter model in the longitudinal plane (equation E.71)
b_0, b_1	terms in the wind turbine response in the asymptotic expansion of the differential lead-lag mode (equation 6.3)
$b_{00}, b_{01},$	terms of the asymptotic expansion in α_m of the differential lead-lag mode (equation F.28 and F.31)
b_1	lateral disc-tilt angle ($b_1>0$ for tiltwards to the azimuth position $\psi = 90^o$)
$b_1, ...b_n$	cyclic modes in the Coleman transformation (equation (D.1))
C	term in the wind turbine response of expression 6.6; damping matrix of an n-dof system
C_1, C_2	constants in the 1-dof response of a mass-spring-damper system
C_d	blade profile drag coefficient $C_d = 0.011 + 0.4\alpha_{ef}$ [-]
C_G	helicopter weight coefficient $C_G = \dfrac{M_{hel} g}{\rho A (\Omega R)^2}$ [-]
C_H	rotor drag force coefficient (equation E.29) [-]
C_{l_α}	blade lift curve slope [rad^{-1}]
$C_{l\,tr_\alpha}$	tailrotor lift curve slope [rad^{-1}]
$C_{l\,vt_\beta}$	vertical tail lift curve slope [rad^{-1}]
$C_{l\,ht_\alpha}$	horizontal tail lift curve slope [rad^{-1}]
$C_{L\,vt}$	vertical tail roll moment coefficient (equation E.57) [rad^{-1}]

C_Q rotor torque coefficient (equation E.28) [-]

C_R damping matrix of an n-dof system of equations in the rotating system in the Coleman transformation

$C_{m\,E}$ coefficient of pitch moment induced by rotor eccentricity (equation E.33)

$C_{m\,ht}$ horizontal tail pitch moment coefficient (equation E.51)

$C_{m\,fus}$ coefficient of fuselage pitch moment (equation E.41)

$C_{n\,fus}$ coefficient of fuselage yaw moment (equation E.46)

$C_{N\,vt}$ vertical tail yaw moment coefficient (equation E.58) [rad^{-1}]

C_{NR} damping matrix of an n-dof system of equations in the non-rotating system in the Coleman transformation (equation D.10)

C_S rotor lateral force coefficient (equation E.27) [-]

C_T chassis damping coefficient

$C_{T\,crit}$ chassis critical damping coefficient $C_{T\,crit} = 2\sqrt{K_T M_{tot}} = 2\omega_T M_{tot}$

C_T^{elem} thrust coefficient w.r.t. disc plane in blade-element theory (equation E.25) [-]

C_T^{Gl} thrust coefficient calculated with Glauert theory (equation E.26)

$C_{T\,tr}^{elem}$ tailrotor thrust coefficient in blade-element theory (equation E.35)

$C_{T\,tr}^{Gl}$ tailrotor thrust coefficient in Glauert theory (equation E.36)

$C_{Y\,fus}$ coefficient of lateral force in sideslip flight (equation E.45)

C_β, C_ζ coefficients of the flap-lag equations of motion (equation 7.2)

$C_{\beta\zeta}$, $C_{\zeta\beta}$ coefficients of the flap-lag equations of motion (equation 7.2)

C_ζ blade lead-lag damping coefficient

$C_{\zeta\,crit}$ blade critical lead-lag damping coefficient $C_{\zeta\,crit} = 2\sqrt{K_\zeta I_{bl}} = 2\omega_\zeta I_{bl}$

c current chord length of blade section [m]; damping in the 1-dof vibration and dynamic absorber problems $\left[\frac{N\,sec}{m}\right]$; helicopter rate of climb [m/sec]

c_2 damping of the motion-induced load

c_c critical damping in the 1-dof vibration problem $c_c = 2\sqrt{k\,m}$ $\left[\frac{N\,kg}{m}\right]$

$c_{c\,\delta}$ critical damping in the dynamic absorber problem $\left[\frac{N\,sec}{m}\right]$

c_{des} helicopter desired rate of climb [m/sec]

c_e equivalent blade chord [m]

D term of the wind turbine response given by equation (6.6)

dD elementary drag force [N]

$\bar{d}(\omega_{excit},\omega)$ non-dimensional distance from an eigenvalue to a line of excitation in the complex plane (equation 2.31) [-]

$d_0, d_1, ..$ terms of wind turbine solution of the collective lead-lag mode (equation 6.3)

$d_{00}, d_{01}, ..$ terms of asymptotic expansion in α_m of collective lead-lag mode (equation F.28 and F.31)

$d_{fus}(x)$ fuselage diameter in horizontal projection [m] (see Figure E.1)

$E(t)$, $E(s)$	external excitation force applied to an n-dof system [N]
$E(\psi_i)$	matrix in Floquet method defined by equation G.11
E_r, E_0, E_{bl}	matrices of rotation defined as in equation F.1
e_{c0},e_{c1}, e_{s0},e_{s1}	terms of asymptotic expansion in ε of collective lead-lag mode (equation F.32 and F.47)
e_β	flapping hinge offset measured from the hub axis of rotation [m]
e_ζ	lagging hinge offset measured from the hub axis in Chapter 3 and from the flapping hinge in Chapter 7 [m]
$F(s)$	transfer function in the critical pole distance method (equation 4.6)
$F(\psi_i)$	matrix in Floquet method defined by equation G.12
F_0	amplitude of the sinusoidal external response (equation 2.10); parasite drag area of the helicopter [m^2]
$F_{appl}(t)$	external force applied to the mass-spring-damper system in the time domain (equation 2.10)
F_{cf}	helicopter blade centrifugal force in the 6-dof helicopter model (equation E.33) [N]
dF_{cf}	centrifugal force on the blade element (equations B.28 and C.27) [N]
F_{ij}, F_{ji}, F_{ik}, F_{jk}	terms respectively defined as T_{ij}/N_i, T_{ji}/N_j, T_{ik}/N_i, and T_{jk}/N_j
dF_i	blade-element inertial force [N]
F_{NR}	vector of external forces of an n-dof system in the non-rotating system in the Coleman transformation (equation D.10)
F_R	vector of external forces of an n-dof system in the rotating system in the Coleman transformation
dF_y	resultant of blade lift and drag force tangential to the blade (equation B.22) [N]
dF_z	resultant of blade lift and drag force perpendicular to the blade (equation B.22) [N]
dG	gravity force on the wind turbine blade element (component in flapping plane defined by equation B.34 and in lagging plane by C.34) [N]
F_{tr}	tailrotor fin blockage factor (equation E.38) [-]
F_{xr}	force component exerted by the blade lead-lag motion on the chassis expressed in the blade rotating system (equation 6.13) [N]
F_{yr}	force component exerted by the blade lead-lag motion on the chassis expressed in the blade rotating system (equation 6.13) [N]
F_{x0}	F_{xr} expressed in the chassis non-rotating system (equation 6.14) [N]
F_{y0}	F_{yr} expressed in the chassis non-rotating system (equation 6.14) [N]
F_ε	term defined as T_ε/N_2 T_ε/N_j
f	position of the rotor hub on the x-axis w.r.t the helicopter body-axes system [m]; ratio between the torsional stiffness of the blade and pitch control system $f = \frac{K_\Phi}{K_\phi}$ [-]; force exerted on the blade due to chassis motion (equation 6.22) [N]
$f(s)$	characteristic equation in flap-lag model of Chapter 7 (equation 7.11)
f_1	position of the rotor hub w.r.t the helicopter body-axes system on the y-

	axis [m]
f_{12}, ...f_{nn}	coupling terms in an n-dof system (terms multiplying $\ddot{x}$)
f_{c0},f_{c1}, f_{s0}, f_{s1}	terms of asymptotic expansion in ε of differential lead-lag mode (equations F.32 and F.49)
G	transfer function (equation 2.17 and 2.27); gravity term in the wind turbine lead-lag equation of motion defined as $G = \frac{g\,\sigma_{bl}}{I_{bl}} = \frac{g\,m_{bl}\,\bar{r}_g\,R}{I_{bl}}$; gravity term in the flap-lag equations of motion defined as $G = \frac{g}{\Omega^2 l}$
G(s)	transfer function defined for the critical pole distance criterion T'_{12}/N_1
$G(\psi_i)$	matrix in Floquet method defined by equation G.13
$G_{bo}(s)$	transfer function giving the answer in pitch to a longitudinal cyclic (equation 5.3) in the body motion
$G_{bo\text{-}fl}(s)$	transfer function giving the answer in pitch to a longitudinal cyclic (equation 5.8) when disc-tilt dynamics included in the body motion
g	gravitational acceleration
g_{12},...$g_{n\ n-1}$	coupling terms on an n-dof system (terms multiplying $\dot{x}$)
g_{c1}, g_{s1}	terms of asymptotic expansion in ε of chassis second bending mode (equation F.40)
H	coefficient used in chapter 7 and defined as $H = m_{bl}/(\rho \pi c l)$
$H(\psi_i)$	matrix in Floquet method defined by equation G.10
H_{dp}	component of the rotor aerodynamic force in the horizontal plane
h	helicopter rotor hub position relative to z-axis [m] (see figure E.1(a)); step integration in Floquet method; hub position w.r.t z-axis in the body system of reference [m]
h, h_{des}	helicopter altitude and desired altitude [m]
h_{12}, .. $h_{n\ n-1}$	coupling terms of an n-dof system (terms multiplying x)
h_{ht}	horizontal tail position w.r.t. body system of reference on the z-axis [m]
h_{tr}	tailrotor position w.r.t. z-axis
h_{vt}	vertical tail position w.r.t. body system of reference on the z-axis [m]
I	unit matrix
I_{bl}	blade moment of inertia of a uniform blade (equation B.31) [kg m^3]
I_k	blade moment of inertia
I_x	helicopter moment of inertia about body x-axis [kg m^2]
I_y	helicopter moment of inertia about body y-axis [kg m^2]
I_z	helicopter moment of inertia about body z-axis [kg m^2]
I_{xz}	helicopter product of inertia about body x and z-axes [kg m^2]
I_β	moment of inertia w.r.t flapping hinge $I_\beta = \int_0^{R(1-e_\beta)} r^2 dm$ [kg m^3]
K	spring constant of the dynamic absorber problem [N/m]; the term $[T_{dp}h + (N/2)K_\beta]/I_y$ in helicopter pitch equation of motion (Chapter 5, section 5.1); stiffness matrix in an n-dof model; matrix of gains in 6-dof

helicopter model

K_c, $K_{corr\ c}$ climb velocity controller $\left[\frac{1}{m/sec}\right]$, [1/m]

K_{fus} correction coefficient in the fuselage pitching moment (figure E.3)

K_h altitude hold controller [1/m]

K_{ht} correction coefficient in the horizontal tail pitching moment (figure E.4)

K_{lat} matrix of gains in 6-dof helicopter model in lateral plane (equation E.76)

K_{long} matrix of gains in 6-dof helicopter model in longitudinal plane (equation E.75)

K_{NR} stiffness matrix of an n-dof system of equations in the non-rotating system in the Coleman transformation (equation D.10)

$K_{P\beta}$ pitch-flap coupling ($K_{P\beta}>0$ for pitch nose up with flap up)

$K_{P\zeta}$ pitch-lag coupling ($K_{P\zeta}>0$ for pitch nose up with lead)

K_p roll rate controller

K_q pitch rate controller

K_R stiffness matrix of an n-dof system of equations in the rotating system in the Coleman transformation

K_r yaw rate hold controller $\left[\frac{1}{rad/sec}\right]$

K_{SR} K in a semi-rigid rotor

K_T stiffness coefficient of wind turbine chassis; K in a teetering rotor

K_{tr} main rotor downwash factor at tailrotor $K_{tr} = 1$

K_u horizontal velocity hold controller $\left[\frac{1}{m/sec}\right]$

K_v lateral velocity hold controller $\left[\frac{1}{m/sec}\right]$

K_x, $K_{x\ corr}$ horizontal distance controller [1/m], [1/ (rad sec)]

K_y, $K_{y\ corr}$ lateral distance hold controller [1/m], [1/(m sec)]

K_β flap hinge spring constant of a helicopter and wind turbine blade [N/m]

K_ζ lagging hinge spring constant of a helicopter and wind turbine blade; stiffness coefficient of wind turbine blade lead-lag [N/m]

K_β, K_ζ coefficients of flap-lag equations of motion (equation 7.2)

$K_{\beta\zeta}$, $K_{\zeta\beta}$ coefficients of flap-lag equations of motion (equation 7.2)

K_Θ, $K_{\Theta\ corr}$ pitch attitude hold controller [1/rad], [1/(rad sec)]

K_Θ term for the distribution of torsional stiffness between the blade and the pitch control system defined as $K_\Theta = \frac{K_\Phi K_\phi}{K_\Phi + K_\phi}$

K_Φ $K_{\Phi\ corr}$ roll angle hold controller [1/rad], [1/(rad sec)]

K_Φ torsion stiffness of the pitch control system

K_Ψ, $K_{\Psi\ corr}$ yaw angle hold controller [1/rad], [1/(rad sec)]

K_ϕ torsion stiffness of the blade

k spring constant of the mass-spring-damper system and in dynamic absorber model [N/m]

L	helicopter total roll moment [Nm]
dL	lift force on the blade element [N]
L_E	roll moment due to flap eccentricity [Nm]
dL_{excit}	lift force on the blade (component independent on the flapping excitation)
L_{NR}	matrix of Coleman transformation coefficients in the non-rotating system
L_p , l_p	dimensional and non-dimensional derivative of L-moment w.r.t. to roll rate [N m sec]
L_R	matrix of Coleman transformation coefficients in the rotating system
L_r , l_r	dimensional and non-dimensional derivative of L-moment w.r.t. to yaw rate [N m sec]
$Lift_{ht}$	horizontal tail lift force [N]
$Lift_{vt}$	vertical tail lift force [N]
L_v , l_v	dimensional and non-dimensional derivative of L-moment w.r.t. to lateral velocity [N sec]
$L_{\theta\,1c}$, $l_{\theta\,1c}$	dimensional and non-dimensional derivative of L-moment w.r.t. to lateral cyclic [N m]
$L_{\theta\,0tr}$, $l_{\theta\,0tr}$	dimensional and non-dimensional derivative of L-moment w.r.t. to tailrotor collective [N m]
$\Delta L\|_{\dot{\beta}}$, $\Delta L\|_{\beta}$	change in lift due to flapping motion (equations B.15, B.16 for helicopter case and equations B.17, B.18 for the wind turbine case) [N]
l	length of blade measured from the flapping hinge (Chapter 7) [m]
l_{ht} , $\bar{l}_{ht}$	dimensional [m] and non-dimensional [-] horizontal tail position w.r.t helicopter system of reference measured along the x-axis (see figure E.1(a)) (measured from the centre of pressure of the horizontal tail)
l_{tr} , $\bar{l}_{tr}$	dimensional [m] and non-dimensional [-] tailrotor position w.r.t helicopter system of reference measured along the x-axis (see figure E.1(a))
l_{vt} , $\bar{l}_{vt}$	dimensional [m] and non-dimensional [-] vertical tail position w.r.t helicopter system of reference measured on the x axis (see figure E.1(a)) (measured from the centre of pressure of the vertical tail)
M	mass in dynamic absorber problem; helicopter total pitch moment (equation E.19) [Nm]
M_1, M_2	maximum elements of the coupling matrices in Milne criterion and in flap-lag problem of Chapter 7 (equation 7.17)
$M_{a\ excit}$	aerodynamic excitation in blade flapping motion (equation B.23) [Nm]
$M_{bo\text{-}fl}$, $M_{fl\text{-}bo}$	maximum of coupling terms in body-disc tilt according to Milne criterion (equation 5.17)
M_{ch}	chassis mass [kg]
M_E	pitch moment due to flapping eccentricity (equation E.32) [Nm]
M_{fus}	fuselage pitch moment (equation E.40) [Nm]
M_{ht}	horizontal tail pitch moment (equation E.48) [Nm]
M_{hel}	helicopter mass [kg]

M_q , m_q dimensional and non-dimensional derivative of M-moment w.r.t. to pitch rate in the helicopter 6-dof linear model [N m sec]

M_R inertia matrix of an n-dof system of equations in the rotating system in the Coleman transformation

M_{sh} the lead-lag moment resulting form the chassis motion when the gravity force is neglected (equation 6.23) [Nm]

M^*_{sh} M_{sh} calculated with the gravity force effect (equation 6.26)

M_{tot} total mass of the wind turbine system $M_{tot}= M_{ch}+N\ m_{bl}$ [kg]

M_u , m_u dimensional [N sec] and non-dimensional [-] derivative of M-moment w.r.t. to horizontal velocity in the helicopter 6-dof linear model

M_w , m_w dimensional [N sec] and non-dimensional [-] derivative of M-moment w.r.t. to vertical velocity in the helicopter 6-dof linear model

$M_{\dot{w}}$, $m_{\dot{w}}$ dimensional [N sec^2]and non-dimensional derivative of M-moment w.r.t. to vertical acceleration in the helicopter 6-dof linear model

M^{β}_{aero} aerodynamic flapping moment (equation B.21) [N m]

M^{ζ}_{aero} aerodynamic lagging moment on the blade (equation C.16) [N m]

$M^{\zeta}_{aero\ init}$ initial aerodynamic lagging moment on the blade (equation C.15) [N m]

M_β restraint moment on the flapping hinge (equation B.32) [N m]

M_ζ restraint moment on the lagging hinge (equation C.32) [N m]

$\Delta M_a|_{\dot{\beta}}$, $\Delta M_a|_{\beta}$ aerodynamic moment induced by the blade flapping motion (equations B.24, B.25 for the helicopter and equations B.26, B.27 for the wind turbine) [N m]

$\Delta M_a|_{\dot{\zeta}}$, $\Delta M_a|_{\zeta}$ aerodynamic moment induced by blade lead-lag motion (for the helicopter equations C.19, C.20, C.21, C.22 and for the wind turbine equations C.23, C.24, C.25, C.26) [N m]

$M_{\theta 1s}$, $m_{\theta 1s}$ dimensional and non-dimensional derivative of M-moment w.r.t. to longitudinal cyclic in the helicopter 6-dof linear model [N m]

$M_{\theta 0}$, $m_{\theta 0}$ dimensional and non-dimensional derivative of M-moment w.r.t. to collective in the helicopter 6-dof linear model [Nm]

m mass in 1-dof vibration problem [kg]; blade mass per unit length in Chapter 7

m^* ratio m/M of masses in dynamic absorber problem [-]

dm blade element mass [kg]

m_{bl} blade mass [kg]

m_k mass of k-th blade [kg]

N number of blades of the rotor [-]; helicopter total yaw moment (equation E.20) [Nm]

N_1,...N_n terms including the uncoupled system characteristics in the critical pole distance criterion $N_i = s^2 + 2\xi_i\omega_i s + \omega_i^2$

$|N_{Freg}\ N_{SP}|$ critical pole distance criterion for short-period/regressing flapping modes coupling (equation 5.24)

$|N_{Freg}\ N_{Roll}|$ critical pole distance criterion for roll-subsidence/regressing flapping

	modes coupling (equation 5.32)
$\|N_{body}\ N_{Freg}\|$	critical pole distance criterion for body/rotor disc-tilt dynamics coupling (final criterion in Critical pole distance criterion)
$\|N_T\ N_{DIF+1}\|$	critical pole distance criterion for chassis/differential lead-lag mode in harmonic ω_{DIF+1} coupling (equation 6.36)
$\|N_T\ N_{DIF-1}\|$	critical pole distance criterion for chassis/differential lead-lag mode in harmonic ω_{DIF+1} coupling (equation 6.39)
$\|N_\beta\ N_\zeta\|$	critical pole distance criterion for flap-lag motion (equation 7.10)
N_{vt}	vertical tail yaw moment w.r.t. body system of reference (equation E.54) [N m]
N_p , n_p	dimensional and non-dimensional derivative of N-moment w.r.t. to roll rate in the helicopter 6-dof linear model [N m sec]
N_r , n_r	dimensional and non-dimensional derivative of N-moment w.r.t. to yaw rate in the helicopter 6-dof linear model [N m sec]
N_v , n_v	dimensional and non-dimensional derivative of N-moment w.r.t. to lateral velocity in the helicopter 6-dof linear model [N sec]
$N_{\theta\,1c}$, $n_{\theta\,1c}$	dimensional and non-dimensional derivative of N-moment w.r.t. to lateral cyclic in the helicopter 6-dof linear model [N m]
$N_{\theta\,0tr}$, $n_{\theta\,0tr}$	dimensional and non-dimensional derivative of N-moment w.r.t. to tailrotor collective in the helicopter 6-dof linear model [N m]
$p,\bar{p}$	helicopter roll rate [rad/s] and its non-dimensional value [-]
p_0	helicopter roll rate in basic motion [rad/sec]
Q	Floquet transition matrix defined by G.14 and used in equation 6.34; rotor torque (equation E.24)
$Q_k^{noncons}$	non-conservative forces in Lagrange equations of motion [N]
q , $\bar{q}$	helicopter pitch rate [rad/sec] and its non-dimensional value [-]
$\hat{q}_{bo}$	helicopter pitch rate response in Laplace domain (equation 5.4)
$\hat{q}_{bo\text{-}fl}$	helicopter pitch rate response in Laplace domain (equation 5.9) when the disc-tilt dynamic is included
q_0	helicopter pitch rate in basic motion [rad/sec]
R	amplitude of response to an external sinusoidal force (equation 2.13) [m]; radius in Milne criterion equal to the minimum of the eigenvalues of subsystem B (of higher dynamics) and of the flapping motion in the flap-lag problem of Chapter 7; helicopter or wind turbine rotor radius (measured from the hub) [m]
R_{a0}	amplitude of collective lead-lag mode (equation 6.11)
R_{fl}	radius of disc-tilt motion in the Milne criterion
R_{fus}	fuselage resistance force (equation E.39) [N]
R_{steady}	static response to applied load in 1-dof model
R_{tr}	tailrotor radius [m]
R_η	amplitude of chassis response in the second bending mode (equation 6.10) [-]

$R_{\zeta\, N/2}$	amplitude of differential lead-lag mode (equation 6.12) [-]
r	current blade-element coordinate along blade axis measured from the hub [m]; radius in Milne criterion equal to the maximum of the eigenvalues of subsystem A (of slow dynamics) and of lead-lag motion in the flap-lag problem of Chapter 7
$r,\bar{r}$	helicopter yaw rate [rad/s] and its non-dimensional value [-]
r_0	helicopter yaw rate in basic motion [rad/sec]
r_{bl}	coordinate of blade in the wind turbine blade/chassis motion [m]
r_{bo}	radius of body motion in the Milne criterion [m]
r_g , $\bar{r}_g$	dimensional and non-dimensional coordinate of the blade centre of gravity along the blade [m]
$S(\psi_i)$	matrix in Floquet method defined by equation G.3
S_{dp}	lateral rotor force defined by equation E.23 [N]
S_{vt} , $\bar{S}_{vt}$	dimensional and non-dimensional vertical tail surface [m^2]
S_{ht} , $\bar{S}_{ht}$	dimensional and non-dimensional horizontal tail surface [m^2]
S_{fus}	fuselage surface [m^2]
s	Laplace variable
$s_{1,2}$	eigenvalues of 1-dof problem (equation 2.5, 2.6 or 2.7)
s_k	the k-th eigenvalues of an n-dof system
s_{bo}^{T}, s_{bo}^{SR}	poles of the helicopter body motion for a teetering and a semi-rigid configuration (equation 5.5)
$s_{bo\text{-}fl}^{T}$, $s_{bo\text{-}fl}^{SR}$	poles of the helicopter body motion for a teetering and a semi-rigid configuration (equation 5.10, 5.11) when disc-tilt dynamics is included
s_{COL}	eigenvalues of the uncoupled collective lead-lag mode
s_{DIF}	eigenvalues of the uncoupled differential lead-lag mode
s_{DIF+1}, s_{DIF-1}	eigenvalues of the uncoupled differential lead-lag mode in the harmonics ω_{DIF+1}, ω_{DIF-1}
s_{fl}	poles of the uncoupled disc-tilt motion (equation 5.14)
s_T	eigenvalues of the uncoupled chassis motion (equation 6.28)
$s_{NR\ adv}$	eigenvalue of the advancing flapping mode (equation D.15)
$s_{NR\ reg}$	eigenvalue of the regressing flapping mode (equation D.15)
$s_{NR\ con}$	eigenvalue of coning mode (equation D.16)
$s_{NR\ \beta N/2}$	eigenvalue of differential flapping mode (equation D.16)
s_ζ	uncoupled lead-lag blade eigenvalue (equations 6.30 and 7.6)
s_β	uncoupled flapping blade eigenvalue (equation 7.5)
$s_{\beta\zeta}$	coupled flap-lag eigenvalue (equation 7.13)
$s_{\zeta\beta}$	coupled lag-flap eigenvalue (equation 7.14)
Δs_i	vector change between the uncoupled and coupled poles in vector shift method
$T_{12}...T_{n\ n-1}$	coupling terms in an n-dof system in the critical pole distance criterion
$T'_{12}...T'_{n\ n-1}$	the negative terms $T_{12}...T_{n\ n-1}$
T_e	term of the external force in the critical pole distance criterion
T_{dp}	helicopter thrust vector w.r.t. the disc plane (defined by E.21) [N]

T_k	kinetic energy of the k-th blade [J]
T_{tot}	total kinetic energy in the wind turbine system of equations of motion (equation F.9) [J]
T_{tr}	tailrotor thrust defined in equation E.34 [N]
t	time variable [sec]
U	vector of helicopter control states
U_0 , $\bar{U}_0$	dimensional [m/sec] and non-dimensional [-] wind turbine crosswind velocity component
U_P	perturbed component of velocity perpendicular to the shaft plane (equation B.9 and B.11) [m/sec]
$U_{P\ init}$	initial component of velocity perpendicular to the shaft plane (equation B.3 for helicopter case and B.6 for wind turbine case) [m/sec]
U_R	perturbed component of velocity along the blade axis due to flapping or lagging motion of the blade (equations B.8, B.10, C.1, C.3) [m/sec]
$U_{R\ init}$	initial component of velocity along the blade axis (equation B.1 and B.4) [m/sec]
U_T	perturbed component of velocity tangential to the shaft plane [m/sec]
$U_{T\ init}$	initial component of velocity tangential to the shaft plane (equation B.2 for the helicopter and B.5 for the wind turbine) [m/sec]
$\Delta U_P\|_{\dot{\beta}}$, $\Delta U_P\|_{\beta}$	variation in the velocity perpendicular to the shaft plane due to the flapping motion [m/sec]
$\Delta U_T\|_{\dot{\beta}}$, $\Delta U_T\|_{\beta}$	variation in the velocity tangential to the shaft plane due to the lead-lag motion [m/sec]
u	helicopter airspeed component along body x-axis [m/sec]
u_0	helicopter airspeed component along x-axis in basic motion [m/sec]
V	potential energy[J]; helicopter velocity [m/sec]
V_0	velocity component perpendicular to rotor disc plane (see figure B.2 for helicopter and Figure B.3 for the wind turbine) [m/sec]
V_{init}	initial velocity on the blade element for helicopter and wind turbines [m/sec]
$(Vol_{fus})_m$	equivalent body volume to the fuselage in the horizontal plane having only circular sections [m^3]
$(Vol_{fus})_n$	equivalent body volume to the fuselage in the lateral plane having only circular sections [m^3]
$(Vol)_{ht}$	horizontal tail volume [m^3]
V_{ht}	helicopter velocity in the horizontal tail region (equation E.49) [m/sec]
V_{vt}	helicopter velocity in the vertical tail region (equation E.55) [m/sec]
v_i	induced downwash velocity [m/sec]
v	component of airspeed along body y-axis [m/sec]
v_0	component of helicopter airspeed along y-axis in basic motion [m/sec]
w	component of airspeed along body z-axis [m/sec]
w_0	component of helicopter airspeed along z-axis in basic motion [m/sec]
X	vector of helicopter motion states; total aerodynamic force on x axis

(equation E.15) [N]

X_A, X_B partitioning an n-dof system in Milne criterion (equation 4.51)

X_q , x_q dimensional and non-dimensional derivative of X-force w.r.t. to pitch rate [N sec]

X_u , x_u dimensional and non-dimensional derivative of X-force w.r.t. to horizontal velocity in the helicopter 6-dof linear model [N sec]

X_w , x_w dimensional and non-dimensional derivative of X-force w.r.t. to vertical velocity in the helicopter 6-dof linear model [N sec/m]

$X_{\theta 0}$, $x_{\theta 0}$ dimensional and non-dimensional derivative of X-force w.r.t. to collective in the helicopter 6-dof linear model [N]

$X_{\theta 1s}$, $x_{\theta 1s}$ dimensional and non-dimensional derivative of X-force w.r.t. to longitudinal cyclic in the helicopter 6-dof linear model [N]

x degree of freedom of the 1-dof problem; displacement of chassis in second bending mode; helicopter longitudinal position (see Figure E.2)

$x_1 ... x_n$ degree of freedom of an n-dof system

x_0 , $\dot{x}_0$ initial conditions in the 1-dof problem

x_{des} helicopter desired longitudinal position [m]

x_{gen} general solution of 1-dof problem (equation 2.9) [m]

x_{part} particular solution of 1-dof problem (equation 2.11) [m]

x_{tot} total solution of 1-dof problem (equation 2.14) [m]

Y total aerodynamic force on y axis (equation E.16) [N]

Y_{fus} fuselage lateral force in sideslip flight (equation E.43) [N]

Y_v , y_v dimensional and non-dimensional derivative of Y-force w.r.t. to lateral velocity in the helicopter 6-dof linear model [N sec/m]

$Y_{\theta 1c}$, $y_{\theta 1c}$ dimensional and non-dimensional derivative of Y-force w.r.t. to lateral cyclic in the helicopter 6-dof linear model [N]

$Y_{\theta 0tr}$, $y_{\theta 0tr}$ dimensional and non-dimensional derivative of Y-force w.r.t. to tailrotor collective in the helicopter 6-dof linear model [N]

y, y_{des} helicopter lateral position and desired lateral position (see Figure E.2) [m]

Z total aerodynamic force on z axis (equation E.17) [N]

Z_u , z_u dimensional and non-dimensional derivative of Z-force w.r.t. to horizontal velocity in the helicopter 6-dof linear model [N sec/m]

Z_q , z_q dimensional and non-dimensional derivative of Z-force w.r.t. to pitch rate in the helicopter 6-dof linear model [N sec]

Z_w , z_w dimensional and non-dimensional derivative of Z-force w.r.t. to vertical velocity in the helicopter 6-dof linear model [N sec]

$Z_{\theta 0}$, $z_{\theta 0}$ dimensional and non-dimensional derivative of Z-force w.r.t. to collective in the helicopter 6-dof linear model [N]

$Z_{\theta 1s}$, $z_{\theta 1s}$ dimensional and non-dimensional derivative of Z-force w.r.t. to longitudinal cyclic in the helicopter 6-dof linear model [N]

z zeros of an eigenvalue problem and in the body/disc-tilt motion (equation

5.12); helicopter position along Earth Z-axis (see Figure E.2) [m]

α_{dp}, α_{sp}, α_{cp} blade incidence w.r.t. respectively disc plane, shaft plane and control plane [rad]

α_{ef} perturbed blade-element angle of attack due to flapping or lead-lag motion (equations B.12 for the flapping motion and C.8 for the lead-lag motion) [rad]

$\alpha_{ef\ init}$ initial blade-element angle of attack (equation B.7 in the flapping motion and C.7 in the lead-lag motion) [rad]

α_{fus} fuselage angle of attack (see Figure E.1a) [rad]

α_{ht} horizontal stabilizer incidence (equation E.50) [rad]

$\alpha_{0\ ht}$ built-in horizontal stabilizer incidence [rad]

α_m coefficient in the blade lead-lag/ chassis second bending modes coupled equations in Chapter 6 ($\alpha_m=2+M_{ch}/m_{bl}$)

$\alpha_{sp\ |\ Mfus=0}$ rotor incidence corresponding to zero fuselage pitching moment [rad]

α_2 inclination of lagging hinge (see Figure 3.7) ($\alpha_2>0$ for lag back with pitch-nose down) [deg]

$\Delta\alpha|_{\dot\beta}$, $\Delta\alpha|_{\beta}$ variation in blade angle of attack due to blade flapping motion (equation B.13, B.14) [rad]

β blade flapping in the helicopter 6-dof model $(\beta = a_0 - a_1\cos\psi - b_1\sin\psi)$

β_0 steady-state flapping angle in the flap-lag motion (equation 7.4) [rad]

β_d blade droop angle (see section H.4.2, Appendix H) [rad]

β_k flapping degree of freedom of the k-th blade [rad]

$\beta_{N/2}$ differential flapping as defined by Coleman transformation [rad]

β_{NR} coordinates of flapping motion in the non-rotating system as defined by the Coleman transformation [rad]

β_{pc} blade precone angle (see section H.4.1, Appendix H) [rad]

β_R coordinates of flapping motion in the rotating system as defined by the Coleman transformation [rad]

β_s helicopter sideslip angle [rad]

β_{vt} vertical tail incidence defined in E.54 [rad]

$\beta_{0\ vt}$ vertical tail built-in incidence [rad]

χ_k general rotor blade degree of freedom of the k-th blade [rad]

χ_{NR} vector of coordinates in the non-rotating system as defined by the Coleman transformation $\chi_{NR} = \{a_0\ a_1\ b_1\ \chi_{N/2} \cdots\ a_N\ b_N\}^T$ [rad]

$\chi_{N/2}$ differential rotor mode in the Coleman transformation [rad]

χ_R vector of coordinates in the rotating system as defined by the Coleman transformation $\chi_R = \{\chi_1\ \chi_2\ \chi_3\ \cdots\ \chi_N\}^T$ [rad]

Δ determinant of characteristic equation in an n-dof linear system (equation 4.48)

$\Delta^*_{j1} \ldots \Delta^*_{jn}$ minors of elements $T_{j1} \ldots T_{jn}$ in critical pole distance criterion (defined by equation 4.34)

$\Delta^*_{I1} \ldots \Delta^*_{In}$ minors of elements $N_1 \ldots T_{In}$ in vector shift method (equation 4.48)

$|\Delta^*_{11}|$, $|\Delta^*_{12}|$ magnitude of modal ratio of pole s_i (equation 4.50)

δ phase angle in 1-dof problem and in response to an external sinusoidal force (equation 2.13); displacement of mass m in dynamic absorber problem; angle between the blade and the centrifugal moment arm defined in Figure C.4

δ_1 inclination of lagging hinge (see Figure 7.1 and 7.2) ($\delta_1>0$ for lag back with pitch-nose down) [deg]

δ_3 inclination of flapping hinge (see Figure 7.1 and 7.2) ($\delta_3>0$ for flap up with pitch-nose down) [deg]

ε small parameter in pendular resonances; unit step input applied to an n-dof system in the critical pole distance criterion; gravity term in the KEWT wind turbine motion defined as $\varepsilon = g / R$

ε_0 downwash angle ($\varepsilon_0 = v_i / V$)

ε_{ht} medium downwash angle at the horizontal tail [rad]

ε_β non-dimensional value of flapping hinge offset e_β

ε_ζ non-dimensional value of lagging hinge offset e_ζ

$\Phi^{(k)}$ the k-th eigenvector of the general solution of an n-dof system of elements ϕ_i

Φ_0 helicopter roll angle in basic motion

Φ, Φ_{des} Euler roll angle and desired roll angle [rad]

ϕ_{init} blade initial inflow angle (equation B.7)

ϕ blade perturbed inflow angle (equation B.12)

γ Lock number $\gamma = \left(\rho C_l^\alpha c_e R^4\right)/I_{bl}$

η non-dimensional wind turbine chassis displacement in the second bending mode $\eta = x / R$

η_0, η_1... terms of the expansion of the wind turbine motion (equation 6.3)

Λ_k eigenvalues of Floquet transition matrix

λ_i non-dimensional uniform induced downwash of the rotor [-]

$\lambda_{i\,tr}$ non-dimensional uniform induced downwash of the tailrotor [-]

λ term $\lambda = -\mu_z + \lambda_i$ in the 6-dof helicopter model [-]

λ_{tr} $\lambda_{tr} = -\mu_{z\,tr} + \lambda_{i\,tr}$ uniform induced downwash of the tailrotor [-]

μ helicopter advance ratio $\mu \approx V / (\Omega R)$

μ_x non-dimensional u component of helicopter velocity $\mu_x = u / \Omega R$ [-]

$\mu_{x\,tr}$ non-dimensional tailrotor velocity along x-axis (equation E.37) [-]

μ_y non-dimensional v component of helicopter velocity $\mu_y = v / \Omega R$ [-]

μ_z non-dimensional w component of helicopter velocity $\mu_z = w / \Omega R$ [-]

$\mu_{z\,tr}$ non-dimensional tailrotor velocity along z-axis (equation E.37) [-]

ν_β non-dimensional rotating flapping frequency $\nu_\beta = \sqrt{1 + \bar{\omega}_\beta^2 + \frac{3}{2}\frac{\varepsilon_\beta}{(1-\varepsilon_\beta)}}$ [-]

ν_ζ	non-dimensional rotating lead-lag frequency $\nu_\zeta = \sqrt{\bar{\omega}_\zeta^2 + \frac{3}{2}\frac{\varepsilon_\zeta}{(1-\varepsilon_\zeta)}}$ [-]
Θ, Θ_{des}	Euler pitch angle and desired pitch angle [rad]
Θ_0	pitch angle in helicopter basic motion [rad]
θ	blade pitch angle in the 6-dof model ($\theta = \theta_0 + \theta_{tw} - \theta_{1c}\cos\psi - \theta_{1s}\sin\psi$)
θ_p	blade pitch angle [rad]
θ_0	blade collective pitch [rad]; steady-state blade pitch angle in flap-lag problem (equation 7.4) [rad]
θ_{0tr}	tailrotor collective [rad]
θ_{1c}	lateral cyclic pitch ($\theta_{1c} > 0$ for pilot stick to the right for the counter-clockwise helicopter, and to the left for the clockwise helicopter) [rad]
θ_{1s}	longitudinal cyclic pitch ($\theta_{1s} > 0$ for stick forward) [rad]
θ_{fus}	helicopter pitch angle (see Figure 5.1) [rad]
θ_{tw}	blade twist [rad]
ρ	air density $\rho = 1.225$ [kg/m^3]
ρ_0	blade displacement in the coupled blade/chassis motion seen in the chassis system of reference [m]
ρ_{bl}	blade displacement in the coupled blade/chassis motion seen in the blade system of reference [m]
σ	decay coefficient in the 1-dof vibrating system ($\sigma = -\xi\omega_n$); rotor solidity (plenitude coefficient) $\sigma = \frac{Nc_e}{\pi R}$ [-]
σ_{bl}	blade static moment of a uniform blade (equation B.30) [N m^2]
σ_{COL}, σ_{DIF}	decay coefficient of collective and differential lead-lag mode
σ_k	decay coefficient damping ratio of transition matrix eigenvalue Λ_k defined in 6.27 and G.8; static moment of inertia of k-th blade
σ_β	blade static moment around the flapping hinge $\sigma_\beta = \int_0^{R(1-\varepsilon_\beta)} r\,dm$ [N m^2]
τ	time constant of response in 1-dof system (equation 2.21 or 2.22 for an oscillatory system); time constant of disc-tilt motion (equation 5.7) [-]
τ_{bo}^T, τ_{bo}^{SR}	time constants of the body motion for a teetering and a semi-rigid rotor (equation 5.6) [-]
τ_{Freg}	time constant of regressing flapping mode (equation 5.30) [-]
τ_i, τ_j	time constants of the degrees of freedom x_i and x_j in an n-dof system [-]
τ_{Roll}	time constant of roll-subsidence mode (equation 5.36) [-]
τ_{SP}	time constant of short-period mode (equation 5.29) [-]
τ_u	helicopter climb angle [rad]
$\tau_{\lambda i}$, $\tau_{\lambda i tr}$	time constants of respectively rotor and tailrotor induced inflow
Ω	rotor rotational speed [rad/sec]
Ω_{tr}	tailrotor rotational speed [rad/sec]
ω	damped frequency $\omega = \omega_n\sqrt{1-\xi^2}$ [rad]

$\omega_1 ... \omega_n$ natural frequency of the $x_1 ... x_n$ degrees of freedom [rad/sec]

ω_{bl} blade angular velocity in the coupled blade/chassis motion seen in blade system of reference [rad/sec]

ω_{COL} natural frequency of collective lead-lag mode [rad/sec]

ω_{DIF} natural frequency of differential lead-lag mode [rad/sec]

ω_{DIF+1}, ω_{DIF-1} partitioning of the natural frequency of differential lead-lag mode with Floquet method (equations 6.38 and 6.40)

ω_{excit} frequency of excitation force [rad/sec]

ω_{Freg} natural frequency of regressing flapping mode (equation 5.28) [rad/sec]

ω_k parametric excitation in pendular instability problem [rad/sec]

ω_k , $\bar{\omega}_k$ frequency of eigenvalue in the Floquet transition matrix [rad/sec]

ω_n natural frequency of 1-dof vibrating system $\omega_n = \sqrt{k/m}$ [rad/sec]

ω_{pend} pendular frequency $\omega^2_{pend} = g\sigma_{bl} / I_{bl}$ [rad/sec]

ω_{Roll} natural frequency of helicopter roll-subsidence mode [rad/sec]

ω_{SP} natural frequency of helicopter short-period mode (equations 5.26 and 5.27) [rad/sec]

ω_T , $\bar{\omega}_T$ natural frequency of chassis motion in the second bending mode [rad/sec]

ω_x natural frequency of mass M in dynamic absorber problem [rad/sec]

ω_β , $\bar{\omega}_\beta$ dimensional [rad/sec] and non-dimensional [-] blade flapping natural frequency of non-rotating blade (Ω=0) (for the flap-lag problem see equation 7.9) $\omega_\beta = \sqrt{K_\beta / I_\beta}$; $\bar{\omega}_\beta = \omega_\beta / \Omega$

ω_δ natural frequency of mass m in dynamic absorber problem [rad/sec]

ω_ζ , $\bar{\omega}_\zeta$ dimensional [rad/sec] and non-dimensional [-] blade lead-lag natural frequency of non-rotating blade (Ω=0) (for the flap-lag problem see equation 7.9) $\omega_\zeta = \sqrt{K_\zeta / I_\zeta}$; $\bar{\omega}_\zeta = \omega_\zeta / \Omega$

ξ damping ratio $\xi = c/c_c$ in 1-dof problem and $\xi = c/c_{c\delta}$ in dynamic absorber problem [-]

$\xi_1 ... \xi_n$ damping ratio of the degrees of freedom $x_1 .... x_n$ in an n-dof problem [-]

ξ_{DIF} damping ratio of differential lead-lag mode [-]

ξ_{DIF+1}, ξ_{DIF-1} damping ratios in the differential lead-lag mode solutions with Floquet method (equations 6.38 and 6.40) [-]

ξ_{Freg} damping ratio of regressing flapping mode (equation 5.28) [-]

ξ_{Roll} damping ratio of helicopter roll-subsidence mode [-]

ξ_{SP} damping ratio of helicopter short-period mode (equations 5.26 and 5.27) [-]

ξ_T damping ratio of chassis motion in the second bending mode $\xi_T = C_T/C_{Tcrit}$ [-]

ξ_β damping ratio of uncoupled flapping eigenvalue in flap-lag problem (equation 7.9) [-]

ξ_ζ damping ratio of blade lead-lag motion in flap-lag problem (equation 7.9) $\xi_\zeta = C_\zeta / C_{\zeta\,crit}$ [-]

Ψ, Ψ_{des}	heading angle and desired heading angle [rad]
Ψ_0	heading angle in helicopter basic motion [rad]
ψ	azimuth angle [rad]
ψ_k	azimuth angle of the k-th blade $\left(\psi_k = \psi + (k-1)\frac{2\pi}{N}\right)$ [rad]
ψ_T	blade periodicity in azimuth angle $\psi_T = 2\pi$ [rad]
ζ	blade lead-lag deflection in helicopter and wind turbine blade [rad]
ζ_0	steady-state lead-lag angle in equation 7.4 [rad]
ζ_k	lead-lag deflection of the k-th blade [rad]
$\zeta_{N/2}$	differential lead-lag mode [rad]

System used in order to non-dimensionalize the equations of motion

Measure	Nondimensionalized with:	Examples
Lengths	R	$\bar{e}_\beta = e_\beta/R$, $\bar{f} = f/R$, $\bar{h} = h/R$ ...
Surfaces	$A = \pi R^2$	$\bar{S}_{ht} = S_{ht}/A$, $\bar{S}_{vt} = S'_{vt}/A$
Volumes	AR	$\bar{V}_{ht} = \frac{S_{ht} l_{ht}}{AR}$, $\bar{V}_{fus} = ...$
Velocities	Ω R	$\mu \approx \frac{V}{\Omega R}$; $\bar{u} = \frac{u}{\Omega R}$; $\bar{v} = \frac{v}{\Omega R}$ ..
Angular velocities	Ω	$\bar{p} = p/\Omega$; $\bar{q} = q/\Omega$; $\bar{r} = r/\Omega$
Time	$\bar{t} = \frac{M_{hel}}{\rho A \Omega R}$	$\tau = t/\bar{t}$
Mass	ρAR	$\bar{\mu} = \frac{m}{\rho AR} = \Omega\bar{t}$
Moments of inertia	$m R^2$	$\bar{I}_x = \frac{I_x}{mR^2}$ $\bar{I}_y = ...$
Forces and derivatives $\delta F/(\delta$ angle)	$\Lambda_0 = \rho A \Omega^2 R^2$	$C_T = T/\Lambda_0$; $C_G = mg/\Lambda_0$ $x_{B_i} = X_{B_i}/\Lambda_0$; $x_{A_i} = ...$
Derivatives $\delta F/(\delta$ velocity)	$\Lambda = \rho A \Omega R$	$x_u = X_u/\Lambda$; $y_v = Y_v/\Lambda$; $z_w = ...$

Derivatives $\delta F/(\delta$ angular velocity) and $\delta M/(\delta$ velocity)	$\Lambda_1 = \rho A \Omega R^2$	$x_q = X_q/\Lambda \;;\; z_q = \ldots$ $m_u' = M_u/\Lambda_1 \;;\; m_w' = \ldots$
Moments and Derivatives $\delta M/(\delta$ angle)	$\Lambda_3 = \rho A \Omega^2 R^3$	$C_Q = M_Q/\Lambda_3$ $m_{B_1'} = M_{B_1}/\Lambda_3 \;;\; m_{\theta_0'} = \ldots$
Derivatives $\delta M/(\delta$ angular velocity)	$\Lambda_2 = \rho A \Omega R^3$	$m_q' = M_q/\Lambda_2 \;;\; l_p' = L_p/\Lambda_2 \;;\; l_r' = \ldots$
Derivatives $\delta M/(\delta$ acceleration)	$\Lambda_4 = \rho A R^2$	$m_{\dot{w}}' = M_{\dot{w}}/\Lambda_4$
Acceleration	$\Omega^2 R$	$\ddot{W} = \dfrac{\ddot{w}}{\Omega^2 R}$

Most Common Subscripts

sp	shaft plane
dp	disc plane
cp	control plane
bl	blade
T	tower
ch	chassis
β	flapping
ζ	lead-lag

Superscripts

$\cdot$	derivative to time
$'$	derivative to azimuth angle $d/dt = \Omega d/d\psi$
$\wedge$	variable in Laplace domain
-	non-dimensional notation

Chapter 1

Introduction

"Things should be done as simply as possible, but not simpler".

Albert Einstein

1.1 General Background

During the design of rotary wing devices (helicopters or horizontal-axis wind turbines), simulation models are developed in order to:

- ascertain the device's performance;
- ensure aeroelastic stability;
- determine the system's response to different external perturbations;
- determine fatigue characteristics as well as extreme loads in critical components;
- design control systems.

The simulations are based on dynamic and aerodynamic models capable of predicting the behaviour of these machines under different conditions. Clearly, developing simulation models for rotary wing devices is a difficult and time-consuming task. Some of the problems the designer has to face in these models are related to the large number of *degrees of freedom** [1] of the rotor and the complex interacting phenomena between the rotating system -the rotor- and the non-rotating system -the body (fuselage or tower)-. The models used in rotary wing design should be as simple as possible, as far as is consistent with the required accuracy and the specific case considered.

In particular, the preparation-phase of the simulation models, when the dynamic equations of motion are analytically derived, is a demanding and time-consuming effort. The effort required to derive the equations of motion, as well as the computational effort, increase exponentially with the number of degrees of freedom being modelled. The reason for this is that every new degree of freedom added to the model gives rise not only to an additional equation of motion, but also to an increasing number of coupling terms in the other differential equations.

Therefore it is important that, before commencing the actual derivation of a simulation model, the designer has some indications as to how much detail should be included in the model, in terms of:

---

[1] The terms in italics and with an asterisk are explained in the Glossary

- how many degrees of freedom are needed
- which are the significant degrees of freedom to be included
- what are the couplings between the degrees of freedom considered (aerodynamic, gyroscopic, coriolis, structural, etc.) and which of them are relevant?

The prediction of the necessary level of detail in the model should take into consideration:

- the configuration being analyzed;
- the kind of loading cases being considered;
- the required accuracy;
- the purpose for which the simulation results will be used.

1.2 Aim of the Dissertation

The aim of the present dissertation is to develop a general method which can be used by the design-analyst to determine the necessary degrees of freedom to be considered in a simulation model for helicopters and horizontal-axis wind turbines, before deriving a complete model.

The proposed procedure, the so-called "critical pole distance method", may be considered as an extension of the classic "Campbell diagram" ("spoke diagram"), a frequently applied tool in rotary wing engineering (see section 4.5.1 of Chapter 4). In the Campbell diagram, subsystems and specific deflection modes are represented by their uncoupled eigenfrequencies as a function of rotor speed. By examining the diagram, it is possible to detect the critical points where dynamic couplings between the different deflection modes may occur.

The critical pole distance method may be used to determine the necessary degrees of freedom to be included in a simulation model. In essence, this method detects the regions of dynamic couplings between different subsystems and modes involved in the motion. In the critical pole distance method the degrees of freedom involved in the motion are represented in the *complex plane** by their uncoupled eigenvalues. Examining the representation in the complex plane, the significant degrees of freedom of the simulation model can be determined by defining "critical regions". A critical region is defined as an area of the complex plane where potential couplings between different modes of motion occur. The critical regions are detected by comparing the relative positions in the complex plane of different uncoupled poles and/or different deflection modes participating in the motion. On the basis of the critical pole distance method, the modes involved in the motion can be divided in three classes:

- modes to be discarded from the model;
- modes to be kept separately in the model (neglecting the couplings terms between these modes and other degrees of freedom);

- modes to be kept in the model including the essential coupling effects.

The benefit of the critical pole distance method relative to the Campbell diagram is that whereas the Campbell diagram gives information only on the system's frequencies, the critical pole distance method reveals both the frequencies and the damping existing in the system. The frequency shows the harmonic character of the motion (whether or not it is a vibration), whereas the damping gives information on the damping-type forces (of aerodynamic, gyroscopic, structural, coriolis or other nature) involved in the system which can have a stabilizing effect on the motion.

The crucial question to be investigated in the critical pole distance method is how the relative distance and position of the poles correlate with the strength of the intermodal couplings or, in other words, what is the interpretation of the relative position and proximity of different poles and/or excitation sources. To answer this question, in section 4.2 of Chapter 4 the so-called "critical pole distance criterion" is formulated which can be applied to quantify the relative position of two poles found in the close proximity. The criterion depends exclusively on the uncoupled frequencies and damping characteristics of the modes involved in the motion, but its quantification is based on the investigation of a coupled model. The quantification of this criterion will be exemplified in Chapter 5, Chapter 6 and Chapter 7 for three types of problems from current helicopter and wind turbine design.

The critical pole distance method can be used both as a design tool and an evaluation tool. The main advantage is that, once this method is quantified for a certain class of problems, it can be applied before the actual derivation of the coupled dynamic equations of motion is undertaken.

As a design tool, the critical pole distance method may be used to investigate different candidate configurations in the preliminary design study. The models developed in the preliminary design phase have a limited number of variables and limited detail. However, it is of the utmost importance in this stage to consider "all" different disciplines involved in the design. In other words, in the preliminary design the models should be as simple as possible, but not simpler. For example, in developing simulation models for either helicopter flight dynamics or wind turbine structural dynamics, the designer must not neglect the overlap between the rotary wing disciplines: handling qualities tests are affected by elastic blade deformations and flight control design; wind turbine structural dynamic models are influenced by control design considerations as well (see Figure 1.1).

As an evaluation tool, the critical pole distance method can be applied to obtain insight in already-existing extensive simulation models. Extensive models are models developed over years of experience including all kinematic, structural, aerodynamic and control dynamic aspects. They are useful to be applied when one attempts to reproduce accurately the characteristics of the system. Nevertheless, using extensive models to

investigate a specific phenomenon is not convenient because no physical insight can be obtained (due to the large number of terms and parameters involved in the model). Therefore, for a certain operating condition, building a case-specific model can be of help in order to get insight in the physics of the problem. The critical pole distance method can be used to build case-specific models since it gives indications on the necessary structure of the analytical model to be developed for a specific case.

As a last application, the critical pole distance method can be used in the evaluation of flight simulation models for flight simulators. Also here, use of specific models depending on the particular helicopter configuration, the flight condition and the fidelity requirements is desirable.

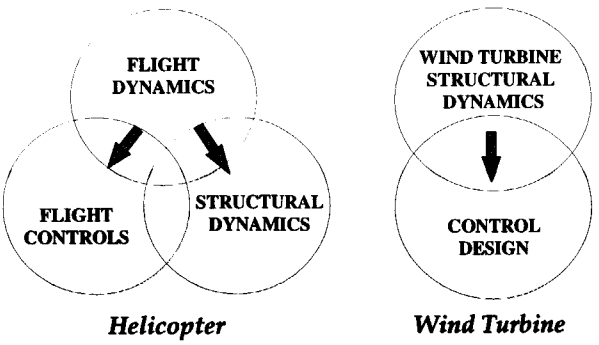

Figure 1.1 Example of interdisciplinary approach in rotary wing engineering

The present dissertation is concerned with the application of the critical pole distance method to investigate the following problems:

- effects of rotor disc-tilt dynamics on helicopter control response and how these can be predicted with the critical pole distance method;
- investigation of the instability of the KEWT [2] in wind turbine;
- prediction of the effects of *blade kinematic couplings** on the flap-lag motion studied in the case of an articulated helicopter in hovering flight. From the multitude of kinematic couplings only the *pitch-flap coupling** and *pitch-lag coupling** are considered.

Criteria and rules of thumb on how to judge whether poles should be considered as remote, or in close proximity, will be developed in each of the problems analyzed. These criteria can be used by the designer as guidelines on the necessary model structure.

---

2 KEWT wind turbine was a two-bladed prototype developed in the 1980's, which experienced violent vibrations during the experimental tests

1.3 Limitations of the Dissertation

The following limitations apply to the present work:

- the level of aerodynamic modeling is kept simple. The inflow is assumed to be uniform and no inflow dynamics are used, except in Chapter 5, section 5.5 where, in order to quantify the critical pole distance criterion for the interaction of the rotor disc-tilt dynamics and helicopter body dynamics, a quasi-steady dynamic inflow is assumed for both rotor and tailrotor. The importance of aerodynamics in simulation modeling will be reviewed to a limited extent in section 3.1 of Chapter 3. No stall effects are included;
- *lumped flexibility** is assumed for the blades;
- the simulation models are linearized in the critical pole distance method;
- for helicopter motion, terms in the equations of motions, resulting from forward flight aerodynamics that are periodic with the rotor rotation, will be neglected. This approximation is valid for low advance ratios and for hovering flight;
- the simulation models described in this work consider only phenomena involving the rigid-body modes of the helicopter fuselage (respectively wind turbine tower) and the rotor modes. From the rotor modes, only the lower blade flap bending mode (first and second), lag bending mode and blade torsional elastic deflections, excluding torsional dynamics, will be included. Accordingly, the frequency range considered in these simulation models will be between 0.1 and 5 Hz for helicopters and between 0.1 and 10 Hz for wind turbines. For helicopters, this range corresponds to handling qualities and flight dynamics applications (see Figure 3.1, in Chapter 3), for wind turbines the frequency ranges of interest correspond to structural dynamic modeling in the low-frequency range. Phenomena that involve blade torsional modes leading to *flutter** and phenomena involving higher blade bending modes and elastic fuselage (tower) modes essential for vibration investigations are not discussed in the dissertation. An important observation should be made here: the frequency range of interest in which these simulation models are valid does cover the class of low-frequency rotor and rotor/body instabilities (such as *ground-resonance** and *air-resonance** or *whirl-flutter**).

The listed limitations will constrain the range of applicability of the critical pole distance method to the design of wind turbines in the normal range of operation and to helicopter applications in the range of standard manoeuvres within the flight envelope.

1.4 Motivation of the Dissertation

Developing quantitative criteria on the necessary degrees of freedom for simulation models is a problem not yet completely solved. This is probably due to the complex phenomena associated with rotary wing devices. Nowadays, the development of simulation modeling is more and more directed towards high-fidelity mathematical

modeling. Although such models have the advantage to be applicable without limitations, they take years of research and development and provide no insight into specific problems. As the development of high-fidelity models continues, the danger exists that the designer will continue to add complexity to the model, without analysing whether or not this is really necessary. It is therefore very useful to have some guidelines on the level of detail to be considered in the models, before actually starting the derivation of the simulation model.
Exemplifying some of the contradictory statements which still exist in the literature **Sopher and Cassarino** [1988][96] compared eight different software codes from industry, university and government in the U.S.A. used for helicopter stability and control response analyses. Their conclusion was that *"...there was considerable disagreement among predictions and no analysis emerged as sufficiently superior and comprehensive....There were insufficient data to isolate factors responsible for the differences. It was unclear how representations established to be important for simple analytical models were included. Also unclear was the extent to which improvements beyond these features were present."*.

Also, the wind turbine community acknowledged that ***"because of the complex interaction of a multitude of phenomena (wind shear*, turbulence*, tower shadow*, up-wind turbine wakes*, yaw angles), there is not much progress made in the understanding of how much detail is required in modeling"*** **(Quarton** [1990][91]).

1.5 Outline of the Dissertation

Following the Introduction, Chapter 2 defines the main concepts used in this dissertation. This chapter is meant to establish an analogy between a one degree-of-freedom vibrating system and the separate rotor blade degrees of freedom. It is demonstrated that the rotor dynamics in different degrees of freedom can be reduced to a one degree-of-freedom vibration problem of a mass-spring-damper system. Chapter 3 presents a literature survey on the necessary degrees of freedom for helicopters and wind turbines. Also, an overview of the so-called *"blade structural (elastic) couplings*"* **in the hingeless rotors and *"blade kinematic couplings"* in** the articulated rotors is presented. These couplings exist both in articulated and hingeless rotor configurations and can be used to tune the level of damping existing in the rotor blade. Rules of thumb on choosing the blade elastic couplings in order to avoid dynamic instabilities and improve the system characteristics are elaborated. In Chapter 4, the "critical pole distance method" is proposed, to determine the level of detail needed in rotary wing simulation models. The method will be compared with other design tools considering the level of detail and couplings in a simulation model. Chapter 5 applies the critical pole distance method, investigating the effects of rotor disc-tilt dynamics on helicopter control response, both for an articulated and a hingeless helicopter configuration. The predictions made in the complex plane are checked by simulating different manoeuvres in the time-domain and using different level-of-complexity coupled body-rotor disc-tilt models. Criteria for the designer on when to consider a body-rotor disc-tilt coupled

model are elaborated using the critical pole distance method. Chapter 6 applies the critical pole distance method to determine the mechanism of instability between the blade lead-lag degree of freedom and the vertical displacement of the tower in fore-aft bending observed in the KEWT two-bladed horizontal axis wind turbine. Solutions which can be used to eliminate this instability are established. Chapter 7 applies the critical pole distance method to the rotor blade coupled flap-lag motion, allowing for the migration of the poles with the blade kinematic couplings existing in the system. Criteria for the design-analyst on a flap-lag coupled model for an articulated helicopter are elaborated. Finally, general conclusions, a review of the assumptions made and future extensions to this work are discussed in Chapter 8.

Chapter 2

Mathematical Tools used in the Dissertation and their Physical Meaning

"It is usually taken for granted that the aeroelasticians can apply Newton's second law without error and when the results of analysis are unsatisfactory the aerodynamic is often faulted. There is evidence that structural dynamics analysis is not yet adequately understood and that prediction of rotating-beam dynamics is not yet solved."

Robert A. Ormiston [1983]

The rotor blade of a helicopter or wind turbine is free to move in space, with its geometrical position in space with respect to a fixed system of coordinates being defined by a multitude of degrees of freedom. One obvious motion of each blade is the rotation around the hub. There are also less visible motions, resulting from blade flexibility, which define the blade degrees of freedom: flapping (out-of-plane deflection), lagging (in-plane deflection), torsion and pitch (see Figure 2.9). The present chapter will demonstrate that the motion of the blade in these degrees of freedom can be reduced to a vibration problem of a one degree-of-freedom mass-spring-damper system.

2.1 One Degree-of-Freedom Vibration Problem

Consider a mass m suspended by means of a vertical spring of spring constant k, including also a damper mechanism of damping constant c (see Figure 2.1). The mass-spring-damper system which is initially in equilibrium, is perturbed at t = 0 by applying a force F_{appl}. Assume as initial conditions $x(0) = x_0$, $\dot{x}(0) = \dot{x}_0$. The force F_{appl} produces a displacement x(t), measured positive downward. One is interested in studying the motion of the mass after the initial perturbation.

The dynamic response of the system depends on the system properties as defined by inertia, damping and stiffness. Applying Newton's second law, the equation of motion of the mass-spring-damper system subject to an external (input) force F_{appl} with specified initial conditions is:

$$\underset{\text{inertia}}{m\ddot{x}(t)} = \underset{\text{load}}{F_{appl}(t)} - \underset{\text{damper}}{c\dot{x}(t)} - \underset{\text{stiffness}}{kx(t)} \quad ; \quad x(0) = x_0 \, , \, \dot{x}(0) = \dot{x}_0 \tag{2.1}$$

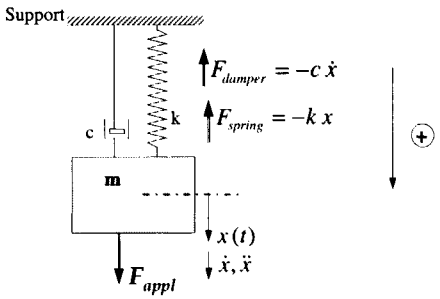

Figure 2.1 One degree-of-freedom vibrating system

The following parameters are defined:

$\xi = c/c_c$ damping ratio where $c_c = 2\sqrt{k\,m}$ is the critical damping in the system. If the damping in the system is smaller than the critical damping $c < c_c$ ($\xi < 1$), the response of the system is oscillatory; if the damping in the system exceeds the critical damping $c \geq c_c$ ($\xi \geq 1$), the response of the system is aperiodic.

$\omega_n = \sqrt{k/m}$ natural frequency of the system (undamped).

Dividing equation (2.1) by mass m and using the above definitions, the equation of motion of the mass-spring-damper system takes the form of the usual one degree-of-freedom vibration problem with known initial conditions:

$$\ddot{x}(t) + 2\xi\omega_n\dot{x}(t) + \omega_n^2 x(t) = F_{appl}(t)/m \qquad x(0) = x_0 \;\; ; \;\; \dot{x}(0) = \dot{x}_0 \tag{2.2}$$

Equation (2.2) enables comparison of the dynamic behaviour of different systems independent of their mass characteristics, by defining a vibrating system by its natural frequency and damping. Mathematically, this equation is a linear non-homogeneous second-order differential equation and its solution (the total response) is the sum of the general solution x_{gen} corresponding to the homogeneous equation (the so-called *free or natural response**) and a particular solution x_{part} corresponding to the applied load (the so-called *forced response**).

2.1.1 The Free Response

The free response of a dynamic system is the solution of its differential equation of motion when the input is identical to zero. This corresponds to the general solution of the homogenous equation:

$$\ddot{x}(t) + 2\xi\omega_n\dot{x}(t) + \omega_n^2 x(t) = 0 \qquad x(0) = x_0 \;\; ; \;\; \dot{x}(0) = \dot{x}_0 \tag{2.3}$$

Solving the characteristic equation of (2.3), the solutions represent the motion eigenvalues:

$$s^2 + 2\xi\omega_n s + \omega_n^2 = 0 \tag{2.4}$$

Depending on the damping in the system, the eigenvalues can be either complex conjugate or real and correspondingly, the motion is periodic, respectively aperiodic. Three different cases may be distinguished:

- *$\xi > 1$ the system is overdamped:*

$$s_{1,2} = -\xi\omega_n \pm \omega_n\sqrt{\xi^2 - 1}\ ; \qquad x_{gen} = C_1 e^{s_1 t} + C_2 e^{s_2 t} \tag{2.5}$$

- *$\xi = 1$ the system is critically damped:*

$$s_{1,2} = -\omega_n ; \qquad x_{gen} = (C_1 + C_2 t)e^{-\omega_n t} \tag{2.6}$$

- *$\xi < 1$ the system is underdamped:*

$$s_{1,2} = -\xi\omega_n \pm i\omega_n\sqrt{1 - \xi^2}\ : \qquad \begin{aligned} x_{gen} &= e^{\sigma t}\left(C_1\cos(\omega t) + C_2\sin(\omega t)\right) = \\ &= R_{gen}\, e^{\sigma t}\cos(\omega t - \delta_{gen}) \end{aligned} \tag{2.7}$$

where $\sigma = \mathrm{Re}(s_{1,2}) = -\xi\omega_n$ is the "decay" and $\omega = \mathrm{Im}(s_{1,2}) = \omega_n\sqrt{1 - \xi^2}$ is the "damped natural frequency" (the frequency of transient oscillations).

The constants C_1 and C_2 can be determined in each case by imposing on the general solution the initial conditions from (2.3). For the underdamped case one obtains:

$$C_1 = x_0 \ ; \ C_2 = \frac{\dot{x}_0}{\omega} \tag{2.8}$$

The amplitude of the solution is $R_{gen} = \sqrt{C_1^2 + C_2^2} = \sqrt{x_0^2 + (\dot{x}_0/\omega)^2}$ and the phase angle is $\delta_{gen} = \tan^{-1}\left(\frac{C_2}{C_1}\right) = \tan^{-1}\left(\frac{\dot{x}_0}{\omega x_0}\right)$.

The general solution then becomes:

$$x_{gen} = e^{\sigma t}\left(x_0\cos(\omega t)+\frac{\dot{x}_0}{\omega}\sin(\omega t)\right) = \sqrt{x_0^2+(\dot{x}_0/\omega)^2}\; e^{\sigma t}\cos(\omega t-\delta_{gen}) \tag{2.9}$$

In a multiple degree-of-freedom system the free response is a linear combination of a number of characteristic motions of the system - the so-called *natural modes of motion**. Each mode of motion corresponds to an eigenvalue (*pole**) of the system as will be seen in section 2.2.

2.1.2 The Forced Response

The forced response of a dynamic system is the solution of its differential equation of motion depending only on the input $F_{appl}(t)$. The case of a sinusoidally applied load is a common one in rotary wing vibration problems. Consider an external sinusoidal force exerted on the system:

$$F_{appl}(t) = F_0\cos(\omega_{excit}t) \tag{2.10}$$

The particular solution of the problem (2.2) has the form:

$$x_{part} = A\cos(\omega_{excit}t)+B\sin(\omega_{excit}t) = R\cos(\omega_{excit}t-\delta) \tag{2.11}$$

The response of the system will also be sinusoidal at a single frequency: the same frequency as the applied load frequency. The constants A and B can be found by substituting the expressions of x_{part} , $\dot{x}_{part}$, $\ddot{x}_{part}$ in equation (2.2) and collecting the terms in A and B. By doing this it results:

$$A = \frac{F_0/m\cdot 2\xi\omega_n\omega_{excit}}{\left(\omega_n^2-\omega_{excit}^2\right)^2+\left(2\xi\omega_n\omega_{excit}\right)^2} \quad ; \quad B = \frac{F_0/m\cdot\left(\omega_n^2-\omega_{excit}^2\right)}{\left(\omega_n^2-\omega_{excit}^2\right)^2+\left(2\xi\omega_n\omega_{excit}\right)^2} \tag{2.12}$$

and the amplitude and phase angle of the forced response are found as:

$$R = \sqrt{A^2+B^2} = \frac{F_0/m}{\sqrt{\left(\omega_n^2-\omega_{excit}^2\right)^2+\left(2\xi\omega_n\omega_{excit}\right)^2}}$$
$$\delta = \tan^{-1}\left(\frac{B}{A}\right) = \tan^{-1}\left(\frac{2\xi\omega_n\omega_{excit}}{\omega_n^2-\omega_{excit}^2}\right) \tag{2.13}$$

2.1.3 The total response

The total response of a linear constant coefficient differential equation is the sum of the free (natural) response and the forced response. In case of a mass-spring-damper harmonic free motion, the total solution is obtained combining (2.9) and (2.11) as:

$$x_{tot}(t) = \sqrt{x_0^2 + \left(\frac{\dot{x}_0}{\omega}\right)^2} e^{-\xi\omega_n t} \cos\left(\omega_n t\sqrt{1-\xi^2} - \delta_{gen}\right) + \frac{(F_0/m)\cos(\omega_{excit} t - \delta)}{\sqrt{\left(\omega_n^2 - \omega_{excit}^2\right)^2 + \left(2\xi\omega_n\omega_{excit}\right)^2}} \qquad (2.14)$$

Considering as a numerical example x(0)= 0.5 m , $\dot{x}(0)$ = 0.2 m/sec, ω_n=2 rad/sec, ξ=0.1, F_0=100 N, m=2 kg, ω_{excit}=10 rad/sec, the general, particular and total response of the vibrating system are represented according to (2.14) in Figure 2.2.

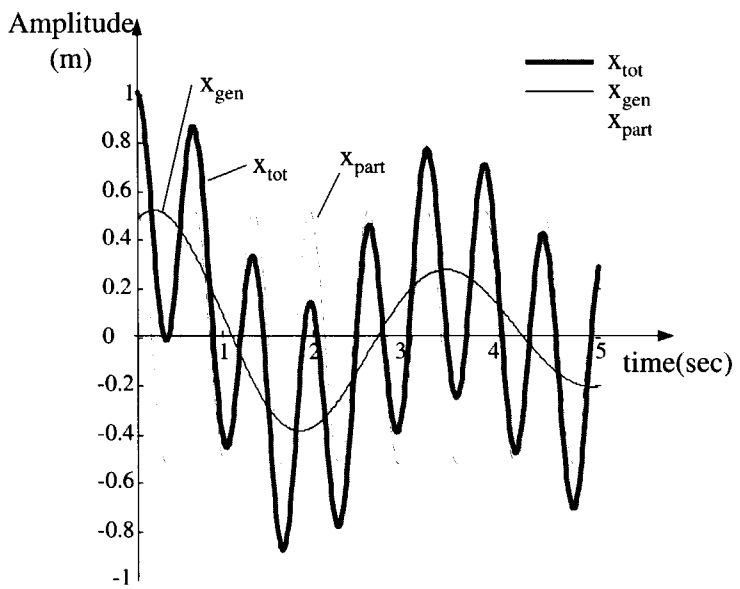

Figure 2.2 The free, forced and the total response of a one degree-of-freedom vibrating system

Usually, the total response is divided into another pair of quantities: the *transient response** and the *steady-state response**. The transient response is that part of the total response which approaches zero as time approaches infinity. The steady-state response is that part of the total response which does not approach zero as time approaches infinity (the response of the system after the transients died out). Usually in dynamic

systems the natural motion dies out quickly compared to the forced motion which persists indefinitely, leading to the custom of referring to the natural motion as the transient and the forced motion as the steady-state.

2.2 Laplace Representation of the Response

The problem of the mass-spring-damper system response in the time-domain (2.14) can be equivalently treated in the Laplace domain. The Laplace transformation is defined in the following manner:

Let x(t) be a real function depending on time t. Then $\mathcal{L}[x(t)] = \hat{x}(s) \overset{def}{=} \int_0^\infty x(t)\, e^{-st}\, dt$ *is called the Laplace transformation of x(t) where s is a complex variable independent of time.*

Applying the Laplace transformation, the vibration problem of equation (2.2) with a sinusoidal force (2.10) can be written as:

$$\left[s^2\hat{x}(s) - s x_0 - \dot{x}_0\right] + 2\xi\omega_n\left[s\hat{x}(s) - x_0\right] + \omega_n^2\hat{x}(s) = F(s) = \frac{F_0}{m}\cdot\frac{s}{s^2+\omega_{excit}^2} \tag{2.15}$$

yielding for the response in the Laplace domain:

$$\hat{x}(s) = \frac{F_0}{m}\frac{s/(s^2+\omega_{excit}^2)}{s^2+2\xi\omega_n s+\omega_n^2} + \frac{(s+2\xi\omega_n)x_0+\dot{x}_0}{s^2+2\xi\omega_n s+\omega_n^2} \tag{2.16}$$

The first term on the right-hand side in (2.16) is the forced response and the second term is the free response of the vibrating system.

Assuming initial conditions zero, the *transfer function** of the system can be defined as the ratio of the Laplace transforms of its output and input:

$$G(s) = \frac{\hat{x}(s)}{F(s)} \tag{2.17}$$

In this way any dynamic system characterized by time-differential equations of motion can be equivalently represented in the Laplace domain by its transfer function as seen

in Figure 2.3.

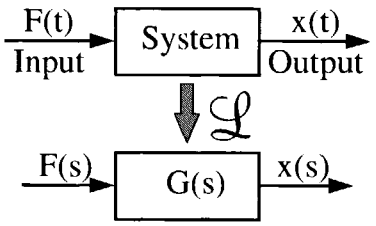

Figure 2.3 Representation of a dynamic system in the Laplace domain

For the vibration problem analyzed in this section, assuming zero initial conditions $x_0 = 0$, $\dot{x}_0 = 0$ in (2.16) yields as the transfer function:

$$G(s) = \frac{1}{s^2 + 2\xi\omega_n s + \omega_n^2} \tag{2.18}$$

Putting the denominator polynomial of G(s) equal to zero defines the system *poles**, whereas putting the numerator polynomial of G(s) equal to zero defines the system *zeros**. For the vibration problem investigated in Figure 2.1, the system has only poles which may be expressed as:

$$s_{1,2} = -\xi\omega_n \pm i\omega_n\sqrt{1-\xi^2} \tag{2.19}$$

The poles and zeros can be represented in the complex plane (the s-plane). The complex plane is defined as the plane in which the abscissa -the so-called "real axis"- gives the damping σ in the system and the ordinate -the so-called "imaginary axis"- the damped frequency ω. The representation of the poles and zeros in the complex plane illustrates the dynamic system response characteristics. There is a strong correlation between the complex plane picture of a dynamic system and the corresponding character of the motion, as will be demonstrated in sections 2.2.1 and 2.2.2.

2.2.1 Physical interpretation of poles

The poles provide information on the nature of the free (natural) motion of the system. There is a certain correlation between the position of the poles in the complex plane and the dynamic behaviour of the system. Miniature pictures of the time response are plotted in the s-plane in Figure 2.4 in order to help the reader to make a mental correlation between the complex plane and the natural response of the dynamic system. The case $\xi<1$ (complex conjugate poles) is analyzed and only the positive quadrant of the left half-plane is represented, the representation in the negative quadrant of the

complex poles being similar. The following conclusion can be drawn looking at these pictures:

- if the poles are on the imaginary axis (Figure 2.4 case (a)), the response of the system is always an undamped oscillation; the farther away from the origin, the higher the frequency;
- if the poles are on the real axis (Figure 2.4 case (b)), the response of the system is always pure exponential; the farther from the origin, the faster the response decreases; in the right half-plane the motion is unstable;
- poles in the left half of the complex plane (Figure 2.4 cases (c) and (d)) are damped oscillations; the more damping is in the system, the quicker the response decays.

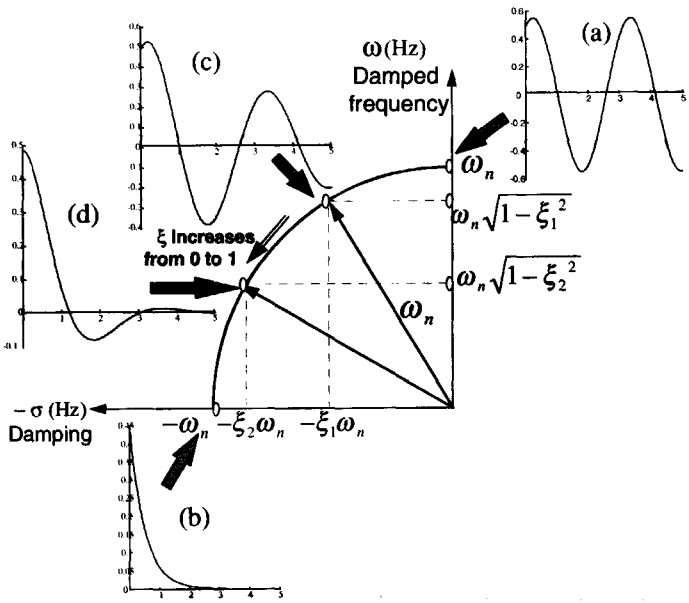

Figure 2.4 The semicircle of the complex eigenvalues and its correlation to the natural response

Observe that when the damping in the system varies, the root loci of the complex eigenvalues move along a semicircle in the left hand side of the complex plane, centred in the origin and with a radius equal to the natural frequency ω_n of equation:

$$\sigma^2 + \omega^2 = \omega_n^2 \quad \rightleftharpoons \quad \left(-\xi\omega_n\right)^2 + \left(\omega_n\sqrt{1-\xi^2}\right)^2 = \omega_n^2 \tag{2.20}$$

The correlation between the position of the poles and the system natural response can

be expressed by means of the *speed of decay of the response**. The commonly used measure of the speed of decay is the *time constant**.

The time constant of a transient motion represents the time in seconds needed for the system to reduce that transient to $e^{-1} = 0.368$ of its initial value.

For $\xi>1$ (the poles are real and distinct), assuming a stable motion ($s_{1,2}<0$), the transient response is a sum of two decaying exponentials, each with its own time constant. For $\xi < 1$ (the poles are complex conjugate), the transient motion is a damped harmonic motion of a certain time constant.

Solving $e^{s\tau} = e^{-1}$ in the time constant definition, the time constant of a decaying exponential can be defined as:

$$\tau = -\frac{1}{s} \tag{2.21}$$

Solving $e^{\xi \omega_n \tau} = e^{-1}$, the time constant in the case of a harmonic motion can be defined as:

$$\tau = -\frac{1}{Real(s)} = \frac{1}{\xi \omega_n} \tag{2.22}$$

The pole closest to the origin (the so-called "slow pole") has the largest time constant and takes longest to decay and is the dominating pole of the motion. To speed up the response of the system (that is, to reduce its time constant), the pole must be moved to the left in the complex plane. In the case of a harmonic motion, looking at (2.22), it follows that to speed up the response of the system, either the damping ratio ξ or the distance ω_n of the poles to the origin must be increased.

2.2.2 Physical Interpretation of Zeros

Additionally to the representation of the poles in the complex plane, a dynamic system is characterized by zeros. The vibration problem defined by equation (2.2) in the time-domain and by transfer function (2.18) has no zero. Zeros are characteristic to a multiple degree-of-freedom system and appear as a consequence of the couplings in the system.

One simple example of a system with a zero is the "dynamic absorber". Consider a mass M suspended on a support as in the previous example of Figure 2.1 by means of a spring of constant K, which can be displaced with x(t) from its initial equilibrium by

applying a force F_{appl}. A small mass m (m « M) is attached to the mass M via a spring of constant k and a damper c (see Figure 2.5). Assume that mass M moves farther and faster than mass m.

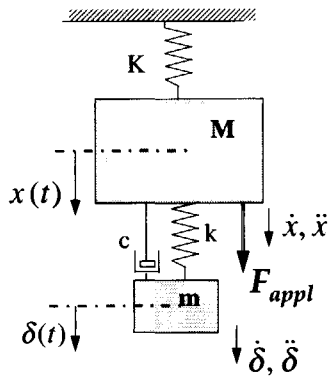

Figure 2.5 Vibrating system with zeros

Using the Newtonian approach, the equations of motion of the configuration of Figure 2.5 are:

$$\begin{cases} M\ddot{x} = -Kx - k(x-\delta) - c(\dot{x}-\dot{\delta}) + F_{appl}(t) \\ m\ddot{\delta} = k(x-\delta) + c(\dot{x}-\dot{\delta}) \end{cases} \tag{2.23}$$

Dividing the first equation of system (2.23) by M and the second equation by m, rearranging the terms and using the following notations:

$$\omega_x = \sqrt{\frac{K}{M}} \; ; \; \omega_\delta = \sqrt{\frac{k}{m}} \; ; \; \xi = \frac{c}{c_{c\delta}} \; ; \; m^* = \frac{m}{M} \; ; \; \frac{c}{M} = 2\xi\omega_\delta m^* \; ; \; \frac{c}{m} = 2\xi\omega_\delta \tag{2.24}$$

the equations of motion (2.23) become:

$$\begin{cases} \ddot{x} + 2m^*\xi\omega_\delta\dot{x} + (\omega_x^2 + m^*\omega_\delta^2)x - 2m^*\xi\omega_\delta\dot{\delta} - m^*\omega_\delta^2\delta = F_{appl}(t) \\ -2\xi\omega_\delta\dot{x} - \omega_\delta^2 x + \ddot{\delta} + 2\xi\omega_\delta\ddot{\delta} + \omega_\delta^2\delta = 0 \end{cases} \tag{2.25}$$

Applying the Laplace transformation to (2.25), the response of the system in x(t) is:

$$\hat{x}(s) = \frac{\begin{vmatrix} F_{appl}(s) & -2m^*\xi\omega_\delta s - m^*\omega_\delta^2 \\ 0 & s^2 + 2\xi\omega_\delta s + \omega_\delta^2 \end{vmatrix}}{\begin{vmatrix} s^2 + 2m^*\xi\omega_\delta s + \omega_x^2 + m^*\omega_\delta^2 & -2m^*\xi\omega_\delta s - m^*\omega_\delta^2 \\ -2\xi\omega_\delta s - \omega_\delta^2 & s^2 + 2\xi\omega_\delta s + \omega_\delta^2 \end{vmatrix}} = \tag{2.26}$$

$$= \frac{\left(s^2 + 2\xi\omega_\delta s + \omega_\delta^2\right) F_{appl}(s)}{s^4 + s^3 \cdot 2\xi\omega_\delta (1 + m^*) + s^2(\omega_\delta^2 + \omega_x^2 + m^*\omega_\delta^2) + s \cdot 2\xi\omega_\delta\omega_x^2 + \omega_x^2\omega_\delta^2}$$

The transfer function showing the effect of F_{appl} on x is then:

$$G(s) = \frac{\hat{x}(s)}{F_{appl}(s)} = \frac{s^2 + 2\xi\omega_\delta s + \omega_\delta^2}{s^4 + s^3 \cdot 2\xi\omega_\delta (1 + m^*) + s^2(\omega_\delta^2 + \omega_x^2 + m^*\omega_\delta^2) + s \cdot 2\xi\omega_\delta\omega_x^2 + \omega_x^2\omega_\delta^2} \tag{2.27}$$

and contains two zeros:

$$z_{1,2} = -\xi\omega_\delta \pm i\omega_\delta\sqrt{1 - \xi^2} \tag{2.28}$$

It can be demonstrated that the small mass m is actually placed to reduce the vibrations x(t) of M, the spring force k(x-δ) and the damper force $c(\dot{x} - \dot{\delta})$ opposing the mass M and propelling the mass m.

Consider the numerical example of ω_x= 10 Hz, ω_δ= 5 rad/sec, ξ= 0.2, m^*= 0.05 and a unit step input $F_{appl}(s)$= 1/s applied to the system. Figure 2.6 represents in the time-domain the response of the system (2.26) for the following cases:

- case a presents the response x(t) to the unit step when no mass m is added to the system (in this case the problem reduces to that of the one degree of freedom with constant amplitude of section 2.1);
- case b presents the response x(t) of the system when a mass m is added to the system;
- case c presents the response x(t) of the system when the eigenfrequency of the subsystem m-k-c is decreased from ω_δ= 5 rad/sec to ω_δ= 1 rad/sec, keeping the damping ratio ξ constant (in the complex plane this means that the system zeros given by (2.28) move further from the origin).

Comparing cases b and c, it appears that moving the pole further from the origin results in a decrease of the amplitude of the response.

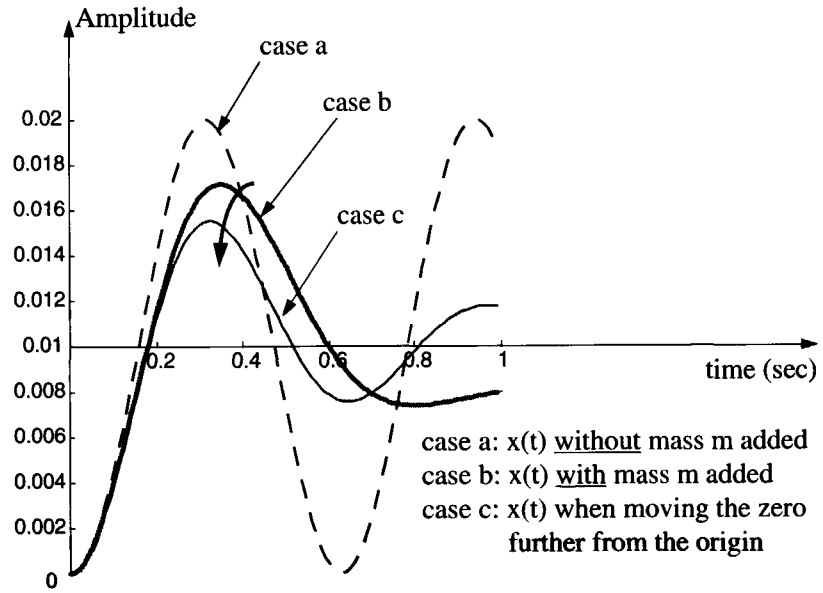

Figure 2.6 Effect of zero on the dynamic absorber

Concluding, whereas the poles give information on how quickly a system can react to a perturbation by means of time constants, the system zeros express how much the system reacts to the perturbation as compared to its steady-state position (the so-called *response overshoot**). The influence of the relative position of the system's poles and zeros in the complex plane can be expressed according to **van de Vegte** [1994][100] as follows: a zero far away from the pole has little effect on the natural response; a zero close to a pole reduces the effect of that pole on the system's response. If a zero coincides with a pole, the effect of that pole on the system response will be cancelled.

2.3 Resonant Excitation (Primary Resonance)

Assume that the forcing frequency ω_{excit} is the same as the natural frequency of the system ω_n. The system can be in resonance (the so-called "*primary or ordinary resonance**") depending on the damping existing in the system. In case of pure resonance (no damping in the system) the equation of motion of the mass-spring damper system is:

$$\ddot{x}(t) + \omega_n^2 x(t) = (F_0/m)\cos\omega_n t \qquad x(0) = x_0 \quad ; \quad \dot{x}(0) = \dot{x}_0 \tag{2.29}$$

and the solution of equation (2.29) is:

$$x = C_1 \cos\omega_n t + C_2 \sin\omega_n t + \frac{F_0/m}{2\omega_n} t \sin\omega_n t \tag{2.30}$$

Because of the presence of the term $t \sin\omega_n t$, the motion becomes unbounded as $t \to \infty$, regardless of the values of C_1 and C_2. Consequently, at resonance, the solution of the motion grows proportional to t.

Returning to (2.11), the non-dimensional response amplitude R/R_{steady} and the phase angle δ as given by (2.13) may be represented as a function of the non-dimensional forcing frequency $\omega_{excit} / \omega_n$ as shown in Figure 2.7. R_{steady} represents the static (steady) response of the system when the applied load is steady (zero excitation frequency $\omega_{excit} = 0$) and is defined by $R_{steady} = \dfrac{F_0 / m}{\omega_n}$.

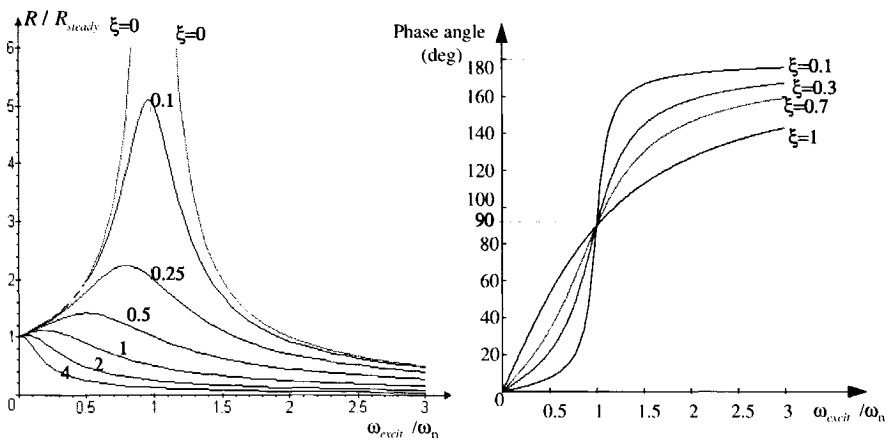

Figure 2.7 Magnification ratio and phase angle of the vibration to a harmonic excitation

Looking at Figure 2.7, the characteristics of a one degree-of-freedom vibration in resonance can be summarized as:

- if the system is excited at its natural frequency $\omega_{excit} \sim \omega_n$ and no damping is present, the system response increases to infinity in amplitude leading to resonance; when damping is present, the response reaches a maximum close to the resonant point. It is often not realized that for very large damping, the response at resonance may even be smaller than the static response, although one excites the system at the resonance frequency;
- at very high excitation frequencies, all system responses attenuate;

- at the resonant condition, the phase angle between the external excitation and the resulting motion is always 90°, irrespective of the amount of damping that exists in the system. This means that the maximum response of the system comes 90° after the maximum excitation was applied.

Returning to the complex plane representation, and assuming the system at resonance $\omega_{exc} = \omega_n$ the relative vertical distance of the system's eigenvalue to the line of excitation $\omega_{exc} = \omega_n$ can be defined as (see Figure 2.8):

$$\bar{d}(\omega_{excit},\omega) = \frac{\omega_{excit}-\omega}{\omega_{excit}} = \frac{\omega_n-\omega_n\sqrt{1-\xi^2}}{\omega_n} = 1-\sqrt{1-\xi^2} \qquad \bar{d}(\omega_{excit},\omega)\in[0;1] \tag{2.31}$$

If no damping is present in the system $\xi = 0$, $\bar{d}(\omega_{excit},\omega) = 0$. If $\xi = 1$, $\bar{d}(\omega_{excit},\omega) = 1$ and the response becomes aperiodic.

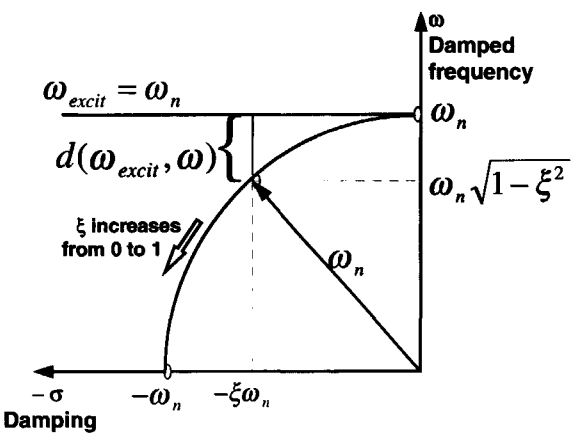

Figure 2.8 Resonant condition in the complex plane

A criterion for resonance in the complex plane can be defined as:

In a resonating system, if the relative distance in the complex plane of the eigenvalue to the excitation line is small, the amplitudes of the response will grow exponentially to the point of structural failure:

$$\bar{d}(\omega_{excit},\omega) = 1-\sqrt{1-\xi^2} << 1 \quad \text{Structure failure in resonating system} \tag{2.32}$$

The acceptable value for condition (2.32) depends on the safety factor of each specific case considered.

2.4 Dynamic Instability. Difference between Resonant Response and Instability

In case of primary resonance, the applied load originates from an external excitation. In rotary wing engineering, an important component of the applied load results from aerodynamic loading. The aerodynamic loading contains not only external excitations (such as gusts and control inputs) but also excitations that arise from the response of the structure (harmonic or non-harmonic). These are the so-called "motion-induced loads" and contain components proportional to both velocity and deflection of the response.

Assume now the applied load in equation (2.1) as a motion-induced load proportional to velocity:

$$m\ddot{x} + c\dot{x} + kx = c_2\dot{x} \tag{2.33}$$

Depending on the value of the coefficient c_2, the problem is equivalent to:

- $c_2 < c$ damped free vibrations where the solution $x \to 0$ when $t \to \infty$;
- $c_2 = c$ undamped free vibrations;
- $c_2 > c$ dynamic instability.

For $c_2 > c$ (dynamic instability) equation (2.33) can be written as:

$$\ddot{x} - 2\xi\omega_n\left(\frac{c_2}{c} - 1\right)\dot{x} + \omega_n^2 x = 0 \tag{2.34}$$

with eigenvalues $s_{1,2} = \xi\omega_n\left(\frac{c_2}{c} - 1\right) \pm \xi\omega_n\sqrt{\left(\frac{c_2}{c} - 1\right)^2 - \left(\frac{1}{\xi}\right)^2}$. The solution of equation (2.34) is:

$$x = Ae^{s_1 t} + Be^{s_2 t} = e^{\xi\omega_n t(c_2/c-1)}\left[Ae^{\xi\omega_n t\left[(c_2/c-1)^2 - (1/\xi)^2\right]^{1/2}} + Be^{-\xi\omega_n t\left[(c_2/c-1)^2 - (1/\xi)^2\right]^{1/2}}\right] \tag{2.35}$$

Whether the motion is harmonic or not depends on the sign of $\sqrt{\left(\frac{c_2}{c} - 1\right)^2 - \left(\frac{1}{\xi}\right)^2}$.

However, because of the term $e^{\xi\omega_n\left(\frac{c_2}{c} - 1\right)t}$ the response increases exponentially in time. Compared with the resonance case, where it was shown that the response increases

linearly with time t, in the case of dynamic instability the system response increases according to e^t. **Bielawa** [1992][6], generalizing this result, comments on the aeromechanical problems: *"Responses that grow linearly with time are typically due to one or more applied external loads oscillating at the resonant frequency; Responses that grow exponentially with time are typically due to one or more motion-induced loads that are in phase with the response velocity such that they feed energy into the system from some outside source. In practice, however it is difficult to clearly distinguish between the class of resonances and dynamic instabilities because of the presence of damping, non-linearities, time-varying dynamic parameters, etc. Typically, a clear-cut exponential growth behaviour may only be in evidence over a short period of time before a (nonlinear) limit cycle mechanism might begin to predominate. However, all identified instabilities should be regarded as being capable of producing responses that can grow exponentially to the point of structural failure".*

2.5 Parametric Excitation. Difference between Resonant and Parametric Excitation

The rotary wing designer also has to deal with the class of *pendular (parametric) resonances**. Pendular resonances and instabilities appear in parametrically-excited systems, i.e. systems in which the excitation depends on the system degree-of-freedom x. If the forcing function is a periodic function and depends on the system's variable through a small parameter ε, the motion of the system is given by a differential equation of the Mathieu type (Mathieu used this equation for the problem of vibrations of an elliptic membrane). For the undamped case of a parametrically excited system, the system equation of motion is:

$$\ddot{x} + \left[\omega_n^2 + \varepsilon \cos(\omega_{excit} t)\right] x = 0 \tag{2.36}$$

A differential equation similar to Mathieu's type but where the forcing function is of more general nature was given by Hill (who used it to study the motion of the Lunar Perigee) in the form:

$$\ddot{x} + \left[\omega_n^2 + \varepsilon \sum_{k=1}^{\infty} \cos(\omega_k t)\right] x = 0 \tag{2.37}$$

Equation (2.36) is usually called a "Mathieu-Hill equation" and represents the simplest form of a parametrically excited system, containing a natural frequency varying harmonically in time. The solutions of Mathieu's equation are given in terms of Mathieu's functions. The important question in pendular resonances is not what the exact solution is, but which are the regions of instability. Assuming small ε, the

regions of parametric instability are in the vicinity of:

$$\omega_{excit} = \frac{2\omega_n}{K} \quad ; \quad K = 1,2,3,...n \tag{2.38}$$

If K = 1, the instability is in the vicinity of $\omega_{excit} = 2\omega_n$ and is the principal parametric resonance. The principal parametric resonance is generally considered as the most dangerous and unstable region. K = 2 and $\omega_{excit} = \omega_n$ corresponds to the secondary parametric resonance. In this case, if the system is excited by a resonant force as well, the two resonances superimpose. Further, as K increases, the regions of instabilities decrease and become less dangerous.

Distinction should be made between the ordinary and parametric resonance, the parametric resonance being characterized by a multitude of regions of instability where the response amplitude increases not linearly, but exponentially with time. Parametric resonance is not only dangerous because of its multiplicity in instability regions but also due to the power of the instability.

2.6 A Parallel between the Rotor Dynamic Characteristics of Helicopters and Wind Turbines

The main blade degrees of freedom are defined in Figure 2.9 as being: flapping (out-of-plane deflection), lagging (in-plane deflection), torsion and pitch degrees of freedom. The blade dynamic characteristics will be derived in this dissertation assuming lumped flexibility for the blades. This is equivalent with the "rigid-blade concept" introduced by Young [1962][104].

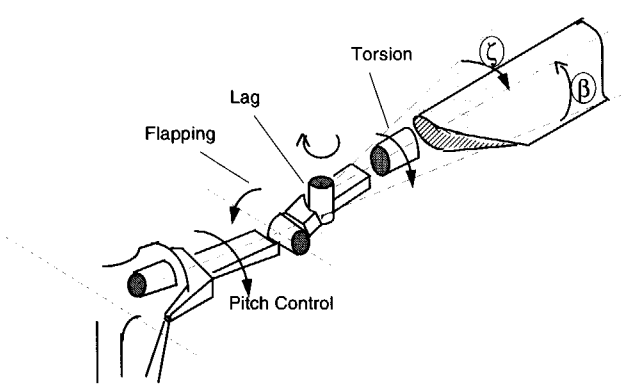

Figure 2.9 Rotor blade degrees of freedom

In the rigid blade concept, the flexible blade is assumed to be rigid in bending and torsion, the flexibility of the blade being concentrated in virtual hinges by means of springs (flexible lumps). Each hinge focuses on blade motion in one of the above mentioned degrees of freedom and is characterized by a specific offset and spring constant (see Figure 2.9).

Assuming the blade flapping, lead-lag and torsion as being uncoupled, the next sections will reduce the motion of the blade to that of a vibrating mass-spring-damper system.

2.6.1 Helicopter and Wind Turbine Flapping Dynamics

Consider the blade of a helicopter or wind turbine rotor, free to move only in the flapping direction by means of a flapping hinge as shown in Figure 2.9. The equation of motion for the flapping degree of freedom was derived in Appendix B under the following assumptions (these assumptions are valid throughout the entire dissertation, except Chapter 5, section 5.5 where quasi-steady dynamic inflow is considered):

- for both helicopters and wind turbines, the blade is modeled as being rigid both in bending and torsion and having a flapping hinge at an offset e_β from the rotor hub of hinge spring K_β;
- the blade rotates at a constant rotor angular speed Ω;
- the effects of the helicopter respectively tower motion on the blade motion are neglected;
- the flapping angle and the inflow angle are both assumed to be small;
- the inflow is assumed to be uniform and no inflow dynamics are used;
- the blade tip loss factor is equal to unity;
- no pitch-flap and pitch-lag couplings are considered;
- the blade has a constant chord;
- the blade is not twisted;
- gravity is neglected in case of helicopters and considered in case of wind turbines;
- for wind turbines, the wind comes to the rotor from axial and lateral (*crosswind**) direction. No *wind-shear** effects are considered;
- the reversed flow region is ignored; no compressibility and stall effects are considered;
- the blade elastic axis, aerodynamic axis, control axis and centre of mass coincide.

All these assumptions were made in order to establish an analogy between the dynamic behaviour of a helicopter and a wind turbine rotor blade. Presuming the helicopter in forward flight with advance ratios not higher than 0.3, the final expression of the

flapping equation of motion is obtained in Appendix B, equation (B.37) as:

$$\ddot{\beta} + \gamma\left(\frac{1}{8} - \frac{\varepsilon_\beta}{8} + \frac{1}{6}\mu\sin\psi\right)(1-\varepsilon_\beta)^3\,\Omega\,\dot{\beta} + \left[\nu_\beta^2 + \gamma\left(1-\varepsilon_\beta\right)^2 \times \right.$$
$$\left. \times\left(\frac{1}{6}\mu\cos\psi - \frac{\varepsilon_\beta}{6}\mu\cos\psi + \frac{\mu^2}{8}\sin 2\psi\right)\right]\Omega^2\beta = \frac{M_{a\,excit}}{I_{bl}} \qquad (2.39)$$

For a wind turbine with the wind attacking the blades in the axial and cross direction, the flapping equation of motion is obtained in Appendix B, equation (B.40) as:

$$\ddot{\beta} + \gamma\left[\frac{1}{8} - \frac{\varepsilon_\beta}{8} + \frac{1}{6}\bar{U}_0\sin\psi\right](1-\varepsilon_\beta)^3\,\Omega\dot{\beta} + \left[\nu_\beta^2 + G\cos\psi + \gamma(1-\varepsilon_\beta)^2 \times\right.$$
$$\left. \times\left(-\frac{1}{6}\bar{U}_0\sin\psi + \frac{\varepsilon_\beta}{6}\bar{U}_0\sin\psi - \frac{1}{8}\bar{U}_0^2\sin 2\psi\right)\right]\Omega^2\beta = \frac{M_{a\,excit}}{I_{bl}} \qquad (2.40)$$

The flapping equations of motion as given by (2.39) and (2.40) can be regarded as the equation of a vibrating system with damping, stiffness, and forcing terms. The dynamic characteristics of the flapping motion as can be deduced from these equations are:

- for both helicopters and wind turbines, damping is introduced in the flapping motion by means of the aerodynamic forces (a perturbation in the flapping velocity will be counteracted by an aerodynamic damping-term);
- for both helicopters and wind turbines, the role of the spring in the vibrating system is taken by the centrifugal force, the spring on the flapping hinge and the aerodynamic forces;
- for both helicopters and wind turbines, the flapping equation of motion contains terms periodic with the blade azimuth. For helicopters, these periodic coefficients seem to be important only in the region of high advance ratios (**Hohenemser and Yin** [1974][43]). For wind turbines, periodic coefficients are introduced by the gravity force and crosswind. The periodic coefficients containing the gravity force are parametric excitations for the system and can lead to parametric resonances defined by (2.38). Usually, the values of frequencies at which the primary resonances appear are out of the range of wind turbine operating conditions, thus presenting no practical importance. The aerodynamic forces affect profoundly the main and secondary parametric regions, having a stabilizing effect and thus preventing the occurrence of parametric resonances (**Feitosa** [1989][29]). For the existing wind turbines, the pendular instabilities in the flapping direction do not present practical importance (**Eggleston** [1987][27]). However, this situation might change in the future larger wind turbines due to the scaling effects (see the discussion from section 3.3.2 of Chapter 3).
- the natural flapping frequency depends on the rotor rotational frequency for both helicopters and wind turbines; there is a non-rotating natural flapping frequency

$\omega_\beta = \sqrt{K_\beta / I_\beta}$ and there are rotating natural flapping frequencies $\Omega^2 \nu_\beta^2 = \Omega^2\left[1 + \frac{3}{2}\frac{\varepsilon_\beta}{(1-\varepsilon_\beta)}\right] + \omega_\beta^2$.

Consider a helicopter in hovering flight with a blade without hinge offset or hinge restraint. In this case, the flapping equation of motion (2.39) becomes:

$$\ddot{\beta} + \frac{\gamma}{8}\Omega\dot{\beta} + \Omega^2\beta = \frac{M_{aexcit}|_{\mu=0}}{I_{bl}} \tag{2.41}$$

In the case of a hovering helicopter, the flapping equation of motion has constant coefficients and the natural flapping frequency becomes equal to the angular speed of rotation Ω. Aerodynamic excitations in $\cos\Omega t$ terms are usually encountered in practice (for example in the shape of a vertical gust): such an excitation is called a "*1-P excitation**" because the aerodynamic force reaches its maximum once per revolution. This means that the 1-P excitation will cause a resonant condition. The helicopter is thus intentionally designed for such resonances to occur! Fortunately, the flapping motion is highly damped -for helicopters the Lock number is $\gamma = 5$ to 15- leading to an aerodynamic damping even close to critical damping. When applying a 1-P disturbance the flapping motion automatically grows so large that the aerodynamic damping cancels the applied aerodynamic moments. Hence, the danger for resonance is eliminated with the 1-P excitation even being beneficial to the flapping motion. For wind turbines the Lock number γ also varies between $\gamma = 5$ to 15 and therefore the flapping motion is characterized by strong aerodynamic damping as well. Note that use of the Lock number presupposes that the blade is in the unstalled region. When the blade approaches the stall region, the γ terms in the flapping equation of motion become small or vanish.

When a rotor blade flaps, it changes its moment of inertia about the rotational axis, resulting in accelerating or decelerating forces appearing on its blade elements (according to the law of conservation of angular momentum). These forces are felt as vibrations at the blade root, with a corresponding in-plane Coriolis vibration for every harmonic of flapping. In the early years of rotary wing engineering, the vulnerability to fatigue of the root attachment due to Coriolis effects was the most difficult problem to solve. To eliminate this problem, **Cierva** introduced the drag (lead-lag) hinge for his autogiros (see **Benett** [1961][5]). However, this led to another destructive vibration of the structure, the so-called "*ground resonance**" phenomenon.

Cierva was also the first one who thought of the solution of inclined hinges in his autogiros in order to control the disc-tilt motion (see section 3.4 and **Benett** [1961][5]).

Concluding, for both helicopters and wind turbines, the flapping dynamics are

characterized by strong aerodynamic damping characteristics. A direct consequence of this fact is that, in rotary wing engineering, the flapping dynamics affect mainly the control response characteristics and much less their aeroelastic stability characteristics.

2.6.2 Helicopter and Wind Turbine Lagging Dynamics

Consider the blade of a helicopter or wind turbine rotor, free to move only in the lagging direction by means of a lagging hinge as shown in Figure 2.9. The blade lagging equation of motion was derived in Appendix B under the following assumptions (these assumptions are valid throughout the present work):

- for both helicopters and wind turbines, the blade is modeled as being rigid both in bending and torsion and with a lagging hinge at an offset e_ζ from the rotor hub, different from e_β and a hinge spring K_ζ;
- the blade rotates at a constant rotor angular speed Ω;
- the effects of the helicopter respectively tower motion on the blade motion are neglected;
- the lagging angle and inflow angle are both assumed to be small;
- the inflow is assumed to be uniform and no inflow dynamics are used;
- the blade tip loss factor is equal to unity;
- no pitch-flap and pitch-lag couplings are considered;
- the blade has a constant chord;
- the blade is not twisted;
- gravity is neglected in case of helicopters and considered in case of wind turbines;
- for wind turbines, the wind comes in the rotor axial and lateral (*crosswind**) directions. No *wind-shear** effects are considered;
- the reversed flow region is ignored; no compressibility and stall effects are considered;
- the blade elastic axis, aerodynamic axis, control axis and centre of mass axis coincide.

Under these assumptions, and considering as in the previous section the helicopter in forward flight at advance ratios not higher than 0.3, the lagging equation of motion as derived in Appendix C, equation (C.37) is:

$$\ddot{\zeta} + \gamma \left[\theta_p \lambda \frac{(1-\varepsilon_\zeta)^3}{6} - \frac{C_d}{C_{l_\alpha}} (1-\varepsilon_\zeta)^3 \left(\frac{1-\varepsilon_\zeta}{4} + \frac{\mu \sin\psi}{3} \right) \right] \Omega \dot{\zeta} + \left\{ \nu_\zeta^2 + \gamma \left[\theta_p \lambda \times \right. \right.$$
$$\left. \left. \times \frac{(1-\varepsilon_\zeta)^2}{4} \mu \cos\psi - \frac{C_d}{C_{l_\alpha}} (1-\varepsilon_\zeta)^2 \left(\frac{1-\varepsilon_\zeta}{3} \mu \cos\psi + \frac{1}{4} \mu^2 \sin 2\psi \right) \right] \right\} \Omega^2 \zeta = \frac{M_{a\,excit}}{I_{bl}} \tag{2.42}$$

For a wind turbine the lagging equation of motion (equation (C.40) of Appendix C) is:

$$\ddot{\zeta} + \gamma\left[\theta_p\lambda\frac{(1-\varepsilon_\zeta)^3}{6} - \frac{C_d}{C_{l_\alpha}}(1-\varepsilon_\zeta)^3\left(\frac{1-\varepsilon_\zeta}{4}+\frac{\bar{U}_0\cos\psi}{3}\right)\right]\Omega\dot{\zeta} + \left\{\nu_\zeta^2 + G\cos\psi + \gamma\left[\theta_p\lambda\frac{(1-\varepsilon_\zeta)^2}{4}\right.\right. \quad (2.43)$$

$$\left.\left.\times\bar{U}_0\sin\psi + \frac{C_d}{C_{l_\alpha}}(1-\varepsilon_\zeta)^2\left(\frac{1-\varepsilon_\zeta}{3}\bar{U}_0\sin\psi + \frac{1}{4}\bar{U}_0^2\sin 2\psi\right)\right]\right\}\Omega^2\zeta = \frac{M_{a\,excit}}{I_{bl}} + G\sin\psi$$

The lead-lag motion of both helicopters and wind turbines is equivalent to a one degree-of-freedom vibrating system characterized by the following features:

- damping is introduced by aerodynamics. However, there are two aerodynamic terms, opposite in sign. The lagging motion is characterized by very small values of damping, being virtually undamped. In articulated helicopters usually mechanical dampers are introduced. In hingeless helicopters, elastic couplings and even mechanical dampers are used to increase the damping. In the wind turbine industry mechanical dampers were not yet added to the system. Only for middle-class (500-600 KW) stall regulated wind turbines, dynamic absorbers were installed on the blades in order to eliminate the serious lead-lag vibrations characteristic to these turbines (**Anderson** [1999][3]);
- in helicopters the spring characteristics are introduced by the centrifugal force (which in this case acts only through the small hinge offset), as well as elastic spring and aerodynamic forces. In wind turbines, the spring characteristics are introduced by the centrifugal force, elastic force and gravity force. The gravity force splits in two terms: one term which may lead to pendular instabilities and a periodic external excitation which can cause ordinary resonances in blade lead-lag motion. Concerning the gravity periodic component which can lead to parametric instabilities, **Miller et. al.** [1978][71] demonstrated that the danger for lead-lag parametric instabilities appear when the ratio $\omega_{pend}/\omega_\zeta > 1$ where ω_{pend} is the blade pendular frequency defined as $\omega_{pend}^2 = G = (g\sigma_{bl})/I_{bl}$. Up to present, the current wind turbine configurations have usually $\omega_{pend}/\omega_\zeta \ll 1$ and thus the parametric instability in the lead-lag motion, is of no practical importance. However, as mentioned in the case of the flapping motion, this situation might change in the future wind turbines due to the scaling effects;
- the natural lagging frequency depends on the rotor rotational frequency; there is a non-rotating natural lagging frequency $\omega_\zeta = \sqrt{K_\zeta / I_\zeta}$ and there are rotating natural lagging frequencies $\Omega^2\nu_\zeta^2 = \omega_\zeta^2 + \Omega^2\frac{3}{2}\frac{\varepsilon_\zeta}{(1-\varepsilon_\zeta)}$.

Concluding, for both helicopters and wind turbines, the lagging dynamics are characterized by low aerodynamic damping characteristics. A direct consequence of this fact is that, in rotary wing engineering, the lagging dynamics mainly affect the aeroelastic stability characteristics and much less the control response characteristics, as

opposed to the flapping dynamics.

2.6.3 Helicopter and Wind Turbine Torsional Dynamics

The question on the necessary degrees of freedom examined in the present dissertation refers to simulation models in the field of helicopter flight dynamics and wind turbine low-frequency structural dynamics. As explained in section 1.3 of Chapter 1, the frequency range of interest for such models for helicopters lies between 0.1 to 5 Hz (dividing by the rotor speed Ω of usual configurations this corresponds to 0.01 to 1/rev) and for wind turbines between 0.1 to 10 Hz (i.e. 0.1 to 3/rev). The natural blade torsion frequency is usually between 3 to 10/rev in the case of a helicopter and 5 to 15/rev for a wind turbine. Modern wind turbines already reached values of the first torsional frequency of 30/rev. It follows that phenomena involving blade torsional modes (such as classical flutter problems) are not explored in the present work. Nevertheless, the blade torsion degree of freedom must be represented in the simulation models by their quasi-steady effects and by the so-called "structural bending- torsion couplings" or shortly "structural couplings". Whereas neglecting the blade torsion dynamics is a valid approximation for helicopter flight dynamics and wind turbine low-frequency structural models, neglecting the structural couplings, especially in hingeless rotors, means neglecting effects in the same order of the blade flapping and lagging dynamics, and thus results in erroneous solutions and danger for rotor and rotor-body instabilities (see examples in Appendix H).

One of the main assumptions on which the present dissertation is based is that of lumped flexibility for the blades. As discussed on page 25, this is equivalent with the rigid blade concept introduced by **Young** [1962][104]. The rigid blade assumption is generally true for an articulated rotor where hinges are placed at different offsets from the rotor hub, allowing the blade to move in a flapping, lagging or pitching direction. A hingeless rotor usually only has a pitch hinge, and in a bearingless rotor no hinges are present at all, the blades being flexible elements bending out-of-plane, in-plane and torsioning simultaneously. For all such rotors, the rigid blade concept can also be used with good approximation, provided that one can find a feasible position of the sequence of the virtual hinges that correctly represents the dynamics of the blade.

The above-mentioned structural couplings characteristic to an elastic blade of a hingeless rotor are transformed in the rigid-blade concept in equivalent pitch-flap and pitch-lag couplings. **Hodges and Ormiston** [1976][40] presented analytical formula's and graphs to determine the equivalent pitch-flap and pitch-lag couplings as a measure of the bending-torsion couplings of an elastic blade. These equivalent couplings depend on the blade pitch angle, torsion frequency, lead-lag frequency, flap-lag coupling and *precone**. For very high torsion frequencies, these couplings are normally small and unimportant, but for typical values of the torsion frequency (5 to 10/rev) they cannot be neglected.

Considering the effect of torsional dynamics in wind turbines, two observations are important here:

- the action of the gravity force gives a periodic term in the torsional stiffness which is dangerous for torsional pendular instabilities. In up to the present wind turbine configurations this term is very small compared to the torsional frequency and therefore the torsional pendular instabilities are not a serious problem (**Eggleston** [1987][27]). This situation might change in the future upscaled wind turbine configurations. It follows that careful predictions of all possible regions of parametric instabilities should be made in the design and development of wind turbines;
- there are special cases in which the torsion dynamics become of importance for the simulation model, for example, in case of a failure in the pitch actuation or pitch link system (**van Holten** [1987][50] presented such a case for the Newecs 45 wind turbine).

2.7 Approaching the Problem of Modeling for Helicopters and Wind Turbines

Helicopters and horizontal-axis wind turbines involve essentially two structures, one rotating -the rotor- and the other non-rotating -the airframe, respectively the tower-. Therefore, when it comes to the problem of building a simulation model, these devices have much in common. There are also specific features which differentiate them. Some of the main differences in building a simulation model for helicopters and wind turbines are included in the present section.

1. The mass and the stiffness properties of wind turbine rotors are quite different from those of helicopter rotors. **Ormiston** [1973][77] compared the blade fundamental flap and lead-lag frequencies for different rotating systems (see Figure 2.10). At that moment, the large wind turbines were designed at non-rotating lead-lag and flap natural frequencies in the range of respectively 2 to 2.5/rev and 1 to 1.7/rev. Concerning the flapping frequencies, the low values belong to a teetering or coning hinge, the moderate values belong to hingeless configurations and the relatively high values are characteristic for stiff configurations. The relatively high value of the wind turbine lead-lag frequency as compared to helicopters is due to the former's typical low operating speeds and the need to stiffen large rotor blades against gravitational stresses.

The relative position between the flap and lead-lag non-rotating natural frequencies was extended in the present work from the wind turbine configurations in the 1970's to the nowadays wind turbines (year 2000) as used in the STABTOOL project (see **van Holten et. al.** [1999][49]) in Figure 2.10.

For variable speed wind turbines, the rotational speed Ω used to obtain the non-dimensional values $\bar{\omega}_\beta$, $\bar{\omega}_\zeta$ (1/rev) corresponds to the range of normal operating

conditions. From this figure it follows that the increasing dimensions of modern wind turbines shifted the flap and lead-lag motions to higher frequencies; for flapping in the range 3 - 6/rev, for lead-lag in the range 4 - 9/rev. Thus, the separation in frequencies between helicopters and wind turbines became more accentuated as time passed. This is an important conclusion which will be further discussed in sections 3.3.1 and 3.3.2 of Chapter 3.

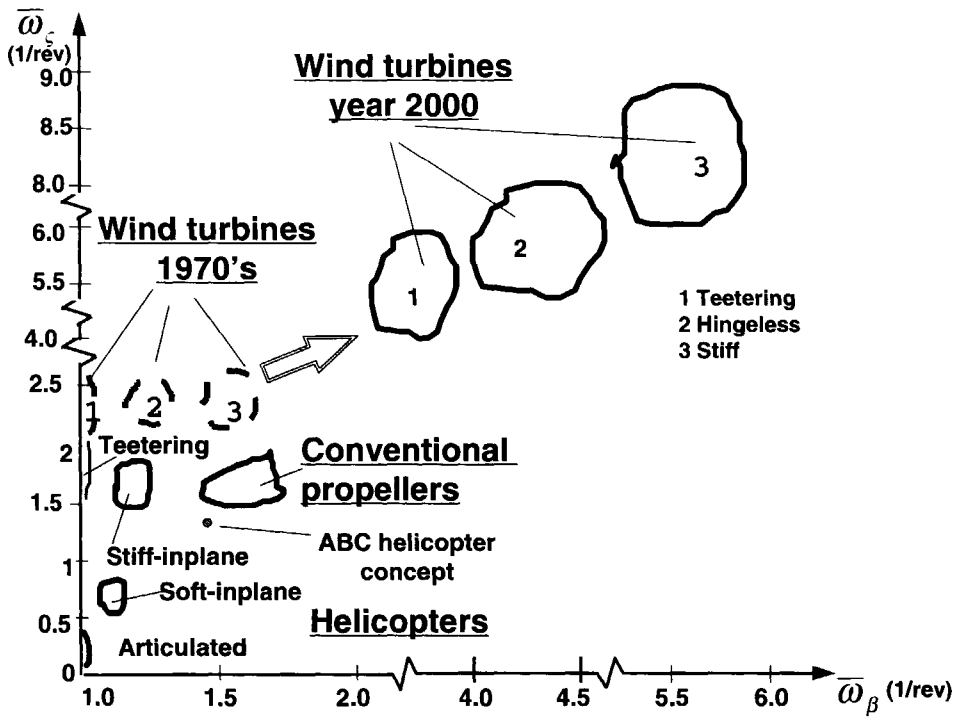

Figure 2.10 Comparison between the relative position of flapping and lagging natural frequencies in the 1970's (Ormiston[1971][77]) and in 2000

2. The structural geometry of wind turbines possesses geometric parameters which do not exist or are less important in helicopter configurations (for example blade twist, blade form and mass unbalance). Also, the helicopter blade has specific geometric parameters (as blade sweep and droop) which are not used in wind turbine configurations.

3. The action of the gravity force has different importance: for helicopters, gravity forces on the blades can be neglected; for wind turbines, this is no longer possible, parametric resonance regions becoming a danger in the design of wind turbines.

4. The wind turbine rotor speed is an order of magnitude less than the corresponding rotational speed of helicopters.

5. Differences between helicopters and wind turbines relate also to the different wind conditions characteristic to the two systems. For a wind turbine, *rotational sampling** or *wind shear** must be accounted for by introducing a variable wind speed as a function of altitude according to a standard logarithmic law.

6. Whereas in simulation models the wind energy community was concentrating mainly on the representation of the response of the structure to different external excitation sources (the so-called "*loading problem**"), the helicopter specialists paid attention mainly to the coupling effects between the different modes of the structure (the so-called "*dynamic instability problem**"). It will be demonstrated in section 3.3.2 of Chapter 3 that nowadays, the attention of both rotary wing worlds will probably have to converge towards both aeroelastic stability problems and response problems: there is more and more evidence that modern wind turbines will encounter aeroelastic instabilities and also that the new flying quality specifications must consider the structural response of the helicopter dynamic modes.

Chapter 3

Literature Survey on Simulation Modeling for Helicopters and Horizontal Axis Wind Turbines

"However, I am somewhat uncertain as to where we now stand. There's no question we have made advances, and there are many instances where very good agreement can be shown between theory and experiment... But, and this is where the uncertainty comes in, there are other situations which reveal large discrepancies between various analytical approaches. I don't believe, however, that we have yet reached a stage where we know which tool is the right one for a particular job."

Alfred Gessow [1986]

The literature survey within this chapter is organized into three parts:

1. literature survey on the necessary degrees of freedom for helicopter handling qualities modeling;
2. literature survey on the necessary degrees of freedom for wind turbine structural dynamics modeling;
3. a general discussion on low-frequency dynamic instabilities in rotary-wing engineering (rotorcraft and wind turbines) and structural couplings in hingeless rotors.

3.1 Literature Survey on Necessary Degrees of Freedom for Helicopter Piloted Simulation Models

The first model for piloted simulation was developed by **Hohenemser** [1939][42] on the basis of the standard equations of airplane motion for small-disturbances and steady, symmetrical, rectilinear 1-g flight as the reference flight condition. The model was a six degree-of-freedom (6-dof) rigid-body linear model in which the contribution of the rotor motion to the body motion was incorporated in a quasi-steady way. The quasi-steady body modes- phugoid, short-period pitching mode and dutch roll mode- are usually obtained using this model. The 6-dof model was used for stability and control analyses, handling quality specifications (*MIL specifications**) and design analyses of the *stability-and-control-augmentation system (SCAS**) for rotorcraft.

For an articulated rotor, a 6-dof model seems sufficient to determine natural aircraft

behaviour. However, for a hingeless rotor helicopter, the classical 6-dof approximation is usually no longer applicable, even if only natural helicopter behaviour -that is, without the augmentation system- is considered. A first reason for this was given by **Curtiss** [1986][21] as follows: "*the dynamics of the fuselage and rotor of an articulated helicopter can usually be seen as a 'cascade problem', i.e. a rapid rotor plane response followed by a slower fuselage response. For hingeless rotor configurations, the body motion "speeds up" and the rotor dynamics enter into the body dynamics*". Further, new requirements for tactical missions -such as *Nap-of-the-Earth (NOE) flight and aerial combat**, high-g manoeuvres- demanded the design of high-gain flight control systems (FCSs), which require the extension of the frequency range of validity for the simulation model to the high-frequency rotor dynamics. Discussing some of the pitfalls in testing the new *ADS-33 Flying Qualities recommendation**, **Kolwey** [1996][59] concluded that the flight test community can no longer afford to separate the flight test disciplines of flying qualities, performance, dynamics and structures. In the old qualification system all manoeuvres had to be carried out in the *Operational Flight Envelope (OFE)**. The new ADS-33 recommendation includes a new spectrum of manoeuvres based on helicopter structural limits.

Therefore, for a hingeless rotor, models including rotor dynamics usually must be used in piloted simulation modeling. The modes of different subsystems for a medium-size helicopter can be divided according to their specific frequency as illustrated in Figure 3.1.

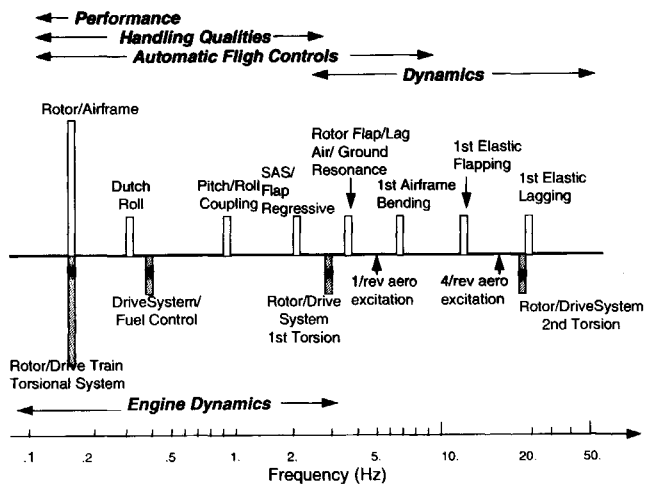

*Figure 3.1 Modes of interest of a medium-size helicopter (**Kuczynski et. al.** [1980][61])*

Chen et. al. [1987][14] presented a review of the research done during a couple of decades on the development and validation of flight dynamics models by NASA/USArmy. His conclusion was that, depending on the specific application, the

number of degrees of freedom considered in the development of helicopter mathematical models and flight laws for handling quality purposes vary between 6-dof fuselage + quasi-static rotor, 9-dof fuselage + rotor flap, 10-dof fuselage + rotor flap + rpm or fuselage + rotor flap + rotor lag and 16-dof fuselage + rotor flap + rotor lag + pitch + rpm, with linear and non-linear aerodynamics. Linear aerodynamics refers to simplifications such as small angle of flapping and inflow, and the use of the simple blade theory with no compressibility or stall effects included. According to Chen et. al., simplified linear aerodynamics models may be used for exploratory investigations within the flight envelope: for basic aircraft, a 6-dof linear model for low frequency manoeuvres, and a 9- or 10-dof model for high frequency manoeuvres; for SCAS research, a 6- or 9-dof linear aerodynamics model to determine the fuselage feedback, and a 9-, 10-, 12- or 16-dof linear aerodynamics model to determine the rotor/fuselage feedback. For investigations involving exploration to the edge of the flight envelope, nonlinear aerodynamics effects must be included in the simulations.

The next sections summarize some of the landmarks in understanding how helicopter flight dynamics simulation models have to be extended. The present literature overview will depict the expansion of the 6-dof model in the following areas:

1. rotor disc-tilt dynamics;
2. rotor lead-lag dynamics;
3. inflow dynamics;
4. engine dynamics.

1. Rotor Disc-Tilt Dynamics

Rotor disc-tilt dynamics (often ambiguously called "flapping dynamics" in literature) is a key element in the selection of the gains in the design of high-gain automatic flight-control systems. Of the disc-tilt modes, the low-frequency regressing flapping mode usually couples with the body dynamics. The inclusion of rotor disc-tilt dynamics in the simulation model depends first and foremost on the rotor type:

- for articulated rotors:

  Miller [1950][70] and **Ellis** [1953][28] were probably the first ones who recognized that disc-tilt dynamics imposed limitations on the design of high-gain attitude-stabilization systems for articulated-rotor helicopters, which otherwise were not present.
  Hall and Bryson [1973][37] demonstrated analytically that applying an optimal control system, derived on the basis of the quasi-steady rotor flapping assumption, to a model including disc-tilt dynamics, results in instabilities that were not predicted using the 6-dof approach.
  Chen and Hindson [1985][15] demonstrated that high-gain flight-control systems cause pitch and roll oscillations in the frequency range around 5 rad/s (i.e $5/2\pi$

Hz ≈ 0.8 Hz). Investigating the problem of roll oscillation for a high-gain control system in an articulated rotor helicopter, they showed that a 9-dof model gave good results.

- for hingeless rotors:

Hohenemser and Yin [1974][43] investigated what is the least sophisticated analytical body + rotor disc-tilt model for a hypothetical hingeless rotor helicopter. A linearized 9-dof body + rotor disc-tilt model was developed and applied to the development of two feedback systems: firstly, a rotor-tilting feedback system to the longitudinal cyclic and secondly a normal-acceleration feedback system to the collective pitch. For the former feedback system, the results showed that a complete 9-dof body + disc-tilt coupled model was required. For the latter feedback system, the 9-dof model seemed to be oversophisticated, an 8-dof model using only the first-order rotor disc-tilt dynamics being sufficient. A 6-dof model always resulted in substantial errors.
Miyajima [1979][73] also developing a 9-dof model, demonstrated that neglecting the blade regressing flap mode in a hingeless rotor actually means neglecting a very important oscillatory mode with short period frequencies.
Fu and Kaletka [1990][34] using parameter identification techniques, investigated for the Bölkow Bö-105 hingeless rotor helicopter which degrees of freedom from rotor dynamics can be identified as important for the helicopter dynamics, on the basis of flight test data. The first-order disc-tilt dynamics added to a 6-dof model (resulting in an 8-dof model) transformed the aperiodic roll mode into an oscillatory one, showing that the roll dynamics couple to the disc-tilt dynamics. Adding also the second-order rotor disc-tilt dynamics to the model (resulting in a 9-dof model) led to good agreement between measurements and model response.
Kaletka and Gimonet [1995][55] on the contrary, also using identification techniques to compare a 6-dof rigid body model to a 9-dof body + disc-tilt model for the same Bölkow Bö-105 in hover flight, concluded that the response of the 9-dof model is only slightly better than the 6-dof model; a 6-dof model was sufficient to simulate the hovering Bö-105.

Curtiss and Shupe [1971][20] referring to the number of modes to be included in piloted simulation models when considering blade elasticity, looked for the minimum number of modes required to represent a hingeless rotor. They concluded that for advance ratios, μ, higher than approximatively 0.2, at least two bending modes are necessary. The first flapping mode effects can be simulated by using the representation given by **Young** [1962][104] in the equivalent rigid blade concept (discussed in section 2.6.3 of Chapter 2). The second flapping mode needed to be considered in the analysis as well, the effect of this mode becoming increasingly important as the advance ratio is increased or when geometrical twist is considered in the model. **Hohenemser and Yin** [1974][43] however demonstrated that the above conclusion is wrong because Curtiss and

Shupe neglected the aerodynamic coupling between the considered bending modes. Hohenemser and Yin showed that including only the first flapping bending mode in the model is sufficient to obtain adequate results for hingeless helicopter models operating in the normal range of speeds. Omitting the aerodynamic coupling terms between the first and the second blade flapping bending mode can induce larger errors in the models than omitting the second mode entirely. The authors commented that this conclusion may not be applicable to medium advance ratios, high-lift conditions or high twist blades including stall or non-uniform inflow effects.

2. Lead-Lag Dynamics

With regard to rotor lead-lag dynamics, until relatively recently it was believed that the blade lead-lag degree of freedom produced little change in the basic helicopter modes of motion, neither for articulated nor for hingeless rotor helicopters. Lead-lag dynamics are of primary importance for aeroelastic stability purposes, because of their lightly-damped characteristics, but for flying quality investigations it was believed that lead-lag dynamics were not important. Only during the 1980's was more attention paid to the study of the influence of the lead-lag degree of freedom on piloted simulation models and automatic flight-control systems. Some highlights of the research in this field are presented below.

Curtiss [1986][21] referring to the importance of lead-lag dynamics in the simulation model, concluded that in the high frequency band (more precisely, the 10-20 rad/sec range, i.e. 1.6 Hz to 3 Hz), the regressing lead-lag mode contributes significantly to the helicopter response and should not be ignored in the design of automatic flight-control systems. He demonstrated that, whereas the attitude feedback gain is primarily limited by body-flap coupling, the roll rate feedback gain is limited by the lead-lag degree of freedom. For an articulated rotor, in a model without a feedback system, the lead-lag degree of freedom produces little change in the helicopter basic modes and therefore it can be neglected.

Fletcher and Tischler [1996][30] using parameter identification techniques concluded that, although the lead-lag dynamics have negligible influence on the rotor disc-tilt response of the UH-60 articulated rotor, they contribute significantly to the roll-rate response for frequencies in the range of 12-100 rad/sec (i.e. 2-16 Hz). They consider that a coupled body + disc-tilt model is adequate to model the rotor response up to 40 rad/sec (6.3 Hz), but that a lead-lag model is required to capture the correct helicopter angular rate-response characteristics.

Houston and Horton [1987][51] verifying a theoretical 12-dof body + disc-tilt + rotor lead-lag model for the articulated Puma helicopter, using parameter identification techniques, failed to predict the helicopter trend in damping ratio and natural frequency above 100 knots, whereas at 80 knots the damping ratio

was underestimated and the natural frequency overestimated.
On the contrary, **Heimbold and Griffith** [1972][38], comparing a 9-dof body + disc-tilt with a 13-dof body + rotor flap + rotor lag + rpm analytical model for a hingeless rotor, from hover up to flight speeds of 200 knots, concluded that the addition of the lead-lag modes to the 9-dof model had little effect on the helicopter flight dynamics. Also, the stability of the lead-lag modes was hardly affected by the variations in rotor disc-tilt dynamics caused by the feedback systems.
Diftler [1988][24] searched for the cause of the strong oscillations which appeared on the UH-60A helicopter in hovering flight when roll-rate gain was used. His conclusion was that the lead-lag degree of freedom played an important role in the mechanism of the oscillation investigated. Examining different helicopter model approximations, he showed that a 6-dof body model did not predict any oscillatory instability; adding rotor disc-tilt dynamics still did not reveal the instability; next adding also the rotor lead-lag dynamics resulted in an instability in the lead-lag mode but at a frequency different from the one reported by the pilot; finally, including also the control dynamics, an instability in the regressing flap mode resulted at the reported frequency. Further expanding the model by including other higher-order dynamics -such as engine/fuel dynamics and inflow dynamics- did not affect the above conclusions.
Aponso et al. [1994][1] presented a relatively new example of how the lead-lag dynamics can influence the body dynamics of the Sikorsky CH-53, 7-bladed, articulated-rotor, heavy-lift helicopter. Using parameter identification to verify a 12-dof body + rotor flap + rotor lead-lag model to flight test data, a discrepancy between theory and experiment was identified. To eliminate this discrepancy a very strong artificial lead-lag spring which does not exist on the real helicopter had to be added to the model. However, the authors could not explain why their model could not be validated without using this artificial spring.
McKillip and Curtiss [1991][69] and **Curtiss** [1992][22] further explored this inconsistency between the real Sikorsky CH-53 and the 12-dof model presented by Aponso et. al. They demonstrated that the need for the artificial lead-lag spring was due to the non-validity of the rigid blade concept usually used in simulation models. The powerful damper installed on the Sikorsky CH-53 articulated helicopter, modifies the blade boundary condition in a way that causes the first lead-lag mode to be poorly predicted by the rigid blade approximation. Considering the blade as flexible, the inconsistency presented in the 12-dof model disappeared without the need to add an artificial lead-lag spring as in the model of Aponso et. al.. It turned out that the damper installed on the real Sikorsky CH-53 converted the lowest lead-lag mode into a hybrid between the hinged and hingeless mode shapes.
Kothmann [1996][60] referring to the problem of validity of the rigid-blade concept established that this concept is valid only if the eigenvalues of the flexible blade are complex conjugates. Any pair of flexible blade eigenvalues can be represented by a rigid blade with some (non-physical) hinge spring and damper.

However, for the stiffness and the damper of the Sikorsky CH-53, there was a third negative real eigenvalue of the same magnitude as the complex pair. Therefore, the disagreement between the rigid and flexible blade concepts is the result of this third purely real eigenvalue.

3. Inflow Dynamics

It had already been recognized for a long time in the literature that the effects of the dynamic inflow on helicopter stability and control characteristics are quite significant:

Carpenter and Fridovich [1953][13] demonstrated that the dynamic inflow plays a key role in the destabilization of the rotor disc-tilt dynamics in transient motions of articulated and especially of hingeless rotors. Analysing the vertical acceleration response to an abrupt input in the collective pitch, Carpenter and Fridovich showed that the initial overshoot in the response originates from the coupling between the rotor disc-tilt with the inflow dynamics. This overshoot becomes more pronounced when either the thrust coefficient or the blade Lock number is reduced.

Sissingh [1968][95] also illustrated how, for certain motions of the rotor, such as steady pitch rate, the dynamic inflow affected the helicopter stability and control characteristics.

Curtiss [1986][21] demonstrated that the time constants associated with the inflow dynamics are of the same order as the low frequency rotor disc-tilt dynamics, and thus, if disc-tilt dynamics are included in the model, it seems likely that the inflow dynamics should be included as well. For hingeless rotors, **Curtiss** [1971][20] arrived at the conclusion that there is a variation in the moment of the aerodynamic forces about the rotor hub which can be explained by a first harmonic variation in the induced velocity. This modification to the airload in hingeless rotors can be incorporated in the definition of the Lock number resulting in a "modified Lock number".

Chen and Hindson [1985][15] showed that inclusion of the inflow dynamics resulted in reducing the predicted frequency of the regressing flap mode to that observed in the flight test of an articulated rotor helicopter.

4. Engine Dynamics

Besides the higher-order effects caused by rotor dynamics, the engine dynamics can also be very important for piloted simulation modeling. **Kuczynski et. al.** [1980][61] discussed the differences in mentality in approaching the problem of piloted simulation modeling by an airframe and an engine specialist: on the one hand, the airframe specialist is looking for high-fidelity models to describe as well as possible the helicopter's behaviour; on the other hand, the engine specialist treats the rotor very simply and concentrates only on the engine design. As a result, dynamic interface problems may appear between the airframe and the engine dynamics. This separate

approach was demonstrated by the authors to result in incompatibilities in the development of articulated helicopters at Sikorsky. For these helicopters, the demand for more responsiveness caused the engine manufacturer to use more responsive engines. As a result, the airframe manufacturer had to consider how to properly include the influence of engine/fuel control law dynamics in piloted simulation modeling. In addition, the engine manufacturer had to investigate how to adequately model helicopter behaviour in the engine/airframe models. The authors explained that the main importance of the inclusion of engine dynamics in the simulation model lies in the fact that it will allow the helicopter fuselage to see a correct variation of rotor torque and corresponding rotor speed as caused by changing airload and engine conditions. The coupling between the airframe rigid-body modes and the rotor/drive train torsional system occurs primarily through a coupling of fuselage yaw with the rotor rpm. The main deficiency of the rotor/drive system model used at Sikorsky was that it could not account for any coupling with flight dynamic motions of the aircraft as a whole - including airframe motions and main rotor pitch and yaw motions-.

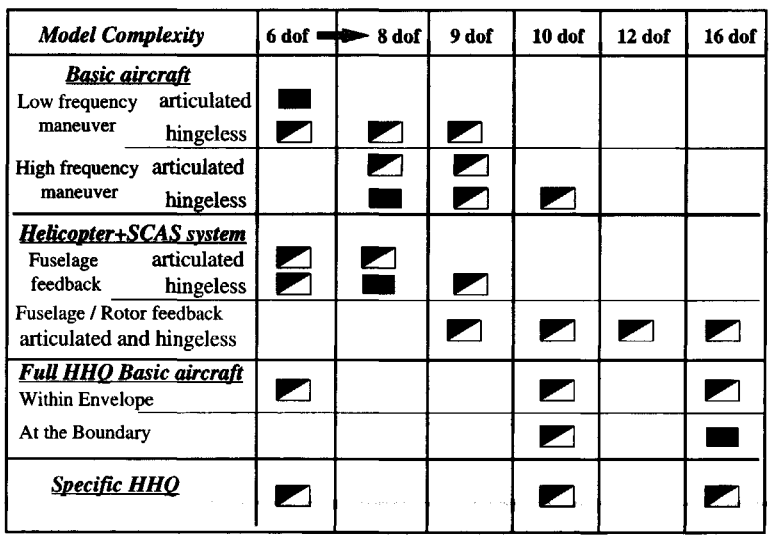

Figure 3.2 Level of complexity in piloted simulation modeling depending on case considered

The models used in the literature cited in this review are summarized in Figure 3.2. Looking at this figure it appears that only for a small number of cases did the designer know which model was valid for use in the piloted simulation modeling.

Concluding, the present literature overview proved that helicopter piloted simulation modeling is a complex process. It is not sufficient to blindly extend a simulation model; one has to identify the right modes to be included in the right situations in order to obtain a good prediction of helicopter behaviour.

3.2 Necessary Degrees of Freedom for Horizontal Axis Wind Turbine Structural Modeling

As mentioned in section 2.7 of Chapter 2, although helicopters and wind turbines are similar configurations, the models developed for these two configurations are based on two different approaches: whereas for helicopters the central problem to be resolved in a simulation model concerns the stability analysis, depending on the coupling effects between the different modes involved in the model, the simulation models developed for wind turbines focus on the loading analysis depending on the accurate representation of the external excitations acting on the structure. Thus, the question of necessary degrees of freedom for wind turbine modeling is hardly mentioned in literature. Usually, the literature on wind turbines presents simulation softwares of different manufactures in which a high number of modes are taken into account in order to calculate the wind turbine dynamic loading properly. This resulted in the course of time in advanced codes to calculate wind turbine dynamic loading (for example PHATAS[65], FLEXLAST[62], ADAMS[67]). Current state-of-the-art models generally include twelve to fifteen degrees of freedom (as for example in PHATAS):

- flapping and lead-lag elastic blade deformations;
- passive or controlled pitch motion;
- blade flapping hinge inclination and teeter hub;
- drive-train torsional deflection; variable rotor speed;
- nacelle pitch and yaw;
- tower torsion and bending (fore-aft and sideways).

Environmental parameters including steady wind, wind shear, gusts, wind direction and turbulence can be considered in these complex models. Some codes (for example ADAMS[67]) that are based on the finite element method, involve a virtually unlimited number of degrees of freedom. However, such models are extremely slow when performing simulations involving wind turbulence inputs.

Concerning the number of modes considered in these models, there exists no guideline on how the modal selection has to be done. The philosophy used in wind turbine modeling is that *"the simulation model must start with suitably detailed models of the subsystems (blades, power train, support system) and then combine them in a manner*

that enables aeroelastic analysis. There is little value of dependability in modal analysis except that of the fully-coupled system" (**Doman** [1994][25]). It is sometimes recognized that there are design features that may uncouple subsystem elements, reducing the number of system modes that will present significant responses. However, the reduction of the number of modes must be done step by step from a complex to a simplified model, each time checking the influence of the deleted modes on the results. Such an approach is very difficult to be followed when the designer is trying to understand the effects of the different parameters involved in the model. This difficulty will increase, in light of the discussion presented in section 2.7 of Chapter 2 on the evolution of the wind turbines towards very flexible configurations.

Because of the limited amount of literature on the necessary degrees of freedom, the present section is concerned firstly with the problem of wind turbine structural modeling from the perspective of the main sources of excitation on the structure and secondly with some considerations on the coupling between the degrees of freedom in the wind turbine structure.

Referring to the first problem, the most important excitation sources on a wind turbine structure result from:

1. Aerodynamic loading causing the following effects:

- *Rotational sampling** effect, which may be explained as follows: consider a wind turbine blade, rotating rapidly through a wind velocity field that varies over the rotor disc but does not vary in time. As the blade rotates through such a wind field it encounters different wind velocities. This cycle is repeated again and again after each complete revolution, such that the wind velocity as seen by the rotating blade will have strong fluctuations in a band of frequencies near the integer multiples of the rotation velocity (1-P, 2-P, etc) (for more detail see **Holley et. al.** [1984][45])
- *Wind shear** (surface roughness), both vertical and horizontal, is an important excitation for hingeless rotor blades. **Leconte and Széchényi** [1990][64] demonstrated that wind shear and yaw have a similar effect on the rotor in that both generate a periodic variation in the angle-of-attack as seen by the blades, influencing the unsteady bending moment;
- *Tower shadow** is a severe excitation especially for a downwind wind turbine and can be the driver in the design of the outboard shell structure of the blade airfoil. **Friedmann** [1975][33] showed that a wind turbine operating in the shadow or wake of the open lattice tower, increases the asymmetry of the airloads of the rotor and may have a significant effect on the aeroelastic stability and response of the combined rotor-tower system. Discussing the so-called "bow wave effect", i.e. the acoustic noise of the blade as it enters and leaves the tower shadow, **Doman** [1994][25] commented that this problem may very likely lead to the abandonment of the downwind solutions;

- Wind Gusts and Atmospheric Turbulence To control fluctuations in the energy added to the system by wind gusts, fluctuations in the wind turbine rotor speed are desirable. Steadiness in the power output of the generator can much better be achieved with a variable speed rotor than with a constant speed rotor;
- Variations in wind direction may induce large lead-lag angles in large wind turbines (**Perkins and Jones** [1981][89]). For a three-bladed wind turbine, **Kaza and Hammond** [1976][56] investigated the effect of an abrupt change in wind direction angle and intensity on the lag damping when no pitch-flap and pitch-lag couplings are included in the model. While a sudden change in wind intensity did not appreciably affect the lead-lag mode damping, a sudden change in wind direction resulted in a significant decrease in the lead-lag damping. For a two-bladed wind turbine, studying the same problem, **Azuma et.al** [1984][4] reported that in both cases a small yawing motion was induced originating from the change of the aerodynamic forces and moments. **Kawamato and Sakakibara** [1988][58] investigating the dynamic characteristics of a free-yawing wind turbine subjected to a change in wind direction, noted that when the rotor was running, there was much difference in the angular change between the rotor axis direction and the wind direction. The yawing turbine is compared to a gyroscope because it has three rotating axes and therefore, up and yaw direction motions interfere with each other, just as in the case of a gyroscope.

2. Gravity load is a 1-P excitation acting on the blade lead-lag motion, but also a source of parametric resonances. In a coned rotor, the 1-P gravity excitation can enter the control linkage, acting on the rotor shaft as a 2-P load unless the rotor is teetered: Using a flap-lag-feather rotor blade model (a non-conventional hinge sequence was used of feather, flap and lead-lag) for a 3-bladed wind turbine, **Chopra and Dugundji** [1979][17] demonstrated that, whereas the blade lead-lag response is primarily influenced by the gravity field, the flapping motion is controlled by wind shear flow. The blade coning angle couples the flap and lead-lag degrees of freedom.

3. Mass, stiffness and aerodynamic unbalance from blade to blade can induce cyclic loads in the wind turbine. **Dugundji** [1976][26] showed that while the gravity load acts directly on the blades, the unbalance shakes the tower which in turn couples into the blades;

4. There are special operating cases in which the control system plays an important role in the loads acting on the structure. The loss of electrical load and the rapid application of pitch angle control are two examples damaging to the wind turbine, leading to overspeed and thrust reversal. Thus, the wind turbine control system must be designed to assure a safe shutdown without structural damage and limited blade pitching rates.

All excitations sources mentioned above induce vibrations in the wind turbine structure. From the very beginning of wind turbine development, the subject of vibrations was of great concern. However, as discussed above, the emphasis in wind turbine simulation

modeling has always been directed towards determining the way in which the external loads are connected to the elastic modes of the construction and not on the coupling effects existing between these modes.

For example, the choice for a three-bladed configuration in the early days of large wind turbine design was motivated by the serious vibrations which were observed in a two-bladed model during changes in wind direction. In 1931, Jacobs Wind Electric reported that, when yawing, the two-bladed rotor experienced a series of jerks produced by changes in gyroscopic inertia about the tower axis each time the blades passed from a vertical to a horizontal position (**Sheperd** [1994][25]). This problem could be eliminated by replacing the two-bladed solution with three blades. The three-bladed rotor eliminated the tower shake, by providing a constant inertia. Also, adding a third blade eliminated the need for a coupled rotor-tower analysis. Later, tower shake of two-bladed rotors was prevented by introducing the *teetering rotor** (however, this solution was not applied in industry) and by allowing low yawing-speed of the nacelle.
Referring to the problem of coupling between the degrees of freedom in the wind turbine, according to **Smith** [1985][97], the key vibrational consideration for a two-bladed wind turbine is the coupling of rotor flapping vibrational modes with the tower translational motion. **Steinhardt** [1981][98] searching for a minimum number of parameters for a realistic representation of the dynamic and aeroelastic characteristics of a complete wind turbine, developed a model for a two-bladed wind turbine including tower bending and torsion + nacelle pitch and yaw + rotor blade bending in the flapping and lead-lag directions. The simulations performed with this model confirmed strong rotor-tower coupling and illustrated typical features of periodic systems. Unstationary aerodynamic terms were found to be of minor importance. The hingeless rotor configurations considered were better damped than the teetering rotors, but tower and blade reactions to gravity and wind gusts were higher.

A good survey on the general problems to be considered in wind turbine design was given by **Miller et.al.** [1978][71] during the NASA Mod-0 program. **Sullivan** [1981][99] reporting further on experience from the NASA Mod-0 program, described the initial and final design solutions of the resonance problem of the two-bladed wind turbines Mod-0 and Mod-1 (see Figure 3.3). In the initial design, resonance points were defined as intersections between the curves giving the variation of the excitation frequencies and the natural system frequencies with the rotor speed, as represented in the Campbell diagram (see section 4.5.1 of Chapter 4). Around each intersection point, a potential resonance region could be defined which must be avoided. The width of these regions was not precisely known. For the Mod-0 and Mod-1 wind turbines in the initial design, they were conservatively set at ±0.5/rev for the even harmonics and ±0.25/rev for the odd harmonics. However, this approach resulted in very narrow regions where the designer was allowed to place the frequencies. Based on field experience, the initial design was refined and the acceptable regions for the natural frequencies were enlarged.

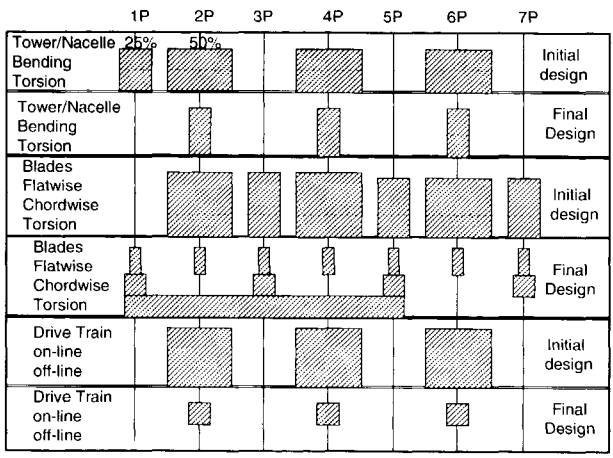

*Figure 3.3 Initial and final resonance avoidance for a two-bladed wind turbine (**Sullivan** [1981][99])*

The final design solutions are represented in Figure 3.3: for flapping, the regions at odd and even harmonic excitations should be avoided; for lagging, only regions at odd harmonic excitations should be avoided; blade/pitch change mechanisms require high stiffness to avoid flutter; for the tower, the 1-P and even harmonic excitations should be avoided; in the drive-train, if the rotor is perfectly balanced, only even harmonic excitations would be expected. However, a strong 1-P excitation in the drive train was experienced in the field, as a result of the mass, stiffness and aerodynamic unbalance between the blades. The main excitations of the tower occurred at frequencies of 1-P and N-P (N is the number of blades), the first excitation arising from the unbalance, the second one from blade passage, wind shear, and yaw error.

3.3 General Discussion on Dynamic Instabilities of Helicopters and Wind Turbines

As discussed in section 1.3 of Chapter 1, for helicopters and wind turbines the distinction between rigid body dynamics and structural dynamics involving vibrations and aeroelasticity phenomena is not applicable. The present section does not aim to provide an overview of the aeroelastic instabilities of helicopters or wind turbines, since the subject of concern of the present dissertation is related to the necessary degrees of freedom in low-frequency simulation modeling (recommended surveys on this subject are **Hohenemser** [1974][41], **Ormiston** [1983][75], **Johnson** [1986][53], **Chopra** [1990][16]). This section is merely intended to stress the general framework in which the dynamic instability problems have to be considered in simulation modeling.

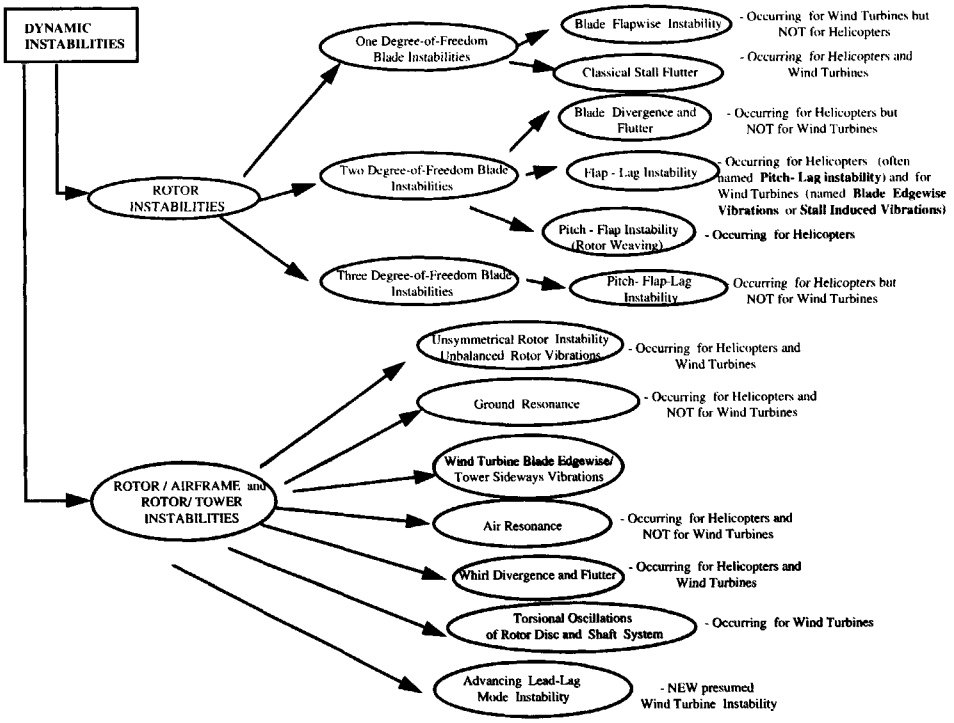

*Figure 3.4 Instabilities in helicopter and wind turbine configurations (**Pavel et.al. [1999]**[83])*

For helicopters, before 1970, using conventional articulated and teetering rotor configurations, two classes of dynamic instabilities were of concern: *flutter** and *ground resonance**. Also, in the isolated rotor, blade flapping stability problems at high advance ratios occurred. After 1970, due to the shift of helicopter design towards hingeless and bearingless configurations, new classes of aeroelastic instability problems emerged. These configurations were poorly understood from the point of view of structural dynamics. In coupled rotor-body dynamics, the hingeless rotors introduced a new complex class of aeromechanical problems, where structural dynamics and aerodynamics were interacting.

For wind turbines, the configurations of the 1970's did not present a great risk of dynamic instabilities. Phenomena such as ground resonance or *whirl-flutter** which

were investigated as potential instabilities, were situated outside the operating range of rotor rotational speed for the wind turbines of that time -exceptions were some experimental configurations as for example the **FLEXHAT** [1990][62] or **KEWT** [1980][46] concepts. However, today, a new generation of large scale wind turbines is discussed with rotor diameters as large as 60 m. In such configurations, known as well as unknown forms of dynamic instabilities are already becoming problematic.

A comparison between the dynamic instabilities in helicopter and wind turbine configurations is presented in Figure 3.4. The instabilities specified in this scheme are defined in the Glossary. Both in the design of helicopter and wind turbine configurations the key problem related to the subject of dynamic instabilities consists of the choice of natural frequencies of both rotating and non-rotating structures. The remainder of the present section is concerned with a misunderstanding between the helicopter and wind turbine communities discovered during the present work about the definition of soft and stiff configurations in relation to blade natural frequencies.

3.3.1 Definition of Soft/Stiff Rotors for Helicopters

For helicopters, hingeless rotors can be classified as either soft or stiff depending on the natural flap and lead-lag frequency. Using as a parameter the blade flapping frequency, **Hohenemser** [1974][41] introduced the concept of soft- and stiff-flapwise rotors in order to characterize helicopter's control response features:

- soft-flapwise rotors have a blade natural flap frequency (at normal rotor speed) of between 1.05 and 1.15/rev
- stiff-flapwise have a blade flapping frequency of 1.4/rev or more.

The natural flapping frequency ω_β of an articulated rotor without hinge offset is exactly equal to the rotor angular speed Ω. Usually, hingeless helicopters are soft-flapwise configurations. The design goal, relative to the flapping frequency for helicopter flight dynamics, as defined by **Hohenemser** [1974][41] is *"to reduce the flapwise stiffness to the minimum value consistent with the structural requirements of adequate margins for the severe trim, gust and manoeuvre conditions."*

Using as a parameter the blade lead-lag frequency, helicopter rotors can be classified according into soft- and stiff-inplane rotors:

- soft-inplane rotors have a blade natural lead-lag frequency smaller than 1/rev;
- stiff-inplane rotors have a blade natural lead-lag frequency larger than 1/rev.

This definition relates to the danger of ground resonance, one of the most dangerous instabilities in early helicopter design. Ground resonance involves the frequency coalescence between the blade lead-lag motion and the inplane motion of the rotor hub in a weakly damped system and may appear in rotors having a natural lead-lag

frequency below 1/rev. It may be eliminated by introducing an adequate amount of artificial damping in the system, both in the blade and in the hub motion. Articulated rotors usually have $\omega_\zeta \leq 0.3\Omega$. Thus, in articulated and soft-inplane hingeless rotors ground resonance may be a cause for concern. In soft-inplane hingeless rotors, due to the structural (elastic) couplings in the system (see Appendix H), ground resonance manifests itself as a much milder instability as compared to the articulated configurations.

Nevertheless, in both stiff- and soft-inplane helicopters, coupling of the lead-lag motion with the flapping and pitching motions -usually resulting from aerodynamics- results in the so-called "*air resonances instabilities*".

Returning to the statement that hingeless helicopter design changed in time from a stiff to a soft rotor design, the present section will clarify the reasons for this evolution for the helicopters. The change in this direction was actually a lesson learned by engineers in order to avoid dynamic instabilities

Reflecting on the danger for ground resonance, (which, as mentioned above, turned out to be of concern especially for articulated and soft-inplane hingeless configurations) in the beginning of helicopter hingeless rotor development, stiff-inplane configurations were preferred since this eliminated the ground resonance instability as well as the need for lead-lag dampers (stiff-inplane rotors were developed by Bell and Lockheed). It was soon realized however, that stiff-inplane rotors were very sensitive to new unknown rotor instabilities involving low frequency flap, lag and torsion motions and rotor-body instabilities, especially in high-speed and manoeuvring flight (see literature survey of Appendix H). These new instabilities were milder than the ground resonance problem of the articulated rotor, but they were much more complex and involved rotor aerodynamics, and additional blade and fuselage degrees of freedom. To protect a stiff-inplane rotor against such instability phenomena proved to be a difficult task due to the small blade deflections. It was very hard to provide the stiff-inplane blades with mechanical damping and to tune the elastic couplings.

As a consequence, the design of helicopter hingeless rotors focused on the development of soft-inplane rotors. Despite the ground resonance problem, the soft-inplane rotors can be provided with effective mechanical dampers of the elastomeric type. It was also realized that by design, the structural couplings existing in a soft-inplane rotor can be used to introduce damping in the lead-lag motion, sometimes even in a resonance point. The MBB, Westland and later Aerospatiale helicopter manufactures followed this line and developed rotor soft-inplane configurations. A difference in approach between the different compromises while developing the soft-inplane rotors may be mentioned here: while Westland, during the development of the WG-13 saw any structural (elastic) coupling as a danger for dynamic instabilities and therefore tried to eliminate such couplings as much as possible, MBB designed the rotor of the Bölkow Bö-105 to take advantage of the structural couplings existing in the system, from an aeroelastic point

of view. Thus, whereas the Westland WG-13 had to be equipped with hydraulic lead-lag dampers to avoid the ground and air resonance instabilities, the Bölkow Bö-105 did not require any lead-lad damper. Nowadays, in helicopter industry soft-inplane rotors are preferred over stiff-inplane rotors.

3.3.2 Definition of Soft-/Stiff Rotors for Wind Turbines

The present dissertation discovered that a misunderstanding in the definition of soft and stiff configurations when looking at the evolution of rotor design within the helicopter and wind turbine communities. Investigating the relative position of the non-dimensional natural flapping and lead-lag frequencies of modern wind turbine configurations as compared to those of the 1970's in Figure 2.10 of Chapter 2, it was surprisingly observed that although in dimensional values ω_β and ω_ζ the blades of the modern wind turbines are softening, in terms of non-dimensional values ω_β/Ω and ω_ζ/Ω, they are stiffening. In the 1970's, wind turbine rotors had non-rotating flap frequencies in the range of 2 to 3/rev. Modern wind turbine configurations have non-rotating flapping frequencies in the range of 3 to 6/rev and are therefore stiff-flapwise according to Hohenemser's classification. In the 1970's, wind turbine rotors had non-rotating lead-lag frequencies in the range of 2/rev to 2.5/rev. Modern wind turbine already reached values of 9/rev and are therefore strictly stiff-inplane configurations according to Hohenemser's classification.

The wind energy community neither uses the concept of soft- and stiff-flapwise nor soft- and stiff-inplane rotors as defined by the helicopter community: whereas for helicopters the soft/stiff concept refers to the non-dimensional blade frequencies ω_β/Ω and ω_ζ/Ω (natural flap and lead-lag frequency non-dimensionalized w.r.t. rotor rotational speed), for wind turbines, the meaning of soft and stiff refers to the dimensional blade frequencies ω_β and ω_ζ. This is an important observation because, for example, although in the design the blades can be softened by decreasing ω_β, if the rotor speed Ω is decreased as well and this decrease is more significant than that of ω_β, the new non-dimensional flap frequency corresponds to a stiff-flapwise configuration. Thus, although in dimensional frequencies the blade may be softened by design, in non-dimensional frequencies it actually is of stiffer nature.

The wind energy community usually associates the term soft/stiff configuration with the tower. The main excitations of the tower structure occur at frequencies of 1-P (due to rotor unbalance) and at N-P (due to blade passage, wind shear and yaw error), where N is the number of blades and 1-P is the rotational frequency of the rotor. As a function of the value of the first tower bending frequency f_t, the towers can be classified as follows:

- stiff when $f_t > N\text{-}P$;
- soft when $1\text{-}P < f_t < N\text{-}P$;
- soft-soft when $f_t < 1\text{-}P$,

This classification is not standard, the second condition sometimes being denoted as soft-stiff and the last as very soft. As a design requirement, the tower eigenfrequencies must stay reasonably clear (even by a margin of ± 25%) of the frequencies 1-P and N-P in order to avoid resonance. In modern wind turbines the solution of the very soft tower is being preferred as being the lightest and most economical solution.

According to **van Holten et. al.** [1999][48], during the "First National Dutch Research Program on Wind Energy" (1976-1981) much attention was paid to investigate the risk of aeroelastic instability problems (such as flutter and rotor instabilities as known from helicopter industry). The conclusion at that moment was that stability problems were of no concern for the then-existing wind turbines and that, for these devices, attention should be paid to the loading problems (the effects of wind fields, turbulence and disturbances on the structure).

The previously discussed observation that wind turbine rotors are stiffening, together with the discussion in section 3.3.1 on the danger of instabilities observed in stiff-inplane rotors, justify the conclusion of this dissertation that modern wind turbine configurations are headed towards a new area of problems where aeroelastic instabilities and vibrations may be difficult to control and eliminate. This serves as a warning to wind turbine designers to be aware that new instabilities may appear in modern wind turbines, as a result of the process of rotor stiffening in the flapping and lead-lag direction. Already, industrial wind turbine applications are presented where dynamic instabilities appeared: on the mid-class wind turbines of 500-600 kW, lead-lag dampers had to be mounted in order to avoid strong lead-lag vibrations of unknown origin (see **Anderson** [1999][3]).

The present conclusion is also supported by **van Holten et. al.** [2000][49] who showed that due to scaling effects, new types of instabilities which are currently not encountered in helicopters may appear in wind turbines. Using the square cube law it was demonstrated that the mutual position of the flapping and lead-lag eigenfrequencies does not change by upscaling. Also, the position of these eigenfrequencies with respect to the aerodynamic excitation frequency remains unchanged. The unsteady aerodynamic effects are unchanged as well, and therefore, the "classical flutter" problem remains unchanged.

However, certain parameters do not quite behave according to this law. For example, this is the case with the flapping eigenfrequency which actually, by upscaling, decreases less rapidly than the lead-lag eigenfrequency (in dimensional values). While for present wind turbines the ratio between the blade flapping and lead-lag eigenfrequency was around a value of 1.5, by upscaling, this ratio approaches 1. This makes the future wind turbines susceptible to flap-lag instabilities, especially in the stall region.

Another potential instability due to the effect of scaling explained by **van Holten et. al.** [2000][49] is the so-called "advancing lead-lag mode instability" (mentioned also in

Figure 3.4). This instability can be qualitatively explained in Figure 3.5 using a similar approach applied to the ground resonance diagrams from the helicopter world. Using the Coleman transformation (see Appendix D), the variation of the lead-lag frequency with the rotor rotational speed can be represented in the non-rotating system by its advancing and regressing lead-lag mode. Representing also the variation of the first and second tower bending modes with the rotor rotational speed, the points of intersection between the lead-lag modes and the tower bending modes represent possible instabilities. Figure 3.5 considers two cases:

- the lead-lag non-rotating frequency was measured on a blade with an infinitely stiff blade-hub connection $\bar{\omega}_{\zeta\ stiff}$ (continuous line);
- the lead-lag non-rotating frequency was measured on a blade with a more flexible blade-hub connection, resulting in a lower lead-lag non-rotating frequency $\bar{\omega}_{\zeta}$ (dotted line).

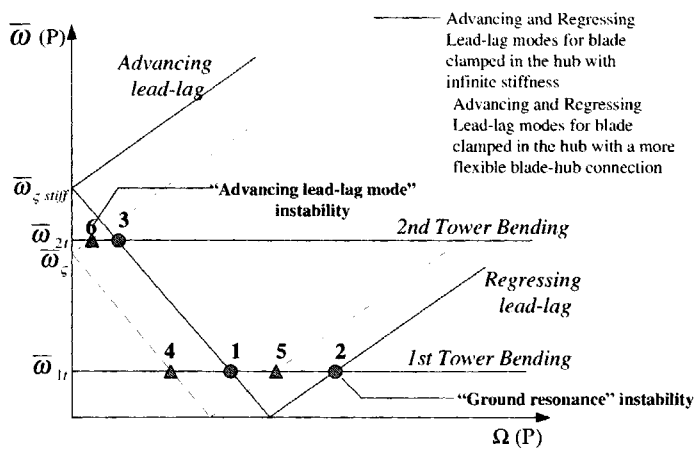

*Figure 3.5 Explanation of the "advancing lead-lag mode" instability, a new kind of instability characteristic to wind turbines (**van Holten et. al.** [2000][9])*

In the first case, the first tower bending mode intersects with regressing lead-lag mode in two points (denoted as 1 and 2). While in point 1 it can be demonstrated that the forces which would cause the instability cancel each other out, point 2 causes the so-called "ground resonance" instability. For present configurations, this point is out of the normal operating range of wind turbines, and can therefore be considered not dangerous. The second tower bending mode intersects with regressing lead-lag mode in point 3, which is not dangerous either for instabilities.

In the second case, when the blade hub connection is more flexible, the first tower bending mode intersects with the regressing lead-lag mode in two points (denoted as 4 and 5). Reasoning as in the previous case, point 4 is not dangerous for an instability

due to the cancellation of the forces which would cause the instability, whereas point 5 may cause the "ground resonance" instability. The second tower bending mode intersects with the branch of the advancing lead-lag mode in point 6. Point 6 denotes a new kind of instability, the so-called "advancing lead-lag mode instability" which is not known in the helicopter world.

3.4 Outline Survey on Structural Couplings in Hingeless Rotors

In the very beginning of this dissertation, in section 1.1 of Chapter 1, it was mentioned that one of the problems the designer has to solve in order to determine the necessary degrees of freedom in a simulation model is to adequately represent the rotor flexibility, especially in hingeless rotor configurations. Further, section 2.6.3 of Chapter 2 introduced the definition of so-called "structural (elastic) couplings", resulting either from the flexibility of the structure or introduced deliberately by the designer when designing the blade geometry (see Appendix H). The structural couplings may be advantageous in many cases, whereas in other cases their use may result in adverse effects. Actually, it is difficult to determine the influence of these parameters over a wide range of operating conditions. The present section defines the basic structural couplings of a helicopter hingeless rotor. Appendix H describes the lessons learned in designing such parameters and their influence on the couplings between the rotor and rotor-body degrees of freedom.

Hingeless rotor systems can include three main forms of structural couplings:

1. Flap-Lag Coupling (defined by the so-called "degree-of-elastic-coupling-parameter R") is used for hingeless rotors to characterize how much flexibility is contained inboard and outboard of the pitch bearing. This coupling was introduced to characterize the difference in dynamic behaviour between rotors for which virtually all bending deflections occur outboard of the pitch hinge (pitch hinge attached to the hub) and rotors for which part of the bending deflections occur inboard of the pitch hinge.

2. Pitch-Flap Coupling $K_{P\beta}$ may be introduced in an articulated rotor either by inclining the flapping hinge by an angle δ_3, or by the control system. In the first case, the inclination of flapping hinge induces a flap deflection in response to a small pitch of the blade and vice-versa, $K_{P\beta} = -\tan \delta_3$ as seen in Figure 3.6. In the second case, since the pitch hinge in an articulated rotor is usually outboard of the flapping and lagging hinge (β,ζ,θ), a change in flap results in a change in pitch as well. In a hingeless rotor, the pitch-flap coupling is in fact the coupling between blade bending in the out-of-plane and torsional direction.

The following sign convention is introduced for the pitch-flap coupling: positive pitch-flap coupling (negative δ_3) $K_{P\beta}>0$ corresponds to pitch up with flap up or pitch down with flap down.

Appendix H will demonstrate that pitch-flap coupling affects in the first place the blade flapping characteristics, and therefore, the helicopter's flying qualities. The designer should bear in mind the following issues:

- in an articulated rotor, positive δ_3 (i.e. flap up with pitch down) should be used in order to avoid *flapping divergence** (especially at low Lock numbers), albeit at the cost of damping in the lead-lag mode;
- in a hingeless rotor, the values of pitch-flap coupling depend in the first place on the blade lead-lag frequency and in the second place on the combination of lead-lag frequency and hub flexibility: a soft-inplane rotor is not sensitive to pitch-flap variation, while a stiff-inplane rotor is very sensitive to it.
  - in a soft-inplane rotor, a negative pitch-flap coupling (i.e. up with pitch down) should be used, independent of the hub flexibility.
  - in a stiff-inplane rotor with a soft-hub, a negative pitch-flap coupling should be used.
  - in a stiff-inplane rotor with a stiff-hub, positive pitch-flap couplings are advisable.
  - in a stiff-inplane rotor with a degree-of-elastic-coupling-parameter R between 0.1 to 0.3, positive as well as negative pitch-flap couplings are possible.

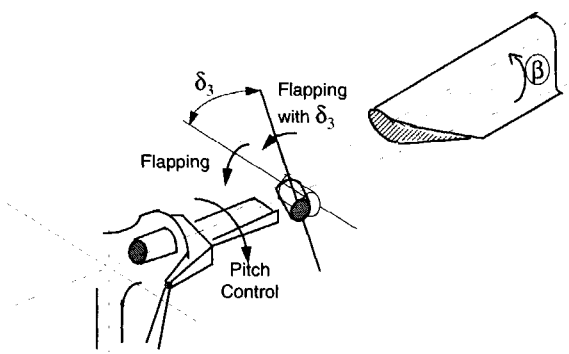

Figure 3.6 δ_3 hinge for pitch-flap coupling

3. Pitch-Lag coupling $K_{P\zeta}$ may be introduced in an articulated rotor by inclining the lagging hinge by an angle α_2 or δ_1 or by the control system. In the first case, inclining the lagging hinge results in a lead-lag deflection when a pitch control input is given to the blade and vice-versa $K_{P\zeta}$= + tan α_2 (see Figure 3.7). In the second case, usually the pitch bearing in an articulated rotor is outboard of the flapping and lagging hinge (β,ζ,θ), which causes a change in lag to result in a change in pitch as well. In hingeless rotors, the pitch-lag coupling represents the coupling between bending in the lead-lag direction and torsion.

The following sign convention is introduced for the pitch-lag coupling: positive pitch-lag coupling $K_{p\zeta}>0$ corresponds to pitch nose down with lag or pitch nose up with lead.

In Appendix H it will be demonstrated that pitch-lag coupling is an important parameter affecting mainly the damping of the blade lead-lag motion and thus the rotor and rotor-body instabilities. As a general criterion:

- in an articulated rotor, negative α_2 should be used (i.e. pitch up with lag) in order to increase the damping of the lead-lag mode, without forgetting that by doing this, the damping in flapping is decreased;
- in a hingeless rotor,
  - in a soft-inplane rotor the damping in lead-lag still seems to be favoured by a negative pitch-lag coupling (i.e. pitch up with lag).
  - in a stiff-inplane rotor, different trends are noticed depending on the elastic coupling used:
  - in a stiff-inplane rotor with a soft hub a negative pitch-lag coupling should be used,
  - in a stiff-inplane rotor with a stiff hub a positive pitch-lag coupling should be used.

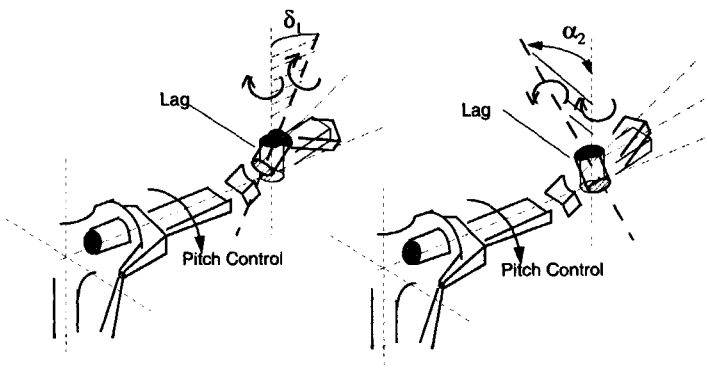

Figure 3.7 α_2 and δ_1 hinges for pitch-lag coupling

Once instabilities are avoided by using pitch-lag coupling, the effect on the flying qualities is usually not substantial. In contrast, pitch-flap coupling always affects the flying qualities significantly.

The pitch-flap and pitch-lag couplings of a hingeless rotor may be influenced by several design parameters (see Figure 3.8) which will be analyzed in detail in the literature survey of Appendix H. These are:

- blade geometric parameters, built-in blade deflections such as precone, droop, sweep (see Figure 3.8);
- torque offset and pitch control flexibility (the distribution of torsion stiffness);
- chordwise offsets between the aerodynamic centre, mass centre and elastic axis used to reduce steady-state blade-bending stiffness.

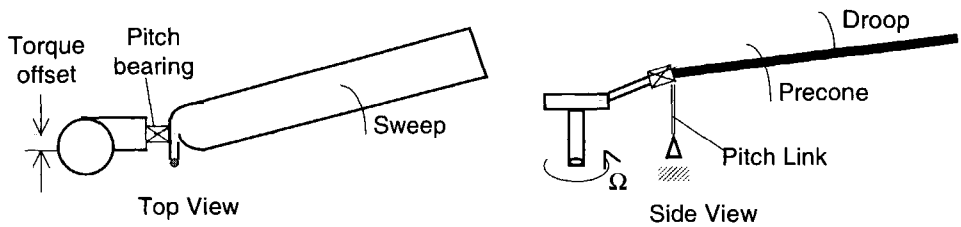

*Figure 3.8 Blade geometrical parameters (**Hodges and Ormiston** [1976][39])*

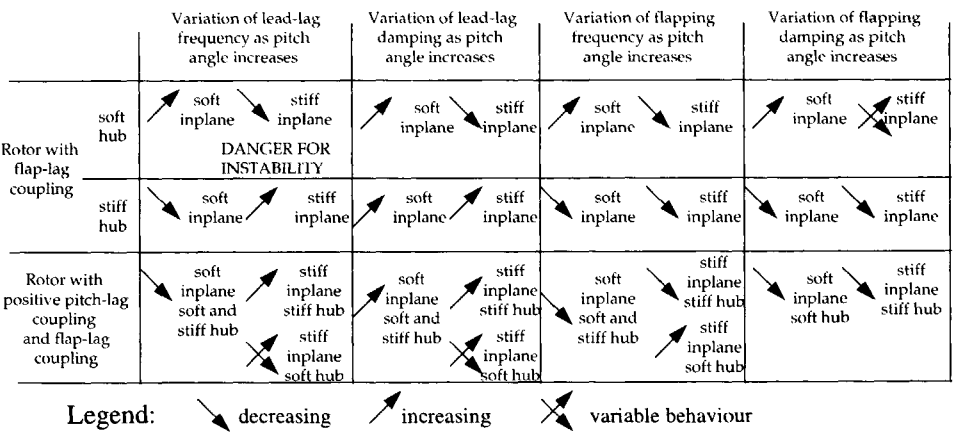

Figure 3.9 Dependence of blade dynamic characteristics on the structural couplings and soft/stiff design

The importance of the division of hingeless rotors in soft and stiff configurations discussed in section 3.3 of the present chapter can best be appreciated by looking at the effects that structural couplings have on the coupling between the rotor and rotor/body modes. Figure 3.9 presents some of the effects of structural couplings on the blade flapping and lead-lag dynamics depending on whether the blade design is stiff or soft. Looking at this figure, one may conclude that blade flapping and lead-lag frequency and damping characteristics are strongly dependent on both the structural couplings and the soft/stiff choice in the design of rotary wing devices. According to this, it also follows that the answer to the question on how many degrees of freedom are necessary in simulation modeling will strongly depend on the structural couplings and the soft-stiff characteristics of the configuration analyzed.

Chapter 4

Critical Pole Distance Method

"Engineers are often more comfortable with requirements than philosophies, but, nevertheless, the end product of their work is always a record of their design philosophy."

Glidden S. Doman [1994]

The aim of the present dissertation is to extend and improve existing procedures used to predict which degrees of freedom are necessary in dynamic simulation modeling of helicopters and horizontal-axis wind turbines. In this context, the present chapter proposes a general procedure - the so-called "critical pole distance method" which may be used by an analyst to determine the necessary structure of simulation models. The proposed procedure is then compared with other existing procedures to predict the level of detail in simulation models.

4.1 Critical Pole Distance Method

The critical pole distance method may be applied in the preparation-phase of simulation models of helicopters or horizontal-axis wind turbines (the phase where the dynamic equations of motion are analytically derived) to determine how much detail should be considered in the models. The critical pole distance method contains the following steps:

1. First, assuming the system (helicopter or horizontal-axis wind turbine) as a summation of mutually uncoupled subsystems -blades, hub, (air)frame etc.-, the equations of motion for every uncoupled deflection mode are derived.

2. Subsequently, for each subsystem, the formulated equations of motion are solved. The solutions represent the uncoupled mode eigenvalues. These solutions are usually complex values, so that they can be represented in the complex plane (see section 2.2 of Chapter 2). The eigenvalue representation in the complex plane has the advantage of providing information on structural mode behaviour in frequency as well as in damping. The frequency shows whether or not the mode under consideration is a vibration, the damping gives information on the damping forces involved in the system which can have a stabilizing effect on the motion. In order to identify all potential coupling effects, the equations of motion associated with the rotating subsystems are transformed to a non-rotating system through the so-called "Coleman transformation" (Multiblade Coordinate Transformation MCT" (see Appendix D).

3. Next, using the representation in the complex plane, "critical regions" are defined. A "critical region" is an area of the complex plane where potential couplings between different modes occur -both within and between subsystems. The criterion for a critical region is the relative position of the poles in the complex plane, i.e.: if in the complex plane the poles associated with the uncoupled motion of different modes are "close" together, one may expect that these modes will couple. The crucial point to be judged here is what actually means "poles close to each other" and "poles sufficiently separated" in order to allow for their mutual coupling effects in the simulation model or not. In other words, a criterion must be developed to quantify the mutual distance between poles and the distance between poles and excitation sources. This is done by analysing a wide variety of test-cases, for a well defined class of systems and unit of measure, by deriving the full set of coupled equations.

4. Finally, conclusions concerning the degrees of freedom to be used in the structural model can be drawn. The modes involved in the structural model will be divided into three classes:

   - modes to be discarded from the model,
   - modes to be kept separately in the model (neglecting the coupling terms between these modes and other degrees of freedom),
   - modes to be kept in the model including the coupling effects that are essential for the model.

4.2 Formulation of a Criterion for the Critical Pole Distance Method

4.2.1 Critical Pole Distance Criterion for a Two Degree-of-Freedom Linearly Coupled System

Consider a two degree-of-freedom linearly coupled system of equations of motion of a dynamic system in the form:

$$\begin{cases} \ddot{x}_1 + 2\xi_1\omega_1\dot{x}_1 + \omega_1^2 x_1 + f_{12}\ddot{x}_2 + g_{12}\dot{x}_2 + h_{12}x_2 = 0 \\ \ddot{x}_2 + 2\xi_2\omega_2\dot{x}_2 + \omega_2^2 x_2 + f_{21}\ddot{x}_1 + g_{21}\dot{x}_1 + h_{21}x_1 = E(t) \end{cases} \tag{4.1}$$

where the terms f_{12}, g_{12}, h_{12}, f_{21}, g_{21}, h_{21} represent the coupling terms and E(t) an external excitation force applied only to the degree of freedom x_2. The present section investigates the conditions under which the degrees of freedom x_1 and x_2 can be assumed as weakly coupled in the model. In the Laplace domain the system of

equations (4.1) can be written as:

$$\begin{cases} \left(s^2+2\xi_1\omega_1 s+\omega_1^2\right)\hat{x}_1(s)+\left(f_{12}s^2+g_{12}s+h_{12}\right)\hat{x}_2(s) = 0 \\ \left(f_{21}+g_{21}+h_{21}\right)\hat{x}_1(s)+\left(s^2+2\xi_2\omega_2 s+\omega_2^2\right)\hat{x}_2(s) = \hat{E}(s) \end{cases} \tag{4.2}$$

Introducing the following notations:

$$\begin{aligned} N_1 &= s^2+2\xi_1\omega_1 s+\omega_1^2 \;,\quad T_{12} = f_{12}s^2+g_{12}s+h_{12} \\ N_2 &= s^2+2\xi_2\omega_2 s+\omega_2^2 \;,\quad T_{21} = f_{21}s^2+g_{21}s+h_{21} \end{aligned} \tag{4.3}$$

the equations of motion (4.2) can equivalently be written as:

$$\begin{cases} N_1\,\hat{x}_1(s)+T_{12}\,\hat{x}_2(s) = 0 \\ T_{21}\hat{x}_1(s)+N_2\,\hat{x}_2(s) = \hat{E}(s) \end{cases} \tag{4.4}$$

Next, define each degree of freedom as an excitation for the other degree of freedom. In the equations of motion (4.4) this is equivalent with separating on the right-hand side of the equation the degrees of freedom involved in the couplings and on the left-hand side the degrees of freedom containing the uncoupled characteristics of the system. The system of equations (4.4) can then be expressed as:

$$\begin{cases} N_1\,\hat{x}_1(s) = T'_{12}\,\hat{x}_2(s) \\ N_2\,\hat{x}_2(s) = T'_{21}\,\hat{x}_1(s)+\hat{E}(s) \end{cases} \tag{4.5}$$

where T'_{12}, T'_{21} are the coefficients T_{12}, T_{21} passed to the right-hand side of the equations with a minus sign. The reason for this is that by doing so the equations of motion can be transformed from an open-loop control system into a closed-loop control system, involving in the forward loop a specific degree of freedom to be investigated and in the backward loop the degrees of freedom which may couple to the degree of freedom analyzed. Note that while the uncoupled eigenvalues are contained in the denominators N_1 and N_2 of the transfer functions, the coupling terms are contained only in the numerator terms T_{12} and T_{21}. Equations of motion (4.4) can be treated as block diagrams involving transfer functions in an open-loop control system; equations (4.5) can be treated as transfer functions in a closed-loop control.

Defining a transfer function F(s) in the feedforward loop and a transfer function G(s) in the feedback loop as:

$$\begin{cases} \dfrac{\hat{x}_1}{\hat{x}_2} = \dfrac{T'_{12}(s)}{N_1(s)} = G(s) \\ \dfrac{\hat{x}_2}{\hat{x}_1} = \dfrac{T'_{21}(s)}{N_2(s)} = F(s) \quad ; \quad \dfrac{\hat{x}_2}{\hat{E}} = \dfrac{1}{N_2(s)} = H(s) \end{cases} \tag{4.6}$$

the equations of motion (4.5) may be represented as in Figure 4.1.

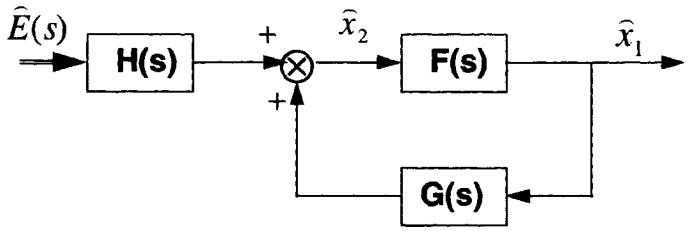

Figure 4.1 Block diagram for a linear positive feedback system

The following relations may be applied to the block diagrams represented in this figure:

$$\begin{cases} \hat{x}_1(s) = G(s)\,\hat{x}_2(s) \\ \hat{x}_2(s) = F(s)\,\hat{x}_1 + H(s)\hat{E}(s) \end{cases} \tag{4.7}$$

Eliminating $\hat{x}_1$ in (4.7) leads to the following closed-loop transfer function:

$$\frac{\hat{x}_2(s)}{\hat{E}(s)} = \frac{H(s)}{1 - F(s)G(s)} \tag{4.8}$$

Returning to the initial question of the present section of whether the degrees of freedom x_1 and x_2 are weakly coupled or not, this question is equivalent to that of whether the closed-loop transfer function $\hat{x}_2(s)/\hat{E}(s)$ differs from $\left(\hat{x}_2(s)/\hat{E}(s)\right)_0$, where the index zero indicates that the feedback G = 0. Substituting G = 0 in (4.8) leads to:

$$G(s) = 0 \Rightarrow T'_{12} = 0 \Rightarrow \left(\frac{\hat{x}_2(s)}{\hat{E}(s)}\right)_0 = H(s) \tag{4.9}$$

Thus, the degrees of freedom x_2 and x_1 are weakly coupled when the relative difference

between the transfer function of the coupled system $\left(\hat{x}_2(s)/\hat{E}(s)\right)$ and that the uncoupled system $\left(\hat{x}_2(s)/\hat{E}(s)\right)_0$ is approximately zero in any point s of the complex plane, that is:

$$\frac{\left(\frac{\hat{x}_2(s)}{\hat{E}(s)}\right)-\left(\frac{\hat{x}_2(s)}{\hat{E}(s)}\right)_0}{\left(\frac{\hat{x}_2(s)}{\hat{E}(s)}\right)_0} = \frac{F(s)\cdot G(s)}{1-F(s)\cdot G(s)} = \frac{1}{\frac{N_1(s)N_2(s)}{T'_{12}(s)T'_{21}(s)}-1} \approx 0 \Rightarrow x_1, x_2 \text{ decoupled} \quad (4.10)$$

Equation (4.10) gives the condition of weak (loose) coupling between the degrees of freedom x_1 and x_2 in a two degree-of-freedom linear coupled system. This condition is fulfilled when $\frac{N_1(s)N_2(s)}{T'_{12}(s)T'_{21}(s)} \to \infty$ or equivalently $\frac{T'_{12}(s)T'_{21}(s)}{N_1(s)N_2(s)} \to 0$, that is, either when:

$$T'_{12}(s)\cdot T'_{21}(s) \to 0 \left(\text{if } N_1(s)\cdot N_2(s) \neq 0\right) \Leftrightarrow T'_{12}(s)\cdot T'_{21}(s) \ll N_1(s)\cdot N_2(s) \quad (4.11)$$

or when:

$$N_1(s)\cdot N_2(s) \to \infty \left(\text{if } T'_{12}(s)\cdot T'_{21}(s) \neq \infty\right) \Leftrightarrow N_1(s)\cdot N_2(s) \ll T'_{12}(s)\cdot T'_{21}(s) \quad (4.12)$$

Condition (4.11) states that two degrees of freedom x_1 and x_2 are weakly coupled when the product of their coupled characteristics is small with respect to that of the uncoupled characteristics. Equivalently, condition (4.12) states that if the product containing the uncoupled characteristics is sufficiently large compared to that containing the coupled characteristics, the degrees of freedom x_1 and x_2 may also be considered weakly coupled. Condition (4.11) is quite often referred to in literature and requires the investigation of the couplings in the system. Condition (4.12) refers in the first place to the uncoupled characteristics of the system and contains the information to be investigated in the critical pole distance criterion.

One may observe that conditions (4.11) and (4.12) may be applied only to certain classes of problems. Indeed, the limit $\frac{T'_{12}(s)T'_{21}(s)}{N_1(s)N_2(s)} \to 0$ cannot be determined in the extreme cases of $\frac{0}{0}$ (zero cross-coupling and zero characteristics) and $\frac{\infty}{\infty}$ (very large cross-coupling and system characteristics). Also the cases

$\frac{0}{\infty} \to 0$; $\frac{\infty}{0} \to \infty$ and $\frac{x}{0} \to \infty$ should not be investigated because these are not relevant for the designer (for example, in case of zero cross-coupling, one is not interested in how large the product of the uncoupled characteristics is, because the two degrees of freedom will not interfere with each other anyway). The class of problems that is relevant to criterion (4.10) is that for which the system is not on the edge of its operating envelope and the coupling and uncoupling terms are in the same order.

Since s is the Laplace operator and thus generally a complex variable $s = a + ib$, it follows that $N_1(s)$; $N_2(s)$; $T'_{12}(s)$; $T'_{21}(s)$ are also complex variables. Using the representation of the complex numbers in the complex plane by their radius and argument, it can be demonstrated that conditions (4.11) and (4.12) may be satisfied if and only if their modulus satisfies the following conditions as well:

$$- \quad |T'_{12} \cdot T'_{21}| \to 0 \quad \Rightarrow \quad |T'_{12} \cdot T'_{21}| \ll |N_1 \cdot N_2| \tag{4.13}$$

- or:

$$- \quad |N_1 \cdot N_2| \to \infty \quad \Rightarrow \quad |N_1 \cdot N_2| \gg |T'_{12} \cdot T'_{21}| \tag{4.14}$$

The next paragraph concentrates on condition (4.14) by demonstrating that a criterion in the critical pole distance method may be derived from this condition and used as an engineering approach in the preparation-phase of simulation models (when the couplings in the system are unknown) in order to determine how much detail should be used in the model.

Returning to the expression of the uncoupled characteristics of the degrees of freedom x_1 and x_2 in the equations of motion (4.1):

$$\begin{aligned} N_1(s) &= s^2 + 2\xi_1\omega_1 s + \omega_1^2 \\ N_2(s) &= s^2 + 2\xi_2\omega_2 s + \omega_2^2 \end{aligned} \tag{4.15}$$

one may observe that putting these terms equal to zero, the system poles are obtained (assuming an oscillatory motion for the system):

$$\begin{aligned} s_{1\pm} &= -\xi_1\omega_1 \pm i\,\omega_1\sqrt{1-\xi_1^2} \\ s_{2\pm} &= -\xi_2\omega_2 \pm i\,\omega_2\sqrt{1-\xi_2^2} \end{aligned} \tag{4.16}$$

Substituting $s = a + ib$ in its general form as a complex variable into (4.15) one obtains:

$$\begin{aligned} N_1(s) &= a^2 - b^2 + 2\xi_1\omega_1 a + \omega_1^2 + 2i(ab + \xi_1\omega_1 b) = a_1 + ib_1 \\ N_2(s) &= a^2 - b^2 + 2\xi_2\omega_2 a + \omega_2^2 + 2i(ab + \xi_2\omega_2 b) = a_2 + ib_2 \end{aligned} \tag{4.17}$$

The product $|N_1N_2|$ of the two uncoupled degrees of freedom can then be calculated as:

$$\begin{aligned} |N_1N_2| = |N_1|\cdot|N_2| = &\sqrt{\left\{\left[\left(a^2-b^2\right)+\omega_1\left(\omega_1+2a\xi_1\right)\right]^2+4b^2\left(a+\xi_1\omega_1\right)^2\right\}}\cdot \\ &\cdot\sqrt{\left\{\left[\left(a^2-b^2\right)+\omega_2\left(\omega_2+2a\xi_2\right)\right]^2+4b^2\left(a+\xi_2\omega_2\right)^2\right\}} = f(a,b,\xi_1,\xi_2,\omega_1,\omega_2) \end{aligned} \tag{4.18}$$

which is a function depending on the coordinates of the complex variable (a,b) and on the system characteristics (ξ_1, ξ_2, ω_1, ω_2).

Condition (4.14) states that the product $|N_1N_2|$ has to be much larger than the product of the coupling terms $|T'_{12}T'_{21}|$ in order to be able to neglect the couplings in the system. This condition should be investigated in every point in the complex plane $s \in \mathbb{C}$, except the points $s_{1\pm}$, $s_{2\pm}$ where $|N_1N_2|$ is always zero and the condition can never be fulfilled.

The question is what are the critical values for s that can reveal valuable information to the designer on the system characteristics as defined by the frequency and damping and by the coupling terms. One should in this context realise that a value s far away from the region of the poles of the system will always lead to a very large value of the product $|N_1N_2|$ and that the information on the system characteristics in damping and frequencies will be lost. Therefore, such points do not contribute to the understanding of the quantification of the product $|N_1N_2|$, unless the couplings are also investigated.

In the other hand, assuming s in the region of the poles $s_{1\pm}$, $s_{2\pm}$ (the "critical region" as defined on page 60) the designer can obtain useful information on the system characteristics by analysing condition (4.14). A large value for the product $|N_1N_2|$ in this region will show that the system poles are situated sufficiently far from each other to neglect the couplings in the systems (assuming the case of non-zero couplings $|T'_{12}T'_{21}|=0$).

On basis of the above discussion, considering a point $s \to \xi_1\omega_1 + i\omega_1$ (beware that this point is not the pole of the motion because it is taken at the coordinate of the undamped frequency of the degree of freedom x_1), and recalling equations (4.18), condition (4.14) will become:

$$\begin{aligned} |N_1N_2| = \xi_1\omega_1\Big\{&\left(9\xi_1^2\omega_1^2+16\omega_1^2\right)\left[\xi_1^4\omega_1^4+2\xi_1^2\omega_1^2\left(\omega_1^2+2\xi_2^2\omega_2^2+\omega_2^2\right)+4\xi_1\omega_1\xi_2\omega_2\times\right. \\ &\left.\times\left(\omega_1^2+\xi_1^2\omega_1^2+\omega_2^2\right)+4\omega_1^2\xi_2^2\omega_2^2+\left(\omega_2^2-\omega_1^2\right)^2\right]\Big\}^{1/2} \gg \left|T'_{12}(\xi_1+i\omega_1)\;T'_{21}(\xi_1+i\omega_1)\right| \end{aligned} \tag{4.19}$$

Condition (4.19) requires the determination of the coupling terms which, incidentally are not known prior to developing a complete coupled model. However, this condition represents a necessary condition in order to consider two degrees of freedom as weakly coupled, that is:

$$\left|N_1 N_2\right| = \xi_1\omega_1\left\{\left(9\xi_1^2\omega_1^2+16\omega_1^2\right)\left[\xi_1^4\omega_1^4+2\xi_1^2\omega_1^2\left(\omega_1^2+2\xi_2^2\omega_2^2+\omega_2^2\right)+4\xi_1\omega_1\xi_2\omega_2\times\right.\right.$$
$$\left.\left.\times\left(\omega_1^2+\xi_1^2\omega_1^2+\omega_2^2\right)+4\omega_1^2\xi_2^2\omega_2^2+\left(\omega_2^2-\omega_1^2\right)^2\right]\right\}^{1/2} \quad \text{is large} \tag{4.20}$$

Of course, the interpretation of the term "large" is subjective and has to be defined for a certain dynamic system, a specified unit of measure and a certain class of problems. In the present dissertation the systems investigated are helicopters and horizontal-axis wind turbines. The unit of measure, the frequencies ω_1 and ω_2, are non-dimensionalized by means of the rotor rotational velocity Ω in order to transform the value for $|N_1N_2|$ into a non-dimensional value. Finally, the class of problems for which the condition (4.20) is applied is that of low-frequency mode modeling in which the limitations presented in section 1.3 are valid. For helicopter and wind turbine systems, the interpretation of the term "large" in condition (4.20) may be quantified only by investigating different case-problems, both with a coupled and an uncoupled model.

Returning to the initial restrictions under which condition (4.20) was derived, it should be remembered that this condition cannot be applied to a system with zero-cross couplings. In such systems it does not matter how large the quantity $|N_1N_2|$ is, the system is always uncoupled.

Condition (4.20) will be considered as a criterion in the critical pole distance method to investigate the critical regions of couplings (defined on page 60). This condition is a necessary condition, but in general it is not sufficient. There are applications in which this condition is also sufficient (such an application for example may be a system that is only coupled through stiffness and in which the inertial couplings are absent). For future work, it would be interesting to determine which are these applications for helicopter and wind turbine systems.

The present dissertation will investigate how the term "large" in the critical pole distance criterion (4.20) may be quantified for the following cases:

- in Chapter 5 for piloted simulation modeling, in order to examine the couplings between the helicopter body modes and rotor disc-tilt modes belonging to critical regions;
- in Chapter 6, to determine the couplings responsible for the instability of the KEWT two-bladed horizontal-axis wind turbine;
- in Chapter 7 to investigate the conditions under which the blade flapping degree of freedom decouples from the lead-lag motion in a two degree-of-freedom flap-

lag model.

Once the meaning of large for the expression $|N_1N_2|$ is quantified on basis of the analysis of the coupled models, the designer has at its disposition a tool to decide whether to include those couplings without the need to derive them. Next, two particular cases of the critical pole distance criterion (4.20) will be derived.

Poles situated near the imaginary axis

When the poles of the motion are near the imaginary axis, the "critical region" is close to the imaginary axis and thus one may assume s as a purely imaginary value $s = i\,b$. The product $|N_1N_2|$ as given by (4.18) can then be calculated as:

$$\left|N_1N_2\right| = \left[\left(\omega_1^2-b^2\right)^2\left(\omega_2^2-b^2\right)^2+16\xi_1^2\xi_2^2\omega_1^2\omega_2^2b^4+4\xi_1^2\omega_1^2b^2\left(\omega_2^2-b^2\right)^2+ +4\xi_2^2\omega_2^2b^2\left(\omega_1^2-b^2\right)^2\right]^{1/2} \quad \text{is large} \tag{4.21}$$

Choosing s close to the pole of the degree of freedom x_1, $s \rightarrow i\omega_1$, in order to obtain information mainly on the system's uncoupled characteristics, condition (4.20) in the critical pole distance criterion becomes:

$$\left|N_1N_2\right| = \sqrt{16\xi_1^2\xi_2^2\omega_1^6\omega_2^2+4\xi_1^2\omega_1^4\left(\omega_2^2-\omega_1^2\right)^2} \quad \text{is large} \tag{4.22}$$

Condition (4.22) may be considered the critical pole distance criterion for two poles situated near the imaginary axis. Observe that condition (4.22) may be satisfied either if:

- the difference between the uncoupled natural frequencies of the degrees of freedom x_1 and x_2 is sufficiently large:

$$\left(\omega_2^2-\omega_1^2\right) \quad \text{is large} \tag{4.23}$$

- or, in case the uncoupled frequencies are almost equal ($\omega_1 \approx \omega_2$), if the product of the damping ratios is large:

$$\xi_1^2 \cdot \xi_2^2 \quad \text{is large} \tag{4.24}$$

In other words, two degrees of freedom with poles situated near the imaginary axis may be considered weakly coupled if their uncoupled eigenvalues are either sufficiently

separated in frequency, or both sufficiently damped. According to (4.24) which refers to the product of damping ratios, two modes both need to be sufficiently damped in order to be considered weakly coupled (or, in other words, it is not sufficient that only one mode be well damped; if the other mode is not sufficiently damped, the two modes remain coupled). This conclusion corresponds to the ground resonance analysis of helicopters, where **Deutsch** [1946][23] derived a criterion to avoid ground resonance phenomena based on the product of the blade and hub damping, which is more significant than the damping in blades and hub individually. The designer is thus left with the choice of how to distribute the damping between two modes as long as their product in damping adds up to a certain value.

Poles situated near the real axis

When the poles of the motion are near the real axis, the "critical region" is close to the real axis and one may assume s as a real value s = a. The product $|N_1N_2|$ as given by (4.18) can then be calculated as:

$$|N_1 N_2| = \sqrt{a^4 + a^2(\omega_1^2 + \omega_2^2) + 2a^3(\omega_1\xi_1 + \omega_2\xi_2) + \omega_1\omega_2(\omega_1 + 2a\xi_1)(\omega_2 + 2a\xi_2)} \text{ is large} \quad (4.25)$$

Choosing s close to the pole of the degree of freedom x_2, $s \rightarrow -\xi_2\omega_2$, condition (4.20) in the critical pole distance criterion becomes:

$$|N_1 N_2| = \left\{ \left| \omega_2^4\xi_2^4 + \omega_2^2\xi_2^2(\omega_1^2 + \omega_2^2) + \omega_1\omega_2(\omega_1\omega_2 + 4\omega_2^2\xi_2^3\xi_1) - 2\omega_2^3\xi_2^3(\omega_1\xi_1 + \omega_2\xi_2) - 2\omega_1\omega_2^2\xi_2(\xi_1 + \xi_2) \right| \right\}^{1/2} \text{ is large} \quad (4.26)$$

Criterion (4.26) may be considered as the critical pole distance criterion of two poles of motion situated near the real axis.

4.2.2 Generalization of the Critical Pole Distance Criterion for an n Degree-of-Freedom Linearly Coupled System

The two degree-of-freedom system (4.1) can be generalized into an n degree-of-freedom

system of form:

$$\begin{cases} \ddot{x}_1 + 2\xi_1\omega_1\dot{x}_1 + \omega_1^2 x_1 + f_{12}\ddot{x}_2 + g_{12}\dot{x}_2 + h_{12}x_2 + \ldots + f_{1n}\dot{x}_n + g_{1n}x_n + h_{1n}\dot{x}_n = 0 \\ f_{21}\ddot{x}_1 + g_{21}\dot{x}_1 + h_{21}x_1 + \ddot{x}_2 + 2\xi_2\omega_2\dot{x}_2 + \omega_2^2 x_2 + \ldots + f_{2n}\dot{x}_n + g_{2n}x_n + h_{2n}\dot{x}_n = 0 \\ \ldots\ldots \\ \ldots\ldots\ldots\ldots\ldots\ldots\ddot{x}_j + 2\xi_j\omega_j\dot{x}_j + \omega_j^2 x_j + \ldots + f_{jn}\dot{x}_n + g_{jn}x_n + h_{jn}\dot{x}_n = E(t) \\ \ldots\ldots \\ f_{n1}\ddot{x}_n + g_{n2}\dot{x}_n + h_{nn}x_n + \ldots\ldots\ldots\ldots\ldots\ldots\ldots + \ddot{x}_n + 2\xi_n\omega_n\dot{x}_n + \omega_n^2 x_n = 0 \end{cases} \tag{4.27}$$

where the terms f_{12}, ... $f_{n,n-1}$, g_{12}, ... $g_{n,n-1}$, h_{12}, ... $h_{n,n-1}$ represent the coupling terms and E(t) an external excitation force applied only to the degree of freedom x_j. The present section will generalize the critical pole distance criterion (4.20) to a criterion giving the condition for which the degree of freedom x_j decouples from the remaining degrees of freedom x_1,... x_n.

Following the same reasoning as in the case of a two degree-of-freedom system, applying the Laplace transformation to the system of equations (4.27) and assuming each degree of freedom as an excitation for the remaining n-1 degrees of freedom, after applying a sudden input ε to the system ($\hat{E}(s) = \varepsilon T_\varepsilon(s)$), the system of equations (4.27) can be equivalently written as:

$$\begin{bmatrix} N_1\hat{x}_1 & & & & \\ & N_2\hat{x}_2 & & 0 & \\ & & \ldots & & \\ & & & N_i\hat{x}_i & \\ & 0 & & & N_j\hat{x}_j \\ & & & & & N_n\hat{x}_n \end{bmatrix} + \begin{bmatrix} 0 & T_{12} & \ldots\ldots & T_{1n} \\ T_{21} & 0 & \ldots\ldots & T_{2n} \\ \ldots & & & \\ T_{i1} & T_{i2} & \ldots\ldots 0 \ldots\ldots & T_{in} \\ \ldots & & & \\ T_{j1} & T_{j2} & \ldots\ldots 0 \ldots\ldots & T_{jn} \\ \ldots & & & \\ T_{n1} & T_{n2} & \ldots\ldots & 0 \end{bmatrix} \begin{Bmatrix} \hat{x}_1 \\ \hat{x}_2 \\ \ldots \\ \hat{x}_i \\ \ldots \\ \hat{x}_j \\ \ldots \\ \hat{x}_n \end{Bmatrix} = \varepsilon \begin{Bmatrix} 0 \\ 0 \\ \ldots \\ 0 \\ \ldots \\ T_\varepsilon \\ \ldots \\ 0 \end{Bmatrix} \tag{4.28}$$

where:

$$N_k = s^2 + 2\xi_k\omega_k s + \omega_k^2 \quad ; \quad T_{kl} = f_{kl}s^2 + g_{kl}s + h_{kl}; \qquad k = 1\ldots n \ , \ l = 1..n \ , \ k \neq l \tag{4.29}$$

Note that also in the generalized case, the system contains its uncoupled characteristics in N_1 to N_n whereas its coupled characteristics are contained in the terms T_{12} .... $T_{n\,n-1}$. The response of the x_j-th degree of freedom to the input ε is:

$$\hat{x}_j = \frac{\Delta_{jj}}{\Delta} = \frac{\begin{vmatrix} N_1 & \dots & T_{1i} & \dots & 0 & \dots & T_{1n} \\ \dots\dots\dots & & & & & & \\ T_{i1} & \dots & N_i & \dots & 0 & \dots & T_{in} \\ \dots\dots\dots & & & & & & \\ T_{j1} & \dots & T_{ji} & \dots & \hat{E} & \dots & T_{jn} \\ \dots\dots\dots & & & & & & \\ T_{n1} & \dots & T_{ni} & \dots & 0 & \dots & N_n \end{vmatrix}}{\Delta} = (-1)^{2j}\,\hat{E}(s)\frac{\Delta^*_{jj}}{\Delta} \tag{4.30}$$

where:

$$\Delta = \begin{vmatrix} N_1 & \dots & T_{1i} & \dots & T_{1j} & \dots & T_{1n} \\ \dots\dots\dots & & & & & & \\ T_{i1} & \dots & N_i & \dots & T_{ij} & \dots & T_{in} \\ \dots\dots\dots & & & & & & \\ T_{j1} & \dots & T_{ji} & \dots & N_j & \dots & T_{jn} \\ \dots\dots\dots & & & & & & \\ T_{n1} & \dots & T_{ni} & \dots & T_{nj} & \dots & N_n \end{vmatrix}, \Delta^*_{jj} = \begin{vmatrix} N_1 & \dots & T_{1\,j-1} & T_{1\,j+1} & \dots & T_{1n} \\ \dots\dots\dots & & & & & \\ T_{j-1\,1} & \dots & N_{j-1} & T_{j-1\,j+1} & \dots & T_{j-1\,n} \\ T_{j+1\,1} & \dots & T_{j+1\,j-1} & N_{j+1} & \dots & T_{j+1\,n} \\ \dots\dots\dots & & & & & \\ T_{n1} & \dots & T_{n\,j-1} & T_{n\,j+1} & \dots & N_n \end{vmatrix} \tag{4.31}$$

The condition under which the degree of freedom x_j decouples from the remaining n-1 degrees of freedom is equivalent in the generalized case to the question of when the transfer function $\hat{x}_j / \varepsilon$ differs from the transfer function $(\hat{x}_j / \varepsilon)_0$. **The transfer function** $(\hat{x}_j / \varepsilon)_0$ in the generalized case is the transfer function $\hat{x}_j / \varepsilon$ in which all the coupling terms $T_{j1}...T_{jn}$ are zero, i.e.:

$$\left(\frac{\hat{x}_j}{\varepsilon}\right)_0 = \left(\frac{\hat{x}_j}{\varepsilon}\right)_{T_{j1}\dots T_{jn}\to 0} = \frac{T_\varepsilon}{N_j} \tag{4.32}$$

Thus, the degree of freedom x_j decouples from the remaining n-1 degrees of freedom of system (4.27) when in any point of the complex plane the relative difference between the transfer function of the coupled system $(\hat{x}_j / \varepsilon)$ and the transfer function of the

system with the degree of freedom x_j weakly coupled $\left(\hat{x}_j / \varepsilon\right)_0$ is approximately zero, that is:

$$\frac{\left(\frac{\hat{x}_j}{\varepsilon}\right)-\left(\frac{\hat{x}_j}{\varepsilon_0}\right)}{\left(\frac{\hat{x}_j}{\varepsilon_0}\right)} = \frac{N_j \Delta_{jj}^*}{\Delta} - 1 = \frac{1}{(-1)^{j+1}\frac{T_{j1}}{N_j}\frac{\Delta_{j1}^*}{\Delta_{jj}^*} + \ldots 1 + (-1)^{j+n}\frac{T_{jn}}{N_j}\frac{\Delta_{jn}^*}{\Delta_{jj}^*}} - 1 \approx 0 \Rightarrow \begin{array}{l} x_j \text{ decouples} \\ \text{from } x_1 \ldots x_n \end{array} \quad (4.33)$$

where Δ_{j1}^*, .. Δ_{jn}^* are the minors of the elements T_{j1} .... T_{jn} and are the determinants obtained by deleting the line j and respectively the columns 1 to n in Δ:

$$\Delta_{j1}^* = \begin{vmatrix} T_{12} & \ldots & T_{1n} \\ \ldots\ldots\ldots & & \\ T_{j-1,2} & \ldots\ldots & T_{j-1,n} \\ T_{j+1,2} & \ldots\ldots & T_{j+1,n} \\ \ldots\ldots\ldots & & \\ T_{n2} & \ldots\ldots & N_n \end{vmatrix} \quad \ldots\ldots \quad \Delta_{jn}^* = \begin{vmatrix} N_1 & \ldots\ldots & T_{1,n-1} \\ \ldots\ldots\ldots & & \\ T_{j-1,1} & \ldots\ldots & T_{j-1,n-1} \\ T_{j+1,1} & \ldots & T_{j+1,n-1} \\ \ldots\ldots\ldots & & \\ T_{n1} & \ldots & T_{n,n-1} \end{vmatrix} \quad (4.34)$$

Observe that in the generalized case, the critical pole distance criterion (4.33) contains both the uncoupled and the coupled terms of the degree of freedom x_j investigated. For example, in a 3 degree-of-freedom system, assuming that the input ε is applied to x_2, the critical pole distance criterion (4.33) becomes:

$$\frac{\left(\frac{\hat{x}_2}{\varepsilon}\right)-\left(\frac{\hat{x}_2}{\varepsilon_0}\right)}{\left(\frac{\hat{x}_2}{\varepsilon_0}\right)} = \frac{\frac{T'_{32}T'_{23}}{N_2N_3}+\frac{T'_{12}T'_{21}}{N_1N_2}-\frac{T'_{12}T'_{23}T'_{31}}{N_1N_2N_3}-\frac{T'_{32}T'_{21}T'_{13}}{N_1N_2N_3}}{1-\frac{T'_{32}T'_{23}}{N_2N_3}-\frac{T'_{12}T'_{21}}{N_1N_2}-\frac{T'_{13}T'_{31}}{N_1N_3}+\frac{T'_{12}T'_{23}T'_{31}}{N_1N_2N_3}+\frac{T'_{32}T'_{21}T'_{13}}{N_1N_2N_3}} \approx 0 \Rightarrow \begin{array}{l} x_2 \text{ decouples} \\ \text{from } x_1 \\ \text{and } x_3 \end{array} \quad (4.35)$$

where T'_{12}, T'_{13}, T'_{21} ,...., T'_{32} are the coefficients T_{12}, T_{13}, T_{21} ,...., T_{32} passed to the right-hand side of the equations (4.28) with a minus sign. Concluding, in an $n \geq 3$ degree-of-freedom linearly coupled system, determining whether one degree of freedom decouples from all the other degrees of freedom requires the computing of the coupling terms in the critical pole distance criterion.

However, the critical pole distance method presented in section 4.1 of this chapter only involves the analysis of those poles situated in critical regions of the complex plane.

Poles situated in such regions signify that the corresponding modes of motion are potentially coupling. It follows that, although n degrees of freedom are involved, in the critical pole distance method one is primarily interested in the degrees of freedom corresponding to critical regions in the complex plane defined on the basis of the relative position of the poles. In these regions one has to decide whether poles are sufficiently separated or whether they are sufficiently close in order to allow for their coupling effects in the model or not. The critical pole distance criterion (4.33) should not be therefore applied to all couplings between one degree of freedom and the remaining degrees of freedom of the system, but to specific couplings as identified by the critical regions.

4.2.3 Critical Pole Distance Criterion Applied for a Critical Region of Two Poles

The present section will demonstrate that the critical pole distance criterion (4.20) derived for a two degree-of-freedom system, can also be used to quantify the coupling effects in a critical region formed by two degrees of freedom x_i and x_j of an n degree-of freedom system. Assume therefore that when representing the uncoupled system eigenvalues in the complex plane by means of the critical pole distance method, the eigenvalue of degree of freedom x_i is "close" to the eigenvalue of degree of freedom x_j, thus forming a critical region. The transfer functions defining the influence of x_i on x_j and vice-versa are (observe that the second transfer function is not defined in the real sense of the word because it contains the input ε):

$$\frac{\hat{x}_i}{\hat{x}_j} = \frac{T'_{ij}}{N_i} + \sum_{k=1,k\neq i}^{n} \frac{T'_{ik}}{N_i}\frac{\hat{x}_k}{\hat{x}_j} = F_{ij} + \sum_{k=1,k\neq i}^{n} F_{ik}\frac{\hat{x}_k}{\hat{x}_j} \tag{4.36}$$

$$\frac{\hat{x}_j}{\hat{x}_i} = \frac{T'_{ji}}{N_j} + \varepsilon\frac{T_\varepsilon}{N_j}\frac{1}{\hat{x}_i} + \sum_{k=1,k\neq j}^{n} \frac{T'_{jk}}{N_j}\frac{\hat{x}_k}{\hat{x}_i} = F_{ji} + \varepsilon F_\varepsilon \frac{1}{\hat{x}_i} + \sum_{k=1,k\neq j}^{n} F_{jk}\frac{\hat{x}_k}{\hat{x}_i} \tag{4.37}$$

Substituting (4.36) into (4.37), one obtains:

$$(1 - F_{ij}F_{ji})\,\hat{x}_j = \varepsilon F_\varepsilon + F_{ji}\sum_{k=1,k\neq i}^{n} F_{ik}\hat{x}_k + \sum_{k=1,k\neq j}^{n} F_{jk}\hat{x}_k \tag{4.38}$$

The response of the x_j-th degree of freedom to the input ε is:

$$\frac{\hat{x}_j}{\varepsilon} = \frac{F_\varepsilon}{1 - F_{ij}F_{ji}} + \frac{F_{ji}\sum_{k=1,k\neq i}^{n} F_{ik}\frac{\hat{x}_k}{\varepsilon} + \sum_{k=1,k\neq j}^{n} F_{jk}\frac{\hat{x}_k}{\varepsilon}}{1 - F_{ij}F_{ji}} \tag{4.39}$$

The question of when the degrees of freedom x_i and x_j are directly uncoupled (x_i and x_j can still couple indirectly via $x_1, x_2, \ldots, x_n$) is equivalent to the question of when the transfer function $\hat{x}_j/\varepsilon$ differs from $(\hat{x}_j/\varepsilon)_0$, where the index 0 indicates that the feedback $F_{ij} = 0$. Substituting $F_{ij} = 0$ into (4.39) leads to:

$$\left(\frac{\hat{x}_j}{\varepsilon}\right)_0 = F_\varepsilon + F_{ji}\sum_{k=1,k\neq i}^{n} F_{ik}\frac{\hat{x}_k}{\varepsilon} + \sum_{k=1,k\neq j}^{n} F_{jk}\frac{\hat{x}_k}{\varepsilon} \tag{4.40}$$

It follows that the degrees of freedom x_i and x_j are uncoupled when in any point s of the complex plane the ratio $\dfrac{(\hat{x}_j/\varepsilon) - (\hat{x}_j/\varepsilon)_0}{(\hat{x}_j/\varepsilon)_0}$ is approximately zero, that is:

$$\frac{\left(\frac{\hat{x}_j}{\varepsilon}\right) - \left(\frac{\hat{x}_j}{\varepsilon}\right)_0}{\left(\frac{\hat{x}_j}{\varepsilon}\right)_0} = \frac{F_{ij}\cdot F_{ji}}{1 - F_{ij}\cdot F_{ji}} = \frac{1}{\frac{N_i N_j}{T'_{ij}T'_{ji}} - 1} \approx 0 \quad \Rightarrow \quad x_j \text{ decouples from } x_i \tag{4.41}$$

Equation (4.41) gives the condition for weak coupling between two degrees of freedom of an n degree-of-freedom system which form a critical region in the complex plane. This criterion is identical to condition (4.10) except that the index 1 is replaced by i and 2 is replaced by j. It follows that the discussion of section 4.2.1 on the coupling between two degrees of freedom can be extended to analysis of the coupling between two degrees of freedom x_i and x_j of an n degree-of-freedom system in a critical region of the complex plane. The critical pole distance criterion (4.20) to quantify the coupling between x_i and x_j in the critical region thus becomes:

$$\begin{aligned}\left|N_i N_j\right| = \xi_i\omega_i\Big\{&\left(9\xi_i^2\omega_i^2 + 16\omega_i^2\right)\Big[\xi_i^4\omega_i^4 + 2\xi_i^2\omega_i^2\left(\omega_i^2 + 2\xi_j^2\omega_j^2 + \omega_j^2\right) + 4\xi_i\omega_i\xi_j\omega_j \times \\ &\times\left(\omega_i^2 + \xi_i^2\omega_i^2 + \omega_j^2\right) + 4\omega_i^2\xi_j^2\omega_j^2 + \left(\omega_j^2 - \omega_i^2\right)^2\Big]\Big\}^{1/2} \quad \text{is large}\end{aligned} \tag{4.42}$$

Expression (4.42) may be considered the critical pole distance criterion providing a necessary condition under which the coupling between two degrees of freedom x_i and x_j belonging to a critical region may be neglected. The particular cases of this criterion are by analogy with the discussion of section 4.2.1:

- when the poles of the degrees of freedom x_i and x_j are lying near the imaginary axis:

$$\left|N_i N_j\right| = \sqrt{16\xi_i^2\xi_j^2\omega_i^6\omega_j^2 + 4\xi_i^2\omega_i^4\left(\omega_j^2 - \omega_i^2\right)^2} \quad \text{is large} \tag{4.43}$$

Again, as in the two degree-of-freedom case, this criterion may be satisfied either when the uncoupled eigenvalues of x_i and x_j are sufficiently separated in frequency, i.e $\left(\omega_j^2 - \omega_i^2\right)$ is large or when they are both sufficiently damped $\xi_i^2 \cdot \xi_j^2$ is large.

- when the poles of the degrees of freedom x_i and x_j are lying near the real axis:

$$\left|N_i N_j\right| = \left\{ \left| \omega_j^4\xi_j^4 + \omega_j^2\xi_j^2\left(\omega_i^2 + \omega_j^2\right) + \omega_i\omega_j\left(\omega_i\omega_j + 4\omega_j^2\xi_j^3\xi_i\right) - 2\omega_j^3\xi_j^3\left(\omega_i\xi_i + \omega_j\xi_j\right) - 2\omega_i\omega_j^2\xi_j\left(\xi_i + \xi_j\right) \right| \right\}^{1/2} \quad \text{is large} \tag{4.44}$$

The critical pole distance criterion as given by (4.43) and (4.44) will first be applied in Chapter 5 in piloted simulation modeling, in Chapter 6, to investigate the couplings responsible for the instability of a two-bladed horizontal-axis wind turbine and in Chapter 7 to study the coupling between the blade flapping and lead-lag motion. As discussed in the two degree-of-freedom case, only analysing the differences in behaviour of a dynamic system when using a coupled and an uncoupled model in different case-problems may give a feeling as to the interpretation of large in (4.42), (4.43) or (4.44) for the dynamic system analyzed.

The critical pole distance criterion as derived in this section assumes that there are only two modes in the critical region. If the critical region contains more than two modes, the critical pole distance criterion must be considered in its general formulation (4.33) and therefore the coupling terms between the degrees of freedom belonging to the critical region must also be determined. A way to avoid calculating these terms may be to consider the degrees of freedom in the critical region in pairs and apply the critical pole distance criterion to each pair. In this way only the uncoupled eigenvalues need to be determined.

4.3 Discussion on the Time Constants of Two Uncoupled Degrees of Freedom

The main idea in the critical pole distance method is that two degrees of freedom can be considered weak coupled if their poles in the complex plane are sufficiently separated. Section 2.2.1 of Chapter 2 showed that the position of the poles in the complex plane can be expressed in the time-domain by their time constant. Consider the time constants τ_i and τ_j (defined according to (2.21) or (2.22)) of two uncoupled

degrees of freedom x_i and x_j of an n degree-of-freedom system. Heuristically, the condition "poles far enough from each other" from the critical pole distance method is equivalent in the time domain with the condition "time constants of different order". Assuming that the pole x_i belongs to the slow mode, this can be written as:

$$\tau_i \ll \tau_j \tag{4.45}$$

Condition (4.45) will be verified in the case-problems studied in Chapter 5 in the present dissertation.

4.4 Discussion on the Effect of System's Zeros

As demonstrated in section 4.2.1, equation (4.23), wide frequency separation between two poles is commonly associated with weak coupling, whereas pole proximity is associated with strong coupling. However, this is not invariably true. The zeros can play an important function in the coupling. **Pass et. al.** [1963][82] demonstrated that the relative spacing of poles and zeros are important in determining whether the coupling will be weak or strong.

Consider the generalized n degree-of-freedom system (4.28) in the Laplace domain to which a unit impulse input to the first degree of freedom was applied ($T_r = 1$):

$$\begin{cases} N_1\hat{x}_1 + T_{12}\hat{x}_2 + T_{13}\hat{x}_3 + \ldots\ldots\ldots\ldots + T_{1n}\hat{x}_n = \varepsilon \\ T_{21}\hat{x}_1 + N_2\hat{x}_2 + T_{23}\hat{x}_3 + \ldots\ldots\ldots\ldots + T_{2n}\hat{x}_n = 0 \\ \qquad\ldots\ldots\ldots\ldots \\ T_{i1}\hat{x}_1 + T_{i2}\hat{x}_2 + T_{i3}\hat{x}_3 + \ldots N_i\hat{x}_i + \ldots\ldots + T_{in}\hat{x}_n = 0 \\ \qquad\ldots\ldots\ldots\ldots \\ T_{n1}\hat{x}_1 + T_{n2}\hat{x}_2 + \ldots\ldots\ldots\ldots + T_{nn-1}\hat{x}_{n-1} + N_n\hat{x}_n = 0 \end{cases} \tag{4.46}$$

The response of the system in each degree of freedom to the unit step is:

$$\frac{\hat{x}_1(s)}{\varepsilon} = \frac{\Delta_{11}^*(s)}{\Delta(s)} \quad ; \quad \frac{\hat{x}_2(s)}{\varepsilon} = \frac{\Delta_{12}^*(s)}{\Delta(s)} \quad ; \quad \ldots; \quad \frac{\hat{x}_n(s)}{\varepsilon} = \frac{\Delta_{1n}^*(s)}{\Delta(s)} \tag{4.47}$$

where $\Delta(s)$ is the determinant of the characteristic equation of the system (4.46) and $\Delta_{11}^*(s) \ldots \Delta_{1n}^*(s)$ are the minors of the elements $N_1, T_{12} \ldots T_{1n}$.

$$\Delta(s) = \begin{vmatrix} N_1 & T_{12} & \dots & T_{1n} \\ T_{21} & N_2 & \dots & T_{2n} \\ \dots\dots & & & \\ T_{n1} & T_{n2} & \dots & N_{nn} \end{vmatrix} \tag{4.48}$$

$$\Delta^*_{11}(s) = (-1)^2 N_1 \begin{vmatrix} N_2 & \dots & T_{2n} \\ \dots\dots & & \\ T_{n2} & \dots & N_n \end{vmatrix} \dots \Delta^*_{1n}(s) = (-1)^{1+n} T_{1n} \begin{vmatrix} T_{21} & N_{22} & \dots & T_{2n-1} \\ \dots\dots & & & \\ T_{n1} & T_{n2} & \dots & T_{nn-1} \end{vmatrix}$$

The ratio of the modal response between the first and the second degree of freedom is defined by:

$$\frac{\hat{x}_1(s)}{\hat{x}_2(s)} = \frac{\Delta^*_{11}(s)}{\Delta^*_{12}(s)} \tag{4.49}$$

Considering any pole s_i belonging to the multitude $\{s_1 \dots s_n\}$ of poles of the characteristic equation $\Delta = 0$, the magnitude of the modal response ratio (4.49) of the pole $s_i \in \{s_1 \dots s_n\}$ was defined by **Pass et. al.** [1963][82] as:

$$\left| \frac{\hat{x}_1(s_i)}{\hat{x}_2(s_i)} \right| = \frac{|\Delta^*_{11}(s_i)|}{|\Delta^*_{12}(s_i)|} \tag{4.50}$$

This magnitude of modal response ratio (4.50) can be correlated with the pole-zero pattern of x_1 and x_2 and thus with the interpretation with respect to the couplings between these degrees of freedom. Figure 4.2 from **Pass et. al.** [1963][82] presented three cases which can appear in the complex plane:

- case 1 corresponds to the situation where poles are closely spaced with no nearby zeros;
- case 2 corresponds to a very large modal response ratio
- case 3 corresponds to a very small modal response ratio.

According to the authors and based probably on their experience, case 1 may be

associated with strong coupling whereas cases 2 and 3 with weak coupling.

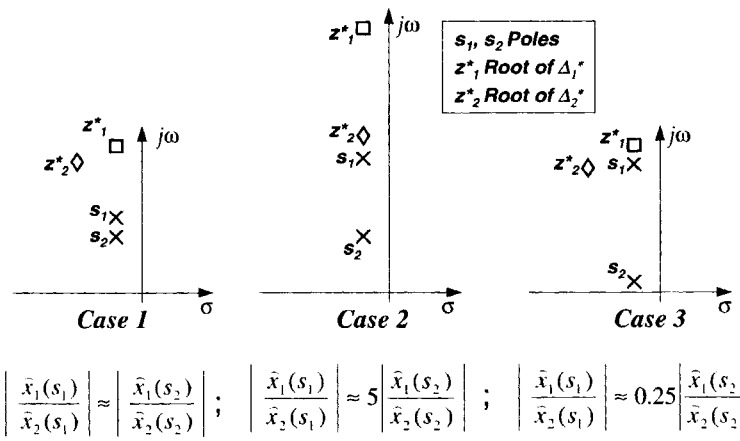

*Figure 4.2 Relative position between the poles and zeros (**Pass et.al** [1963][82])*

4.5 Comparison between the Critical Pole Distance Method and Other Prediction Tools

4.5.1 Campbell Diagram (Spoke-Diagram)

As discussed in Chapter 1, the "critical pole distance method" may be considered as an extension and refinement of the so-called "Campbell diagram" ("spoke-diagram", "Southwell diagram", "fan plot"). The classical Campbell diagram defines the resonance points of a rotating dynamic system. The diagram represents the uncoupled natural (eigen)frequencies of subsystems and specific deflection modes as a function of rotor speed. Examining the diagram, the resonance points are defined as intersection points either between two different curves of natural frequencies or between a curve of a natural frequency and a curve of an excitation frequency. The resonance points indicate that in the range of frequencies around these points dynamic couplings may occur in the system (either between two or more subsystems, or between a subsystem and important excitation sources). However, the resonance points may or may not be critical points for the system, depending on the damping in the system.

Just as in the spoke diagram, the critical pole distance method also deals with the uncoupled modes. However, the critical pole distance method analyses not only the frequency of the uncoupled modes but also the damping of these modes. Therefore, the critical pole distance method can be seen as a more general method because it provides complete information on a system's structural characteristics in frequency as well as in damping. The information in damping mainly represents the aerodynamic damping

forces in the system and may either have a stabilizing or a destabilizing effect on the periodic motion. The Campbell diagram knows two kinds of resonance points defined as:

1. an intersection between an excitation force and a natural frequency;
2. an intersection between two natural frequencies.

1. Resonance between an Excitation Force and a Natural Mode

Consider a point $P(\omega_\beta, \Omega_1)$ in the Campbell diagram defined as the intersection between the curve of blade flap frequency variation and the 2-P excitation line as seen in the left-hand side of Figure 4.3. For the designer, such a point will represent a dangerous point in which the structure may resonate with the 2-P excitation.

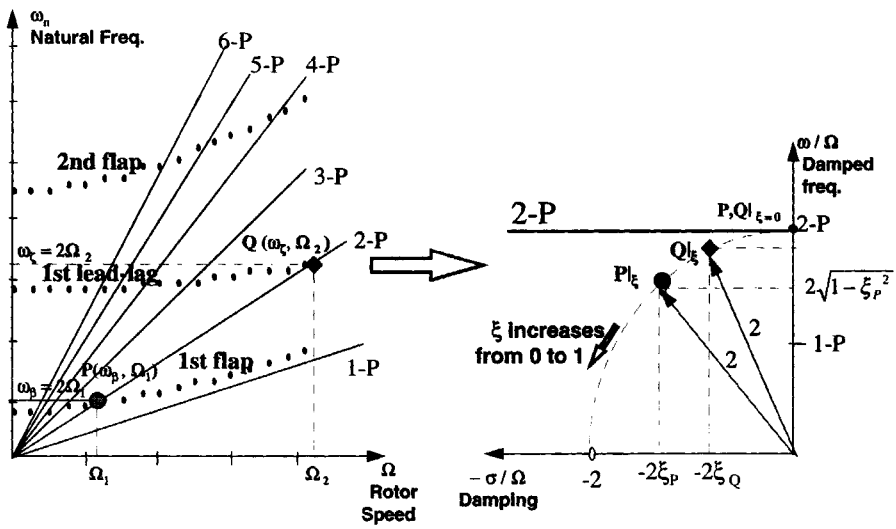

Figure 4.3 Resonance points between natural and excitation frequencies as seen in the Campbell diagram and in the complex plane

In the critical pole distance method point $P|_\xi$ is situated on the semicircle of radius 2 the so-called "circle of 2-P excitation". Its position on this semicircle is determined by the damping ξ_P existing in the system, as seen in the right-hand side of Figure 4.3. Representing also the excitation line 2-P, it is clear that point P is on the excitation line only if the damping in the system equals zero. Otherwise, point P is found in the complex plane at a certain distance from the excitation line 2-P at a point $P|_\xi$ (it was presumed that the response of the system is harmonic, therefore the damping ratio can take a value between 0 and 1). As discussed in Chapter 2, depending on the distance between the excitation line and point P, point P may or may not represent a critical

point for the system. In the Campbell diagram, there are similar intersections between natural frequencies and excitation forces (see for example point Q representing the intersection between the curve of natural lead-lag frequency variation with the rotational speed and the 2-P linc). In the critical pole distance method, point Q is also situated on the circle of 2-P excitation, albeit with a different damping ratio than P. In order to determine whether these points form a critical region for the system, their relative positions in the complex plane should be investigated.

2. Interference between Two Natural Modes

Consider next a point R in the Campbell diagram as an intersection between the flap and lead-lag frequencies (see left-hand side of Figure 4.4). This point represents a dangerous point where the condition leading to an instability is created. However, in the Campbell diagram two modes may intersect or come very close to each other (the so-called "curve veering") without leading to instability.

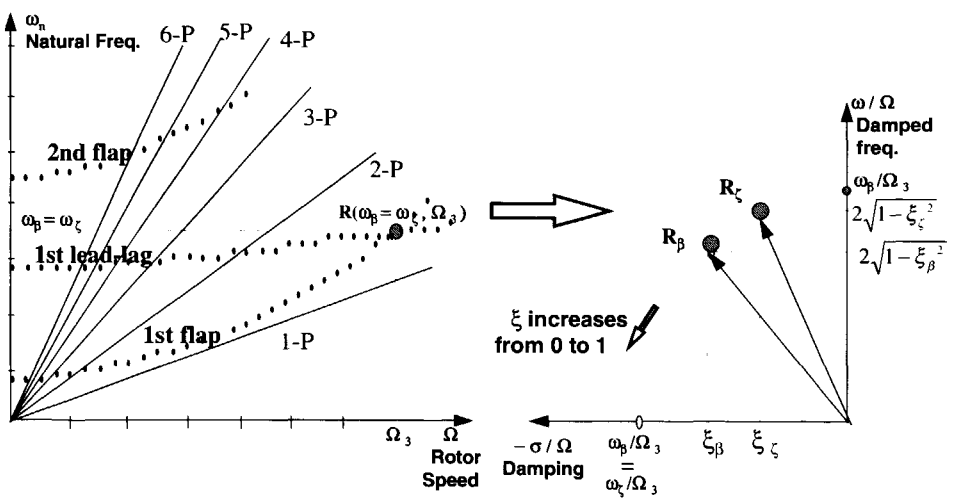

Figure 4.4 The intersection between two natural frequencies as seen in the Campbell diagram and in the complex plane

For the critical pole distance method this point has to be transposed in the complex plane. Point R from the Campbell diagram transposes in the complex plane as two points, one corresponding to the flapping eigenvalue R_β and the other corresponding to the lagging eigenvalue R_ζ. These points are both located on a circle of radius $\omega_\beta/\Omega_3 = \omega_\zeta/\Omega_3$. Usually the point corresponding to the lead-lag motion R_ζ corresponds to a lower damping ratio than point R_β. Depending on the relative position between R_β and R_ζ, the poles may be considered sufficiently close or sufficiently separated in order to allow for their coupling effects in the simulation model or not. Therefore, also in this

case, the relative position in the complex plane between the two poles should be investigated in order to determine whether these points form a critical region for the system.

4.5.2 Milne Criterion

Milne [1965][72] derived a general criterion which allows dividing a multiple degrees of freedom system into a series of weakly coupled sub-systems. The Milne criterion (also called Weakly Coupled Systems Criterion) is actually a criterion used to separate the slow-motion from the fast-motion dynamics. Consider an n-dimensional homogeneous system that may be partitioned into two levels of sub-systems A and B:

$$\begin{bmatrix} \dot{X}_A \\ \hline \dot{X}_B \end{bmatrix} - \left[\begin{array}{c|c} A-A & A-B \\ \hline B-A & B-B \end{array}\right] \begin{bmatrix} X_A \\ \hline X_B \end{bmatrix} = 0 \tag{4.51}$$

Assume also that system A is of slower dynamics than system B (or system B of faster dynamics than A); in the complex plane this means that the eigenvalues of smaller modulus belong to system A. Defining two circles, one of radius r as the maximum of the eigenvalues of the sub-system A, $r = \max(|s_A|)$, and R as the minimum of the eigenvalues of the sub-system B, $R = \min(|s_B|)$, the Milne criterion states that the systems A and B are weakly coupled if and only if the following two conditions are satisfied (see Figure 4.5):

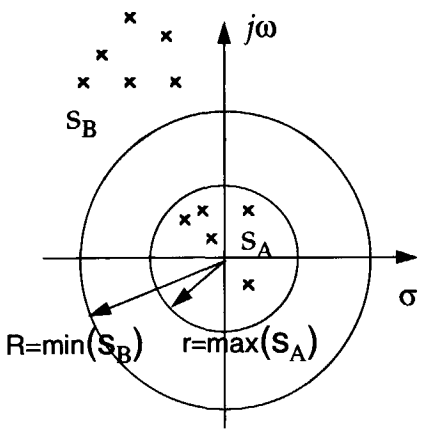

Figure 4.5 Milne criterion in the complex plane ***Milne*** *[1965][72]*

1. the eigenvalues in the complex plane are well separated, i.e.:

$$\left[\frac{r}{R}\right] << 1 \tag{4.52}$$

2. the coupling terms are small. Denoting with M_1 and M_2 the maximum elements of the coupling matrices A-B and B-A then:

$$\left|\frac{\dim(A)\cdot M_1\cdot M_2}{R^2}\right| << 1 \tag{4.53}$$

Under these conditions, the coupled modes may be approximated by weakly coupled modes, given in the fast motion by the uncoupled eigenvalues of subsystem B, but in the slow motion both by the uncoupled eigenvalues of subsystem A and an approximation of the fast motion at steady-state values. Therefore, while the fast motion may be approximated by its uncoupled eigenvalues, the slow motion is strongly affected by the fast motion. *"The motion in the slow modes does not develop enough to affect the overall motion, while in the longer term, the faster modes have reached their steady-state values and can be represented by quasi-steady effects."* (**Padfield** [1996][81])

Padfield [1980][80] applied the Milne criterion to study the characteristics of the longitudinal motions of both an articulated and a hingeless helicopter in forward flight. While the classical low modulus phugoid and high modulus short period modes are well separated in magnitude, for the articulated helicopter r/R= O(0.2), for the stiff rotor helicopter this classical form of the two longitudinal modes breaks down. The higher the forward speed, the more the helicopter phugoid resembles the fixed-wing phugoid where the approximation works very well for aircraft with strong positive manoeuvre margins.

4.5.3 Vector Shift Method

The question of necessary degrees of freedom to be considered in the simulation models was posed also for fixed-wing aircraft. In this case, the influence of the elastic modes on the rigid body modes had to be investigated during the development of the aircraft. **Pass et.al.** [1963][82] tried to resolve the topic of rigid-elastic coupling that occurs during control-fixed flight of an aircraft by using the so-called "Vector Shift Method" between the uncoupled and coupled roots. The eigenvalues of the coupled equations of motion for an elastic aircraft can be determined by solving the equation of

motion of form:

$$\begin{vmatrix} \text{Rigid-body} & \text{Coupling-terms} \\ \text{Coupling-terms} & \text{Elastic-modes} \end{vmatrix} = 0 \tag{4.54}$$

If s_i is a root of the characteristic equation of system (4.54), the coupling may be characterized by the vector change between the uncoupled and coupled root in the complex plane Δs_i (see Figure 4.6):

$$|\Delta s_i| = \sqrt{(\sigma_2 - \sigma_1)^2 + (\omega_2 - \omega_1)^2} \tag{4.55}$$

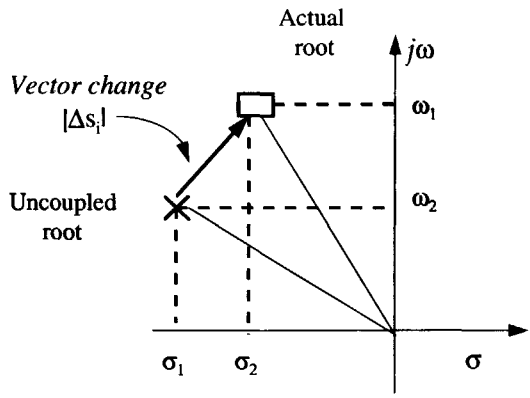

*Figure 4.6 Vector shift from the uncoupled to the coupled root (**Pass et. al** [1963]*[82] *)*

*Table 4.1 Degree of Coupling Quantitative Criteria (**Pass et. al.** [1963]* [82]*)*

Degree of Coupling	$\lvert \Delta s_i/s_i \rvert$
Very lightly coupled	0 - 0.05
Lightly coupled	0.05 - 0.10
Moderately coupled	0.10 - 0.20
Heavily coupled	0.20 - 0.30
Very Heavily Coupled	0.30 - 1.0

The degree of elastic coupling can be defined as the ratio between the vector shift Δs_i and the modulus of s_i, that is $| \Delta s_i/s_i |$. Pass et. al. quantified the degree of elastic coupling from their judgement and experience as presented in Table 4.1.

4.5.4 Root Locus Method

The vector shift method is an appropriate form for servo analysis via root locus. The root locus method is a classical design method in control theory, showing in the complex plane how the system poles move when the gain is changed. Therefore, the root loci can be used to design a control law, giving a graphical picture of the effect of selected parameters on the system poles and suggesting what values should be chosen for the gain to obtain a specified damping ratio or time constant. In system design, the shape of the loci can be changed in a desirable direction by:

- adding a pole or a zero. As a general rule, adding a pole pushes the loci away from the pole, and adding a zero pulls the loci in toward that zero;
- pole-zero cancellations. If a dominant pole is in an undesirable location and it cannot easily be changed by feedback alone, the effect of that pole may be minimized by choosing a zero at the same location or in the near vicinity of the dominating pole. For example a "slow" pole (close to the imaginary axis, that is with a large time constant) or a high oscillatory pair (small damping ratio) may be acceptable if nearby zeros are added to these poles.

4.5.5 Force-Phasing Matrix Technique

The force-phasing matrix technique (also called Energy Flow-Diagram Method) (**Bielawa** [1992][6]) may be used to determine the mechanism of instability of any linear multiple-degree-of-freedom system. The theoretical development of this method follows from three simple principles governing any unstable motion:

- the cause of any instability can be found in the fact that any unstable system has destabilizing forces acting on it that have components in phase with the system's velocity. These forces produce work on the system.
- each degree of freedom of an unstable system has so-called "drivers" - destabilizing forces acting on that degree of freedom which are in phase with the velocity of the corresponding degree of freedom.
- any instability involving two or more degrees of freedom possesses so-called "multiplicity of energy flow paths" (vicious circles) - paths involving two or more degrees of freedom in which energy is alternately transferred from one degree of freedom to the other.

Consider the eigenvalue problem of a second-order linear differential equation of

motion:

$$\left(\left[M\right]s^2+\left[C\right]s+\left[K\right]\right)\left\{X\right\}=\left\{0\right\} \tag{4.56}$$

where [M], [C], and [K] are, respectively, the inertia, damping and stiffness matrices which are assumed to be constant. The general solution to the homogeneous differential equation (4.56) is:

$$\left\{X\right\}=\sum_{k=1}^{K}\left\{\Phi^{(k)}\right\}e^{s_k t} \tag{4.57}$$

where $s_k = \sigma_k \pm i\omega_k$ denotes the k-th eigenvalue which in general is a complex value and $\{\Phi^{(k)}\}$ denotes the corresponding k-th eigenvector. Inserting the general solution (4.57) into (4.56), each equation can be rewritten as the sum of mass, damper, and spring forces of the i-th diagonal element along with the coupling terms gathered as a combined excitation force f_i of all off-diagonal terms :

$$\underset{\text{inertia}}{m_{ii}\,s_k^2\,\phi_i^{(k)}} + \underset{\text{damper}}{c_{ii}\,s_k\,\phi_i^{(k)}} + \underset{\text{spring}}{k_{ii}\,\phi_i^{(k)}} + \underbrace{\sum_{l=1!=i}^{n}\left(m_{il}\,s_k^2+c_{il}\,s_k+k_{il}\right)\phi_l^{(k)}}_{f_i\ \text{excitation}} = 0 \tag{4.58}$$

Equation (4.58) represents the equilibrium of forces acting on the i-th degree of freedom and can be represented in the complex plane. For an unstable oscillatory mode ($\sigma_k > 0$) the vector f_i contains both individual terms that have a positive real part and are the drivers for the i-th degree of freedom, and individual terms that have a negative real part and are quenchers for that degree of freedom. Identifying the relatively large positive values in the force terms in the equations of motion (4.58) defines the critical drivers of the instability. The lines on which the critical drivers are located show the critical degrees of freedom involved in the instability. The principal function of the FPM technique is to identify these critical drivers and the degrees of freedom involved in the instability. Once they are determined, a matrix can be defined containing the degrees of freedom involved in the instability containing as elements the critical drivers corresponding to each degree of freedom, the so-called force-phasing matrix. In the force-phasing matrix, energy-flow paths can now be defined as different closed-loop combinations between the different critical drivers via the main diagonal of the force-phasing matrix (see Figure 4.7). The energy-flow paths show how energy is exchanged between the different degrees of freedom involved in the instability and therefore define

the mechanism of the instability.

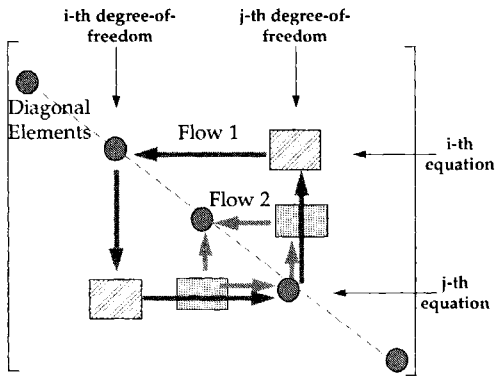

*Figure 4.7 Energy-flow paths representing the flow of energy between the i-th and j-th degrees of freedom involved in instability (**Bielawa** [1992]*[6])

For an application of the force-phasing matrix technique, the reader may consult **Bielawa** [1992][6] where the energy-flow paths characteristic for helicopter ground and air resonance are defined.

4.5.6 Energy-Flow Method

A more qualitative description of the force-phasing matrix technique in the sense that the designer does not need to determine the complete solutions of eigenvectors in order to define the vicious circles of instability, and providing more physical insight, was elaborated by **van Holten** [2000][47] in the so-called "Energy-Flow method". The energy-flow method determines the mechanism of instabilities using the principle that the motion is likely to become unstable when several vibration modes mutually transfer energy into each other.

Chapter 5

Criteria for the Inclusion of the Rotor Disc-Tilt Dynamics in Helicopter Piloted Simulation Modeling[&]

How good a model is... is like asking what the weather is like on Earth? ...The answer is quite simple- it depends!... it depends on where you are and the time of the year, etc., etc...."

Gareth Padfield [1996]

The outline survey of Chapter 3 illustrated that the rotor disc-tilt dynamics should be included in piloted simulation as an extension of the conventional six degree-of-freedom model, especially in the design analysis of a SCAS system or for certain types of rotor systems. The present chapter applies the critical pole distance method in order to determine when the rotor disc-tilt dynamics should be included in the helicopter piloted simulation modeling.

5.1 A Simple Manoeuvre Analyzed in the Complex Plane

To get some insight in the coupling between the body motion and the disc-tilt motion of the rotor, the present section investigates a simple helicopter manoeuvre, that is, the first few instants during the transition from hover to forward flight, after a step input of longitudinal cyclic pitch. One may assume that, at the very beginning of this manoeuvre, before forward speed builds up and becomes important, the helicopter just rotates in the pitch direction as seen in Figure 5.1. The equation of motion describing the helicopter pitch in the shaft plane is (see Figure 5.1):

$$-T_{dp}\, h\left(\theta_{1s} - a_1\right) - \frac{N}{2} K_\beta \left(\theta_{1s} - a_1\right) = I_y \dot{q} \quad \Leftrightarrow \quad \dot{q} = -K\left(\theta_{1s} - a_1\right) \tag{5.1}$$

where $K = \left[\, T_{dp} h + (N/2) K_\beta \,\right] / I_y$ is the moment exerted on the body per radian of rotor disc-tilt, due to the thrust vector T_{dp} offset w.r.t. the centre of gravity ($T_{dp} = M_{hel}\, g$), as well as due to direct spring moments of constant K_β, whereas N is the number of blades, I_y is the helicopter moment of inertia, h is the distance to the rotor hub, θ_{1s} is the longitudinal tilt of the swashplate, a_1 is the longitudinal disc tilt, and q is the

---

& This chapter is a revised version of paper no. 39 by Pavel and van Holten, van [1997][86] *"On the Prediction of the Necessary Rotor Dynamics for Helicopter Flight Simulation"* and paper no. FM.03 by Pavel [1998][87] *"Effects of Rotor Disc-Tilt on Helicopter Piloted Simulation"*

pitching velocity of the body.

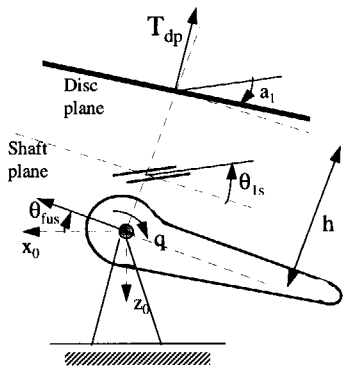

Figure 5.1 Helicopter pitch motion after a step input of longitudinal cyclic

Equation (5.1) includes the flapping motion through the steady-state longitudinal rotor disc-tilt a_1, neglecting the transient disc-tilt dynamics. This assumption is generally true, because the transient disc-tilt indeed damps out very quickly after a disturbance. Therefore, in the classical treatment of the subject, the rotor disc tilt is often assumed to respond instantaneously to a pitching motion:

$$a_1 = -\frac{16}{\gamma}\frac{q}{\Omega} \tag{5.2}$$

where γ is the Lock number, and Ω is the rotor angular speed. Together, equations (5.1) and (5.2) represent the equations of motion for a pitching helicopter. These equations characterize the body pitch dynamics, the disc-tilt being included in a steady-state form.

The influence of different rotor systems on helicopter pitch behaviour will be investigated in this section by considering different characteristic values of the hinge spring stiffness K_β. The blade is assumed to be hinged at the hub. Zero spring stiffness corresponds to a teetering rotor, a relatively large stiffness represents the semi-rigid system, whereas the articulated rotor with hinge-offset is an intermediate case. Two cases will be examined, namely the case of a teeter rotor with K_β= 0 Nm and the case of a semi-rigid rotor of K_β= 460000 Nm, both applied to a middle-size helicopter of characteristics presented in Table 5.1.

Consider an input in the longitudinal cyclic (for example θ_{1s}= -1°). Applying the Laplace transformation to the system of equations (5.1) and (5.2) with zero initial conditions, leads to the transfer function:

$$G_{bo}(s) = \frac{\hat{q}_{bo}(s)}{\hat{\theta}_{1s}(s)} = \frac{-K}{s + K\frac{16}{\gamma}\frac{1}{\Omega}} = \frac{1}{\frac{\gamma\Omega}{16K}s + 1} \tag{5.3}$$

Table 5.1 Helicopter Data

γ *Lock number*	M_{hel} *Body mass*	Ω *Rotor speed*	h	I_y *Inertia moment*	*Case 1* K_β*: Teeter*	*Case 2* K_β*: Semi-rigid*
6	2200 kg	260 rpm	1 m	10625kgm^2	0 Nm	460000Nm

The response in pitch of the helicopter for a step input $\theta_{1s} = -1^\circ$ ($\hat{\theta}_{1s} = -1/s$) becomes:

$$\hat{q}_{bo}(s) = G_{bo}(s)\cdot\hat{\theta}_{1s} = \frac{1}{s\left(s\frac{\gamma\,\Omega}{16\,K} + 1\right)} \tag{5.4}$$

The body motion as given by (5.3) may be represented in the complex plane for both the teetering and semi-rigid helicopter. The system has one real eigenvalue (pole) which includes the influence of the rotor system via the K value (which depends on K_β):

$$s^{T}_{bo} = -K_T\frac{16}{\gamma\,\Omega} \quad ; \quad s^{SR}_{bo} = -K_{SR}\frac{16}{\gamma\,\Omega} \tag{5.5}$$

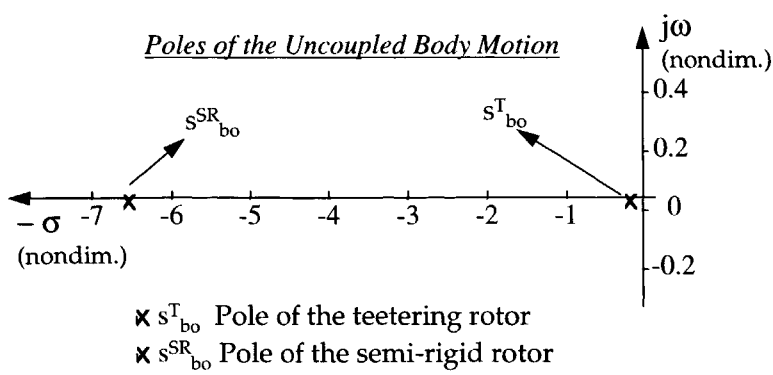

Figure 5.2 Poles of the Uncoupled Body Pitch Motion as seen in the Complex Plane

Looking at Figure 5.2 one may see that the poles are situated in the left-hand half of the s-plane and therefore the motion is stable for both the teetering and semi-rigid

rotors. However, the closer the pole is to the origin, the slower the motion becomes. Accordingly, the teetering rotor will respond much slower to the longitudinal cyclic than the semi-rigid rotor. This conclusion can also be verified by defining the body time constant which, according to (2.21), is:

$$\tau^{T}_{bo} = \frac{\gamma}{16}\frac{\Omega}{K_T} \quad ; \quad \tau^{SR}_{bo} = \frac{\gamma}{16}\frac{\Omega}{K_{SR}} \tag{5.6}$$

For the example considered here, one obtains for the teetering rotor a time constant τ^{T}_{bo}= 5.044 sec whereas for the semi-rigid rotor τ^{SR}_{bo} = 0.153 sec. Thus, the teetering rotor is much slower that the semi-rigid rotor (or, equivalently, the semi-rigid rotor is much faster than the teetering rotor). According to section 2.2.1 of Chapter 2, to speed up the response of the teetering body, its pole has to be moved to the left-hand side of the complex plane.

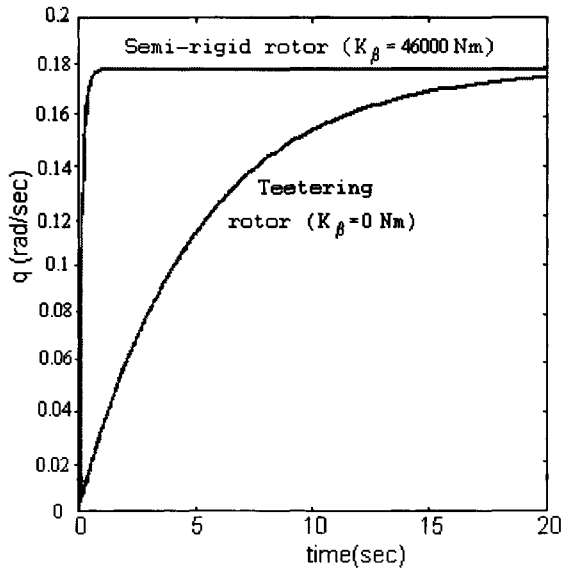

Figure 5.3 Pitch response of a semi-rigid and a teetering rotor

Figure 5.3 confirms the previous results in the time domain. The teetered rotor shows a response typical for acceleration control, whereas the semi-rigid case is more characteristic for velocity-control (since the response reaches a constant value of pitch rate already within 1 sec), the latter requiring much less anticipation from the pilot.

The assumption given by equation (5.2), of instantaneous response of the rotor to

control inputs, will now be removed and some dynamics of rotor disc tilting will be introduced by means of a time constant τ :

$$\tau \dot{a}_1 + a_1 = -\frac{16}{\gamma}\frac{q}{\Omega} \tag{5.7}$$

Equations (5.1) and (5.7) are the equations of motion for the pitching helicopter including rotor disc-tilt dynamics. Appendix D, section D.4 will demonstrate that this corresponds to taking into account the (low frequency) regressing flap mode, on top of the steady solution. Combining (5.1) and (5.7), and applying the Laplace transformation, the transfer function representing the motion of the helicopter in this case becomes:

$$G_{bo-fl}(s) = \frac{\hat{q}}{\hat{\theta}_{1s}} = \frac{-K(\tau s + 1)}{s(\tau s + 1) + K\frac{16}{\gamma}\frac{1}{\Omega}} \tag{5.8}$$

The helicopter response in pitch to a step input θ_{1s}= - 1° ($\hat{\theta}_{1s} = -1/s$) becomes in this case:

$$\hat{q}_{bo-fl}(s) = G_{bo-fl}(s)\cdot\hat{\theta}_{1s}(s) = \frac{K(\tau s + 1)}{s\cdot\left(s(\tau s + 1) + K\frac{16}{\gamma}\frac{1}{\Omega}\right)} \tag{5.9}$$

The poles of the body + disc-tilt motion as given by (5.8) are either real or complex values, depending on the sign of the term $1 - 4\tau K\frac{16}{\gamma\,\Omega}$. For the numerical examples considered, the teetering rotor has real poles, whereas the semi-rigid rotor has complex poles:

$$s^{T}_{bo-fl\,1,2} = -\frac{1}{2\tau} \pm \frac{\sqrt{1 - 4\tau K_T\cdot(16/(\gamma\,\Omega))}}{2\tau} \in \mathbb{R} \quad \text{Teetering rotor} \tag{5.10}$$

$$s^{SR}_{bo-fl\,1,2} = -\frac{1}{2\tau} \pm i\,\frac{\sqrt{4\tau K_{SR}\cdot(16/(\gamma\,\Omega)) - 1}}{2\tau} \in \mathbb{C} \quad \text{Semi-rigid rotor} \tag{5.11}$$

From equation (5.9) one may observe that introducing rotor disc-tilt dynamics in the simulation model introduces a zero in the system:

$$z = -1/\tau \tag{5.12}$$

Figure 5.4 and Figure 5.5 present the pole-zero pattern as obtained for the teetering and the semi-rigid rotor for time constants τ varying between 0.05 and 0.3.

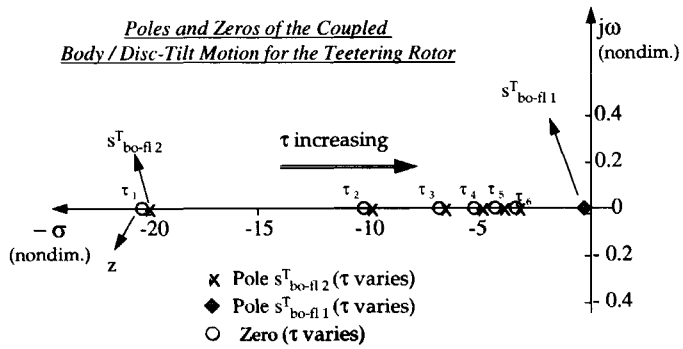

Figure 5.4 Representation of the Coupled Body/ Disc-Tilt Motion for a Teetering Rotor

Table 5.2 Poles and Zeros of the Coupled Body / Disc-Tilt Motion for a Teetering Rotor

τ (sec)	$\tau_1 = 0.05$	$\tau_2 = 0.1$	$\tau_3 = 0.15$	$\tau_4 = 0.2$	$\tau_5 = 0.25$	$\tau_6 = 0.3$
$s^T_{bo\text{-}fl\,1}$	-.2003	-.2023	-0.2045	-.2068	-.2092	-.2117
$s^T_{bo\text{-}fl\,2}$	-19.7997	-9.7977	-6.4621	-4.7932	-3.7908	-3.1216
z	-20.00	-10.00	-6.6667	-5.00	-4.00	-3.3333

For the teetering rotor (see Figure 5.4) the motion has two real poles: one pole very close to the origin - which corresponds mainly to the body motion -and another pole far away from the origin - corresponding mainly to the disc-tilt motion-. By increasing the time constant τ, the far pole moves rapidly towards the origin. Since the poles are real and distinct, as demonstrated in chapter 2, the motion is a sum of two decaying exponentials. For each pole, a time constant may be defined which, according to (2.21), are of form $-1/s^T_{bo\text{-}fl}$. Calculating these two time constants for different τ, it appears that the teetering rotor is characterized by a large time constant, corresponding to the pole close to the origin and a smaller one corresponding to the pole far away from the origin. The pole close to the origin is the dominating one and the motion characteristics are mainly determined by this pole. For the case analyzed here, this pole is situated between [- 0.2003; - 0.2117] (see Table 5.2) and corresponds mainly to the body motion. To speed up the motion, the dominating pole has to be moved to the left.

However, looking at Figure 5.4 it becomes clear that as the disc-tilt time constant τ increases (the disc-tilt motion slows down), the flap-body pole approaches the body-flap pole, increasing its influence on the general motion.

The motion has a zero located very close to the fast pole for all analyzed cases. As stated in Chapter 2, if a zero is far away from a pole, it does not influence the transient motion and therefore it can be neglected, whereas a zero situated close to a pole neutralizes the effect of that pole on the motion. For the teetering rotor, the pole is situated near the flap-body mode and therefore it eliminates the effect of the disc-tilt motion on the total pitch motion.

For the semi-rigid rotor, the pole-zero pattern of the coupled body / disc-tilt motion is illustrated in Figure 5.5.

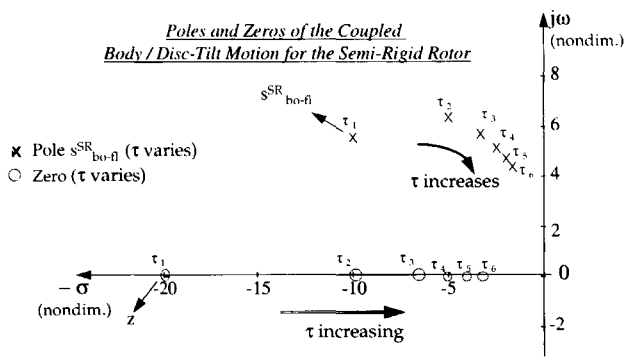

Figure 5.5 Representation of the Coupled Body / Disc-Tilt Motion. Semi-Rigid Rotor

Table 5.3 Poles and Zeros for the Coupled Body / Disc-Tilt Motion. Semi-rigid Rotor

τ (sec)	$\tau_1 = 0.05$	$\tau_2 = 0.1$	$\tau_3 = 0.15$	$\tau_4 = 0.2$	$\tau_5 = 0.25$	$\tau_6 = 0.3$
s^{SR}_{bo-fl}	-10.0 ± i 5.5435	-5.00 ± i 6.3534	-3.333 ± i 5.6979	-2.5 ± i 5.1413	-2.00 ± i 4.706	-1.66 ± i 4.36
z	-20.00	-10.00	-6.6667	-5.00	-4.00	-3.3333

In this case, the poles are complex values representing an oscillatory motion. The motion is stable, as the poles are situated in the left-hand side of the complex plane. As the time constant τ increases (as the disc-tilt motion gets slower), the poles approach the origin, thus increasing the response overshoot, and deteriorating the relative stability characteristics of the motion. A time constant of the body + disc-tilt motion may be defined according to (2.22) as $\tau^{SR}_{bo-fl} = 1/(\zeta\,\omega_n) = 2\,\tau$. The body/disc-tilt time constant is reduced (i.e. the speed of decay of the response is increased) by reducing the time constant of the disc-tilt motion (i.e. speeding up the disc-tilt motion) which also results

in increasing the real part of the poles (damping) and improving the stability characteristics. The system's speed of response is increased by increasing the distance of the poles to the origin, in this case by increasing K. Therefore, compared to the teetering rotor, the motion speeds up for the semi-rigid rotor.

Concerning the zero's position, as the zeros are approaching the origin, the response overshoot is increasing (negative effect) while the peak time is decreasing (positive effect). For the design, the position of a zero is a trade-off between the overshoot and the speed of response. For the semi-rigid rotor, one may observe that as the disc-tilt time constant increases, the poles approach the origin (i..e. the disc-tilt motion slows down).

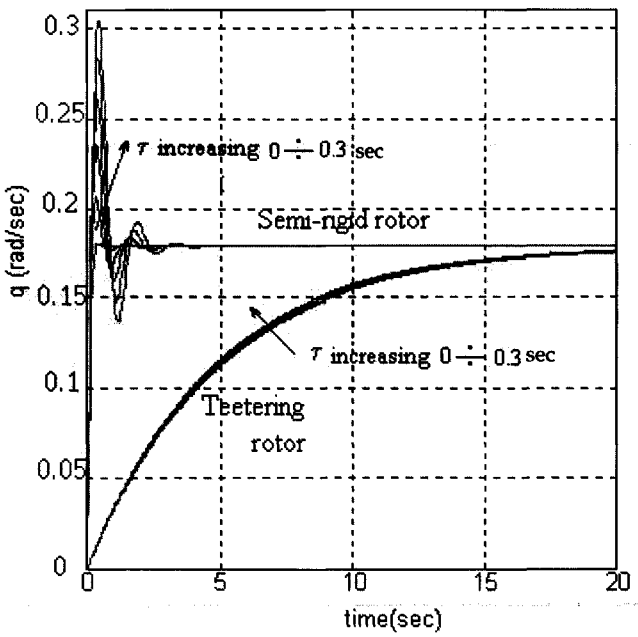

Figure 5.6 Effects of rotor disc-tilt dynamics on the helicopter pitch response

The pitch response represented in the time domain with rotor disc-tilt dynamics was included is illustrated in Figure 5.6.

The previous discussion confirmed that the addition of the first-order term da_1/dt does influence the response of the semi-rigid system rather profoundly, in such a way that it will probably be noticeable to the pilot. On the other hand, in the case of the teetering system, the additional dynamics due to da_1/dt is hardly noticeable.

5.2 Critical Pole Distance Method Applied to the Simple Manoeuvre Analyzed

One question arises at this point of the analysis: would it be possible for the designer to predict the effect of the disc-tilt dynamics on the body motion before having developed the coupled body/disc-tilt equations of motion? At a first look the designer may use the principles presented in the critical pole distance method to try and determine the importance of the disc-tilt dynamics for the teetering and the semi-rigid rotors in the case of the longitudinal cyclic pitch manoeuvre. To this end, the uncoupled body/disc-tilt motion and the uncoupled disc-tilt motion have to be determined. The poles of the uncoupled pitch motion are as given in Figure 5.2. The poles of the uncoupled disc-tilt motion may be simply determined by writing the uncoupled disc-tilt equation of motion:

$$\tau \dot{a}_1 + a_1 = 0 \tag{5.13}$$

The uncoupled poles of the disc-tilt motion corresponding to the eigenvalue are:

$$s_{fl} = -1/\tau \tag{5.14}$$

For different values of the disc-tilt time constant τ, the poles of the uncoupled disc-tilt motion are represented in Figure 5.7. As expected, increasing the time constant slows down the disc-tilt motion.

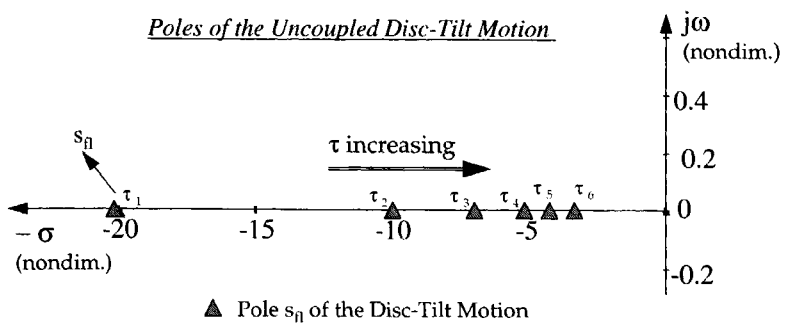

Figure 5.7 Poles of the uncoupled disc-tilt motion

In the present section the critical pole distance method will be applied to the teetering and semi-rigid rotor. Figure 5.8 and Figure 5.9 present the relative position of between the body-flap poles for different values of the disc-tilt time constant τ.

For the teetering rotor it is obvious that for any value of τ, the body and disc-tilt

eigenvalues are relatively far from each other and therefore, the rotor disc-tilt dynamics does not influence the pitch dynamics. For the semi-rigid rotor, as the uncoupled disc-tilt motion slows down (time constant τ increases) it interacts with the region of the uncoupled body pole. For a time constant $\tau \geq 0.1$ sec, the body and rotor disc-tilt motion couple together. This result agrees with the conclusions obtained in the time domain. Essentially, for a semi-rigid rotor the disc-tilt motion slows down and the body motion speeds up, thus coupling with each other. This is the fundamental explanation of the body/disc-tilt coupling characteristic to semi-rigid rotors.

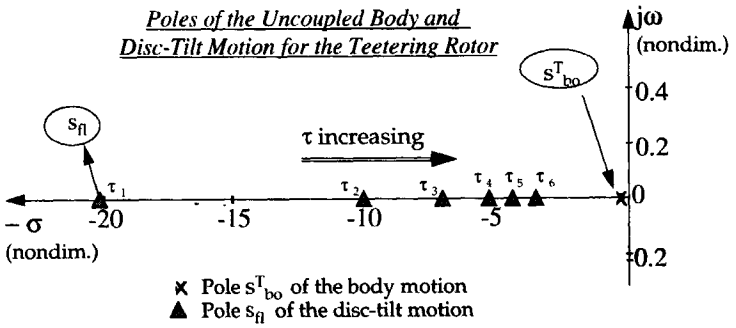

Figure 5.8 Critical Pole Distance Method Applied to the Teetering Rotor

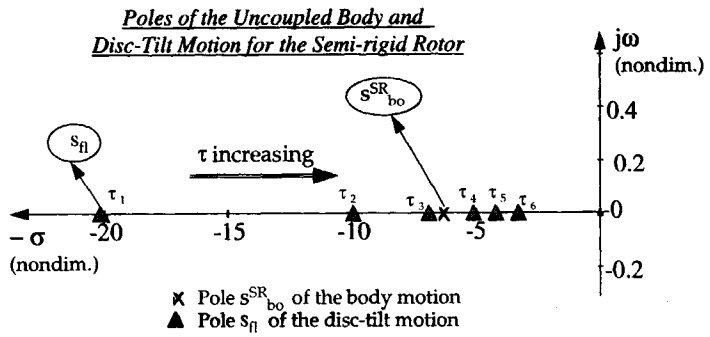

Figure 5.9 Critical Pole Distance Method Applied to the Semi-Rigid Rotor

5.3 Milne Criterion Applied to the Simple Manoeuvre Analyzed

Separating the body and rotor disc-tilt motion, the disc-tilt motion is weakly coupled to the body motion for the simple case considered, if and only if:

1. $$\left|\frac{r_{bo}}{R_{fl}}\right| << 1 \qquad (5.15)$$

2. $$\left|\frac{M_{bo-fl} \cdot M_{fl-bo}}{R_{fl}^2}\right| << 1 \tag{5.16}$$

Defining the radius of the body motion as $r_{bo} = |s_{bo}|$ and the radius of the disc-tilt motion $R_{fl} = |s_{fl}|$ and observing that the coupling terms in the equations of motion (5.1) and (5.7) are:

$$M_{bo-fl} = -K \quad ; \quad M_{fl-bo} = \frac{16}{\gamma \Omega \tau} \tag{5.17}$$

the second condition (5.16) reduces to the first condition (5.15). Consequently, the rotor disc-tilt and body motion can be considered weakly coupled during the first few instants during the transition from hover to forward flight if and only if:

$$\left|\frac{s_{bo}}{s_{fl}}\right| << 1 \tag{5.18}$$

For the teetering rotor, for a variation of the disc-tilt time constant $\tau[0.05;0.1;0.2;0.25;0.3]$ (sec) the Milne criterion is illustrated in Figure 5.10 and is equivalent to:

$$\left|\frac{s_{bo}}{s_{fl}}\right| \in [0.00991;0.01982;0.0297;0.0396;0.05946] \Rightarrow \left|\frac{s_{bo}}{s_{fl}}\right| << 1 \tag{5.19}$$

Thus, the body motion may be separated from the rotor disc-tilt motion.

For the semi-rigid rotor, as the disc-tilt time constant varies, the Milne criterion is equivalent to (see Figure 5.11):

$$\left|\frac{s_{bo}}{s_{fl}}\right| \in [0.3268; 0.6537; 0.9805; 1.3073; 1.6341; 1.9610] \tag{5.20}$$

Thus, the body motion may not be separated from the rotor disc-tilt motion for any of the cases analyzed.

One may observe, that for this simple example, the Milne criterion is equivalent to the critical pole distance method, with the second condition of the Milne criterion depending only on the uncoupled characteristics of the motion.

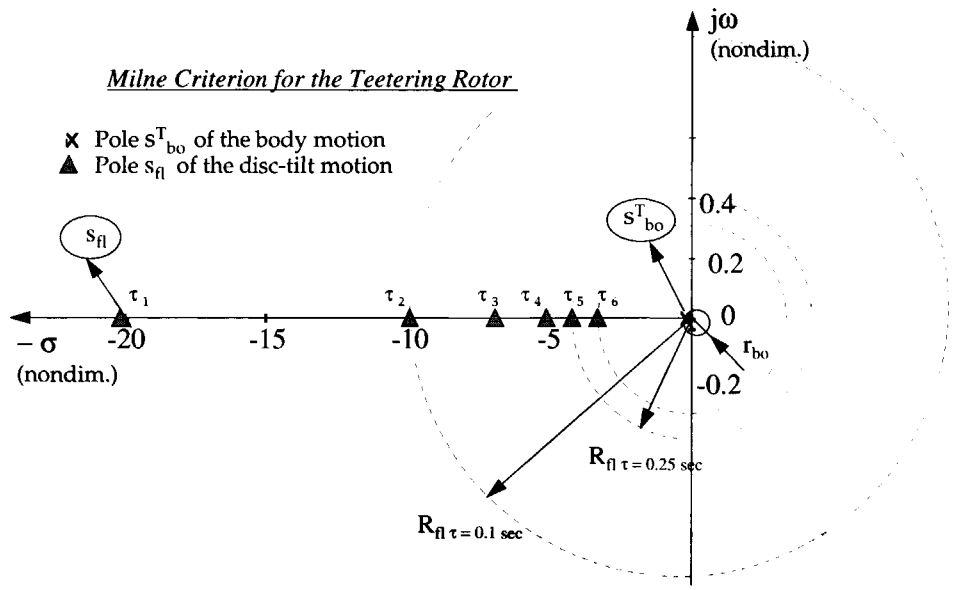

Figure 5.10 Milne criterion applied to the teetering helicopter

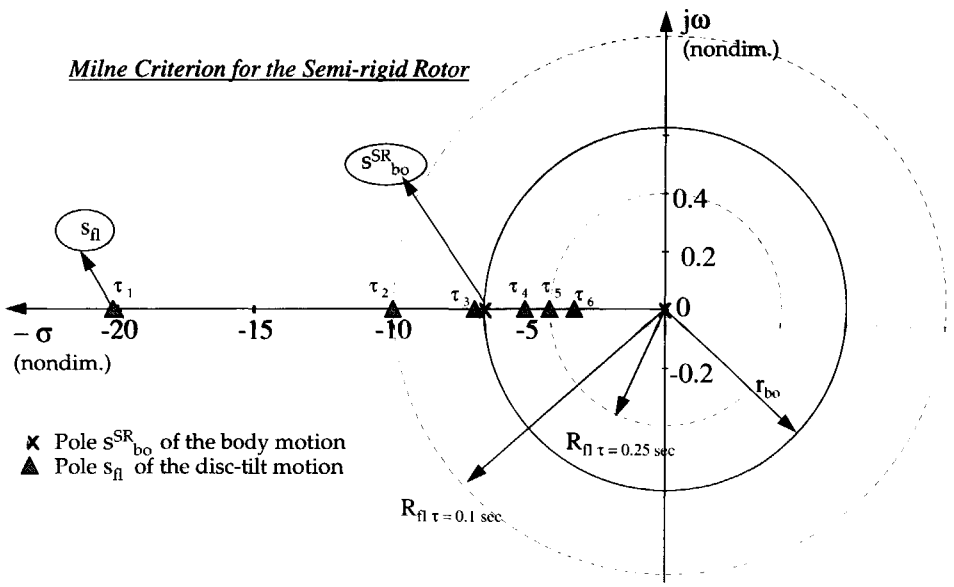

Figure 5.11 Milne criterion applied to the semi-rigid helicopter

5.4 Vector Shift Method Applied to the Simple Manoeuvre Analyzed

According to section 4.5.3 of Chapter 4, for the vector shift method, the distance between the eigenvalues corresponding to uncoupled body motion and the body/disc-tilt motion has to be calculated. For the teetering rotor, the coupled poles are real values. Considering the pole closest to the origin as the body-flap pole and varying the time constant $\tau \in [0.05;0.1;0.2;0.25;0.3]$ one obtains:

$$\left|\frac{\Delta s}{s}\right| = \left|\frac{s^{T}_{bo} - s^{T}_{bo-fl}}{s^{T}_{bo-fl}}\right| \in [\,0.0100;\,0.0202;\,0.0307;\,0.0414;\,0.0523;\,0.0635\,] \tag{5.21}$$

which corresponds to the case of very-light to light coupling according to Table 4.1.

For the semi-rigid rotor, the coupled poles are imaginary values and the vector shift between the body and body-flap mode with the variation of the time constant τ is:

$$\left|\frac{\Delta s}{s}\right| = \frac{\sqrt{\left|\Im(s^{SR}_{bo-fl})^2 - (s^{SR}_{body} - \Re(s^{T}_{bo-fl})^2)\right|}}{\left|s^{T}_{bo-fl}\right|} \in [0.5717;0.8085;0.9902;1.1434;1.2783;1.4] \tag{5.22}$$

All these cases correspond to very heavily coupled body / disc-tilt motion according to Table 4.1.

5.5 General Investigation on the Inclusion of the Disc-Tilt Dynamics in Piloted Simulation Modeling

The present section gives a global approach of the phenomena discussed in section 5.1. Primarily, the present section addresses the rotor disc-tilt dynamics associated with a rigid blade model.

The blade flapping motion, as seen from a frame of reference rotating with the blade, can be divided in three distinct time scales:

- fast motions, corresponding to transients associated with the eigenfrequency of the blade (angular frequency in the order of the rotor rotational frequency);
- intermediate motions, corresponding to the steady state response of the blade to

control inputs and body rotations;
- slow motions, corresponding to the steady state response of the blade to variations in helicopter speed.

In the so-called six degree-of-freedom (6-dof) helicopter models, one concentrates on the intermediate and slow time-scales. This would seem to be obvious at first sight, since these time-scales are clearly relevant for flight dynamics. The fast time-scale blade motions are more relevant for vibration, aero-elastic stability, etc. Accordingly, the fast blade motions are neglected in a 6-dof model and the blade is assumed to respond instantaneously to control inputs, pitching motion and helicopter velocity. This is actually an asymptotic approximation to the complete dynamics of the flapping motion. However, such an approximation may be misleading. Actually, what is important for flight dynamics is the body motion. The blade flapping behaviour should therefore not be considered in the rotating frame of reference, but rather in the non-rotating frame of reference fixed to the body. It is therefore essential to first transform the blade flapping equations to the body frame. This may be done by applying the so-called "Coleman transformation" (see Appendix D, section D.1). The Coleman transformation is a multiblade transformation which also takes into account the summation or cancelling effects due to different blades of the rotor. When the Coleman-transformation is applied, it appears that in general, the transient blade motion splits into three levels: a relatively low-frequency "regressing mode", an intermediate "coning" mode, and a high-frequency "advancing mode".

Under certain circumstances it is therefore conceivable that the regressing mode indeed becomes relevant for flight dynamics, despite the fact that it originates from the fast time-scale motions in the rotating frame. If this happens to be the case, the regressing flapping mode will probably couple to the body motion of the intermediate time scale. For certain types of rotor system this phenomenon of coupling has indeed been observed (see the literature survey on the disc-tilt dynamics of Chapter 3). Recall, that similar couplings might become relevant in the case of higher disc-tilt modes, lead-lag or torsion modes, where they may even be coupled to higher-order body modes.

There are now two questions, to which the remainder of this chapter is devoted:

1 Under what circumstances will it be essential to derive "coupled" body/disc-tilt helicopter models?
2 Is it possible to predict whether blade disc-tilt dynamics should be included in the piloted simulation model using the critical pole distance method?

Concerning the first question, time-domain simulations will be performed in the present section, with fully coupled non-linear body and body/disc-tilt models. First, a general 6-dof non-linear piloted simulation model is developed in Appendix E and used to fly two mission tasks -a deceleration and a side-step manoeuvre- with two helicopters- the Puma SA-330 articulated rotor helicopter and the Bölkow Bö-105 semi-rigid rotor

helicopter of numeric data as given in Appendix E, section E.6. In a typical 6-dof model the helicopter motion is represented by three translations {u, v, w} and three rotations {p,q,,r} around the body axis-system (see Figure E.1 in Appendix E).

The following assumptions are made:

- the helicopter body is modeled by subdividing it into its main components -rotor, fuselage, tailrotor, horizontal stabilizer, vertical fin- and adding the contribution of each part to the general system of forces and moments;

- aerodynamic forces and moments are calculated using the blade element theory;
- the tailrotor is modeled as an actuator disc;
- the fuselage, horizontal tail and vertical tails are modeled with linear aerodynamics;
- rotor disc-tilt dynamics is neglected, and only steady-state rotor disc-tilt motion $\{a_0, a_1, b_1\}$ is considered;
- the dynamic inflow of both rotor and tailrotor are included in the model as state variables and can be described as a "quasi-steady dynamic inflow" by means of the time constants $\tau_{\lambda i}$ and $\tau_{\lambda itr}$ of a value between 0.1 to 0.5 sec. (in the simulations a value of 0.1 was used for both time constants);
- the rotor is modeled with a flapping hinge situated at a distance e_β from the rotor hub;
- the lead-lag motion of the blades is neglected;
- the blades are rectangular;
- there is no pitch-flap or pitch-lag couplings
- there are no tip losses;
- the rotor is placed at the coordinates $\{f, f_1, h\}$ from the helicopter centre of mass;
- gravitational forces are small compared to aerodynamic, inertial and centrifugal forces;
- a linear twist θ_{tw} is applied;
- the helicopter body system of reference {x,y,z} is assumed parallel to the rotor shaft plane;
- the flapping and flow angles are small;
- the rotor angular velocity is constant Ω = const. and is anticlockwise in the case of Bölkow Bö-105 and clockwise in the case of Puma SA-330. Figure E.1 in Appendix E presented the forces and moments on the helicopter components in the case of a anticlockwise rotor. For a clockwise rotor, the tailrotor thrust T_{tr} and lateral force S_{dp} are in the opposite direction
- the longitudinal rotor disc-tilt a_1 is assumed positive when the rotor disc plane tilts backwards;
- the lateral rotor disc-tilt b_1 is assumed positive when the rotor disc plane tilts to the azimuth ψ=90°, this is to the right for an anticlockwise rotor and to the left for a clockwise rotor;

- the longitudinal cyclic θ_{1s} is assumed positive when the pilot moves the stick forward;
- the lateral cyclic θ_{1c} is assumed positive when the pilot moves the stick to the right for an anticlockwise rotor and to the left for a clockwise rotor;
- no reverse flow regions are considered;
- the flow is incompressible;
- the blades have a uniform mass distribution with the mass centre and aerodynamic centre located on the quarter chord line

The free motion of the helicopter in an inertial system of reference is given by the equations of motion (E.1) to (E.14) in Appendix E. To fly the helicopter in the 6-dof model developed, a pilot model had to be implemented by developing four stabilization functions for each helicopter control:

- the collective controls the vertical speed via an "altitude hold controller", feeding back the height to the vertical speed (see (E.59), (E.60));
- the longitudinal cyclic controls the pitch attitude via a "longitudinal position hold controller", feeding back the helicopter's longitudinal position to the pitch angular velocity (see (E.61), (E.62));
- the lateral cyclic controls the roll attitude via a "lateral position hold controller", feeding back the helicopter's lateral position to the roll angular velocity (see (E.63), (E.64));
- the tailrotor collective controls the heading angle (see (E.65)).

The piloted 6-dof simulation model will first be used to fly the two mentioned manoeuvres for both mentioned helicopter types. The 6-dof model will subsequently be extended to the so-called "eight degree-of-freedom model" (8-dof) by including the low frequency regressing flapping mode in the model. In the 6-dof model one takes into account the body motion and of the disc-tilt motion only the steady-state solution. Section D.4 of Appendix D demonstrated that in the 8-dof model, adding the regressing flapping mode to the model is equivalent with considering of the disc-tilt dynamics, only the first-order rotor disc-tilt dynamics added to the body motion. The final equations of motion in an 8-dof model are presented in Appendix E. The two mission tasks are flown again with both helicopters and the effects of first order rotor disc-tilt dynamics on the pilot controls are investigated.

Concerning the second question, the critical pole distance method will be applied using the representation in the complex plane of the body natural modes of motion and the uncoupled disc-tilt dynamics as represented in the non-rotating system by the Coleman transformation. To represent the body natural modes, the non-linear 6-dof model was linearized by assuming as a basic motion a uniform forward flight on a trajectory contained in the longitudinal plane of symmetry and decoupling the longitudinal from the lateral motion. The linearized 6-dof model is presented in Appendix E, section E.4.

5.5.1 Description of the Deceleration and Side-Step Manoeuvres

Description of the Deceleration Manoeuvre The deceleration-to-stop manoeuvre basically has two phases: from horizontal cruising flight at 50 m/s the helicopter has to be slowed down to hover within a distance of 2 km from the starting point over a given point situated on the ground (see Figure 5.12).

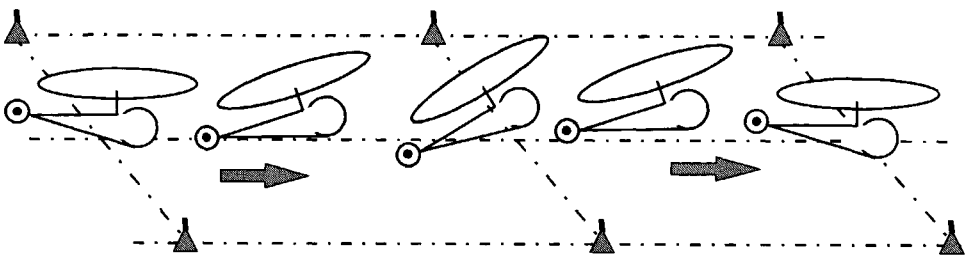

Figure 5.12 Deceleration-to-stop manoeuvre

Description of the Side-Step Manoeuvre The side-step manoeuvre is performed in the lateral plane, as opposed to the deceleration which is executed in the longitudinal plane. The side-step manoeuvre consists of the following stages: starting from hover, an initial abrupt side-step acceleration is carried out. After reaching the maximum allowable lateral speed, an abrupt deceleration back to hover is carried out. After hovering for 5 sec, the manoeuvre is repeated in the opposite direction (see Figure 5.13).

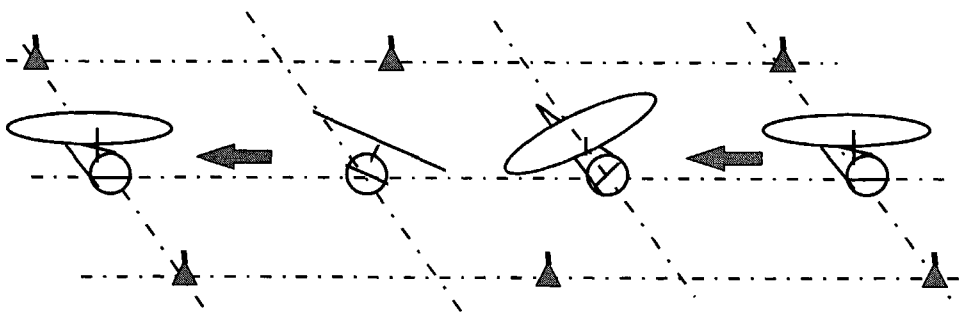

Figure 5.13 Side-step manoeuvre

5.5.2 Deceleration Manoeuvre with the Puma Helicopter in a Six and Eight Degree-of-Freedom Model

The deceleration manoeuvre was simulated with the Puma helicopter, first using the 6-dof non-linear piloted simulation model described in section 5.1 and developed in Appendix E. Figure 5.14 presents the pilot inputs in collective, pedal, longitudinal cyclic and lateral cyclic in this manoeuvre. The deceleration manoeuvre is performed in three phases:

1) forward flight for approximately 2 minutes (110 sec);
2) abrupt deceleration;
3) recovering and transient flight till hover.

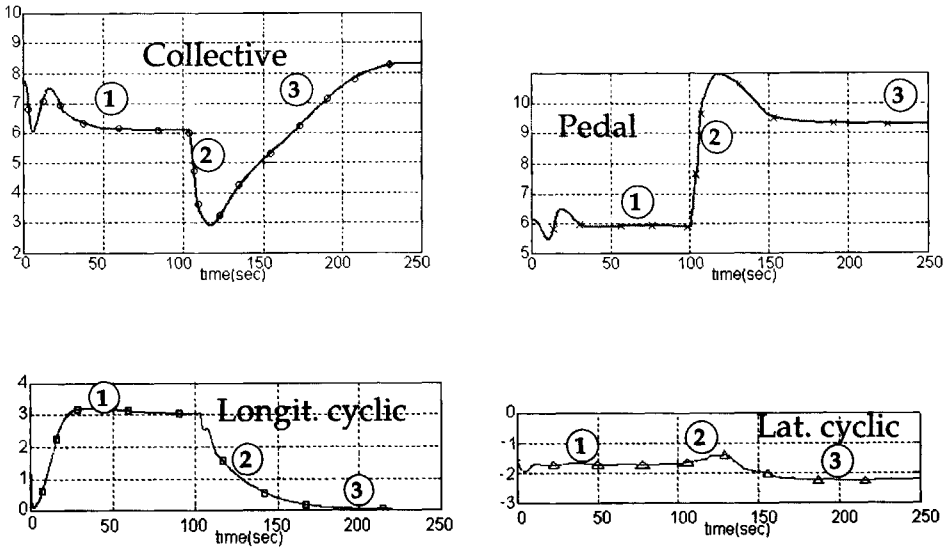

Figure 5.14 Pilot controls in deceleration manoeuvre with Puma SA-330, 6-dof model

The values used for the gains to simulate the deceleration manoeuvre with the Puma in the 6-dof are presented in Table 5.4.

Table 5.4 Gains used in flying the deceleration manoeuvre with Puma, 6-dof model

$K_\Theta = 2.5$	$K_q = 1.0$	$K_{corr\,\Theta} = 0.4$
$K_\Phi = 0.75$	$K_p = -0.57$	$K_{corr\,\Phi} = 0.5$
$K_\Psi = 1.5$	$K_r = -0.57$	$K_{corr\,\Psi} = 1.25$
$K_c = 0.05$		$K_{corr\,c} = 0.05$
$K_x = -0.0005$	$K_u = 0.05$	
$K_y = 0.06$	$K_v = -0.1$	
$K_h = 0.5$		

The following pilot inputs can be read from the graphs:

- With respect to the longitudinal cyclic: 1) the pilot flies straight for the first 110 seconds and 2) then gradually pulls back the stick in order to decelerate to the hover. 3) The rotor disc tilts back, resulting in a tendency of the helicopter to climb. The longitudinal stick variation is closely related to the helicopter pitch attitude;

- With respect to the collective, 2) in the 110th second, the collective is lowered from 7.2 degrees to 3.6 degrees (this is in fact a reaction to the helicopter's climb tendency). 3) After this, the collective is gradually increased to the hover trim position of 8 degrees;
- With respect to the lateral cyclic, 2) some action can be observed after 110 seconds when the stick is moved to the left -this action is simultaneous with a change to the left in the roll angle;
- With respect to the pedal position, 2) lowering the collective in the 110th second requires an input in the right pedal in order to correct the yaw motion. 3) Then, as collective is increased in order to transit to the hover, left pedal is applied.

Subsequently, the deceleration manoeuvre was performed with the 8-dof model. The differences obtained between the results when simulating the Puma with a 6- and 8-dof model are hardly visible. The main differences with the 8-dof model are present in the collective and longitudinal cyclic and are given in Figure 5.15 (the doted line gives the controls in the 6-dof model, the continuous line gives the controls in the 8-dof model). The control gains were not changed in order to simulate this manoeuvre with the extended model, being those given in Table 5.4. This leads to the conclusion that the first order disc-tilt dynamics applied to the Puma helicopter in the deceleration manoeuvre does not influence the pilot's behaviour.

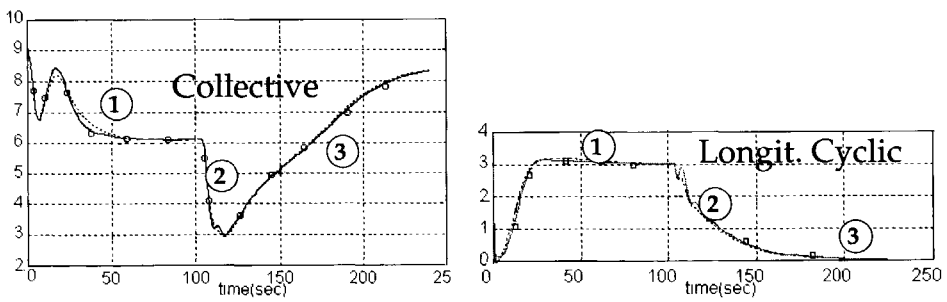

Figure 5.15 Pilot controls in deceleration manoeuvre with Puma SA-330, 8-dof model

5.5.3 Deceleration Manoeuvre with the Bö-105 Helicopter in a Six and Eight Degree-of-Freedom Model

Next, the deceleration manoeuvre was simulated with the Bö-105 hingeless rotor helicopter using the 6-dof non-linear model. The pilot inputs when flying the Bö-105 in the 6-dof model are plotted in Figure 5.16. Generally, the pilot again follows the three phases described in section 5.5.2 for the Puma helicopter. Table 5.5 presents the values used for the control gains in this manoeuvre for the Bö-105.

Table 5.5 Gains used in flying the deceleration manoeuvre with the Bö-105, 6-dof

$K_\Theta = 0.2$	$K_q = 0.5$	$K_{corr\,\Theta} = 0.5$
$K_\Phi = -0.5$	$K_p = -0.05$	$K_{corr\,\Phi} = -0.5$
$K_\Psi = 1.25$	$K_r = 0.75$	$K_{corr\,\Psi} = 1.25$
$K_c = 0.08$		$K_{corr\,c} = 0.1$
$K_x = -0.0075$	$K_u = 0.065$	
$K_y = 0.06$	$K_v = -0.1$	
$K_h = 0.7$		

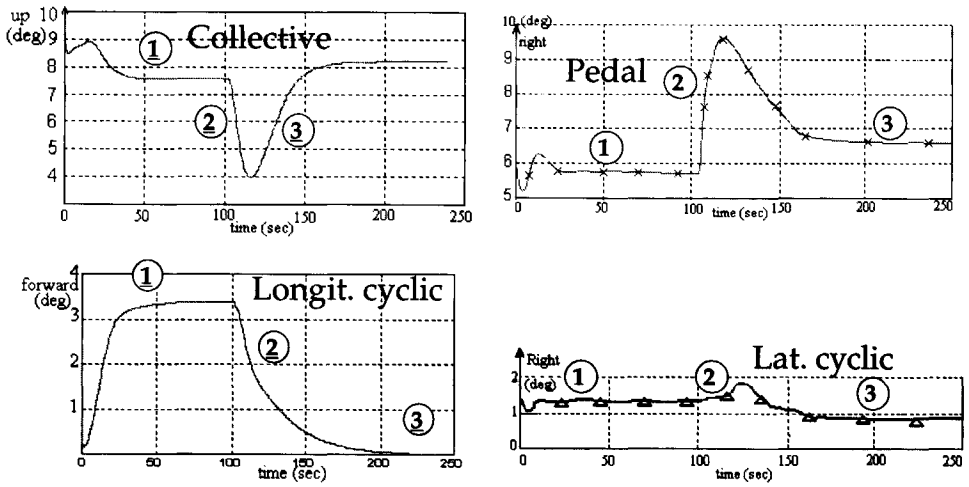

Figure 5.16 Pilot controls in deceleration manoeuvre with Bölkow Bö-105, 6-dof model

From Figure 5.16 one may see that the pilot basically carries out the same actions as in the case of the Puma, of course using corresponding gains. Because the Bö-105 rotor rotates anticlockwise, the lateral cyclic is applied opposite to that of the Puma. Therefore, when flying the deceleration manoeuvre with the Bö-105, the lateral cyclic is applied first to the right and then to the left. The 6-dof model was replaced by the 8-dof model and the deceleration manoeuvre was simulated again. Performing the manoeuvre with the gains as derived in the 6-dof model (Table 5.5) gave different results in pilot actions (as an example, the pilot actions in collective and longitudinal cyclic are presented in the left-hand side of Figure 5.17 for the manoeuvre with an 8-dof model using the gains from the 6-dof model. The dotted lines in this figure are the inputs in the 6-dof model, the continuous lines are the inputs in the 8-dof). The gains were adjusted such as to approach the pilot actions described in the 6-dof model. For this, new gains were chosen in the 8-dof model as presented in Table 5.6. The pilot actions simulated in the 8-dof model using the new gains may be seen for the collective and longitudinal cyclic in the right-hand side of Figure 5.17. Figure 5.18 presents the variation of different flight parameters when simulating the deceleration manoeuvre with three different models: 1) a 6-dof model (dotted lines) 2) an 8-dof model using the gains as in the 6-dof model (continuous lines on the left-hand side of the figure) and 3)

an 8-dof model using the new gains of Table 5.6 (continuous lines on the right-hand side of the figure).

Table 5.6 Gains used in flying the deceleration manoeuvre with Bölkow Bö-105, 8-dof

$K_\Theta = 0.8$	$K_q = 0.8$	$K_{corr\,\Theta} = 0.5$
$K_\Phi = 1.5$	$K_p = -0.5$	$K_{corr\,\Phi} = -0.5$
$K_\Psi = 1.4$	$K_r = -0.5$	$K_{corr\,\Psi} = 1.4$
$K_c = 0.06$		$K_{corr\,c} = 0.1$
$K_x = -0.06$	$K_u = 0.09$	
$K_y = 0.06$	$K_v = 0.022$	
$K_h = 0.015$		

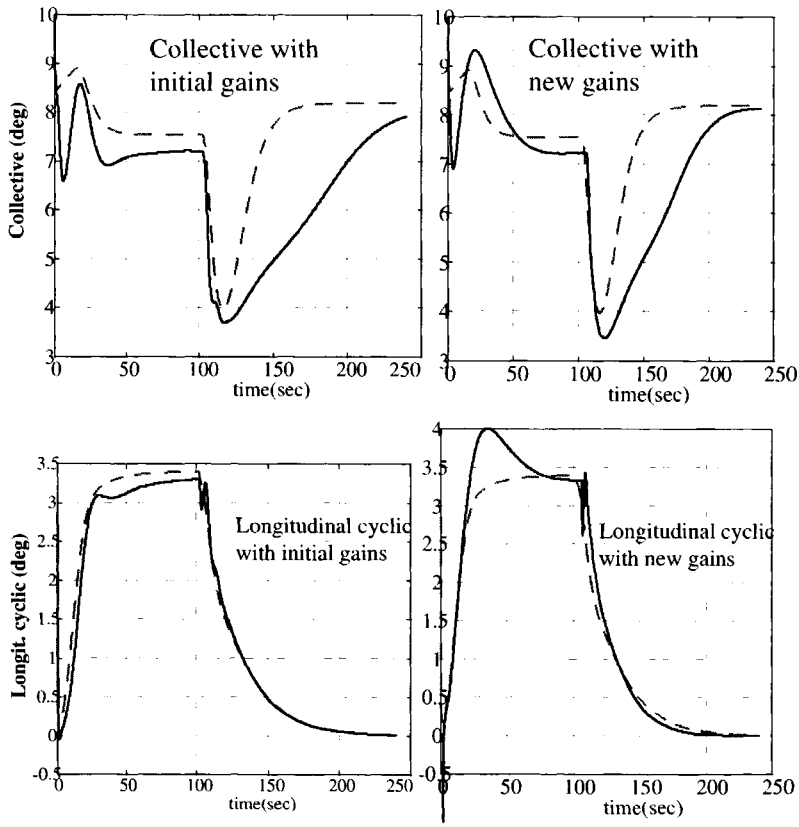

Figure 5.17 Pilot controls in deceleration manoeuvre with Bölkow Bö-105, 8-dof model with original gains and new gains

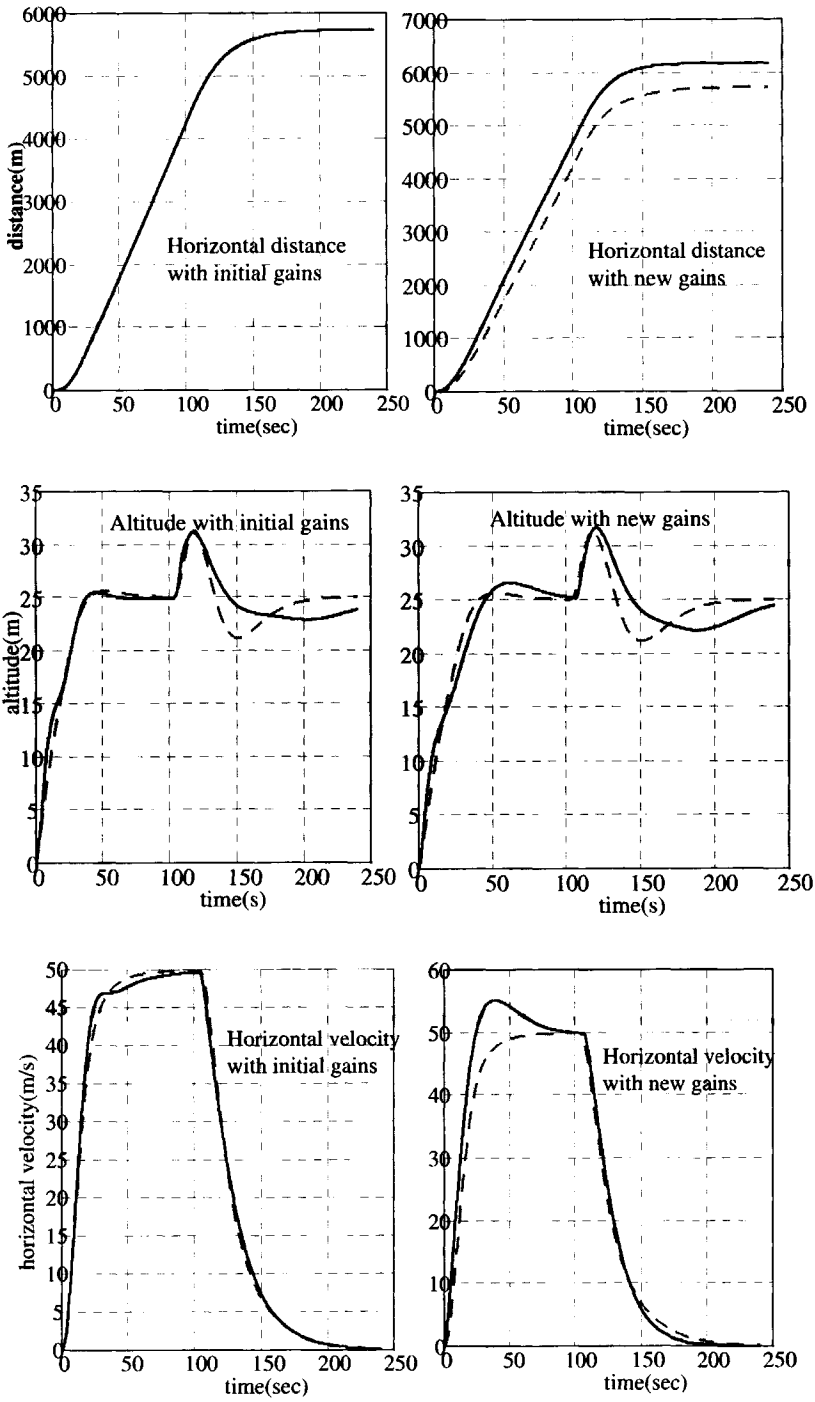
distance(m)
Horizontal distance
with initial gains
time(sec)
Horizontal distance
with new gains
time(sec)
altitude(m)
Altitude with initial gains
time(s)
Altitude with new gains
time(s)
horizontal velocity(m/s)
Horizontal velocity
with initial gains
time(sec)
Horizontal velocity
with new gains
time(sec)

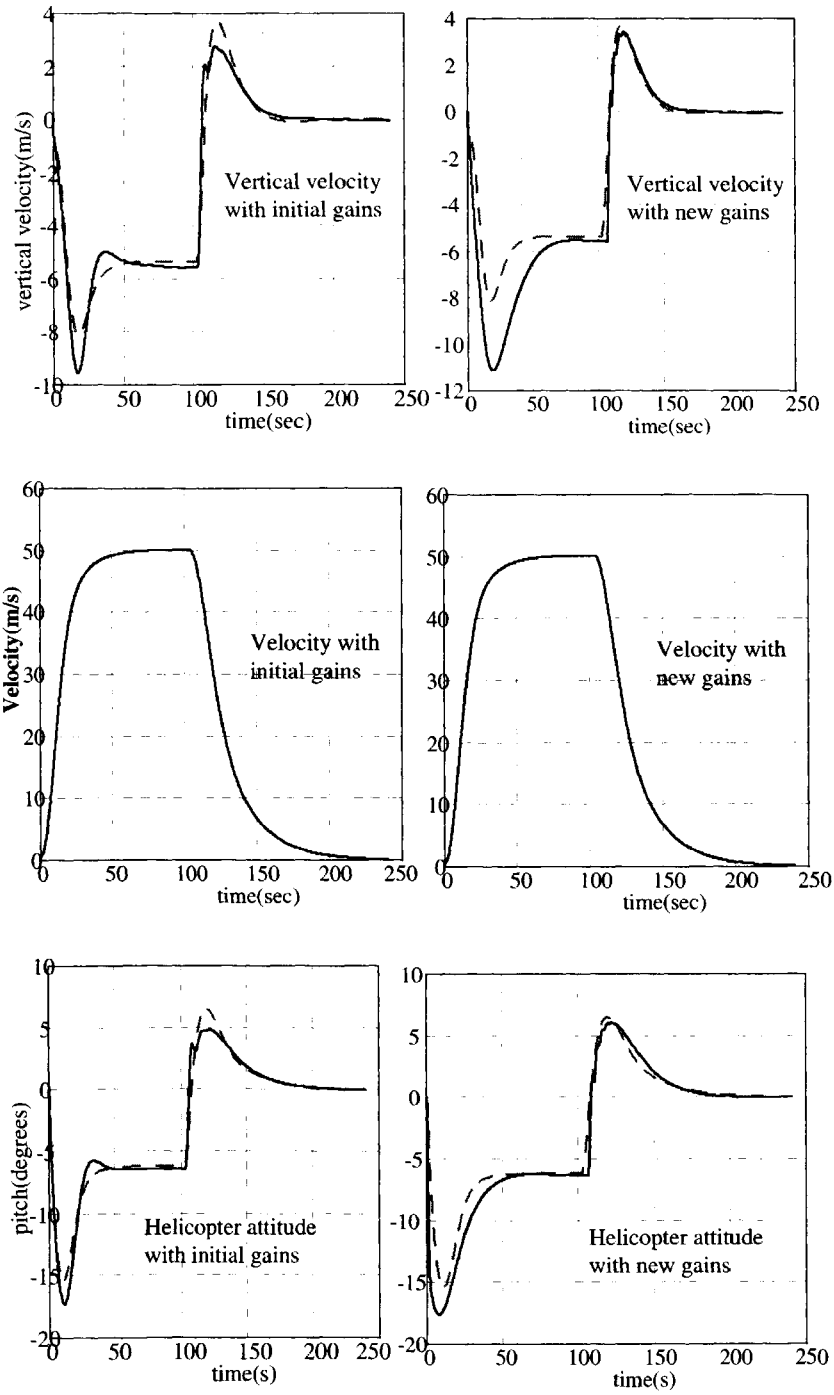
vertical velocity(m/s)
Vertical velocity with initial gains
time(sec)
Vertical velocity with new gains
time(sec)
Velocity(m/s)
Velocity with initial gains
time(sec)
Velocity with new gains
time(sec)
pitch(degrees)
Helicopter attitude with initial gains
time(s)
Helicopter attitude with new gains
time(s)

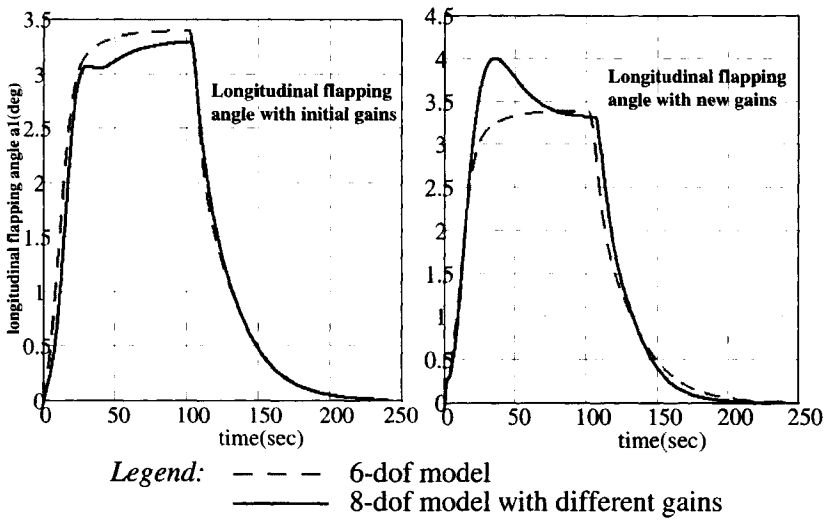

Figure 5.18 Variation of the on-axis response parameters in the deceleration manoeuvre in a 6-dof model, 8-dof with initial gains and 8-dof with new gains

Since the pilot gives inputs with different amplitude when using a 6-dof and an 8-dof model, the conclusion is justified that the rotor disc-tilt dynamics influences the piloted simulation model of the Bö-105 when flying the deceleration manoeuvre. One may expect that a model including the first disc-tilt dynamics is needed in this case, as opposed to the Puma, where disc-tilt dynamics did not influence the pilot gains used in the deceleration manoeuvre.

5.5.4 Side-Step Manoeuvre with the Bö-105 Helicopter in a Six and Eight Degree-of-Freedom Model

The side-step manoeuvre is first performed with the 6-dof model developed in Appendix E for the Bö-105 helicopter. The side-step manoeuvre can be divided in seven phases:

1) hover flight;
2) start of a first abrupt acceleration to the left from hover;
3) after reaching the maximum allowable lateral speed, an abrupt deceleration back to hover;
4) hovering for 5 seconds;
5) a second abrupt acceleration to the right from hover;
6) after reaching the maximum allowable lateral speed, an abrupt deceleration back to hover;
7) hover flight.

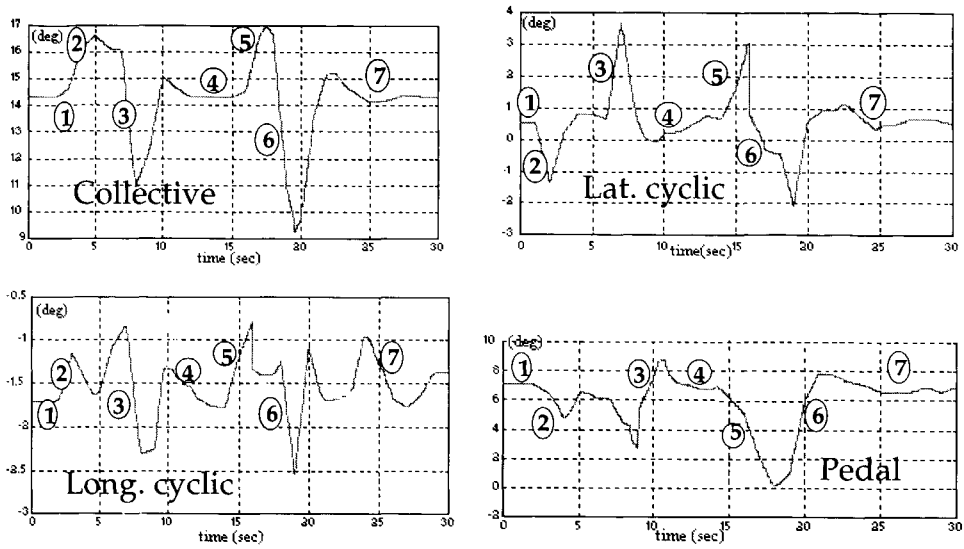

Figure 5.19 Pilot controls in side-step manoeuvre with Bö-105, 6-dof model

Table 5.7 Gains used in side-step manoeuvre with Bö-105, 6-dof model

$K_\Theta = 1.72$	$K_q = + 0.3$	$K_{corr\,\Theta} = 1.43$
$K_\Phi = 1.72$	$K_p = - 0.57$	$K_{corr\,\Phi} = 1.43$
$K_\Psi = 1.72$	$K_r = - 0.57$	$K_{corr\,\Psi} = 1.43$
$K_c = 0.06$		$K_{corr\,c} = 0.05$
$K_x = - 0.06$	$K_u = 0.09$	
$K_y = 0.015$	$K_v = 0.0225$	
$K_h = 0.015$		

Flying the Bö-105 helicopter, the pilot performs the manoeuvre as follows (see Figure 5.19):

- With respect to lateral control, 2) the lateral acceleration is initiated by moving the stick to the left. 3) The acceleration is followed by a deceleration when the pilot moves the stick to the left. 4) After hovering for 5 sec the manoeuvre is repeated in the opposite direction. The amount of lateral stick can be correlated with the roll angle;
- With respect to longitudinal control, 2) the acceleration is initiated by firmly pushing the stick forward and then 4) back in order to hover. 5) In the deceleration phase, the stick is pulled back and then slightly pushed forward for the final hover;
- With respect to the collective: in order to keep the altitude constant, the collective has to be increased first and then constantly adjusted;
- With respect to the pedal: each movement in the collective results in a yawing

motion which is corrected with the pedal.

The gains used to fly this manoeuvre with the 6-dof model are given in Table 5.7.

Next, simulating the side-step manoeuvre with the Bö-105 using the 8-dof model, the gains had to be changed to new values. As an example, the pilot inputs in collective, using new values for the gains, are presented in Figure 5.20 compared to those used in the 6-dof model (the dotted line is the collective in the 6-dof model, the continuous line is the collective in the 8-dof model). The new gains are presented in Table 5.8.

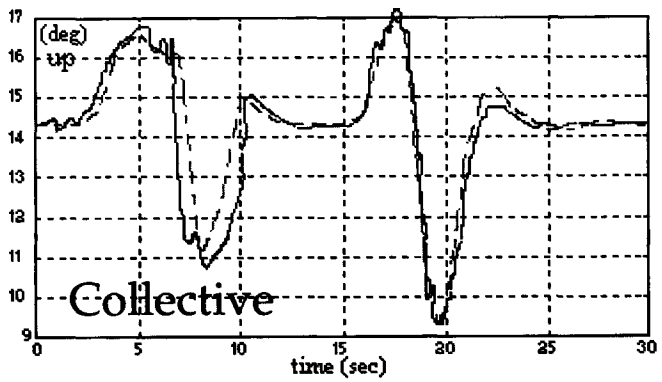

Figure 5.20 Pilot collective in side-step manoeuvre with Bö-105, 8-dof model

Table 5.8 Gains used in side-step manoeuvre with Bö-105, 8-dof model

$K_\Theta = 2.3$	$K_q = +1$	$K_{corr\,\Theta} = 1.43$
$K_\Phi = -0.5$	$K_p = -0.57$	$K_{corr\,\Phi} = 1.43$
$K_\Psi = 1.23$	$K_r = -0.57$	$K_{corr\,\Psi} = 1.43$
$K_c = 0.1$		$K_{corr\,c} = 0.05$
$K_x = -0.06$	$K_u = 0.09$	
$K_y = 0.06$	$K_v = 0.0225$	
$K_h = 0.08$		

Again, the conclusion is justified that the first order disc-tilt dynamics influences the pilot model for the Bö-105 helicopter, both in the side-step manoeuvre as well as in the deceleration manoeuvre.

5.5.5 Side-Step Manoeuvre with the Puma in a Six and Eight Degree-of-Freedom Model

The side-step manoeuvre is next performed with the Puma helicopter, first using the 6-dof model. The pilot inputs in the 6-dof model with the corresponding pilot model can be seen in Figure 5.21 and the gains used to simulate the side-step manoeuvre with the

Puma are given in Table 5.9.

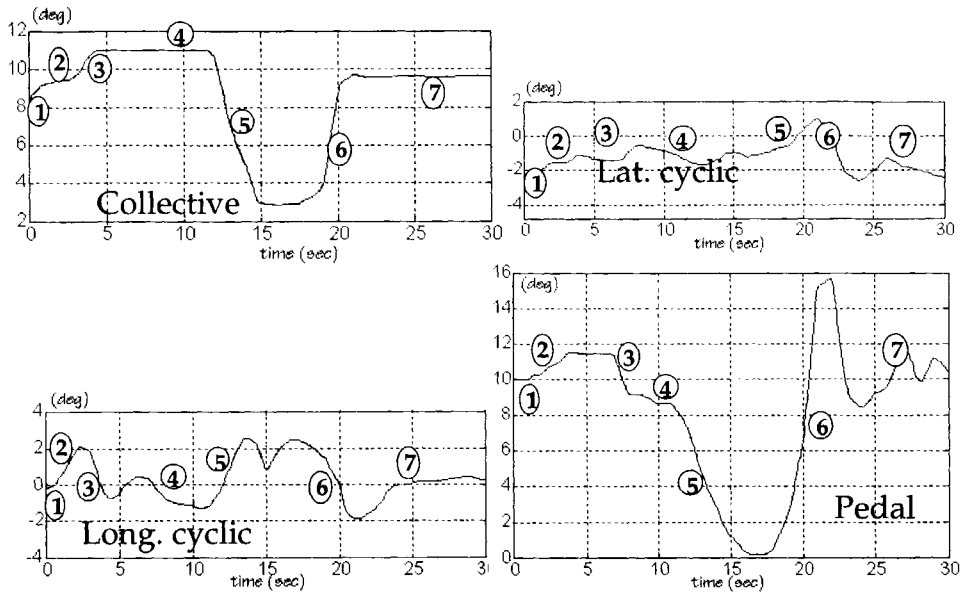

Figure 5.21 Pilot controls in side-step manoeuvre with Puma SA-330, 6-dof model

Table 5.9 Gains used in side-step manoeuvre with Puma SA-330, 6-dof model

$K_\Theta = 1.72$	$K_q = +0.57$	$K_{corr\,\Theta} = 1.43$
$K_\Phi = 1.72$	$K_p = -0.57$	$K_{corr\,\Phi} = 1.43$
$K_\Psi = 1.72$	$K_r = -0.57$	$K_{corr\,\Psi} = 1.43$
$K_c = 0.06$		$K_{corr\,c} = 0.05$
$K_x = -0.06$	$K_u = 0.09$	
$K_y = 0.015$	$K_v = 0.0225$	
$K_h = 0.015$		

The side-step manoeuvre is now simulated using the 8-dof model presented in Appendix E. Keeping the gains equal to that of the 6-dof model, the pilot inputs could not be kept smooth. New values for gains in the 8-dof model were tried. In this context, the pitch controller K_q was changed from the value of +0.57 in the 6-dof model to a value of +0.8 in the 8-dof model. Accordingly, one may conclude that the first-order disc-tilt dynamics influence the way a pilot flies the side-step manoeuvre with the Puma helicopter, in contrast to the deceleration manoeuvre which could be flown using the original gains of the 6-dof model.

Summarizing, the effects of the first-order disc-tilt dynamics on the piloted simulation model in the time-domain were investigated by comparing the pilot inputs in a 6-dof

model and an 8-dof model for two different rotor type helicopters given in Appendix E. The conclusions drawn from the time-domain simulations are:

- flying the deceleration manoeuvre with the Bö-105 semi-rigid rotor helicopter, the regressing flapping mode does influence the pilot simulation model;
- flying the deceleration manoeuvre with the Puma articulated rotor helicopter, the regressing flapping mode does not influence the pilot simulation model;
- flying the side-step manoeuvre with the Bö-105 semi-rigid rotor helicopter, the regressing flapping mode does influence the pilot simulation model;
- flying the side-step manoeuvre with the Puma articulated rotor helicopter, the regressing flapping mode does influence the pilot simulation model.

These results suggest that the low frequency regressing flapping mode should be included in the piloted simulation model when analysing a semi-rigid rotor configuration. When analysing an articulated rotor helicopter, the inclusion of the low frequency regressing flapping mode depends on the manoeuvre analyzed. Therefore, the effects of the disc-tilt dynamics on the piloted simulation depends both on the rotor configuration and on the manoeuvre performed.

5.6 Critical Pole Distance Method Applied to Investigate the Coupling between the Natural Helicopter Motion and the Disc-Tilt Motion

The present section will apply the critical pole distance method in order to investigate if it would have been possible to predict the necessity of the first order disc-tilt dynamics on both helicopter configurations before actually developing the 8-dof model. First, the critical pole distance method will be applied to analyze the natural behaviour of the helicopter, without any pilot model included. Next, the critical pole distance method will be applied to the Puma and the Bö-105 helicopters with the piloted model as described in section 5.1 added to the simulation model.

In order to apply the critical pole distance method, the uncoupled helicopter body and disc-tilt motions have to represented in the complex plane. The representation in the complex plane of the natural motion of the helicopter without any kind of augmentation can be obtained by linearizing the 6-dof non-linear model about a suitable trim condition. Under the assumptions of Appendix E, the common form of the linear 6-dof equations of motion is obtained as:

$$\dot{X} = A \cdot X + B \cdot U \tag{5.23}$$

where A is the matrix of motion derivatives, B is the matrix of control derivatives, X the vector of motion states $X = \left\{ u, v, w, p, q, , r, \Theta, \Phi, \Psi \right\}^T$ and U the vector of control

states $U = \left\{\theta_0, \theta_{1s}, \theta_{1c}, \theta_{0tr}\right\}^T$. The eigenvalues of matrix A, defining the natural eigenvalues of the body corresponding to the natural modes of motion, can be seen in Figure 5.22 and Figure 5.23 for the articulated Puma SA-330 respectively the semi-rigid Bölkow Bö-105 (in these figures the root locus of the body eigenfrequencies as a function of the advance ratio was represented by going from hover to forward flight at advance ratio $\mu = 0.35$).

Looking at these figures, one should realize that an articulated configuration behaves differently from a semi-rigid rotor. The eigenvalues of the Puma articulated helicopter are more classical in the sense that they are very similar to a fixed-wing aircraft: the longitudinal eigenvalues consist of two complex roots corresponding to the unstable phugoid and the stable oscillatory pitch short period mode; the lateral eigenvalues consist of five roots, of which one is always zero, two are real negative and two form a complex conjugate pair corresponding to the stable Dutch roll mode. In comparison to this, the short period mode of the Bö-105 is not oscillatory. The longitudinal eigenvalues of the Bö-105 consist of two complex eigenvalues corresponding to the unstable phugoid mode and two real negative roots (only at high advance ratios are the roots are complex conjugate); the lateral eigenvalues have the same character as those of the Puma: one zero root, two real negative roots and the complex pair of the Dutch roll mode. The non-oscillatory nature of the short period mode is in general a characteristic of hingeless rotors and arises from the positive contribution of the hub moment to the M_w derivative (derivative of pitch moment w.r.t a perturbation in the vertical velocity w) which always results in a positive value for M_w changing this mode from an oscillatory one into a real one.

The uncoupled blade flapping equation of motion as seen in a frame of reference rotating with the blade, was derived in Appendix B assuming the blade as rigid and modeling the flexibility by an offset flapping hinge with spring restraint. The equation of motion can be transformed to the non-rotating system using the Coleman transformation as presented in Appendix D. The equations of the rotor disc-tilt dynamics are given by (D.24). These equations contain the advancing and the regressing flapping modes and can be represented in the complex plane.
With these preparations, the relative position in the complex plane of the uncoupled body and disc-tilt eigenvalues can be compared. Figure 5.22 and Figure 5.23 represent the variation of the relative position of the uncoupled disc-tilt and body poles when the advance ratio varies between hover and $\mu = 0.35$ forward flight. Looking at these figures one may see that the closest distance between the disc-tilt and body modes is between:

1 the short-period mode and the regressing flapping mode;
2 the roll-subsidence and the regressing flapping mode.

The advancing flapping mode is located far from the body modes, whereas the coning and differential mode do not enter into the discussion, being highly damped modes.

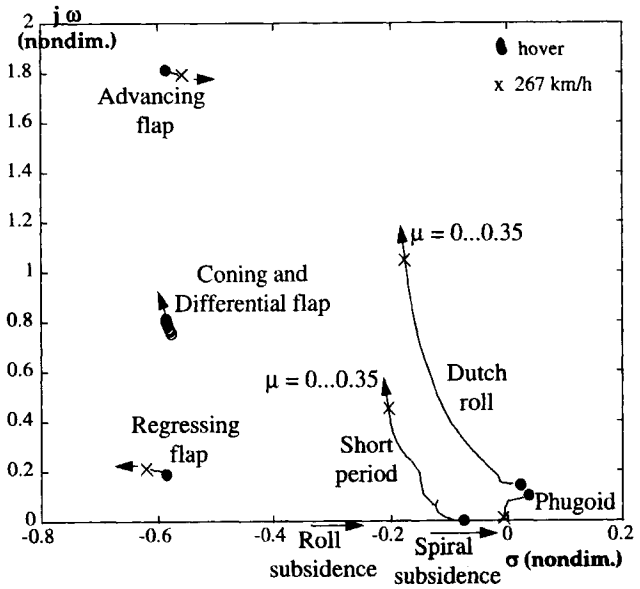

Figure 5.22 Relative position of body and disc-tilt modes for Puma articulated helicopter

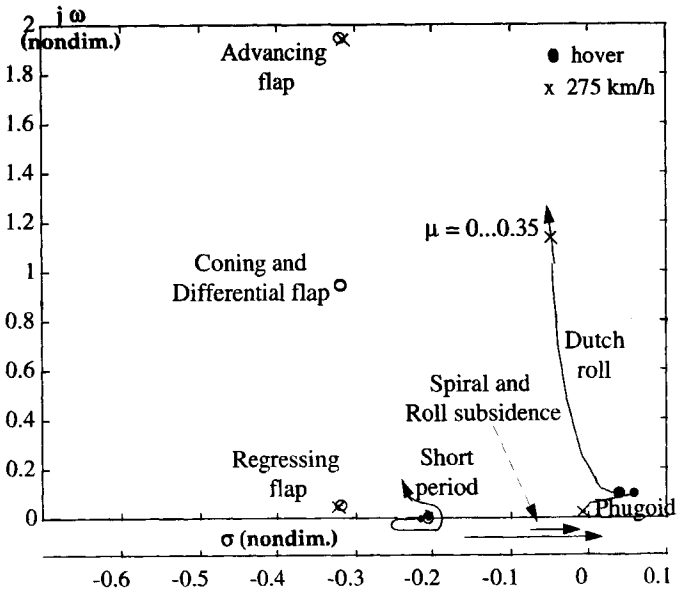

Figure 5.23 Relative position of body and disc-tilt modes for Bö-105 hingeless helicopter

5.6.1 Investigations on the Body Short-Period Mode and Regressing Flapping Mode Coupling

Concerning the position between the short-period and regressing flapping modes, comparing Figure 5.22 and Figure 5.23, it seems that in the case of the Bö-105, the regressing flapping mode is much closer to the short-period mode than in the case of the Puma. Therefore, it is likely that the regressive flapping mode couples to the short-period mode in the case of semi-rigid rotor systems, but it cannot be excluded that this coupling is of importance also for the articulated configuration.

Next consider the critical pole distance criterion (4.43) deduced in Chapter 4, with respect to the condition of coupling between two degrees of freedom which are "close" as represented in the complex plane. The critical pole distance criterion will first be applied to investigate the short-period mode and regressing flapping mode coupling. The critical pole distance criterion (4.43) can be written in this case as:

$$\left|N_{Freg}\, N_{SP}\right| = \sqrt{16\,\xi_{Freg}^2\,\xi_{SP}^2\,\omega_{Freg}^6\,\omega_{SP}^2 + 4\,\xi_{Freg}^2\,\omega_{Freg}^4\left(\omega_{SP}^2 - \omega_{Freg}^2\right)^2} \quad \text{is large} \tag{5.24}$$

The eigenvalues of the body short-period mode were calculated using the 6-dof linear model and are indicated by s_{SP}. It can be verified that these eigenvalues may be well approximated by solving the equation (**Padfield** [1996][81]):

$$s^2 - \left(z_w + m_q\right)s + z_w\, m_q - \mu\, m_w = 0 \tag{5.25}$$

where z_w, m_q and m_w are non-dimensional derivatives of the helicopter forces and moments w.r.t the body velocities. Expressing s_{SP} as (2.7), the short-period damping ratio and the natural frequency of this mode can be obtained as:

$$\omega_{SP} = |s_{SP}| \;;\quad \xi_{SP} = -\frac{|\mathrm{Re}(s_{SP})|}{|s_{SP}|} \;;\quad |s_{SP}| = \sqrt{\mathrm{Re}(s_{SP})^2 + \mathrm{Im}(s_{SP})^2} \tag{5.26}$$

or equivalently using (5.25), (5.35):

$$\omega_{SP}^2 = z_w\, m_q - \mu\, m_w \quad ;\quad \xi_{SP} = -\frac{1}{2\,\omega_{SP}}\left(z_w + m_q\right) \tag{5.27}$$

Considering different advance ratios, these characteristics were calculated both for the

Puma and the Bö-105 helicopters. The results are summarized in Table 5.10.

Table 5.10 Body short-period characteristics for Puma SA-330 and Bö-105

Helicopter velocity forward flight Puma	*0 m/s*	*14.85 m/s*	*29.7 m/s*	*52 m/s*	*74 m/s*
ω_{SP} *(nondim.) Puma*	*0.105128*	*0.178*	*0.28574*	*0.371057*	*0.497419*
ξ_{SP} *(nondim.)Puma*	*1.06194*	*0.80226*	*0.5648923*	*0.5115577*	*0.4112079*
Helicopter velocity forward flight Bö-105	*0 m/s*	*10.25 m/s*	*30.75 m/s*	*51 m/s*	*74 m/s*
ω_{SP} *(nondim.) Bö-105*	*0.1247056*	*0.1362865*	*0.1877294*	*0.2036588*	*0.230878*
ξ_{SP} *(nondim.) Bö-105*	*1.129565*	*1.1730278*	*1.00088534*	*0.99194742*	*0.972619*

The regressing flapping mode can usually be approximated by (D.26) as demonstrated in Appendix D. From (D.26) the regressive flapping mode characteristics are deduced as:

$$\omega^2_{F\,reg} = \frac{\left(1 - \nu_\beta^2\right)^2 + \frac{\gamma^2}{64}\left(1 - \frac{\mu^4}{4}\right)}{\left(4 + \frac{\gamma^2}{64}\right)} \quad ; \quad \xi_{F\,reg} = \frac{1}{2\,\omega_{Freg}} \frac{\frac{\gamma}{4}\left(1 + \nu_\beta^2\right)}{\left(4 + \frac{\gamma^2}{64}\right)} \tag{5.28}$$

and for different advance ratios their values are summarized in Table 5.11.

Table 5.11 Regressing flapping mode characteristics for Puma SA-330 and Bö-105

Helicopter velocity forward flight Puma	*0 m/s*	*14.85 m/s*	*29.7 m/s*	*52 m/s*	*74 m/s*
ω_{Freg} *(nondim.) Puma*	*0.5074*	*0.5074*	*0.5074*	*0.5072*	*0.5065*
ξ_{Freg} *(nondim.) Puma*	*0.9037*	*0.9036*	*0.9036*	*0.904*	*0.9053*
Helicopter velocity forward flight Bö-105	*0 m/s*	*10.25 m/s*	*30.75 m/s*	*51 m/s*	*74 m/s*
ω_{Freg} *(nondim.) Bö-105*	*0.3856*	*0.3856*	*0.3856*	*0.3856*	*0.3856*
ξ_{Freg} *(nondim) Bö-105*	*0.9362*	*0.9362*	*0.9362*	*0.9362*	*0.9362*

The values of the critical pole distance criterion (5.24) were calculated for different

advance ratios and are summarized in Table 5.12.

Table 5.12 Critical pole distance criterion applied to body short-period/regressing flapping modes for Puma SA-330 and Bö-105

Helicopter velocity forward flight Puma	*0 m/s*	*10.25 m/s*	*30.75 m/s*	*51 m/s*	*74 m/s*
$\lvert N_{Freg} N_{SP} \rvert$ *Puma*	*0.1262*	*0.1248*	*0.1118*	*0.1054*	*0.0963*
Helicopter velocity forward flight Bö-105	*0 m/s*	*10.25 m/s*	*30.75 m/s*	*51 m/s*	*74 m/s*
$\lvert N_{Freg} N_{SP} \rvert$ *Bö-105*	*0.0478*	*0.0499*	*0.0512*	*0.0527*	*0.0551*

Looking at the values of the product $|N_{Freg} N_{SP}|$ (non-dimensional) it can be seen that whereas the Puma helicopter is characterized by values in excess of 0.1, the Bö-105 is characterized by values smaller than 0.1. Based on the results of the simulations with a coupled model the critical pole distance criterion for the coupling between the short-period and regressing flapping mode may be stated as: for values of $|N_{Freg} N_{SP}| > 0.1$ the body short-period mode decouples from the regressing flapping mode.

5.6.2 Discussion on the Time Constants of Body Short-Period and Regressing Flapping Modes

The time constant of the short-period answer is, according to (2.21):

$$\tau_{SP} = - \bar{t} / \text{Real}(s_{SP\,1,2}) \quad (\text{sec}) \tag{5.29}$$

where $s_{SP\,1,2}$ are the non-dimensional real or complex conjugate roots of the stable short-period mode and $\bar{t}$ is used to non-dimensionalize the time variable in the 6 degree of freedom model and is defined as $\bar{t} = \frac{M_{hel}}{\rho A \Omega R}$. The short-period time constant was calculated using the non-dimensional eigenvalues of the short period mode as resulted from the 6-dof body model. When the eigenvalues of the short period mode are real values, the time constant of the dominating pole, i.e., the pole closest to the origin are considered. The results are presented in Table 5.13.

For the uncoupled disc-tilt motion, the time constant of the regressing flapping mode

can be calculated looking at (D.15) and (2.22):

$$\tau_{Freg} = -\ 1 / \text{Real}\left(s_{Freg\ 1,2}\right) / \Omega = (16/\gamma)/\Omega \quad (\text{sec}) \tag{5.30}$$

where $s_{reg\ 1,2}$ are the eigenvalues of regressing flapping mode. One may observe that using (D.26) the time constant does not depend on the advance ratio and is determined only by the Lock number. The time constant of the uncoupled disc-tilt motion according to (5.30) is:

$$\begin{aligned} \tau_{Freg} &= 0.06 \quad \text{sec} \qquad \text{Puma} \\ \tau_{Freg} &= 0.07 \quad \text{sec} \qquad \text{Bö -105} \end{aligned} \tag{5.31}$$

Table 5.13 Short-period mode characteristics for Puma SA-330 and Bö-105

Helicopter velocity forward flight Puma	*0 m/s*	*14.85 m/s*	*29.7 m/s*	*52 m/s*	*74 m/s*
Short Period Root Puma (nondim.)	*- 0.0741*	*-0.1428 ± 0.1062 i*	*- 0.16141 ± 0.2357 i*	*- 0.1898 ± 0.31883 i*	*-0.20454 ± 0.4534 i*
Time constant Puma (sec)	*1.707*	*0.885*	*0.784*	*0.665*	*0.617*
τ_{Freg} / τ_{SP} Puma	*0.035*	*0.067*	*0.0765*	*0.09*	*0.097*
Helicopter velocity forward flight Bö-105	*0 m/s*	*10.25 m/s*	*30.75 m/s*	*51 m/s*	*74 m/s*
Short period root Bö-105 (nondim.)	*- 0.0753*	*- 0.0763*	*- 0.1801*	*-0.2020 ± 0.0258 i*	*- 0.2245 ± 0.05365 i*
Time constant Bö-105 (sec)	*1.375*	*1.357*	*0.575*	*0.513*	*0.461*
τ_{Freg} / τ_{SP} Bö-105	*0.0515*	*0.052*	*0.123*	*0.138*	*0.153*

Comparing the ratio τ_{Freg}/τ_{SP} of the time constants of the regressing flapping mode and the body short-period mode as given in Table 5.13 one can see that whereas for the Puma helicopter $\tau_{Freg}/\tau_{SP} \ll 1$ throughout the entire advance ratio envelope, for the Bö-105 helicopter, the disc-tilt and body short period time constants stay much closer to each other, especially at high advance ratios. This may indicate that the regressing flapping mode couples to the short-period mode in case of the semi-rigid Bö-105 helicopter.

5.6.3 Investigations on the Roll-Subsidence and Regressing Flapping Modes Coupling

The critical pole distance criterion will next be applied to the roll-subsidence and regressing flapping modes coupling. The roll-subsidence is a real root and according to (4.44) the critical pole distance criterion becomes:

$$\left|N_{Freg}\ N_{Roll}\right| = \left(\left| \omega_{Roll}^4 \xi_{Roll}^4 + \omega_{Roll}^2 \xi_{Roll}^2 \left(\omega_{Freg}^2 + \omega_{Roll}^2\right) + \omega_{Freg}\omega_{Roll}\left(\omega_{Freg}\omega_{Roll} + 4\,\omega_{Roll}^2 \xi_{Roll}^3 \xi_{Freg}\right) - \right.\right.$$
$$\left.\left. -2\,\omega_{Roll}^3 \xi_{Roll}^3 \left(\omega_{Freg}\xi_{Freg} + \omega_{Roll}\xi_{Roll}\right) - 2\,\omega_{Freg}\omega_{Roll}^2 \xi_{Roll}\left(\xi_{Freg} + \xi_{Roll}\right) \right| \right)^{1/2} \text{ is large} \tag{5.32}$$

One needs to determine the damping ratio ξ_{Roll} and the natural frequency ω_{Roll} in order to apply the criterion (5.32). For this, observe that the characteristic equation of body lateral motion is an equation of fourth order. Solving this equation two real roots are obtained corresponding to the roll-subsidence and spiral-subsidence modes and two complex roots corresponding to the Dutch roll mode. It follows that by grouping the roll-subsidence eigenvalue s_{Roll} and the spiral-subsidence eigenvalue s_{Spi} together in the characteristic equation, a second order equation is obtained which can express the uncoupled characteristics N_i (4.3) in the critical pole distance criterion:

$$\left(s - s_{Roll}\right)\cdot\left(s - s_{Spi}\right) = 0 \tag{5.33}$$

From (5.33), the expressions of the damping ratio ξ_{Roll} and the natural frequency ω_{Roll} needed in the critical pole distance criterion (5.32) may be expressed as:

$$\omega_{Roll} = \sqrt{s_{Roll}\cdot s_{Spi}} \quad ; \quad \xi_{Roll} = -\frac{s_{Roll} + s_{Spi}}{2\,\omega_{Roll}} \tag{5.34}$$

The eigenvalues of the body roll-subsidence mode s_{Roll} and spiral-subsidence mode s_{Spi} were calculated as a function of advance ratio using the 6-dof linear model from Appendix E, section E.4 and are presented in Table 5.14.

These eigenvalues are good approximated according to **Padfield** [1996][81] by the following expressions:

$$s_{Roll} = l_p \quad ; \quad s_{Spi} = \frac{C_G}{l_p}\cdot\frac{l_v n_r - n_v l_r}{\mu\, n_v + l_v\left(C_G - \mu\, n_p\right)/\, l_p} \tag{5.35}$$

where l_p l_v, l_r n_v, and n_p are non-dimensional derivatives of the helicopter forces and

moments w.r.t the body velocities and angular rates and C_G is the helicopter weight coefficient defined as $C_G = \dfrac{M_{hel}\, g}{\rho A(\Omega^2 R^2)}$.

Table 5.14 Body roll- and spiral-subsidence eigenvalues for Puma SA-330 and Bö-105

Helicopter velocity forward flight Puma	*0 m/s*	*14.85 m/s*	*29.7 m/s*	*52 m/s*	*74 m/s*
s_{Roll} *(nondim.) Puma*	*- 0.317805*	*- 0.3201009*	*- 0.3312707*	*- 0.3228592*	*- 0.2741088*
s_{Spi} *(nondim.) Puma*	*- 0.088029*	*- 0.0203606*	*- 0.0057172*	*- 0.0005374*	*+ 0.004389*
Helicopter velocity forward flight Bö-105	*0 m/s*	*15.26 m/s*	*30.5 m/s*	*54.5 m/s*	*76.3 m/s*
s_{Roll} *(nondim.)Bö-105*	*- 0.1498359*	*- 0.127955*	*- 0.1354727*	*- 0.1037327*	*+ 0.031756*
s_{Spi} *(nondim.)Bö-105*	*- 0.01757877*	*- 0.0025361*	*- 0.0003763*	*+ 0.005921*	*- 0.020055*

Using the values of Table 5.14, the characteristics of the roll-subsidence mode as given by (5.34) for the Puma SA-330 and Bö-105 helicopters were calculated and are summarized in Table 5.15.

Table 5.15 Body roll-subsidence characteristics for Puma SA-330 and Bö-105

Helicopter velocity forward flight Puma	*0 m/s*	*14.85 m/s*	*29.7 m/s*	*52 m/s*	*74 m/s*
ω_{Roll} *(nondim.) Puma*	*0.16726*	*0.0807307*	*0.043519*	*0.0132*	*unstable*
ξ_{Roll} *(nondim.) Puma*	*1.213178*	*2.1086239*	*3.8717064*	*12.2499*	*unstable*
Helicopter velocity forward flight Bö-105	*0 m/s*	*15.26 m/s*	*30.5 m/s*	*54.5 m/s*	*76.3 m/s*
ω_{Roll} *(nondim.)Bö-105*	*0.05132185*	*0.0180144*	*0.00712*	*unstable*	*unstable*
ξ_{Roll} *(nondim.)Bö-105*	*1.6310276*	*3.62185446*	*9.5331*	*unstable*	*unstable*

The values of the product $|N_{Freg} N_{Roll}|$ in the critical pole distance criterion (5.32) applied to the two helicopters, for different advance ratios, are presented in Table 5.16.

Analysing the product $|N_{Freg} N_{Roll}|$ (non-dimensional) from these tables on the basis of the simulations with a coupled model one can conclude that as was the case for the short-period and regressing flapping modes coupling, the roll-subsidence and regressing flapping modes coupling is also characterized by values in excess of 0.1 for the Puma

SA-330 helicopter and values much smaller than 0.1 for the Bö-105 helicopter.

Table 5.16 Critical pole distance criterion for body roll-subsidence and regressing flapping modes coupling applied to Puma SA-330 and Bö-105

Helicopter velocity forward flight Puma	*0 m/s*	*14.85 m/s*	*29.7 m/s*	*52 m/s*	*74 m/s*
$\lvert N_{Freg}\ N_{Roll} \rvert$ *Puma*	*0.2191*	*0.1703*	*0.1553*	*0.1361*	-
Helicopter velocity forward flight Bö-105	*0 m/s*	*15.26 m/s*	*30.5 m/s*	*54.5 m/s*	*76.3 m/s*
$\lvert N_{Freg}\ N_{Roll} \rvert$ *Bö-105*	*0.08173*	*0.0572*	*0.0548*	-	-

The critical pole distance criterion in this case can be stated as $|N_{Freg}\ N_{Roll}| > 0.1$ is sufficiently large to consider the roll-subsidence mode decoupled from the regressing flapping mode. Note that this conclusion is valid only when the natural behaviour of the helicopters is investigated.

5.6.4 Discussion on the Time constants associated with the Roll-Subsidence and Regressing Flapping Mode

Regarding the relative position between the roll-subsidence and regressing flapping modes, the time constants associated with the roll subsidence for the eigenvalues obtained from the 6-dof model can be calculated from (2.21) as:

$$\tau_{Roll} = -\ \bar{t}\ /\ \mathrm{Real}\left(s_{Roll\ 1,2}\right) \tag{5.36}$$

where s_{Roll} are the non-dimensional roll subsidence eigenvalues as obtained from the 6-dof linear model (the eigenvalues are negative real roots) and $\bar{t}$ is used to non-dimensionalize the time variable in the 6 degree of freedom model and is defined as $\bar{t} = \dfrac{M_{hel}}{\rho A \Omega R}$. The roll-subsidence time constant was calculated for different advance ratios and is presented in Table 5.17.

Comparing the ratio τ_{Freg}/τ_{SP} of the time constants of the regressing flapping mode and the body roll-subsidence mode as given in Table 5.17 one may see that for the Puma helicopter throughout the entire advance ratio envelope the disc-tilt and body roll subsidence time constants stay closer to each other than in the case of Bö-105 helicopter. This may indicate that the regressing flapping mode couples to the roll subsidence mode in case of the semi-rigid Puma helicopter.

Table 5.17 Roll-subsidence characteristics for Puma SA-330 and Bö-105

Helicopter velocity forward flight Puma	*0 m/s*	*14.85 m/s*	*29.7 m/s*	*52 m/s*	*74 m/s*
Roll Subsidence Puma (nondim.)	*- 0.3178*	*-0.3201*	*- 0.33127*	*- 0.32286*	*- 0.2741*
Time constant Puma (sec)	*0.397*	*0.395*	*0.38*	*0.39*	*0.46*
τ_{Freg} / τ_{Roll} *Puma*	*0.15*	*0.15*	*0.157*	*0.153*	*0.13*
Helicopter velocity forward flight Bö-105	*0 m/s*	*15.26 m/s*	*30.5 m/s*	*54.5 m/s*	*76.3 m/s*
Roll Subsidence	*- 0.1498*	*- 0.12795*	*- 0.13547*	*-0.10373*	*+0.03175*
Time constant Bö-105 (sec)	*6.674*	*7.815*	*7.38*	*9.64*	-
τ_{Freg} / τ_{Roll} *Bö-105*	*0.102*	*0.087*	*0.093*	*0.071*	-

5.7 Critical Pole Distance Method Applied to the Helicopter with Pilot Model

When the pilot model described in section 5.1 is used, the matrix U of controls in (5.23) can be written as:

$$U = K \cdot X \tag{5.37}$$

where K is the matrix containing the gains used in the pilot model to stabilize the motion in the longitudinal and lateral plane. Substituting (5.37) into (5.23), the 6-dof linear piloted simulation model becomes:

$$\dot{X} = (A + B\,K) \cdot X \tag{5.38}$$

The short-period mode can be approximated in this case as:

$$s^2 - \left(z_w + m_q + \frac{K_q}{\bar{t}}\, m_{\theta_{ls}}\right)s + z_w m_q - \mu\, m_w + \frac{K_q}{\bar{t}}\left(m_{\theta_{ls}} z_w - m_w z_{\theta_{ls}}\right) = 0 \tag{5.39}$$

It may be observed that the short-period eigenvalues are influenced by the K_q gain. The

characteristics in frequency and damping of the short period mode become:

$$\omega_{SP}^2 = z_w m_q - \mu m_w + \frac{K_q}{\bar{t}}\left(m_{\theta_{ts}} z_w - m_w z_{\theta_{ts}}\right) \quad ; \quad \xi_{SP} = -\frac{1}{2\,\omega_{SP}}\left(z_w + m_q + \frac{K_q}{\bar{t}}\, m_{\theta_{ts}}\right) \qquad (5.40)$$

The critical pole distance criterion expressed by (5.24) in this case has to consider relations (5.40) for the short period-mode, whereas the regressing flapping characteristics are unchanged and given by (5.28).

The critical pole distance criterion will be applied to investigate the way in which the body short-period motion couples to the regressing flapping mode when simulating the deceleration and side-step manoeuvres using the gains as obtained in sections 5.5.2 to 5.5.5. To this end, the uncoupled body and disc-tilt motion need to be represented in the complex plane, this time including the pilot model.

5.7.1 Investigations on the Body Short-Period Mode and Regressing Flapping Mode Coupling in the Deceleration Manoeuvre

In section 5.5.2 it was shown that the decelerating manoeuvre with the Puma does not require a change in the gains when extending a 6-dof model to a 8-dof model. In contrast, section 5.5.3 concluded that the decelerating manoeuvre performed with the Bö-105 does require such a change in the gains.

Figure 5.24 gives the representation in the complex plane for the Puma helicopter in the region of the short-period and regressing flapping mode coupling using a gain $K_q = 1$ as in the deceleration. The poles are represented for different advance ratios, the case of velocity 50 m/s (point 4) corresponding to the deceleration manoeuvre. The short-period mode without pilot model was also represented in order to observe how this mode changes when the pilot model is included. It may be seen that using a pilot model which stabilizes the longitudinal motion around the pitch axis, transforms the oscillatory short-period mode into two real roots.

Figure 5.25 gives the representation in the complex plane for the Bö-105 in the region of the short-period mode and regressing flapping mode coupling using a gain $K_q = 0.5$ as in the 6-dof model and $K_q = 0.8$ as in the 8-dof model. Again, the case of velocity 50 m/s (point 4) corresponds to the deceleration manoeuvre. In this case, the oscillatory short-period mode is represented by two real roots at velocities up to 30 m/s (point 3), while being oscillatory at higher velocities. In the 8-dof model, changing the value of K_q increases the damping in flapping.

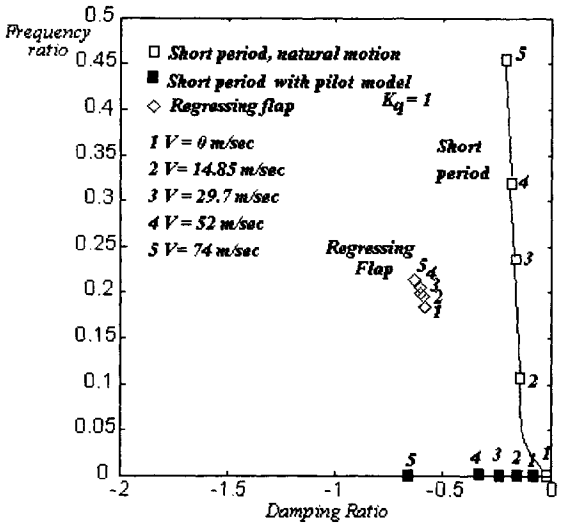

Figure 5.24 Short period and regressing flapping for deceleration manoeuvre: Puma

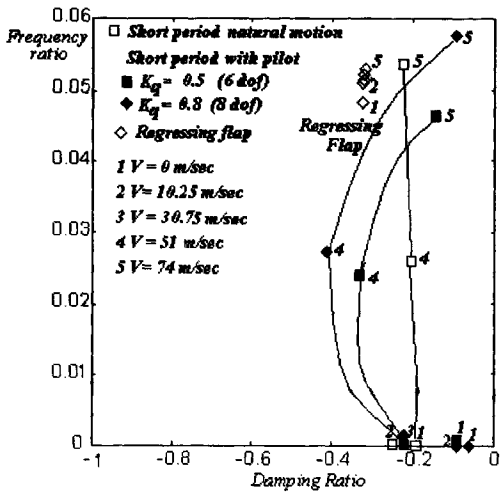

Figure 5.25 Short period and regressing flapping for deceleration manoeuvre: Bö-105

The critical pole distance criterion (5.24) was applied using the gains characteristic to the deceleration manoeuvre. The results for the two analyzed helicopters are presented in Table 5.18.

Table 5.18 Critical pole distance criterion for body/disc-tilt coupling for Puma SA-330 and Bö-105 in 6- and 8-dof piloted simulation models. Deceleration Manoeuvre

Helicopter velocity Puma (K_q = 1)	*0 m/s*	*14.85 m/s*	*29.7 m/s*	*52 m/s*	*74 m/s*
$\lvert N_{freg} N_{SP} \rvert$ (6-and 8-dof)	*0.15048*	*0.258278*	*0.34473*	*0.40358*	*0.46029*
Helicopter velocity Bö-105 (K_q = 0.5 6-dof and K_q = 0.8 8-dof)	*0 m/s*	*10.25 m/s*	*30.75 m/s*	*51 m/s*	*74 m/s*
$\lvert N_{freg} N_{SP} \rvert$ (6-dof)	*0.041932*	*0.05982*	*0.111509*	*0.071918*	*0.03890*
$\lvert N_{freg} N_{SP} \rvert$ (8-dof)	*0.06502*	*0.09555*	*0.174552*	*0.10802*	*0.0747*

Analysing the values of the product $|N_{Freg}N_{SP}|$ (non-dimensional) from these tables it may be seen that the Bö-105 hardly passes the value of 0.1 in both the 6-dof and 8-dof models, whereas the Puma SA-330 is characterized by values situated between 0.25 and 0.45. On the basis of the simulations with a coupled model it may be concluded that the interpretation of "large" in the critical pole distance criterion for the body short-period and regressing flapping mode coupling in this case is in excess of the value 0.3. For values smaller than 0.1, as in the case of the Bö-105, the two investigated modes are coupling.

5.7.2 Investigations on the Body Short-Period Mode and Regressing Flapping Mode Coupling in the Side-Step Manoeuvre

The side-step manoeuvre for both the Puma and the Bö-105 required different gains when using the 6- and the 8-dof models. For the Puma these new values were not calculated, but it seems that they must be changed when performing the deceleration in the 8-dof model as demonstrated in section 5.5.4.

Figure 5.26 gives the representation in the complex plane for the Puma in the region of the short-period mode and regressing flapping mode coupling using first a gain K_q = 0.57 in the 6-dof model and subsequently changing the gain to K_q = 0.8 in the 8-dof model with increased damping in the short period mode.

Figure 5.27 gives the representation in the complex plane for the Bö-105 in the region of the short-period mode and regressing flapping mode coupling using first a gain K_q = 0.3 in the 6-dof model and subsequently changing the gain to K_q = 1 in the 8-dof model.

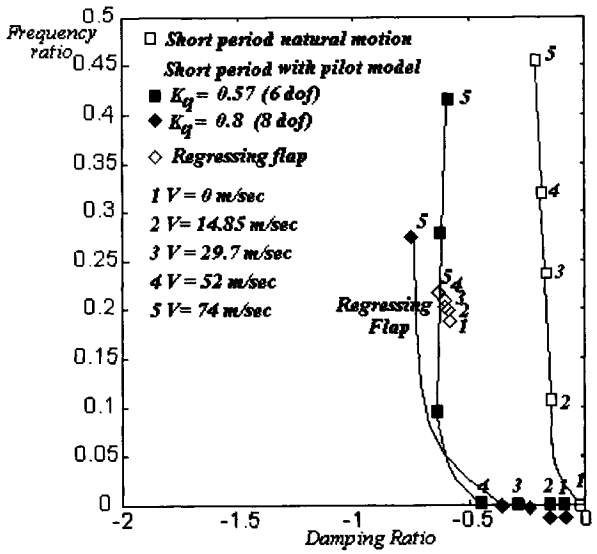

Figure 5.26 Short-period mode and regressing flapping for side-step manoeuvre: Puma

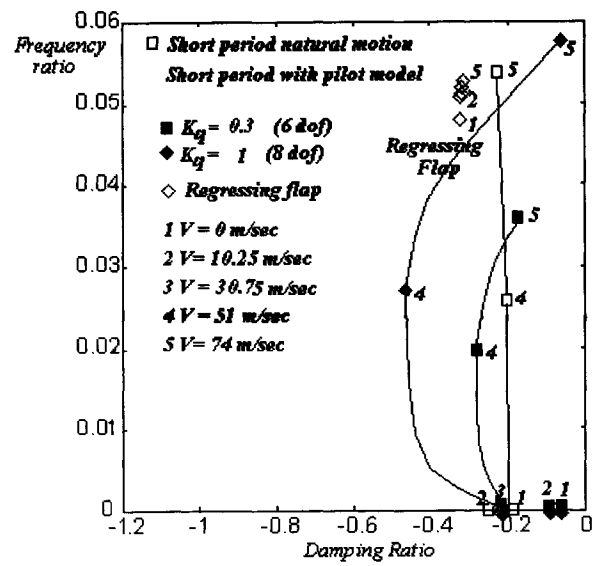

Figure 5.27 Short-period and regressing flapping for side-step manoeuvre: Bö-105

The critical pole distance criterion (5.24) was subsequently applied and using the gains as calculated for the side-step manoeuvre. The results are presented in Table 5.19.

Table 5.19 Critical pole distance criterion for body/disc-tilt coupling for Puma SA-330 and Bö-105 in 6- and 8-dof piloted simulation models. Side-step Manoeuvre

Helicopter velocity Puma (K_q = 0.57 6-dof and K_q = 0.8 8-dof)	*0 m/s*	*14.85 m/s*	*29.7 m/s*	*52 m/s*	*74 m/s*
$\|N_{Freg}\ N_{SP}\|$ (6-dof)	*0.097353*	*0.177524*	*0.25648*	*0.318048*	*0.39192*
$\|N_{Freg}\ N_{SP}\|$ (8-dof)	*0.126557*	*0.22272*	*0.306738*	*0.367691*	*0.43301*
Helicopter velocity Bö-105 (K_q = 0.3 6-dof and K_q = 1 8-dof)	*0 m/s*	*10.25 m/s*	*30.75 m/s*	*51 m/s*	*74 m/s*
$\|N_{Freg}\ N_{SP}\|$ (6-dof)	*0.0419324*	*0.05982*	*0.11151*	*0.0719*	*0.0389*
$\|N_{Freg}\ N_{SP}\|$ (8-dof)	*0.055954*	*0.08163*	*0.15043*	*0.09258*	*0.05725*

Analysing the product $|N_{Freg}\ N_{SP}|$ (non-dimensional) when the pilot model is included it can be seen that at low advance ratios, the Puma helicopter is characterized by relatively small values of this product, which increase as the advance ratio is increasing. Therefore, for small advance ratios, the short-period mode of the Puma helicopter couples to the regressing flapping mode, a conclusion also supported by the time-domain simulations performed in section 5.5.4. The product $|N_{Freg}\ N_{SP}|$ for the Bö-105 helicopter is relatively small for all advance ratios considered and therefore, the two modes must be considered as coupled, independent of the advance ratio.

5.8 Conclusion on the Critical Pole Distance Criterion Applied to the Body / Rotor Disc-Tilt Interaction on Basis of the Examples Analyzed

The coupling between the body and disc-tilt dynamics using the critical pole distance criterion was investigated in the previous sections, using as an example two helicopters which differ by their rotor system, first looking at their natural behaviour and subsequently including a piloted model. The critical pole distance criterion was applied to investigate firstly the coupling between the short-period mode and regressing flapping mode with and without the pilot model, and secondly the roll-subsidence and regressing flapping mode without pilot model, using 6-dof and 8-dof models. Analysing the values of the product $|N_{Freg}\ N_{SP}|$ and $|N_{Freg}\ N_{Roll}|$ from Table 5.12, Table 5.16, Table 5.18, Table 5.19 and the preliminary conclusions following these tables of sections 5.6.1, 5.6.3, 5.7.1 and 5.7.2 the critical pole distance criterion was quantified for the body-rotor disc-tilt coupling as:

For piloted simulation modeling, the strength of the coupling between the body modes and the regressing flapping mode can be quantified as follows according to the critical pole distance criterion:

$$\begin{aligned} &|N_{body}\ N_{Freg}| > 0.3 \quad \textit{Very Lightly Coupled;} \\ 0.1 < &|N_{body}\ N_{Freg}| > 0.3 \quad \textit{Moderately to Lightly Coupled;} \\ &|N_{body}\ N_{Freg}| < 0.1 \quad \textit{Heavily Coupled.} \end{aligned}$$

The articulated Puma SA-330 helicopter is in this sense characterized by very light to moderate couplings but the semi-rigid Bö-105 helicopter is characterized by strong coupling between the body short-period and regressing flapping and also between the roll-subsidence and regressing flapping modes. This conclusion was supported amongst others by **Miyajima** [1979][73] who demonstrated that for a semi-rigid helicopter, the blade regressing flapping mode should be included in the piloted simulation because this mode couples with the fuselage motion and results in an oscillatory mode with short period frequencies which otherwise is not present in a 6-dof model. Also other references enumerated in the literature survey of Chapter 3 support this conclusion. The present chapter attempted to quantify this known conclusion into a designer criterion for general applications.

Chapter 6

Investigation of a Wind Turbine Rotor-Tower Instability Using the Critical Pole Distance Method[&]

The present chapter applies the critical pole distance method to investigate a case of dynamic instability observed on a horizontal axis wind turbine. It will be demonstrated how, using this method, the dangerous modes which couple together leading to instability can be identified. The instability which will be investigated was encountered on the KEWT wind turbine prototype, a two-bladed wind turbine designed in the 1980's. During the tests, two regions of violent vibrations were measured as the rotor angular velocity increased: a first vibration involved large deformations in the torsion of the tower and blade lead-lag modes whereas a second vibration was mainly concerned with the vertical displacement of the chassis (tower+nacelle system) in the tower second bending mode fore-aft and blade first lead-lag mode. By the vertical displacement of the chassis is meant the vertical motion of the chassis as a result of the inclination angle of the nacelle when the tower bends fore and aft in the second bending mode (see Figure F.1). This motion of the chassis will be shortly named during this chapter as the chassis second bending mode. Investigating these instabilities, **van Holten** [1980][46] concluded that the strong vibrations were resonances of the rotor-tower coupled system, wherein the combination of the gravity force and the constant rotor angular velocity forms a continuous energy input condition for the vibration, the energy being supplied by the generator. Analysing the experimental data, some similarities in both oscillations were observed:

- in both cases, large displacements of the rotor centre were observed: the tower torsion resulted in a large horizontal motion of the rotor centre, whereas the chassis second bending mode resulted in a large vertical translation of the rotor centre;
- in both cases, the oscillations appeared at an angular velocity equal to half that of the involved tower mode frequency;
- in both cases, the oscillations of the tower + nacelle system increased dramatically in comparison to the lead-lag motion, which showed a more moderate increase in amplitude.

Figure 6.1 presents the mechanism of the instability as explained at that time by **van Holten** [1980][46]. Gravity acts as a 1-P excitation to the lead-lag motion, giving rise to a

---

& This chapter is a revised version of paper AIAA-2000-0068 by Pavel and Holten, van [2000][88] "*A Rotor-Tower Instability Associated with the Advancing Lead-Lag Mode*"

forced 1-P blade response in the lead-lag direction. The lead-lag blade oscillation is felt as a 2-P excitation by the non-rotating system, that is, the tower. When a tower eigenfrequency lies in the vicinity of the 2-P excitation, a large amplitude tower oscillation will appear. This tower oscillation, in turn, will be transmitted back to the blades first as a 1-P excitation reinforcing the initial blade 1-P lead-lag oscillations and secondly as a 3-P excitation for the lead-lag motion of the blades. The forced 1-P and 3-P blade lead-lag oscillations are transmitted back again to the tower as a 2-P excitation, with the tower in return reinforcing the rotor oscillation, and so forth in a vicious circle.

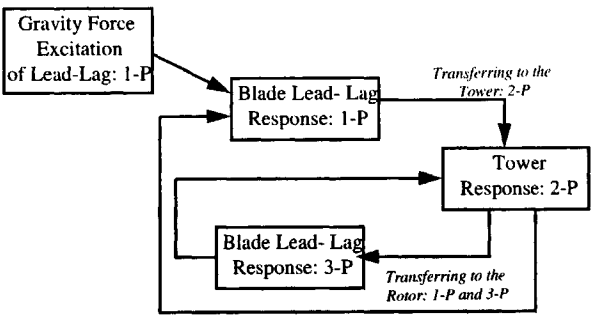

*Figure 6.1 : Mechanism of Rotor-Tower Induced Oscillations (**van Holten** [1980]*[46])

The following sections will focus on the instability of the blade lead-lag and chassis second bending mode since most experimental data were available for this case. It will be demonstrated that the chassis is not actually reinforcing the rotor lead-lag oscillations, but on the contrary, is acting as a vibration absorber for the rotor motion and because of this oscillates heavily. Criteria for coupling in the complex plane for the KEWT wind turbine will be developed based on the critical pole distance method.

6.1 Investigations of the KEWT Instability with a Coupled Rotor-Chassis Model

In Appendix F a two degree-of-freedom coupled blade lead-lag + chassis second bending model is developed, first in the rotor rotating system of reference and next transposed to the non-rotating system using the Coleman Transformation. The final non-dimensional equations of motion for the rotor-chassis motion of a 2-bladed wind turbine, in the rotating system of reference of the blade, were developed in Appendix F,

section 7.1, equation (F.17) assuming that the blades are uniform and the angles small:

$$\begin{cases} \eta'' + 2\xi_T\bar{\omega}_T\eta' + \bar{\omega}_T^2\eta + \sum_{k=1}^{2} \frac{\alpha_m}{2}\frac{d^2}{d\psi^2}\left(\zeta_k \sin\psi_k\right) = 0 \\ \eta''\sin\psi_k + \zeta_k'' + 2\xi_\zeta\bar{\omega}_\zeta\zeta_k' + \left(\bar{\omega}_\zeta^2 - \varepsilon\cos\psi_k\right)\zeta_k = \varepsilon\sin\psi_k \qquad \psi_1 = \psi\ ,\ \psi_2 = \psi + \pi \end{cases} \tag{6.1}$$

where η represents the tower displacement in the second bending mode and ζ_k the lead-lag degree of freedom of the k-blade. The blade lead-lag motion is characterized by a natural frequency $\bar{\omega}_\zeta$ and a damping ratio ξ_ζ and the chassis fore-aft bending motion in the second mode by a natural frequency $\bar{\omega}_T$ and a damping ratio of ξ_T. Parameter α_m was defined as $\alpha_m = 1/\left(2 + M_{ch}/m_{bl}\right)$ and the gravity force is contained in the term $\varepsilon = g\,\sigma_{bl}/I_{bl} \approx g/R$, contributing to the motion both as an external and a parametric excitation.

The equations of motion (6.1) were transformed to the non-rotating system of reference of the chassis in Appendix F, section F.3 by means of the Coleman transformation (F.18) for a 2-bladed rotor. The final equations of motion of the rotor-chassis system in the non-rotating system are obtained as (equations (F.24)):

$$\begin{cases} \left(1 - \frac{\alpha_m}{2} + \frac{\alpha_m}{2}\cos2\psi\right)\eta'' + 2\xi_T\bar{\omega}_T\eta' + \bar{\omega}_T^2\eta + \alpha_m\left[2\left(\xi_\zeta\bar{\omega}_\zeta\sin\psi - \cos\psi\right)\zeta_{N/2}' + \left(1 + \bar{\omega}_\zeta^2\right)\sin\psi\,\zeta_{N/2} + \right. \\ \left. + \frac{\varepsilon}{2}a_0\sin2\psi\right] = \frac{\alpha_m\varepsilon}{4}\left(-1 + \cos2\psi - \sin2\psi\right) \\ \left(1 - \frac{\alpha_m}{2} + \frac{\alpha_m}{2}\cos2\psi\right)a_0'' + 2\xi_\zeta\bar{\omega}_\zeta\left(1 - \frac{\alpha_m}{2} + \frac{\alpha_m}{2}\cos2\psi\right)a_0' + \bar{\omega}_\zeta^2\left(1 - \frac{\alpha_m}{2} + \frac{\alpha_m}{2}\cos2\psi\right)a_0 + \\ + \left[\varepsilon\cos\psi\left(1 - \frac{\alpha_m}{4}\right) + \frac{\alpha_m\varepsilon}{4}\cos3\psi\right]\zeta_{N/2} = \frac{\varepsilon}{2}\left(1 - \frac{3\alpha_m}{4}\right)\sin\psi + \frac{\varepsilon}{2}\left(-1 + \frac{\alpha_m}{4}\right)\cos\psi + \frac{\alpha_m\varepsilon}{8}\sin3\psi - \\ - \frac{\alpha_m\varepsilon}{8}\cos3\psi\left(1 - \frac{\alpha_m}{2} + \frac{\alpha_m}{2}\cos2\psi\right)\zeta_{N/2}'' + \left(2\xi_\zeta\bar{\omega}_\zeta - \alpha_m\sin2\psi\right)\zeta_{N/2}' + \left[\bar{\omega}_\zeta^2 + \frac{\alpha_m}{2}\left(1 - \right.\right. \\ \left.\left. - \cos2\psi\right)\right]\zeta_{N/2} + 2\xi_T\bar{\omega}_T\sin\psi\,\eta' + \omega_T^2\sin\psi\,\eta + \varepsilon\cos\psi\,a_0 = -\frac{\varepsilon}{2}\left(\sin\psi + \cos\psi\right) \end{cases} \tag{6.2}$$

According to (6.2), the coupled rotor-chassis motion in the non-rotating system of reference may be represented by the degrees of freedom η of the tower second bending mode, a_0 of the collective lead-lag mode and $\zeta_{N/2}$ of the differential lead-lag mode. The system of equations (6.2) contains the angular position of the blade ψ in periodic terms proportional to $\sin\psi$, $\cos\psi$, $\sin 2\psi$, $\cos 2\psi$, $\sin 3\psi$ and $\cos 3\psi$. These terms cannot be neglected, the Coleman transformation for a 2-bladed rotor retaining the periodicity of

the blade in the coupled rotor-chassis equations of motion in the non-rotating system. The stability of the linear system of equations (6.2) with periodic coefficients may be determined by applying the Floquet method as presented in Appendix G. However, system (6.2) can be solved approximatively assuming solutions in an asymptotic expansion. Presume solutions in the form:

$$\begin{cases} \eta = \eta_0 + \alpha_m \eta_1 + \dots \\ a_0 = d_0 + \alpha_m d_1 + \dots \\ \zeta_{N/2} = b_0 + \alpha_m b_1 + \dots \end{cases} \tag{6.3}$$

Appendix F, section F.3 demonstrated that the response of the rotor-chassis system in the first order approximation of the solution $O(\alpha_m^1, \varepsilon^1)$ is obtained as (equation (F.53) in Appendix F):

$$\begin{cases} \eta = \dfrac{\alpha_m \varepsilon}{\left[\left(\bar{\omega}_\zeta^2 - 1\right)^2 + 4\xi_\zeta^2 \bar{\omega}_\zeta^2\right]\left[\left(\bar{\omega}_T^2 - 4\right)^2 + 16\xi_T^2 \bar{\omega}_T^2\right]} \left(C\cos 2\psi + D\sin 2\psi\right) \\ a_0 = \dfrac{\varepsilon}{\left[\left(\bar{\omega}_\zeta - 1\right)^2 + 4\xi_\zeta^2 \bar{\omega}_\zeta^2\right]} \left[\left(-A + \alpha_m A_2^*\right)\cos\psi + \left(B + \alpha_m B_2^*\right)\sin\psi\right] + \dfrac{\alpha_m \varepsilon \left[A_3^* \cos 3\psi + B_3^* \sin 3\psi\right]}{\left[\left(\bar{\omega}_\zeta - 1\right)^2 + 4\xi_\zeta^2 \bar{\omega}_\zeta^2\right]\left[\left(\bar{\omega}_\zeta - 9\right)^2 + 36\xi_\zeta^2 \bar{\omega}_\zeta^2\right]} \\ \zeta_{N/2} = \dfrac{\varepsilon}{\left[\left(\bar{\omega}_\zeta - 1\right)^2 + 4\xi_\zeta^2 \bar{\omega}_\zeta^2\right]} \left[B\cos\psi - A\sin\psi\right] + \dfrac{\alpha_m \varepsilon}{\left[\left(\bar{\omega}_\zeta - 1\right)^2 + 4\xi_\zeta^2 \bar{\omega}_\zeta^2\right]\left[\left(\bar{\omega}_T^2 - 4\right)^2 + 16\xi_T^2 \bar{\omega}_T^2\right]} \times \\ \times \left[B_4^* \cos\psi + A_4^* \sin\psi\right] + \dfrac{\alpha_m \varepsilon \left[B_5^* \cos 3\psi + A_5^* \sin 3\psi\right]}{\left[\left(\bar{\omega}_\zeta - 1\right)^2 + 4\xi_\zeta^2 \bar{\omega}_\zeta^2\right]\left[\left(\bar{\omega}_T^2 - 4\right)^2 + 16\xi_T^2 \bar{\omega}_T^2\right]\left[\left(\bar{\omega}_\zeta - 9\right)^2 + 36\xi_\zeta^2 \bar{\omega}_\zeta^2\right]} \end{cases} \tag{6.4}$$

where the terms A, B, C, D, A_2^*, B_2^*, A_3^*, B_3^*, A_4^*, B_4^*, A_5^*, B_5^* were derived in Appendix F, section F.3 as being:

$$A = \frac{\left[\left(\bar{\omega}_\zeta - 1\right) + 2\xi_\zeta \bar{\omega}_\zeta\right]}{2} \quad ; \quad B = \frac{\left[\left(\bar{\omega}_\zeta - 1\right) - 2\xi_\zeta \bar{\omega}_\zeta\right]}{2} \tag{6.5}$$

$$C = \left(-\frac{3}{2}\xi_\zeta\bar{\omega}_\zeta - \frac{3}{4}\bar{\omega}_\zeta^2 + \frac{3}{4}\right)\bar{\omega}_T^2 + \left(3 + 6\xi_\zeta\bar{\omega}_\zeta - 3\bar{\omega}_\zeta^2\right)\xi_T\bar{\omega}_T + 3\bar{\omega}_T^2 + 6\xi_T\bar{\omega}_T - 3$$
$$D = \left(-\frac{3}{2}\xi_\zeta\bar{\omega}_\zeta + \frac{3}{4}\bar{\omega}_\zeta^2 - \frac{3}{4}\right)\bar{\omega}_T^2 + \left(3 - 6\xi_\zeta\bar{\omega}_\zeta - 3\bar{\omega}_\zeta^2\right)\xi_T\bar{\omega}_T - 3\bar{\omega}_T^2 + 6\xi_T\bar{\omega}_T + 3 \tag{6.6}$$

$$A_2^* = \frac{2B+1}{8}\left(\bar{\omega}_\zeta^2 - 1\right) - 6\xi_\zeta\bar{\omega}_\zeta\frac{2A-1}{8} \quad ; \quad B_2^* = 3\frac{2A-1}{8}\left(\bar{\omega}_\zeta^2 - 1\right) + 2\xi_\zeta\bar{\omega}_\zeta\frac{2B+1}{8}$$
$$A_3^* = -\frac{2B+1}{8}\left(\bar{\omega}_\zeta^2 - 9\right) + 6\xi_\zeta\bar{\omega}_\zeta\frac{2A-1}{8} \quad ; \quad B_3^* = -\frac{2A-1}{8}\left(\bar{\omega}_\zeta^2 - 9\right) - 6\xi_\zeta\bar{\omega}_\zeta\frac{2B+1}{8} \tag{6.7}$$

$$B_4^* = \left[B\left[\left(\bar{\omega}_T^2 - 4\right)^2 + 16\xi_T^2\bar{\omega}_T^2\right] + \left(2\xi_T\bar{\omega}_T C - \frac{\bar{\omega}_T^2}{2}D\right)\right]\left(\bar{\omega}_\zeta^2 - 1\right) - 2\xi_\zeta\bar{\omega}_\zeta\left[A\left[\left(\bar{\omega}_T^2 - 4\right)^2 + 16\xi_T^2\bar{\omega}_T^2\right] + \right.$$
$$\left. + \left(2\xi_T\bar{\omega}_T D + \frac{\bar{\omega}_T^2}{2}C\right)\right]$$
$$A_4^* = \left[A\left[\left(\bar{\omega}_T^2 - 4\right)^2 + 16\xi_T^2\bar{\omega}_T^2\right] + \left(2\xi_T\bar{\omega}_T D + \frac{\bar{\omega}_T^2}{2}C\right)\right]\left(\bar{\omega}_\zeta^2 - 1\right) + 2\xi_\zeta\bar{\omega}_\zeta\left[B\left[\left(\bar{\omega}_T^2 - 4\right)^2 + 16\xi_T^2\bar{\omega}_T^2\right] + \right.$$
$$\left. + \left(2\xi_T\bar{\omega}_T C - \frac{\bar{\omega}_T^2}{2}D\right)\right] \tag{6.8}$$

$$B_5^* = \left[-B\left[\left(\bar{\omega}_T^2 - 4\right)^2 + 16\xi_T^2\bar{\omega}_T^2\right] + \left(-2\xi_T\bar{\omega}_T D + \frac{\bar{\omega}_T^2}{2}C\right)\right]\left(\bar{\omega}_\zeta^2 - 9\right) - 6\xi_\zeta\bar{\omega}_\zeta\left[-A\left[\left(\bar{\omega}_T^2 - 4\right)^2 + 16\xi_T^2\bar{\omega}_T^2\right] + \right.$$
$$\left. + \left(-2\xi_T\bar{\omega}_T D - \frac{\bar{\omega}_T^2}{2}C\right)\right]$$
$$A_5^* = \left[-A\left[\left(\bar{\omega}_T^2 - 4\right)^2 + 16\xi_T^2\bar{\omega}_T^2\right] + \left(-2\xi_T\bar{\omega}_T D - \frac{\bar{\omega}_T^2}{2}C\right)\right]\left(\bar{\omega}_\zeta^2 - 9\right) + 6\xi_\zeta\bar{\omega}_\zeta\left[-B\left[\left(\bar{\omega}_T^2 - 4\right)^2 + 16\xi_T^2\bar{\omega}_T^2\right] + \right.$$
$$\left. + \left(-2\xi_T\bar{\omega}_T D + \frac{\bar{\omega}_T^2}{2}C\right)\right] \tag{6.9}$$

Looking at (6.4) the following conclusions may be drawn:

- there are two resonance frequencies for the blade at frequencies $\bar{\omega}_\zeta^2 = 1 \Leftrightarrow \Omega = \omega_\zeta$ and $\bar{\omega}_\zeta^2 = 9 \Leftrightarrow \Omega = \omega_\zeta / 3$;
- the chassis also has a resonance region situated at $\bar{\omega}_T^2 = 4 \Leftrightarrow \Omega = \omega_T / 2$ which corresponds to the instability encountered during the experimental tests. Therefore, the model developed in this chapter is capable to predict the KEWT instability;
- the lead-lag motion is strongly "contaminated" with 3-P terms, conclusion which corresponds also to the experimental tests;

- analysing the chassis-rotor coupling in the non-rotating system of reference, the chassis motion couples to the lead-lag motion in the differential lead-lag mode (see equation (6.2));
- the gravity excitation is contained as an external and a parametric excitation. It will be demonstrated next that the parametric excitation is contained only in the high order terms of the solution in the asymptotic expansion.

Demonstration: the gravity excitation is contained as a parametric excitation for the blade lead-lag mode in the term $-\varepsilon\zeta_k\cos\psi_k$ in the blade rotating system of reference (see equation (6.1)) which transposes in the chassis non-rotating system of reference into the terms $1/2\varepsilon\alpha_m a_0 \sin 2\psi$ in the chassis equation, $\varepsilon\zeta_{N/2}\cos\psi$, $-1/4\varepsilon\alpha_m\zeta_{N/2}\cos\psi$, $1/4\varepsilon\alpha_m\zeta_{N/2}\cos 3\psi$ in the collective lead-lag equation and $\varepsilon a_0\cos\psi$ in the differential lead-lag equation (see equation (6.2)). Using the solution in the asymptotic expansion (6.3), (F.28), (F.30), (F.39), (F.44), (F.45), the parametric excitation in the chassis equation may be written as

$$\frac{\varepsilon\alpha_m}{2}a_0\sin 2\psi = \frac{\varepsilon\alpha_m}{2}(\varepsilon d_{01}+\alpha_m\varepsilon d_{11}+\ldots)\sin 2\psi = \frac{\varepsilon^2\alpha_m d_{01}+\varepsilon^2\alpha_m^2 d_{11}+\ldots}{2}\sin 2\psi.$$

Thus, the parametric excitation is contained in the solution in the approximation of order higher than $\alpha_m\varepsilon^2$.

Equivalently, the parametric excitations from the collective and differential lead-lag mode may be expressed as:

$$\varepsilon\zeta_{N/2}\cos\psi = (\varepsilon^2 b_{01}+\alpha_m\varepsilon^2 b_{11}+\ldots)\cos\psi,$$

$$-1/4\,\varepsilon\alpha_m\zeta_{N/2}\cos\psi = -1/4(\alpha_m\varepsilon^2 b_{01}+\alpha_m^2\varepsilon^2 b_{11}+\ldots)\cos\psi,$$

$$1/4\,\varepsilon\alpha_m\zeta_{N/2}\cos 3\psi = 1/4(\alpha_m\varepsilon^2 b_{01}+\alpha_m^2\varepsilon^2 b_{11}+\ldots)\cos 3\psi$$

$$\varepsilon a_0\cos\psi = (\varepsilon^2 d_{01}+\alpha_m\varepsilon^2 d_{11}+\ldots)\cos\psi.$$

Again, one can see that the parametric excitation is contained in the solution in the approximation higher than ε^2.

The lead-lag and chassis amplitudes of the response (6.4) may be calculated as:

$$R_\eta = \frac{\alpha_m\varepsilon\sqrt{C^2+D^2}}{\left[\left(\bar\omega_\zeta^2-1\right)^2+4\xi_\zeta^2\bar\omega_\zeta^2\right]\left[\left(\bar\omega_T^2-4\right)^2+16\xi_T^2\bar\omega_T^2\right]} \tag{6.10}$$

$$R_{a_0} = \frac{\varepsilon\sqrt{\left(-A+\alpha_m A_2^*\right)^2+\left(B+\alpha_m B_2^*\right)^2}}{\left[\left(\bar\omega_\zeta-1\right)^2+4\xi_\zeta^2\bar\omega_\zeta^2\right]} + \frac{\alpha_m\varepsilon\sqrt{A_3^{*2}+B_3^{*2}}}{\left[\left(\bar\omega_\zeta-1\right)^2+4\xi_\zeta^2\bar\omega_\zeta^2\right]\left[\left(\bar\omega_\zeta-9\right)^2+36\xi_\zeta^2\bar\omega_\zeta^2\right]} \tag{6.11}$$

$$R_{\zeta_{1,2}} = \frac{\varepsilon\sqrt{A^2+B^2}}{\left[\left(\bar{\omega}_\zeta - 1\right)^2 + 4\xi_\zeta^2\bar{\omega}_\zeta^2\right]} + \frac{\alpha_m\varepsilon\sqrt{A_4^{*2}+B_4^{*2}}}{\left[\left(\bar{\omega}_\zeta - 1\right)^2 + 4\xi_\zeta^2\bar{\omega}_\zeta^2\right]\left[\left(\bar{\omega}_T^2 - 4\right)^2 + 16\xi_T^2\bar{\omega}_T^2\right]} + \frac{\alpha_m\varepsilon\sqrt{A_5^{*2}+B_5^{*2}}}{\left[\left(\bar{\omega}_\zeta - 1\right)^2 + 4\xi_\zeta^2\bar{\omega}_\zeta^2\right]\left[\left(\bar{\omega}_T^2 - 4\right)^2 + 16\xi_T^2\bar{\omega}_T^2\right]\left[\left(\bar{\omega}_\zeta - 9\right)^2 + 36\xi_\zeta^2\bar{\omega}_\zeta^2\right]} + \tag{6.12}$$

Next consider the KEWT data of the experimental tests (case 1 of Table 6.1) and cases 2 to 6 as modifications to the initial parameters in an effort to eliminate the instability.

Table 6.1 KEWT Numerical Cases

Case	*1 Actual Experiment*	*2 More lag damping*	*3 More tower damping*	*4 Stiffening the tower*	*5 Softening the tower*	*6 Stiffening the blades*
ω_T *nondim.*	*2*	*2*	*2*	*2*	*2*	*2*
ω_ζ *nondim.*	*1.635*	*1.635*	*1.635*	*1.05*	*3.68*	*2.666*
ξ_T	*0.02*	*0.02*	*0.05*	*0.02*	*0.02*	*0.02*
ξ_ζ	*0.05*	*0.07*	*0.05*	*0.05*	*0.05*	*0.05*
$\varepsilon=g/(R\Omega^2)$	*0.0245*	*0.0245*	*0.0245*	*0.0101*	*0.1242*	*0.0245*
α_m	*0.05*	*0.05*	*0.05*	*0.05*	*0.05*	*0.05*
$\Omega=\omega_T/2$*(Hz)*	*1.125*	*1.125*	*1.125*	*1.75*	*0.5*	*1.125*

Figure 6.2 to Figure 6.7 present the variation with the rotor speed of the amplitudes of the chassis, lead-lag collective and lead-lag differential modes. Figure 6.2, corresponding to the experimental test, shows that there exist two critical angular velocities where the amplitudes of the chassis and lead-lag motion increase abruptly:

- a first peak corresponds to a rotor rotational speed $\Omega=(1/2)\omega_T=1.125$ Hz;
- a second peak corresponds to a rotor rotational speed $\Omega=\omega_\zeta=1.84$ Hz.

These peaks were also predicted by the analytical formula's (6.4) and they correspond to the solution in the expansion $O(\alpha_m^1, \varepsilon^1)$. This chapter will focus on studying the instability region of the experimental test at a rotor rotational speed $\Omega=(1/2)\omega_T$ (absolute value). In an attempt to remove this instability, different system characteristics were varied (cases 2 to 6 of Table 6.1):

- case 2 analyses an increase of the lead-lag damping ratio from $\xi_\zeta=0.05$ to 0.07;
- case 3 analyses an increase of the tower damping ratio from $\xi_T=0.02$ to 0.05;

- case 4 corresponds to stiffening of the tower from ω_T= 2.25 Hz to 3.5 Hz;
- case 5 corresponds to softening of the tower from ω_T= 2.25 Hz to 1 Hz;
- case 6 considers the stiffening of the blades from ω_ζ= 1.84 Hz to 3 Hz.

The following conclusions can be drawn w.r.t. the region of the instability investigated:

- increasing the lead-lag damping ratio (case 2) does not influence the instability (it mainly decreases the pure resonance of the lead-lag mode situated at $\Omega=\omega_\zeta$=1.84 Hz);
- increasing the tower damping ratio (case 3) almost removes the instability;
- stiffening the tower (case 4) worsens the instability, in this case the instability superimposes on the pure lead-lag resonance;
- softening the tower (case 5) almost removes the instability;
- stiffening the blades (case 6) almost removes the instability.

Therefore, increasing the tower damping ratio as in case 3, softening the tower as in case 5 or stiffening the blades as in case 6 may be used as valid solutions to eliminate the investigated instability. Note that the chassis resonances at frequencies $\Omega=(1/4)\omega_T$=0.56 Hz, $\Omega=(1/6)\omega_T$=0.375 Hz, etc., (as predicted by the rotor-chassis coupled model when high-order terms are used in the expansion, see section F.4 of Appendix F) are not considered when calculating the amplitudes of the response (6.10), (6.11) or (6.12). However, these instabilities are much smaller than the instability in the first region $\Omega=(1/4)\omega_T$=1.125 Hz.

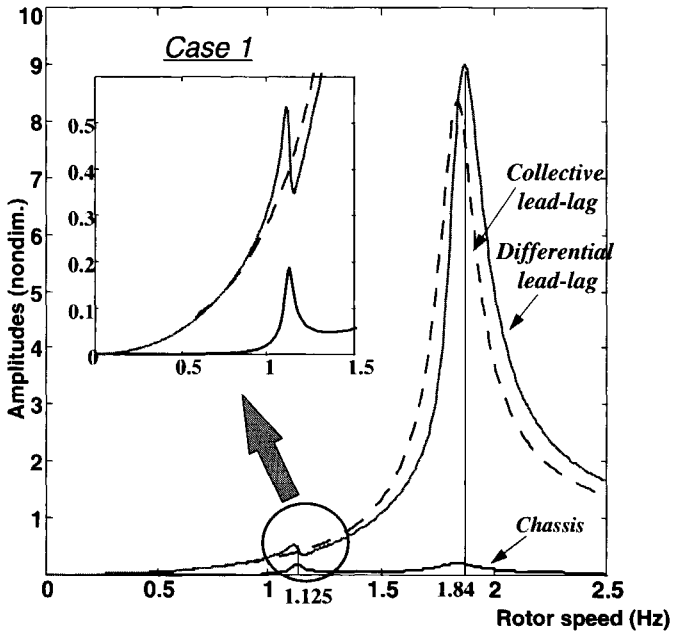

Figure 6.2 Wind turbine response to gravity load as the rotor speed varies: Case 1

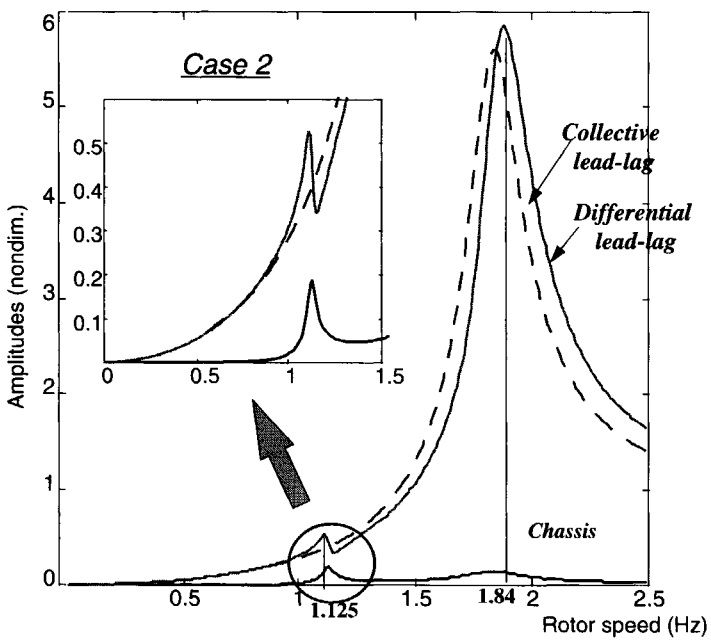

Figure 6.3 Wind turbine response to gravity load as the rotor speed varies: Case 2

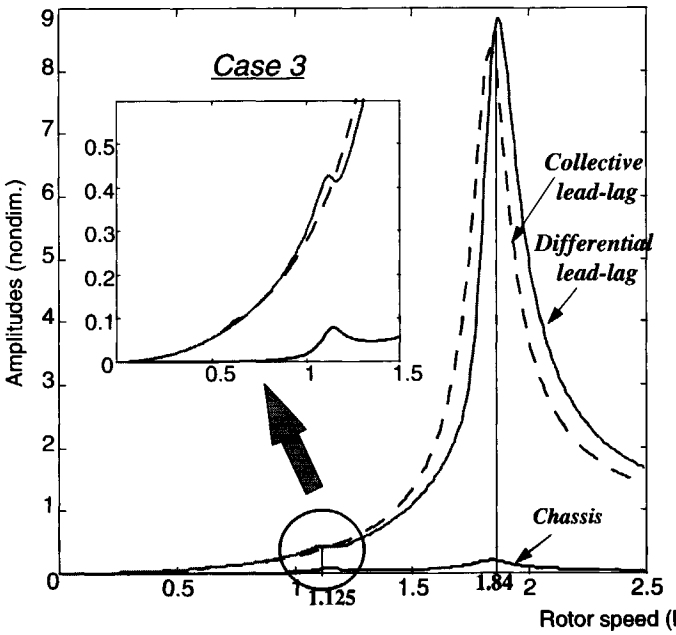

Figure 6.4 Wind turbine response to gravity load as the rotor speed varies: Case 3

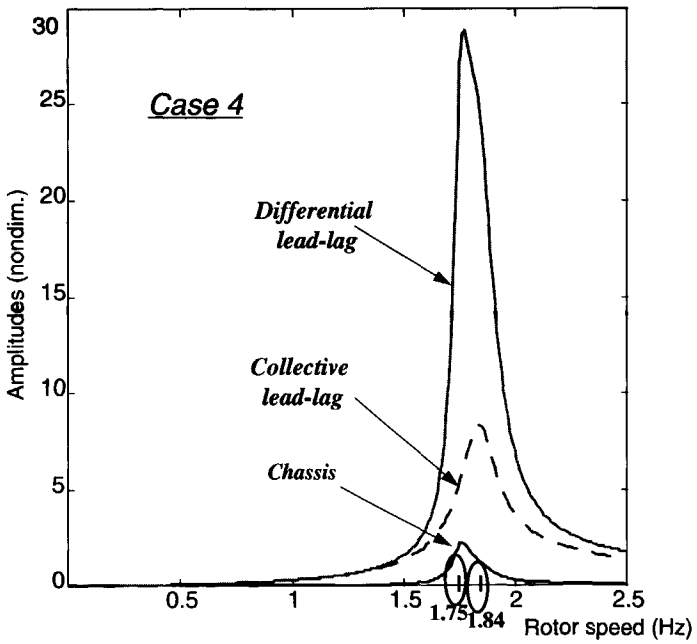

Figure 6.5 Wind turbine response to gravity load as the rotor speed varies: Case 4

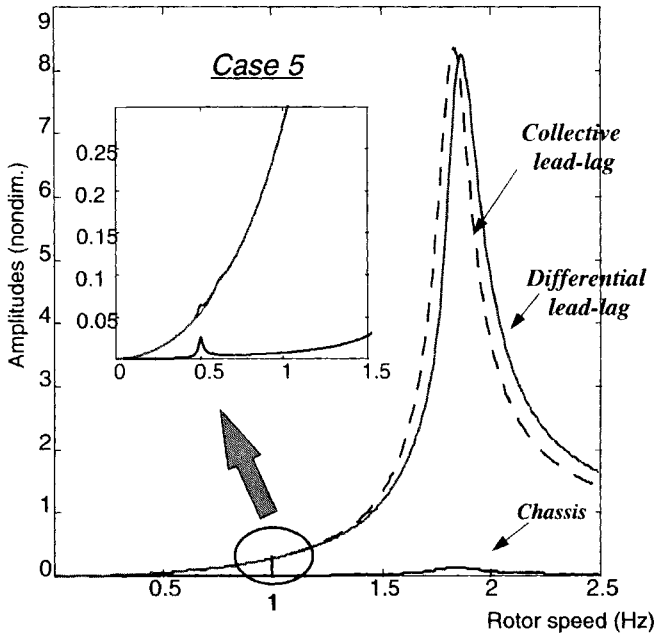

Figure 6.6 Wind turbine response to gravity load as the rotor speed varies: Case 5

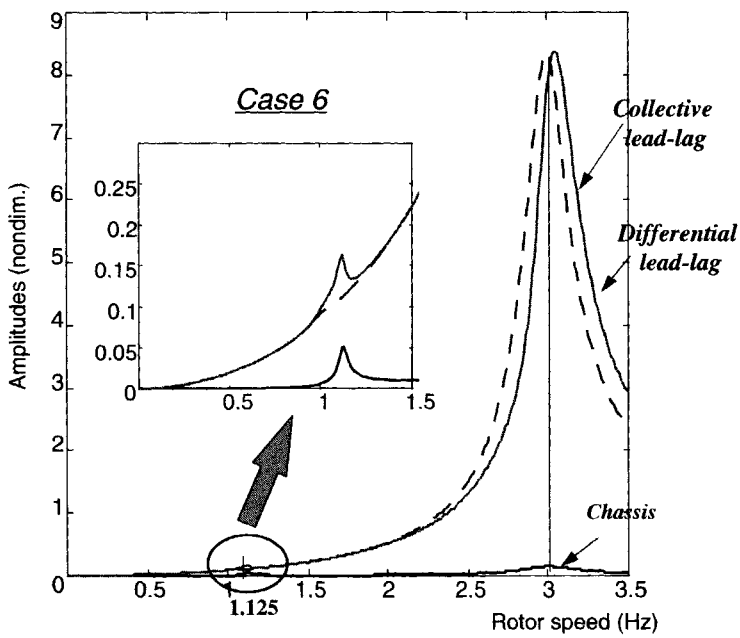

Figure 6.7 Wind turbine response to gravity load as the rotor speed varies: Case 6

6.2 The Mechanism of KEWT Instability

The present section will explain the cause of the KEWT instability as revealed in the experimental tests.

Consider first that the lead-lag motion is an external excitation on the chassis system. According to (6.1), in the blade rotating system of reference, each blade excites the chassis with forces proportional to $-\ddot{\zeta}_k \sin\psi_k$; $-\Omega\dot{\zeta}_k \cos\psi_k$; $\Omega^2\zeta_k \sin\psi_k$ (the minus sign results from the separation of the excitation in the right-hand side of the chassis equation) which respectively correspond to the inertial, Coriolis and centrifugal forces of each blade lead-lag motion. In the rotating system of reference (x_r,y_r,z_r) of Figure F.1 the components of these forces exerted on the chassis in the direction of the blade lead-lag motion ζ_k are:

$$\begin{aligned} F_{xr} &= (-\ddot{\zeta}_k + \Omega^2\zeta_k)\, m_{bl} R \\ F_{yr} &= -2\Omega\dot{\zeta}_k\, m_{bl} R \end{aligned} \tag{6.13}$$

In the fixed system of reference (x_0,y_0,z_0) these forces become (after applying the rotation matrix $[\ \psi_k\ ]$ defined in equation (F.1)):

$$\begin{aligned} F_{x0} &= F_{xr}\cos\psi - F_{yr}\sin\psi \\ F_{y0} &= F_{xr}\sin\psi + F_{yr}\cos\psi \end{aligned} \tag{6.14}$$

Recalling the system response in the differential lead-lag mode (6.4) and observing that in the numerical cases of Table 6.1 the coefficients A>0, B>0, $B_4^*>0$, $A_4^*<0$, one may write:

$$\zeta_{N/2} = \zeta_{N/2\,c}\cos\psi - \zeta_{N/2\,s}\sin\psi \tag{6.15}$$

where $\zeta_{N/2\,c}$ and $\zeta_{N/2\,s}$ are the initial differential lead-lag mode displacements at t = 0. The blade lead-lag oscillation in the rotating system of reference will be also assumed in the same harmonics as the differential lead-lag mode:

$$\zeta_k = \zeta_c\cos\psi - \zeta_s\sin\psi \tag{6.16}$$

where ζ_c and ζ_s are the initial blade lead-lag displacements at t = 0. Differentiating (6.16) with respect to ψ gives the blade velocity and acceleration as:

$$\begin{aligned} \dot{\zeta}_k &= \Omega\,(-\zeta_c \sin\psi - \zeta_s \cos\psi) \\ \ddot{\zeta}_k &= \Omega^2 (-\zeta_c \cos\psi + \zeta_s \sin\psi) \end{aligned} \tag{6.17}$$

Substituting (6.16) and (6.17) into (6.13) the forces on the chassis due to the lead-lag motion in the rotating system are obtained as:

$$\begin{aligned} F_{xr} &= 2\Omega^2 (\zeta_c \cos\psi - \zeta_s \sin\psi)\, m_{bl} R \\ F_{yr} &= 2\Omega^2 (\zeta_c \sin\psi + \zeta_s \cos\psi)\, m_{bl} R \end{aligned} \tag{6.18}$$

where R and m_{bl} are respectively the blade radius and mass. Equations (6.18) transposed in the non-rotating frame (6.14) yield the components:

$$\begin{aligned} F_{x0} &= 2\Omega^2 (\zeta_c \cos 2\psi - \zeta_s \sin 2\psi)\, m_{bl} R \\ F_{y0} &= 2\Omega^2 (\zeta_c \sin 2\psi + \zeta_s \cos 2\psi)\, m_{bl} R \end{aligned} \tag{6.19}$$

Recalling now the chassis response η as given by (6.4) and observing that in the numerical cases of Table 6.1 the coefficients $C > 0$ (except case 4 where $C \approx 0$) and $D<0$, one may write:

$$\eta = \eta_c \cos 2\psi - \eta_s \sin 2\psi \tag{6.20}$$

Thus, the chassis velocity and acceleration are:

$$\begin{aligned} \dot{\eta} &= -2\Omega (\eta_c \sin 2\psi - \eta_s \sin 2\psi) \\ \ddot{\eta} &= 4\Omega^2 (\eta_c \cos 2\psi + \eta_s \sin 2\psi) \end{aligned} \tag{6.21}$$

It is known that a harmonic force acting on a vibrating system of the same frequency produces work on the system if the force is in phase with the velocity of the vibration. Comparing (6.21) to (6.19) it follows that the component F_{x0} of the lead-lag excitation contains the harmonic $\sin 2\psi$ in phase with the chassis velocity. Thus the blade motion produces work on the system, with energy being transferred from the blades to the chassis.

Next, consider that the chassis acts as an external excitation on the blades. The chassis oscillates in the harmonics $\cos 2\psi$ and $\sin 2\psi$ as represented in (6.20). The force on the blade due to the chassis motion is using D'Alembert principle:

$$f = -f_c \cos 2\psi + f_s \sin 2\psi \tag{6.22}$$

The extra lead-lag moment resulting from the chassis motion can then be calculated as:

$$M_{sh} = f\,R\sin(\psi+\zeta) \approx f\,R\,(\sin\psi+\zeta\cos\psi) \tag{6.23}$$

Substituting (6.22) and (6.16) into (6.23) after some trigonometric computations one obtains:

$$M_{sh} = \frac{f_s\zeta_c+f_c\zeta_s}{4}\sin4\psi+\frac{-f_c\zeta_c+f_s\zeta_s}{4}\cos4\psi-\frac{f_c}{2}\sin3\psi-\frac{f_s}{2}\cos3\psi+f_s\frac{\zeta_c}{2}\sin2\psi- \\ -f_c\frac{\zeta_c}{2}\cos2\psi+\frac{f_c}{2}\sin\psi+\frac{f_s}{2}\cos\psi-\frac{f_c\zeta_c}{4} \tag{6.24}$$

It follows that the components in $\sin\psi$ and $\cos\psi$ of the shaft moment (6.24) are not in phase with the blade lead-lag velocity as given by (6.17) and thus no energy is transferred from the chassis to the blade.

However, the previous case did not consider the gravity force in the system. With gravity, the D'Alembert force on the blade due to the chassis motion (6.22) is:

$$f = -f_c\cos2\psi+f_s\sin2\psi-m_{bl}\,g \tag{6.25}$$

The shaft moment (6.24) in this case becomes:

$$M^*_{sh} = M_{sh}+\frac{m_{bl}\,g}{2}\left(\zeta_s\sin2\psi-\zeta_c\cos2\psi\right)-m_{bl}\,g\sin\psi-\frac{m_{bl}\,g}{2}\zeta_c \tag{6.26}$$

Comparing the shaft moment (6.26) to the blade lead-lag velocity (6.17), it is obvious that the components in $\sin\psi$ of the blade lead-lag velocity are in phase with a component of the shaft moment originating from the action of the gravity force. Therefore, in this case, energy is added from the chassis to the blade.

Concluding, the differential lead-lag mode feeds energy to the chassis via the gravity force action. In the KEWT case, the control system enforces a constant rpm. The tower acts as a dynamic absorber (Frahm damper) whenever alternating forces start to be induced in the rotor, stoping any tendency of the rotor to oscillate. The oscillations of the rotor-chassis system would tend to slow down, but because of the interaction of the gravity with the constant rpm control system, energy is continuously fed into the system. As a result, the rotor oscillations amplify. In response, the tower oscillations increase with the effort to stop the rotor oscillations. This explanation agrees with the experimental test observations that the oscillations of the chassis increased dramatically

compared to the lead-lag oscillations. Thus, the gravity force action, the system constant rpm and the tower behaviour as a dynamic absorber are three important factors in the KEWT instability.

6.3 Critical Pole Distance Method Applied to the KEWT Instability

Next, the critical pole distance method will be applied to determine the regions of dynamic couplings for the investigated KEWT instability. To apply the critical pole distance method, the equations of motion of the uncoupled chassis bending motion and the blade lead-lag motion first have to be derived.

6.3.1 Uncoupled Tower Second-Bending Motion

The uncoupled equation of motion for the second bending mode of the chassis system is obtained by putting the blade lead-lag $\zeta = 0$ in (6.1):

$$\eta'' + 2\xi_T\bar{\omega}_T\eta' + \bar{\omega}_T^2\eta = 0 \tag{6.27}$$

which gives the eigenvalues of the chassis vertical displacement in fore and aft bending motion as:

$$s_T = -\bar{\omega}_T\xi_T \pm i\bar{\omega}_T\sqrt{1-\xi_T^2} \tag{6.28}$$

6.3.2 Uncoupled Blade Lead-Lag Motion in the Non-Rotating System

In the rotating system, the lead-lag equation of motion of one blade is obtained by neglecting the chassis motion in (6.1) as:

$$\zeta'' + 2\xi_\zeta\bar{\omega}_\zeta\zeta' + \bar{\omega}_\zeta^2\left(1 - \frac{\varepsilon}{\bar{\omega}_\zeta^2}\cos\psi\right)\zeta = \varepsilon\sin\psi \tag{6.29}$$

which contains the gravity force both as parametric and external coefficients. When the gravity force is neglected, i.e. $\varepsilon = 0$, the eigenvalues of (6.29) are:

$$s_{\zeta\,1,2} = -\bar{\omega}_\zeta\xi_\zeta \pm i\bar{\omega}_\zeta\sqrt{1-\xi_\zeta^2} \tag{6.30}$$

With the gravity force, equation (6.29) contains the gravity force as a parametric excitation. However, the lead-lag motion (6.29) is written in the blade rotating system and therefore has to be transformed to the non-rotating system in order to compare it with the chassis motion. For the 2-bladed KEWT wind turbine, the motion can be

transposed into the non-rotating system by means of Coleman transformation (equation (F.18) of Appendix F). The motion of the blades in the rotating system in the lead-lag degree of freedom is obtained by writing equation (6.29) for each blade:

$$\begin{Bmatrix}\zeta_1\\ \zeta_2\end{Bmatrix}'' + \begin{bmatrix}2\xi_\zeta\bar{\omega}_\zeta & 0\\ 0 & 2\xi_\zeta\bar{\omega}_\zeta\end{bmatrix}\begin{Bmatrix}\zeta_1\\ \zeta_2\end{Bmatrix}' + \begin{bmatrix}\bar{\omega}_\zeta^2-\varepsilon\cos\psi & 0\\ 0 & \bar{\omega}_\zeta^2-\varepsilon\cos(\psi+\pi)\end{bmatrix}\begin{Bmatrix}\zeta_1\\ \zeta_2\end{Bmatrix} = \begin{Bmatrix}\varepsilon\sin\psi\\ \varepsilon\sin(\psi+\pi)\end{Bmatrix} \quad (6.31)$$

Applying the Coleman transformation (F.18) to the system of equations (6.31) as presented in Appendix F, section F.3, the lead-lag motion in the non-rotating system is equivalent to the motion of the collective a_0 and the differential lead-lag modes $\zeta_{N/2}$:

$$\begin{Bmatrix}a_0\\ \zeta_{N/2}\end{Bmatrix}'' + \begin{bmatrix}2\xi_\zeta\bar{\omega}_\zeta & 0\\ 0 & 2\xi_\zeta\bar{\omega}_\zeta\end{bmatrix}\begin{Bmatrix}a_0\\ \zeta_{N/2}\end{Bmatrix}' + \begin{bmatrix}\bar{\omega}_\zeta^2 & \varepsilon\cos\psi\\ \varepsilon\cos\psi & \bar{\omega}_\zeta^2\end{bmatrix}\begin{Bmatrix}a_0\\ \zeta_{N/2}\end{Bmatrix} = \begin{Bmatrix}(\varepsilon/2)(\sin\psi-\cos\psi)\\ (\varepsilon/2)(-\sin\psi-\cos\psi)\end{Bmatrix} \quad (6.32)$$

Equations (6.32) are coupled via parameter ε. Neglecting this parameter, the collective lead-lag decouples from the differential lead-lag mode and the eigenvalues of the two non-rotating modes coincide with the eigenvalues (6.30) from the rotating system. With gravity effect, that is with ε, the Floquet transition matrix has to be computed as presented in Appendix G. To facilitate this, the system of equations (6.32) has first to be written in its canonical form:

$$\begin{Bmatrix}a_0\\ \zeta_{N/2}\\ a_0'\\ \zeta_{N/2}'\end{Bmatrix}' = \underbrace{\begin{bmatrix}0 & 0 & 1 & 0\\ 0 & 0 & 0 & 1\\ -\bar{\omega}_\zeta^2 & -\varepsilon\cos\psi & -2\xi_\zeta\bar{\omega}_\zeta & 0\\ -\varepsilon\cos\psi & -\bar{\omega}_\zeta^2 & 0 & -2\xi_\zeta\bar{\omega}_\zeta\end{bmatrix}}_{S(\psi)}\begin{Bmatrix}a_0\\ \zeta_{N/2}\\ a_0'\\ \zeta_{N/2}'\end{Bmatrix} \quad (6.33)$$

The Floquet transition matrix can now be calculated with (G.14) in a single integration pass. Assuming a step $h=\pi/2$ and the period $\psi_T=2\pi$ it follows that:

$$[Q] = [H(0)]\cdot[H(\pi/2)]\cdot[H(\pi)]\cdot[H(3\pi/2)] \quad (6.34)$$

where the matrices $[H(\psi_i=0)]$, ... ,$[H(\psi_i=3\pi/2)]$ are simply calculated by applying (G.10), (G.11), (G.12) and (G.13). Once the Floquet transition matrix is determined, its eigenvalues Λ_k can be used to calculate the eigenvalues of the system (6.32) according to (G.8):

$$\sigma_k = \frac{1}{2\psi_T}\ln\left(\Re(\Lambda_k)+\Im(\Lambda_k)\right) \quad ; \quad \bar{\omega}_k = \frac{1}{\psi_T}\operatorname{atan}\left(\frac{\Im(\Lambda_k)}{\Re(\Lambda_k)}\right) + K \quad ; \quad K = 0 \pm 1, \pm 2, \ldots \qquad (6.35)$$

Characteristic for equations with periodic coefficients, as stated in Appendix G, is a multiplicity of frequencies in the solutions (the so-called "aliasing" of the frequencies). Due to the presence of the atan function in the solution, the motion as given by (6.29) is not even periodic, each mode of motion consisting of a fundamental frequency $\bar{\omega}_k$ plus harmonics of frequency $\bar{\omega}_\zeta + K$ where K=0, ±1, ±2, ... is an integer.

For the KEWT numerical cases presented in Table 6.1, the tower eigenvalues s_T as calculated with (6.28), the blade lead-lag eigenvalues in the rotating system s_ζ as calculated with (6.30) and, in the non-rotating system, the collective lead-lag eigenvalues $s_{COL} = \sigma_{COL} \pm i\omega_{COL}$ and the differential lead-lag eigenvalues $s_{DIF} = \sigma_{DIF} \pm i\omega_{DIF}$ computed with the Floquet algorithm, are summarized in Table 6.2. Observe that for the system of equations (6.33), the basic eigenvalues of the collective and differential lead-lag modes superimpose, $s_{COL} = s_{DIF}$, and they are very close to the eigenvalues of the rotating system s_ζ. Nevertheless, the fundamental frequency for both modes splits into an infinite number of harmonics, which, as said before, is characteristic for the solutions of equations with periodic coefficients.

The relative position of the eigenvalues of Table 6.2 can now be represented in the complex plane using the critical pole distance method. Note that for the uncoupled case, the eigenvalues of the collective and lead-differential modes coincide.

Table 6.2 The eigenvalues of the motion for the KEWT numerical cases

Cases	*1 Actual Experiment*	*2 More lag damping*	*3 More tower damping*	*4 Stiffening the tower*	*5 Softening the tower*	*6 Stiffening the blades*
s_T	*- 0.04 ± 1.9995 i*	*- 0.04 ± 1.9995 i*	*- 0.04 ± 1.9995 i*	*- 0.04 ± 1.9995 i*	*- 0.04 ± 1.9995 i*	*- 0.04 ± 1.9995 i*
s_ζ	*-0.0818 ± 1.633 i*	*-0.1145 ± 1.631 i*	*-0.08175 ± 1.63295 i*	*-.0525 ± 1.0487 i*	*-0.184 ± 3.6754 i*	*-0.1333 ± 2.6627 i*
s_{COL}	*-0.083 ± 1.645 i*	*-0.117 ± 1.65 i*	*-0.089 ± 1.647 i*	*-.0504 ± 1.0892 i*	*-0.178 ± 3.681 i*	*-0.1558 ± 2.743 i*
s_{DIF}	*-0.083 ± 1.645 i*	*-0.117 ± 1.65 i*	*-0.089 ± 1.647 i*	*-.0504 ± 1.0892 i*	*-0.178 ± 3.681 i*	*-0.1558 ± 2.743 i*

Figure 6.8 to Figure 6.13 present the relative position between the chassis eigenvalues and the collective and differential lead-lag mode eigenvalues in cases 1 to 6 (only the positive imaginary part is used throughout) in the instability region at $\Omega=(1/2)\omega_T$.

Generally, as demonstrated in section 2.2.1 of Chapter 2, the eigenvalues s_T of the chassis bending mode and the rotating lead-lag eigenvalues s_ζ move along a semicircle of radius $\bar{\omega}_T$ respectively $\bar{\omega}_\zeta$ as the damping varies. These eigenvalues in frequency shift upwards, respectively downwards with ±1P, ±2P, ... from their basic values s_{COL} and s_{DIF}.

In the critical pole distance method, regions have to be identified where potential couplings between different modes occur. A critical region is defined as an area in the complex plane where different deflection modes are located close together. Looking at Figure 6.8 including the line of gravity excitation, one may see that a critical region may be defined which includes the gravity excitation, the differential mode in the harmonic of frequency ω_{DIF+1} (indicated by s_{DIF+1}) and the chassis eigenvalue s_T (the collective mode is not a dangerous one as being enough damped). Analysing Figure 6.9 through Figure 6.13, the evolution of this critical region can be followed:

- Figure 6.9 presents the position of the uncoupled pole corresponding to case 2 where the lead-lag damping was increased to 7%. The critical region as defined in case 1 remains unchanged.

- Figure 6.10 represents the situation of case 3 where the tower damping was increased to 5%. The chassis eigenvalue moves to the left, but the critical region as defined in case 1 does not change.

- Figure 6.11 corresponds to case 4 where the tower was stiffened. This case brings the differential lead-lag mode, chassis mode and gravity excitation very close to each other.

- Figure 6.12 represents the case 5 when the tower was softened. The modes situated in the critical region of case 1 move away from each other.

- Finally, Figure 6.13 presents case 6 when blades were stiffened. Also in this case, the modes situated in the critical region of case 1 move away from each other.

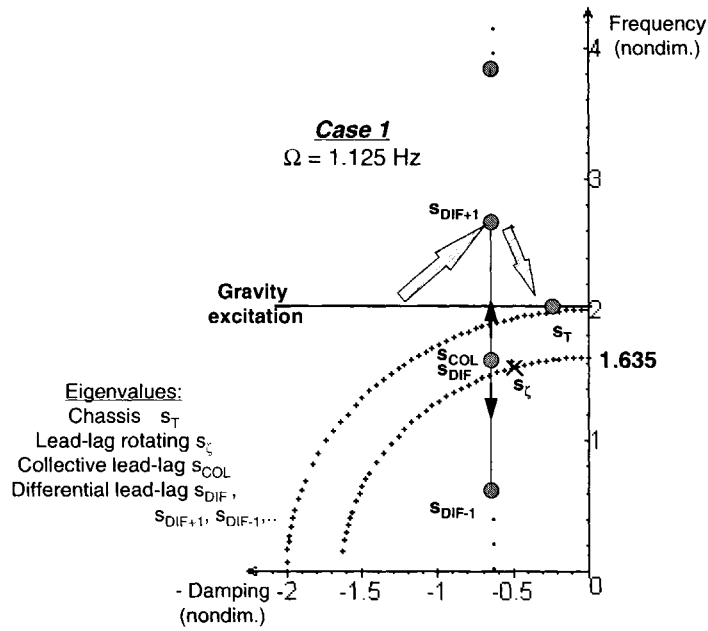

Figure 6.8 Uncoupled chassis and rotor eigenvalues in the instability region: Case 1

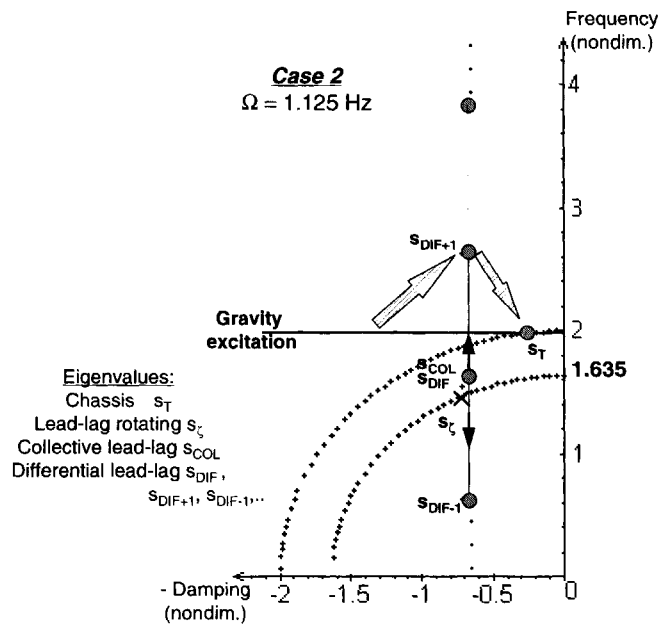

Figure 6.9 Uncoupled chassis and rotor eigenvalues in the instability region: Case 2

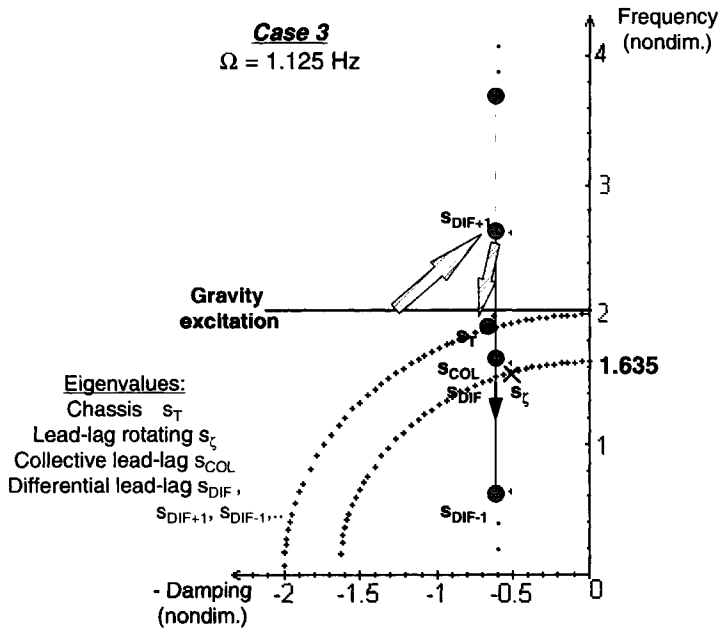

Figure 6.10 Uncoupled chassis and rotor eigenvalues in the instability region: Case 3

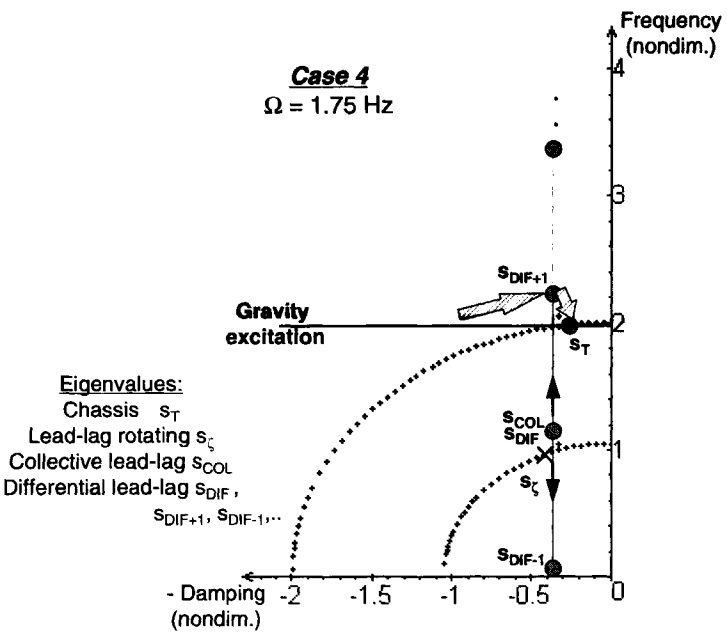

Figure 6.11 Uncoupled chassis and rotor eigenvalues in the instability region: Case 4

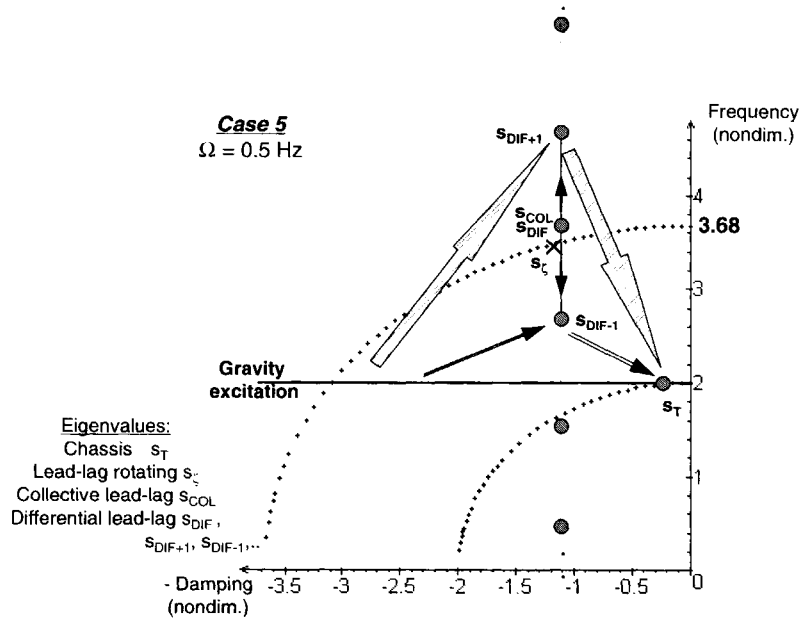

Figure 6.12 Uncoupled chassis and rotor eigenvalues in the instability region: Case 5

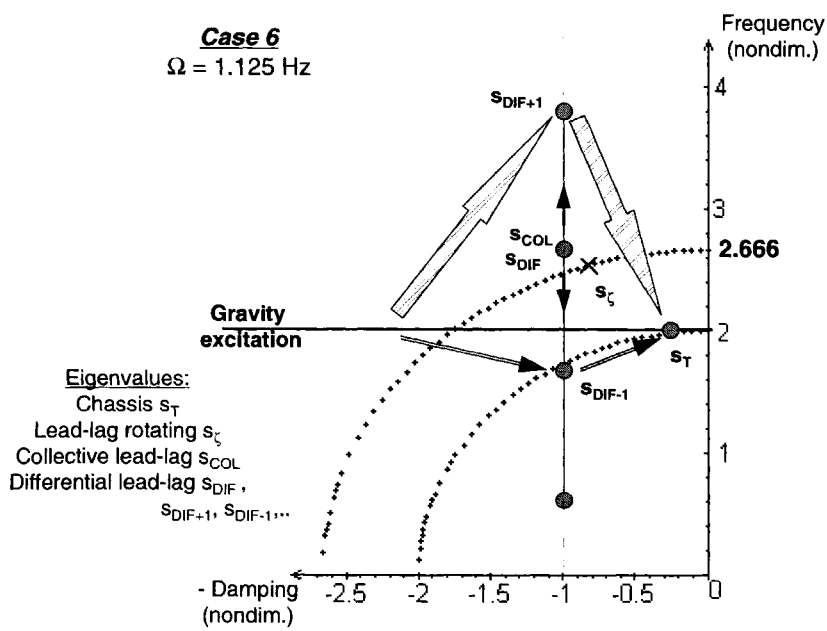

Figure 6.13 Uncoupled chassis and rotor eigenvalues in the instability region: Case 6

However, sometimes (as in cases 5 and 6) it seems that the chassis eigenvalue approaches the eigenvalue s_{DIF-1} representing a harmonic of frequency ω_{DIF}-1. How may one know whether this situation is not a dangerous one for the KEWT instability? To answer this, the critical pole distance criterion as derived in section 4.2.2 of Chapter 4 has to be applied to the poles presumed to be involved in the instability.

6.4 Application of the Critical Pole Distance Criterion to the KEWT Instability

The critical pole distance criterion developed in section 4.2.2 of Chapter 4 will be applied to the critical region as defined above, formed by the differential lead-lag mode + chassis + gravity excitation. There are three couplings to be investigated in the critical region revealed by the complex plane pictures:

1) a coupling between the first harmonic of the differential lead-lag mode of eigenvalue s_{DIF+1} and the chassis bending mode of eigenvalues s_T. In the critical pole distance criterion (4.43), this is equivalent with analysing the following relation:

$$|N_T \cdot N_{DIF+1}| = \sqrt{16\xi_T^2\xi_{DIF+1}^2\,\bar{\omega}_T^6\,\bar{\omega}_{DIF+1}^2 + 4\xi_T^2\bar{\omega}_T^2\left(\bar{\omega}_{DIF+1}^2 - \bar{\omega}_T^2\right)^2} \tag{6.36}$$

The values of damping ratio ξ_{DIF+1} and frequency ω_{DIF+1} may be determined from:

$$s_{DIF+1} = \sigma_{DIF} \pm i\left(\bar{\omega}_{DIF}+1\right) = -\bar{\omega}_{DIF+1}\xi_{DIF+1} \pm i\,\bar{\omega}_{DIF+1}\sqrt{1-\left(\xi_{DIF+1}\right)^2} \tag{6.37}$$

Equating the real and imaginary parts in (6.37), the equivalent frequency $\bar{\omega}_{DIF+1}$ and damping ξ_{DIF+1} characteristics of the harmonic s_{DIF+1} may be obtained as:

$$\bar{\omega}_{DIF+1} = \sqrt{\left(\bar{\omega}_{DIF}+1\right)^2 + \sigma^2} \quad ; \quad \xi_{DIF+1} = \frac{\xi_{DIF}}{\sqrt{\left(\bar{\omega}_{DIF}+1\right)^2 + \sigma^2}} \tag{6.38}$$

2) a coupling between the second harmonic of the differential lead-lag mode of eigenvalue s_{DIF-1} and the chassis bending of eigenvalues s_T, which seems to play a role in the KEWT instability in cases 5 and 6. The critical pole distance criterion can be expressed in this case as:

$$|N_T \cdot N_{DIF-1}| = \sqrt{16\xi_T^2\xi_{DIF-1}^2\,\bar{\omega}_T^6\,\bar{\omega}_{DIF-1}^2 + 4\xi_T^2\bar{\omega}_T^2\left(\bar{\omega}_{DIF-1}^2 - \bar{\omega}_T^2\right)^2} \tag{6.39}$$

in which the frequency and damping corresponding to the s_{DIF-1} mode can be calculated

as:

$$\bar{\omega}_{DIF-1} = \sqrt{(\bar{\omega}_{DIF} - 1)^2 + \sigma^2} \quad ; \quad \xi_{DIF-1} = \frac{\xi_{DIF}}{\sqrt{(\bar{\omega}_{DIF} - 1)^2 + \sigma^2}} \tag{6.40}$$

3) the gravity excitation is situated close to the first and second harmonic of the differential lead-lag mode. According to criterion (2.32) of Chapter 2, the distances $|2 - \bar{\omega}_{DIF+1}|$ and $|2 - \bar{\omega}_{DIF-1}|$ should therefore be investigated.

Table 6.3 summarizes the numerical results of the critical pole distance criterion (6.36) and (6.39) and the values for the distances of interest for cases 1 to 6 investigated in this chapter.

Table 6.3 Critical Pole Distance Criterion Applied to the KEWT Instability

Cases	*1 Actual Experiment.*	*2 More lag damping*	*3 More tower damping*	*4 Stiffening the tower*	*5 Softening the tower*	*6 Stiffening the blades*
$\|N_{DIFF+1}\, N_T\|$	*0.2409*	*0.246*	*0.6022*	*0.0372*	*1.4363*	*0.7598*
$\|N_{DIFF-1}\, N_T\|$	*0.2921*	*0.2963*	*0.7303*	*0.3214*	*0.2812*	*0.1294*
$\|2 - \omega_{DIF+1}\|$	*0.6342*	*0.6335*	*0.6342*	*0.0494*	*2.679*	*1.6657*
$\|2 - \omega_{DIF-1}\|$	*1.3618*	*1.3587*	*1.3618*	*1.9284*	*0.6817*	*0.3314*

How to interpret the magnitude of the values in Table 6.3 with respect to the KEWT instability? Recalling the simulations performed in section 6.1 of this chapter with a coupled model, it should be observed that cases 5 and 6, in which the instability was eliminated, show in the coupling between the harmonic ω_{DIF-1} of the differential lead-lag mode and the chassis bending mode, a value almost equal to that of case 1, representing the case of the instability. Therefore, the harmonic ω_{DIF-1} of the differential lead-lag mode does not participate in the KEWT instability. This is not the case for the harmonic ω_{DIF+1} of the differential lead-lag mode, which shows an increase of the value $|N_{DIFF+1} \cdot N_T|$ in the critical pole distance criterion. Concerning the distance between the gravity excitation and the harmonic ω_{DIF+1} of the differential lead-lag mode, in case 1 this distance may be considered sufficiently small, such that the gravity excitation is transmitted to this harmonic, this distance has become 4 times larger for the case 5 and 6 where the instability was eliminated. The gravity excitation in case 1 is far from the harmonic ω_{DIF-1}.

The interpretations of the dangerous pole distances in the critical pole distance method

are based on the conclusions obtained using a coupled model. Without this model, one would not be able to consider the harmonic of frequency ω_{DIF-1} as being harmless for the KEWT instability. In the preliminary design when no coupled model is developed, the energy flow method described in Chapter 4 may be of help in the interpretation of the critical pole distance method. However, the present section demonstrated that the results obtained in critical pole distance method are consistent to the posed problem.

Concluding, the harmonic ω_{DIF-1} of the differential lead-lag mode is not involved in the instability of the KEWT wind turbine. From the differential lead-lag mode harmonics involved in the instability, the prime responsible for this instability is the harmonic ω_{DIF+1}. The main path of coupling through which the gravity excitation is transmitted to the chassis and back is via the harmonic ω_{DIF+1} of the differential lead-lag mode. A quantification of the critical pole distance criterion on the basis of the data in Table 6.3 may be specified as follows:

If the quantity $|N_{DIFF+1} \cdot N_T| > 0.75$, *the instability of the KEWT wind turbine at a rotational speed* $\Omega = 1/2\omega_T$ *can be eliminated. A value* $|N_{DIFF+1} \cdot N_T| < 0.3$ *leads to a strong instability in this operating regime.*

Recalling the fact that in a 2-bladed wind turbine, the differential lead-lag mode replaces the cyclic modes, it follows that the KEWT instability is a special case involving an interaction between low-frequency chassis second bending mode and the high-frequencies of the differential lead-lag mode (actually corresponding to the cyclic lead-lag modes of a 3- or more-bladed rotor).

Concluding, the critical pole distance method applied to investigate the instability of the KEWT two-bladed wind turbine revealed new insight into the mechanism of this instability. The quantity $|N_{DIFF+1} \cdot N_T|$ in the critical pole distance criterion proved to be consistent with the physical insight into the problem and can be applied as a valid criterion in this instability.

Chapter 7

Quantification of the Flap-Lag Coupling in the Critical Pole Distance Method

The present chapter will derive quantitative criteria for the critical pole distance method concerning the coupling between the flapping and lead-lag motion in an articulated rotor when structural couplings (called kinematic couplings in articulated configurations) are included in the design of the rotor.

As described in section 3.4 of Chapter 3, structural couplings are introduced in articulated and hingeless rotors in order to improve the stability and response characteristics of helicopters and wind turbines. Although in most of the operating conditions these couplings may be advantageous, there are also cases when their effect is adverse. Appendix H described the most important structural couplings present in a rotor and their effect on helicopter behaviour. This chapter endeavours to verify whether the critical pole distance method is able to determine the effects that structural couplings have on helicopter modeling. From the structural couplings described in Appendix H only the influence of pitch-flap and pitch-lag couplings on helicopter rotor modeling will be investigated.

7.1 Derivation of a Coupled Flap-Lag Linear Model

Consider the rotor of an articulated helicopter as represented in Figure 7.1:

- the flapping hinge axis is assumed to be in the horizontal (x_R, y_R) plane, and is considered to be offset from the axis of rotation by a distance e_β (non-dimensional ε_β). A pitch-flap coupling $K_{P\beta}$ is introduced in the system by inclining the flapping hinge axis at an angle δ_3 to a line parallel to the y_R-axis (see Figure 7.2 (b));
- the lagging hinge axis is assumed to be in the vertical (x_R, z_R) plane, and is considered to be offset from the flapping hinge axis by a distance e_ζ (non-dimensional ε_ζ). A pitch-lag coupling $K_{P\zeta}$ is introduced in the system by inclining the lagging hinge axis at an angle δ_1 to a line parallel to the z_R -axis (see Figure 7.2 (a));

Observe that in a rotor with the lagging axis inclined, the lagging degree of freedom ζ is not the blade rotation about the lagging hinge axis but the projection of this rotation (noted as ζ_δ) on the lagging plane (x_R, y_R) as seen in Figure 7.2 (a); similarly the flapping degree of freedom β represents the projection of the blade rotation about the flapping hinge axis β_δ on the flapping plane (x_R, z_R) as seen in Figure 7.2 (b).

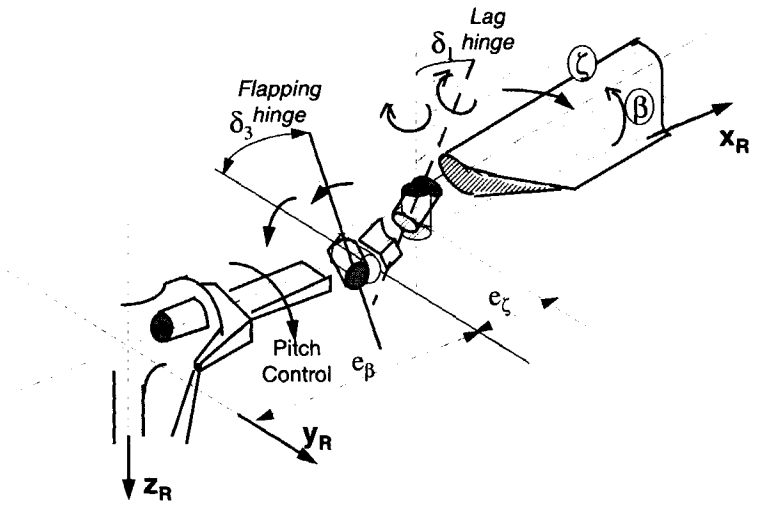

Figure 7.1 Rotor blade with inclined flapping and lag hinges

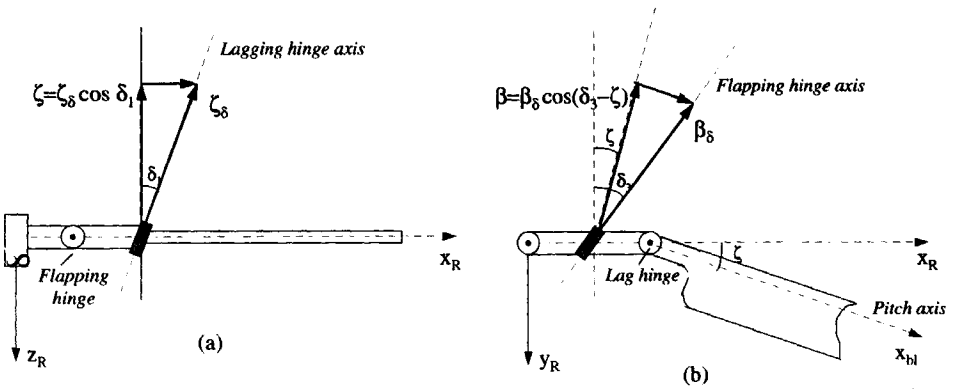

Figure 7.2 Flapping and lagging degrees of freedom in a rotor with inclined hinges

The sign conventions used for the pitch-flap and pitch-lag couplings are:

- the pitch-flap coupling (equivalent in this case with the so-called "δ_3 hinge") is positive ($\delta_3>0$) for flap up with pitch nose-down or flap down with pitch nose-up;
- the pitch-lag coupling (equivalent in this case with the so-called "δ_1 hinge") is positive for lag back with pitch down or blade lead with pitch up.

Morduchow [1950][74] derived the linear flap-lag equations of motion for an articulated

rotor helicopter in hovering flight under the following assumptions:

- the rotor angular speed is constant;
- no twist is included in the blade;
- the induced downwash is constant throughout the rotor disc v_i = const.

Assuming also that the blade has a constant chord c = const. and that the blade mass per unit chord is constant m = const, the taper integrals used in the equations of motion derived by **Morduchow** [1950][74] on page 12 can be analytically solved, hence the non-dimensional equations of motion of the coupled flap-lag motion of a helicopter blade in hovering flight become:

$$\begin{cases} M_\beta\,\beta'' + C_\beta\beta' + K_\beta\beta + & + C_{\beta\zeta}\zeta' + K_{\beta\zeta}\zeta = 0 \\ C_{\zeta\beta}\beta' + K_{\zeta\beta}\beta + M_\zeta\,\zeta'' + C_\zeta\zeta' + K_\zeta\zeta & = 0 \end{cases} \tag{7.1}$$

where the coefficients M_β, C_β, K_β, M_ζ, C_ζ, K_ζ are calculated neglecting the terms of order higher than ε_β^3, ε_β^4,... ε_ζ^3, ε_ζ^4, etc. The final expressions of the coefficients of the flap-lag equations (7.1) are:

$$\begin{aligned}
M_\beta &= H\left(\varepsilon_\beta+\varepsilon_\zeta\right)\left(1+\varepsilon_\zeta-\varepsilon_\beta\right)\\
M_\zeta &= H\left(\varepsilon_\beta+\varepsilon_\zeta\right)\\
C_\beta &= \left(\varepsilon_\beta+\varepsilon_\zeta+\varepsilon_\beta\,\varepsilon_\zeta+\frac{3\varepsilon_\zeta^2-\varepsilon_\beta^2}{2}\right)\\
C_\zeta &= \frac{C_{d0}}{\pi}\left(\varepsilon_\beta+\varepsilon_\zeta-\varepsilon_\beta\,\varepsilon_\zeta-\frac{\varepsilon_\beta^2+\varepsilon_\zeta^2}{2}\right)\\
K_\beta &= \left\{H\left(\varepsilon_\beta+\varepsilon_\zeta\right)\left[\beta_0 G\left(\frac{\varepsilon_\beta-\varepsilon_\zeta}{2}-1\right)+1+\varepsilon_\zeta\right]+\zeta_0\left(\varepsilon_\beta+\varepsilon_\zeta\right)^2+\left(\varepsilon_\beta+\varepsilon_\zeta+2\varepsilon_\beta\,\varepsilon_\zeta+\right.\right.\\
&\quad\left.\left.+\frac{\varepsilon_\beta^2+3\varepsilon_\zeta^2}{2}\right)\left(\tan\delta_3-\zeta_0\sec^2\delta_3\right)\right\}\\
K_\zeta &= \left(\varepsilon_\beta+\varepsilon_\zeta\right)\left\{H\left(\varepsilon_\beta+\varepsilon_\zeta\right)+v_i\left(\tan\delta_1-\beta_0\sec^2\delta_3\right)\right\}\\
C_{\beta\zeta} &= \left(\varepsilon_\beta+\varepsilon_\zeta\right)\left[\left(\varepsilon_\beta-1\right)\left(v_i+H\right)+\theta_0\left(2+\varepsilon_\zeta-\varepsilon_\beta\right)\right]\\
C_{\zeta\beta} &= H\left(\varepsilon_\beta+\varepsilon_\zeta\right)\left\{\left(1-\varepsilon_\beta\right)\left(H+2v_i\right)+\theta_0\left(1+\frac{\varepsilon_\beta-\varepsilon_\zeta}{2}\right)\right\}\\
K_{\beta\zeta} &= \left\{\beta_0\left(\varepsilon_\beta+\varepsilon_\zeta\right)^2+\left(\varepsilon_\beta+\varepsilon_\zeta+2\,\varepsilon_\beta\varepsilon_\zeta+\frac{\varepsilon_\beta^2+3\,\varepsilon_\zeta^2}{2}\right)\left(\tan\delta_1-\beta_0\sec^2\delta_3\right)\right\}\\
K_{\zeta\beta} &= \left(\varepsilon_\beta+\varepsilon_\zeta\right)v_i\left(\tan\delta_3-\zeta_0\sec^2\delta_3\right)
\end{aligned} \tag{7.2}$$

The following notations are used in (7.2): $H = \frac{m}{(\rho l \pi c)}$ where m is the blade mass per unit length, c the blade chord, ρ the air density, l the blade length measured from the lagging hinge; ε_β is the non-dimensional flapping hinge offset and ε_ζ the offset of the lagging hinge axis to the flapping hinge (see Figure 7.1); C_{d0} is the profile-drag coefficient of the blade section, and G the gravity term defined as $G = \frac{g}{\Omega^2 l}$, β_0, ζ_0 and θ_0 respectively are the steady-state flapping, lead-lag and pitch angles and v_i is the induced downwash. The constant induced downwash v_i throughout the rotor disc is calculated according to the simple momentum theory:

$$v_i = \sqrt{\frac{M_{hel}\, g}{2\pi R^2 \rho \Omega^2 l^2}} \tag{7.3}$$

The steady-state flapping β_0, lagging ζ_0 and pitch angles θ_0 may be determined by solving the following system:

$$\begin{cases} H\beta_0(\varepsilon_\beta+\varepsilon_\zeta)(1+\varepsilon_\zeta)+HG(\varepsilon_\beta+\varepsilon_\zeta)\left(1+\frac{\varepsilon_\zeta-\varepsilon_\beta}{2}\right)+\beta_0\zeta_0(\varepsilon_\beta+\varepsilon_\zeta)^2(1+\varepsilon_\zeta)+ \\ +\frac{v_i}{\Omega l}\left(1+\frac{C_{d0}}{2\pi}\right)(\varepsilon_\beta+\varepsilon_\zeta)(1+\varepsilon_\zeta)-\theta_0\left(\varepsilon_\beta+\varepsilon_\zeta+2\varepsilon_\beta\varepsilon_\zeta+\frac{\varepsilon_\beta^2+3\varepsilon_\zeta^2}{2}\right)=0 \\ H\zeta_0\frac{1}{2}(\varepsilon_\beta+\varepsilon_\zeta)(1+\varepsilon_\beta+\varepsilon_\zeta)(2-\varepsilon_\beta-\varepsilon_\zeta)-\frac{C_{d0}}{4\pi}(\varepsilon_\beta+\varepsilon_\zeta)(2+\varepsilon_\beta+\varepsilon_\zeta)- \\ -\frac{v_i}{\Omega l}\theta_0(\varepsilon_\beta+\varepsilon_\zeta)+\left(\frac{v_i}{\Omega l}\right)^2\frac{1}{2}(2-\varepsilon_\beta-\varepsilon_\zeta)(1+\varepsilon_\beta+\varepsilon_\zeta)=0 \\ \theta_0=\dfrac{\frac{1}{2}(2+\varepsilon_\beta+\varepsilon_\zeta)\left[\frac{M_{hel}g}{N\Omega^2\rho\pi c_0 l}+\beta_0\zeta_0\frac{v_i}{\Omega l}\left(1+\frac{C_{d0}}{2\pi}\right)+\beta_0\zeta_0(\varepsilon_\beta+\varepsilon_\zeta)\right]}{\varepsilon_\beta+\varepsilon_\zeta+\frac{2}{3}\varepsilon_\beta\varepsilon_\zeta+1+\frac{\varepsilon_\beta^2+\varepsilon_\zeta^2}{3}} \end{cases} \tag{7.4}$$

The next section will determine the strength of the coupling between the flapping and the lagging degrees of freedom by applying the critical pole distance method to the blade motion as described by (7.1). Subsequently, the predictions on the flap-lag coupling as obtained from the critical pole distance method will be compared to the results obtained when applying the vector shift method and the Milne criterion. Finally, based on the application of the critical pole distance method, criteria on the flap-lag

coupling will be established as a function of the kinematic pitch-flap and pitch-lag couplings.

7.2 Application of the Critical Pole Distance Method to the Flap-Lag Coupling

In order to apply the critical pole distance method one first has to represent the uncoupled flapping and lagging eigenvalues in the complex plane. The uncoupled flapping s_β and lagging s_ζ eigenvalues can be obtained by solving the equations (7.1) after putting the lead-lag, respectively flapping to zero in the first and second equation of motion. One obtains:

$$s_\beta = -\frac{C_\beta}{2M_\beta} \pm i\sqrt{\frac{K_\beta}{M_\beta} - \left(\frac{C_\beta}{2M_\beta}\right)^2} \tag{7.5}$$

$$s_\zeta = -\frac{C_\zeta}{2M_\zeta} \pm i\sqrt{\frac{K_\zeta}{M_\zeta} - \left(\frac{C_\zeta}{2M_\zeta}\right)^2} \tag{7.6}$$

The uncoupled flapping and lead-lag eigenvalues depend on the pitch-flap and pitch-lag couplings through the coefficients M_β, C_β, K_β, M_ζ, M_ζ, M_ζ of equations (7.1).

The critical pole distance criterion (4.43) derived in section (4.26) of Chapter 4 can be applied to investigate the conditions under which the blade flapping decouples from the lead-lag degree of freedom. For the flap-lag coupling, the critical pole distance criterion (4.43) gives that the flap-lag motion of a hovering helicopter may be assumed as being uncoupled when the quantity:

$$\left|N_\beta \cdot N_\zeta\right| = \sqrt{16\,\xi_\beta^2\,\xi_\zeta^2\,\omega_\beta^6\,\omega_\zeta^2 + 4\,\xi_\beta^2\,\omega_\beta^4\,(\omega_\zeta^2 - \omega_\beta^2)^2} \quad \text{is large} \tag{7.7}$$

The uncoupled flapping and lagging eigenvalues as given by (7.5) and (7.6) have to be transformed into the form used in the critical pole distance method, i.e.:

$$s_\beta = -\xi_\beta\,\omega_\beta \pm i\,\omega_\beta\sqrt{1-\xi_\beta^2} \quad ; \quad s_\zeta = -\xi_\zeta\,\omega_\zeta \pm i\,\omega_\zeta\sqrt{1-\xi_\zeta^2} \tag{7.8}$$

Equating the real and imaginary coefficients of the expressions s_β and s_ζ in (7.5) and (7.6) to the expressions of (7.8), the uncoupled flapping and lead-lag characteristics are

obtained as:

$$\omega_\beta^2 = \frac{K_\beta}{M_\beta} \quad ; \quad \xi_\beta = \frac{C_\beta}{2}\sqrt{\frac{1}{M_\beta K_\beta}}$$
$$\omega_\zeta^2 = \frac{K_\zeta}{M_\zeta} \quad ; \quad \xi_\zeta = \frac{C_\zeta}{2}\sqrt{\frac{1}{M_\zeta K_\zeta}} \tag{7.9}$$

Substituting (7.9) into (7.7), the critical pole distance criterion becomes:

$$\left|N_\beta \cdot N_\zeta\right| = \sqrt{\frac{C_\beta K_\beta}{M_\beta^2} \times \left[\frac{C_\zeta}{M_\zeta}\frac{K_\beta}{M_\beta} + \left(\frac{K_\zeta}{M_\zeta} - \frac{K_\beta}{M_\beta}\right)^2\right]} \quad \text{is large} \tag{7.10}$$

in which the coefficients M_β, C_β, K_β, M_ζ, M_ζ, M_ζ are given as in (7.2).

The meaning of "large" in the critical pole distance criterion (7.10) may be quantified by considering different pitch-flap and pitch-lag couplings in the articulated helicopter rotor. The following cases will be investigated:

1. no pitch-flap coupling and different pitch-lag couplings: $\delta_3 = 0$, $\delta_1 \neq 0$;
2. no pitch-lag coupling and different pitch-flap couplings: $\delta_1 = 0$, $\delta_3 \neq 0$;
3. positive pitch-lag coupling and negative pitch-flap coupling and $|\delta_1| = |\delta_3|$;
4. negative pitch-lag coupling and positive pitch-flap coupling and $|\delta_1| = |\delta_3|$;
5. negative pitch-lag coupling and negative pitch-lag coupling and $|\delta_1| = |\delta_3|$;
6. positive pitch-lag coupling and positive pitch-flap coupling and $|\delta_1| = |\delta_3|$.

Consider the numerical example of a 3-bladed helicopter rotor as given in Table 7.1 (the same numerical data used by **Morduchow** [1950][74]).

The relative position in the complex plane of the uncoupled flapping and lead-lag eigenvalues for different combinations of pitch-flap and pitch-lag coupling is presented in Figure 7.3 to Figure 7.8 and the corresponding values of the critical pole distance criterion (7.10) for each combination are calculated in Table 7.2 to Table 7.7.

On the one hand, looking at Figure 7.3 to Figure 7.8, it may be concluded that, according to the critical pole distance method, the flap-lag motion in Figure 7.3, Figure 7.6 and Figure 7.8 can be assumed as uncoupled, whereas in Figure 7.4, Figure 7.5 and Figure 7.7 it should be considered as coupled. Varying the pitch-lag coupling mainly affects the blade lead-lag frequency of the uncoupled lead-lag motion: a positive δ_1 inclination (negative pitch-lag coupling) increases the lead-lag frequency, a negative δ_1 inclination (positive pitch-lag coupling) decreases the lead-lag frequency

(see Figure 7.3). Varying the pitch-flap coupling primarily affects the blade uncoupled flapping characteristics. Decreasing the δ_3 angle to negative values (positive pitch-flap coupling) leads to an abrupt decrease of the flapping frequency and even instability (see Figure 7.4). This instability is a pure flapping divergence and can be explained as follows: usually, an upward flapping perturbation β results in a component of the aerodynamic moment on the blade, trying to counteract the motion, as demonstrated in Appendix B on page 204. Using a negative δ_3 transforms this moment into one reinforcing the blade flapping motion, thus leading to divergence.

Table 7.1 Numerical example of a 3-bladed helicopter

Helicopter weight	$M_{hel}\, g$ = *3000 pounds*
Number of blades	$N = 3$
Rotor speed	Ω = *25 rad/sec*
Tip radius of the rotor	R = *21.5 feet*
Length of the Blade	l = *20 feet*
Eccentricity	e_β=*1 feet*
Eccentricity	e_ζ= *0.5 feet*
Blade Mass per unit length at root	m = *5.5347 kg/m*
Blade Chord	c=*1 foot*
Profile drag coefficient	$C_{d\,0}$= *0.01*

On the other hand, one may observe from the values of the critical pole distance criterion of Table 7.2 to Table 7.7 that $|N_\beta N_\zeta|$ varies between 0 and 3.13. The question that arises is: how to quantify the term "large" for $|N_\beta N_\zeta|$ in order to consider the flapping and lead-lag degrees of freedom uncoupled? The investigation of the magnitude of $|N_\beta N_\zeta|$ in the critical pole distance criterion will be analyzed in the next sections by comparing the results of the critical pole distance criterion with two other prediction methods presented in chapter 4: the vector shift method and the Milne criterion. To apply these last two methods, the coupling terms in the flap-lag equations of motion (7.1) have to be known as well.

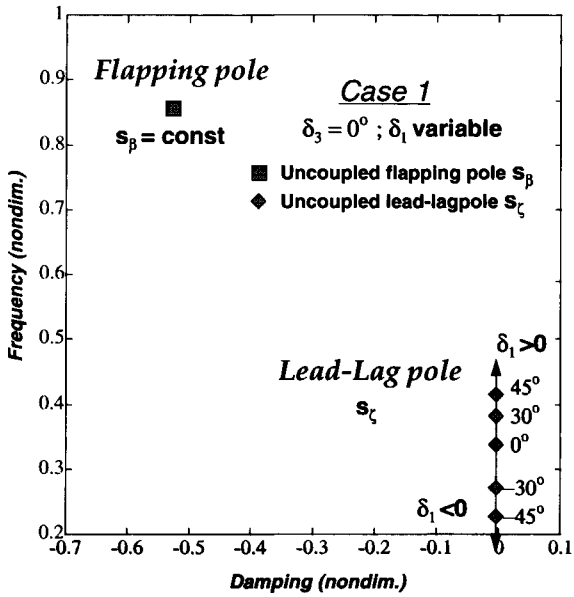

Figure 7.3 Uncoupled flapping and lead-lag eigenvalues with varying pitch-lag coupling: Case 1

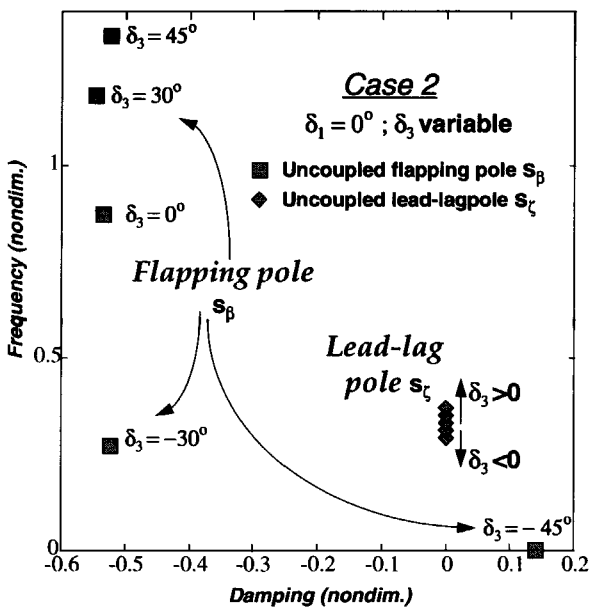

Figure 7.4 Uncoupled flapping and lead-lag eigenvalues with varying pitch-flap coupling: Case 2

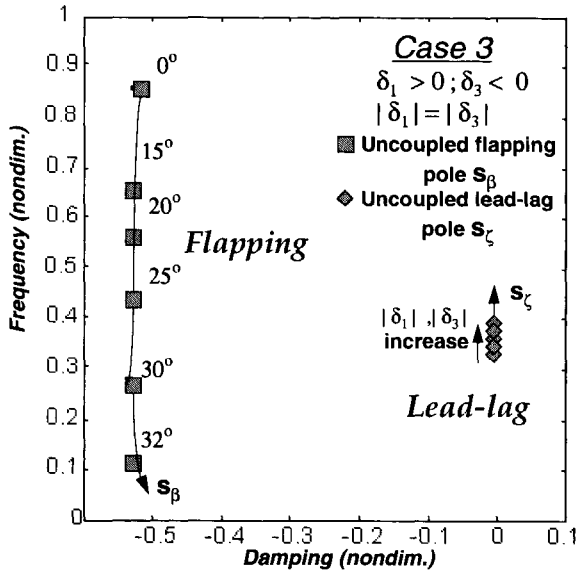

Figure 7.5 Uncoupled flapping and lead-lag poles as both pitch-flap and pitch-lag couplings vary: Case 3

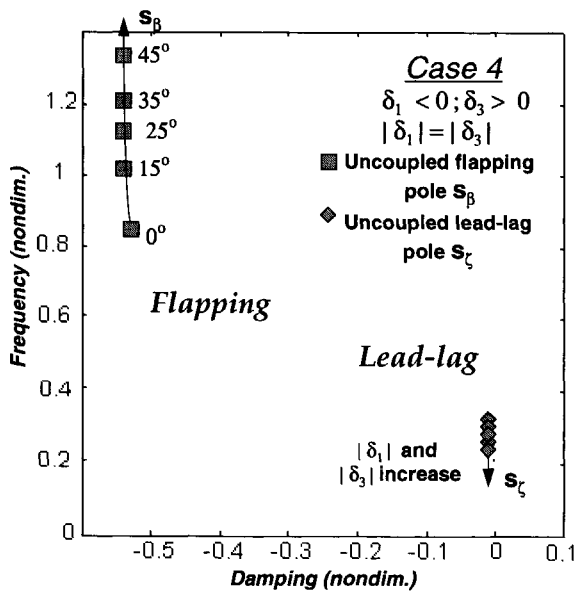

Figure 7.6 Uncoupled flapping and lead-lag poles as both pitch-flap and pitch-lag couplings vary: Case 4

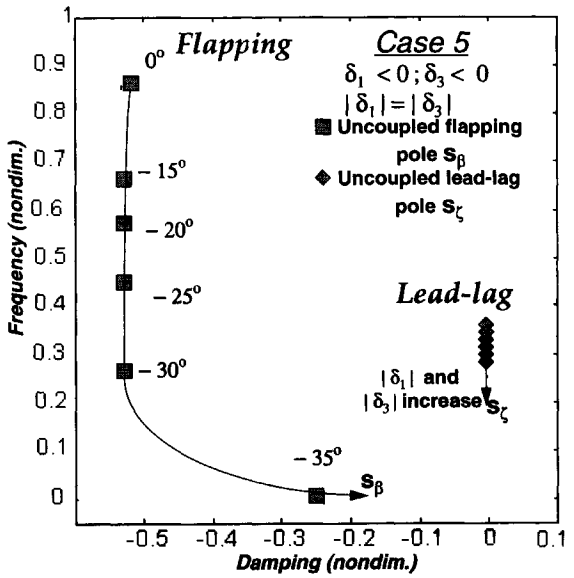

Figure 7.7 Uncoupled flapping and lead-lag poles as both pitch-flap and pitch-lag couplings vary: Case 5

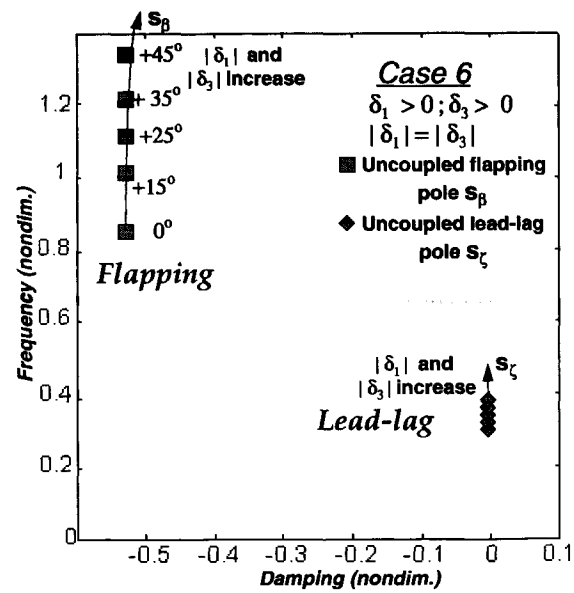

Figure 7.8 Uncoupled flapping and lead-lag poles as both pitch-flap and pitch-lag couplings vary: Case 6

Table 7.2: Critical Pole Distance Criterion: Case 1

$\delta_1(deg)$	$\lvert N_\beta N_\zeta \rvert$
45°	*0.9129*
30°	*0.9399*
0°	*0.9768*
-30°	*1.0137*
-45°	*1.0408*

Table 7.3: Critical Pole Distance Criterion: Case 2

δ_3 *(deg)*	$\lvert N_\beta N_\zeta \rvert$
45°	3.0398
30°	2.1039
0°	0.9768
-30°	0.1532
-45°	instability

Table 7.4: Critical Pole Distance Criterion: Case 3

$\delta_1(deg)$	$\delta_3(deg)$	$\lvert N_\beta N_\zeta \rvert$
0°	0°	0.9768
15°	-15°	0.5291
20°	-20°	0.3896
25°	-25°	0.2559
30°	-30°	0.1318
32°	-32°	0.0868

Table 7.5: Critical Pole Distance Criterion: Case 4

$\delta_1(deg)$	$\delta_3(deg)$	$\lvert N_\beta N_\zeta \rvert$
0°	0°	0.9768
-15°	15°	1.4923
-25°	25°	1.9078
-35°	35°	2.4276
-45°	45°	3.1314

Table 7.6: Critical Pole Distance Criterion: Case 5

$\delta_1(deg)$	$\delta_3(deg)$	$\lvert N_\beta N_\zeta \rvert$
0°	0°	0.9768
-15°	-15°	0.5577
-20°	-20°	0.4253
-25°	-25°	0.2967
-30°	-30°	0.1747
-35°	-35°	0.0664

Table 7.7: Critical Pole Distance Criterion: Case 6

$\delta_1(deg)$	$\delta_3(deg)$	$\lvert N_\beta N_\zeta \rvert$
0°	0°	0.9768
15°	15°	1.4533
25°	25°	1.8347
35°	35°	2.3092
45°	45°	2.9482

7.3 Application of the Vector Shift Method to the Investigation of Flap-Lag Coupling

The main idea in the vector shift method is that if the uncoupled poles are close to the corresponding coupled poles, the poles may be assumed as uncoupled, whereas if the uncoupled and the coupled poles are separated from each other, the poles may be considered coupled. According to Table 4.1, in the vector shift method the vector $|\Delta s_i/s_i|$ has to be computed. For the flap-lag case this means that two distances have to be determined: that between the uncoupled flap pole s_β and the coupled flap-lag pole $s_{\beta\zeta}$, and that between the uncoupled lag pole s_ζ and the coupled lag-flap pole $s_{\zeta\beta}$.

The coupled flap-lag $s_{\beta\zeta}$ and lag-flap $s_{\zeta\beta}$ eigenvalues can be obtained by solving the coupled equations of motion (7.1). A good approximation of the solution of system (7.1) may be obtained using the Ferrari method (see **Morduchow** [1950][74]). According to this method, the solution of an equation $f(x) = 0$ is $x_0 - f(x_0)/\frac{df}{dx}(x_0)$ where x_0 is considered a first approximation of the sought solution.

Assuming as first approximation for the flap-lag problem (7.1) the uncoupled flap eigenvalue s_β as given by (7.5) and the uncoupled lag eigenvalue s_ζ as given by (7.6), and defining the function f(s) as the characteristic equation of system (7.1):

$$f(s) = \begin{vmatrix} M_\beta s^2 + C_\beta s + K_\beta & C_{\beta\zeta} s + K_{\beta\zeta} \\ C_{\zeta\beta} s + K_{\zeta\beta} & M_\zeta s^2 + C_\zeta s + K_\zeta \end{vmatrix} = 0 \tag{7.11}$$

the coupled eigenvalues may be obtained using the Ferrari method as:

$$s_{\beta\zeta} = s_\beta - \frac{f(s_\beta)}{\frac{df}{ds}(s_\beta)} \quad ; \quad s_{\zeta\beta} = s_\zeta - \frac{f(s_\zeta)}{\frac{df}{ds}(s_\zeta)} \tag{7.12}$$

Performing the calculation in (7.12), the following expressions of the coupled flap-lag

eigenvalues are obtained:

$$s_{\beta\zeta} = s_\beta - \frac{\begin{array}{c} M_\beta M_\zeta s_\beta^4 + (M_\beta C_\zeta + M_\zeta C_\beta) s_\beta^3 + (M_\beta K_\zeta + M_\zeta K_\beta + C_\beta C_\zeta - C_{\beta\zeta} C_{\zeta\beta}) s_\beta^2 + \\ + (C_\beta K_\zeta + C_\zeta K_\beta - C_{\beta\zeta} K_{\zeta\beta} - C_{\zeta\beta} K_{\beta\zeta}) s_\beta + K_\beta K_\zeta - K_{\beta\zeta} K_{\zeta\beta} \end{array}}{\begin{array}{c} 4M_\beta M_\zeta s_\beta^3 + 3(M_\beta C_\zeta + M_\zeta C_\beta) s_\beta^2 + 2(C_\beta C_\zeta + M_\beta K_\zeta + M_\zeta K_\beta - C_{\beta\zeta} C_{\zeta\beta}) s_\beta + \\ + C_\beta K_\zeta + C_\zeta K_\beta + M_\zeta K_\beta - C_{\beta\zeta} K_{\zeta\beta} - C_{\zeta\beta} K_{\beta\zeta} \end{array}} \quad (7.13)$$

$$s_{\zeta\beta} = s_\zeta - \frac{\begin{array}{c} M_\beta M_\zeta s_\zeta^4 + (M_\beta C_\zeta + M_\zeta C_\beta) s_\zeta^3 + (M_\beta K_\zeta + M_\zeta K_\beta + C_\beta C_\zeta - C_{\beta\zeta} C_{\zeta\beta}) s_\zeta^2 + \\ + (C_\beta K_\zeta + C_\zeta K_\beta - C_{\beta\zeta} K_{\zeta\beta} - C_{\zeta\beta} K_{\beta\zeta}) s_\zeta + K_\beta K_\zeta - K_{\beta\zeta} K_{\zeta\beta} \end{array}}{\begin{array}{c} 4M_\beta M_\zeta s_\zeta^3 + 3(M_\beta C_\zeta + M_\zeta C_\beta) s_\zeta^2 + 2(C_\beta C_\zeta + M_\beta K_\zeta + M_\zeta K_\beta - C_{\beta\zeta} C_{\zeta\beta}) s_\zeta + \\ + C_\beta K_\zeta + C_\zeta K_\beta + M_\zeta K_\beta - C_{\beta\zeta} K_{\zeta\beta} - C_{\zeta\beta} K_{\beta\zeta} \end{array}} \quad (7.14)$$

The relative positions of the coupled and uncoupled poles in the vector shift method for cases 1 to 6 are represented in Figure 7.10 to Figure 7.15. As can be seen in Figure 7.10 in case 1 where only pitch-lag coupling is used in the model, varying the pitch-lag coupling δ_1 affects both the coupled flapping and lagging damping and frequency characteristics. When only pitch-flap coupling is used (Figure 7.11), varying the pitch-flap coupling δ_3 affects primarily the flapping eigenvalues and secondly the lagging characteristics (the large variation of flapping characteristics is caused by the flapping divergence described in the previous section).

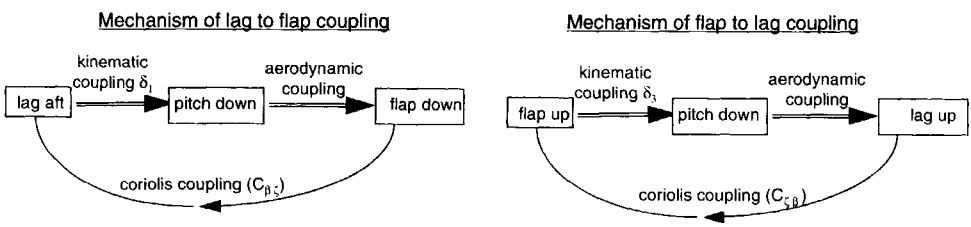

Figure 7.9 Mechanism of flap-lag coupling

The mechanism of coupling between the flap and lead-lag degrees of freedom can be described as seen in Figure 7.9: a lag aft or a flap up of the blade induces a pitch down deflection via the kinematic pitch-lag and pitch-flap couplings respectively. Via the aerodynamic coupling this pitch deflection is transmitted further as a flap and lag deflection respectively, coupling the motion of the lag to the flap and vice versa. For example, the mechanism of lag to flap coupling can be explained as follows: as the blade moves aft in the lead-lag plane (decreasing lag angle) the pitch angle decreases. This decrease in pitch produces a decrease in lift force and the blade flaps down. This

downward flapping in turn produces a backward Coriolis force which tends to push the blade further backward.

On the basis of the coupled eigenvalue representation of Figure 7.10 and Figure 7.11, the following design criterion in choosing the kinematic couplings may be derived:

- for the pitch-lag coupling: a negative δ_1 (pitch down with lead) should be used in order to increase the damping in the lagging motion and avoid the instability in lagging, without forgetting that by doing so, the damping and frequency in flapping both decrease.
- for the pitch-flap coupling: a positive δ_3 (flap up with pitch-nose down) should be used in order to avoid the flapping divergence, without forgetting that by doing so, the damping in lagging is decreased.

Figure 7.12 to Figure 7.15 show the relative position of the coupled and uncoupled poles as both the pitch-flap and pitch-lag couplings vary. One may observe that using inclination both for the flapping and lagging hinges, the position of the flapping pole is mainly determined by the pitch-flap angle, whereas the position of the lead-lag pole is mainly determined by the pitch-lag coupling. Cases 3 and 5 show strong coupling between the flapping and lagging degrees of freedom. This is due to the fact that in these cases an unfavourable coupling is used (in case 3 the pitch-flap coupling is adverse, whereas in case 5 both the pitch-flap and pitch-lag coupling are adverse).

As described above, two distances have to be calculated when using the vector shift method for the flap-lag coupling analysis: one is between the uncoupled flap pole and the coupled flap-lag pole $(s_{\beta\zeta}-s_\beta)/s_\beta$ and an other between the uncoupled lag pole and the coupled lag-flap pole $(s_{\zeta\beta}-s_\zeta)/s_\zeta$. Table 7.8 to Table 7.13 summarize the values of these distances and their interpretation in the vector shift method for cases 1 to 6. Since there are two distances to be interpreted, for clarity the strength of the flap-lag coupling is underlined in Table 7.10 to Table 7.13.

Looking at Table 7.8 it is obvious that, for example, for a pitch-lag coupling $\delta_1 = -45^\circ$ (lead-lag retreating with pitch up) the results are contradictory: the distance in flap should be interpreted as very lightly coupled whereas the distance in lag should be considered as very heavily coupled. Since the pitch-lag coupling mainly influences the lead-lag motion, it is therefore considered that only the distance in lag is of importance. Accordingly, for a $\delta_1 = -45^\circ$ one should consider the motion as heavily coupled. This result is correct, the motion is heavily coupled in a useful way in this case, since a negative pitch-lag coupling of -45° increases the damping in the lead-lag motion four times as much as compared to a 0° pitch-lag coupling.

Also, the results presented in Table 7.9 relative to the distance between the flap and flap-lag poles and lag and lag-flap poles are contradictory. For example, in the case of pitch-flap coupling $\delta_3 = -45^\circ$ (flap up with pitch up), the motion should be considered

either heavily or moderately coupled. However, since the pitch-flap coupling mainly affects the flap motion, the strength of the flap-lag coupling should be judged only by the distance between the flap and flap-lag poles. It follows that a pitch-flap coupling $\delta_3 = -45°$ is heavily coupled motion, which is correct since the flapping motion is unstable for this value of the pitch-flap coupling.

When both pitch-flap and pitch-lag couplings are used, one should interpret the flap-lag coupling according to the strongest indication of coupling between the flap and flap-lag poles respectively lag and lag-flap poles.

Before comparing the results of the vector shift method to the critical pole distance method, the next section will apply the Milne criterion to the flap-lag problem as well.

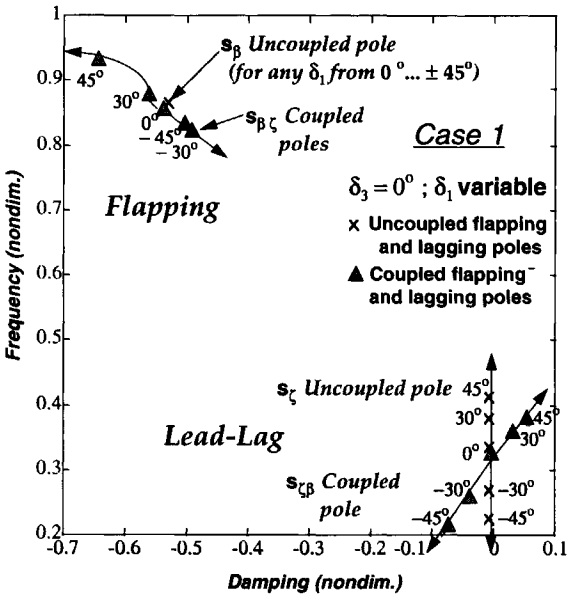

Figure 7.10 Coupled and uncoupled flapping and lead-lag poles with varying pitch-lag coupling: Case 1

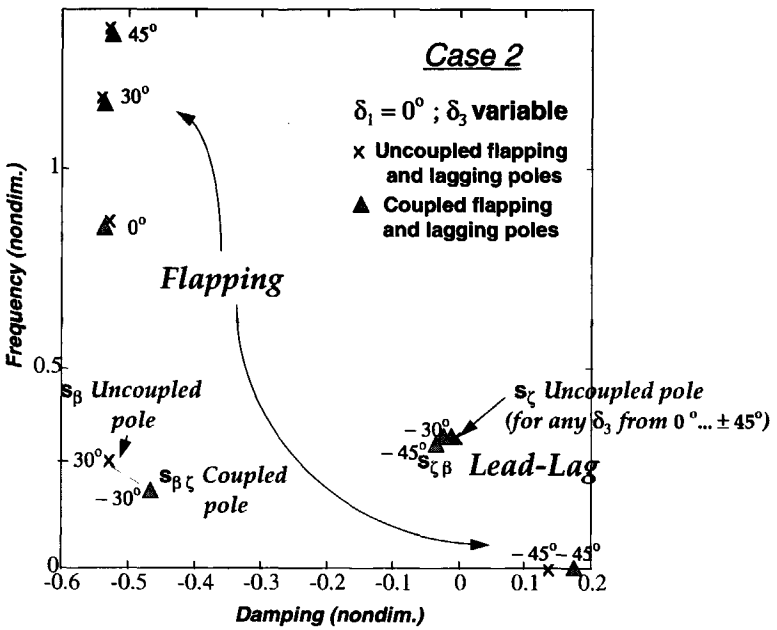

Figure 7.11 Coupled and uncoupled flapping and lead-lag poles with varying pitch-flap coupling: Case 2

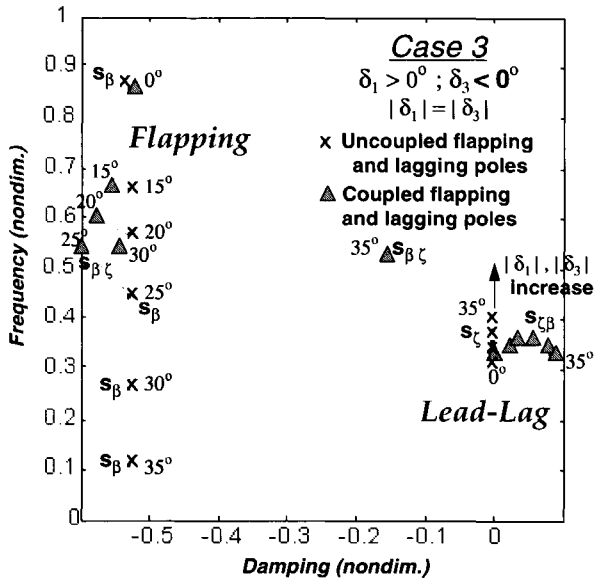

Figure 7.12 Coupled and uncoupled flapping and lead-lag poles as the pitch-flap and pitch-lag couplings vary: Case 3

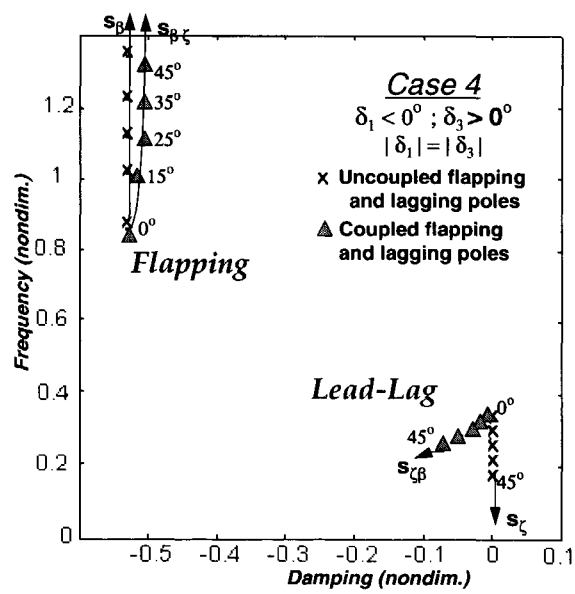

Figure 7.13 Coupled and uncoupled flapping and lead-lag poles as the pitch-flap and pitch-lag couplings vary: Case 4

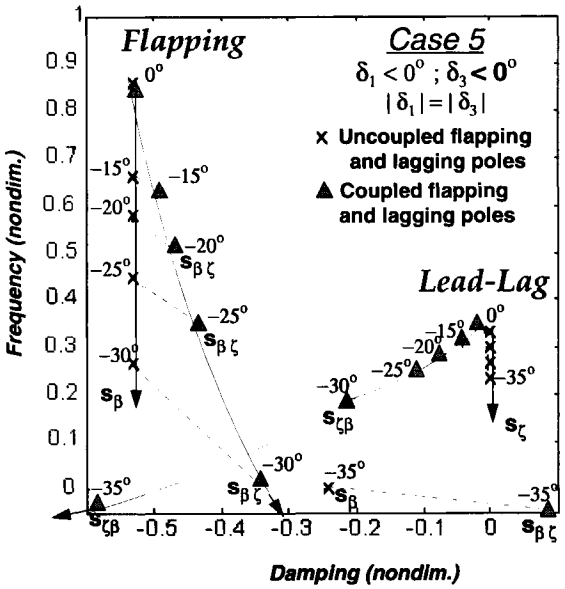

Figure 7.14 Coupled and uncoupled flapping and lead-lag poles as the pitch-flap and pitch-lag couplings vary: Case 5

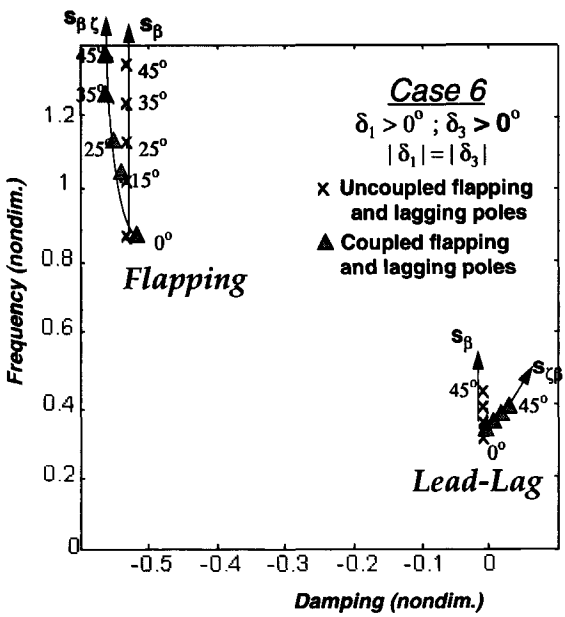

Figure 7.15 Coupled and uncoupled flapping and lead-lag poles as the pitch-flap and pitch-lag couplings vary: Case 6

Table 7.8: Vector Shift Method when only Pitch-Lag Coupling is used: Case 1

δ_1	Flap		Lag	
45°	0.1160	MC	0.1790	**MC**
30°	0.0424	VLC	0.0979	**LC**
0°	0.0119	LC	0.0142	**VLC**
-30°	0.0568	LC	0.1669	**MC**
-45°	0.0425	VLC	0.3514	**VHC**

Table 7.9: Vector Shift Method when only Pitch-Flap coupling is used: Case 2

δ_3	Flap		Lag	
45	0.0039	VLC	0.0161	VLC
30	0.0043	VLC	0.0137	VLC
0°	0.0119	VLC	0.0142	VLC
-30	0.1729	MC	0.0843	LC
-45	0.2356	HC	0.1910	MC

Table 7.10: Vector Shift Method for the Pitch-Flap and Pitch-Lag Variation Case 3

δ_1 δ_3	Flap		Lag	
0°, 0°	0.0089	VLC	0.0146	VLC
15°,-15°	0.0307	VLC	0.0611	LC
20°,-20°	0.0654	LC	0.1025	LC
25°,-25°	0.1396	MC	0.1594	MC
30°,-30°	0.3734	HC	0.2372	HC
32°,-32°	1.0224	VHC	0.2749	HC

Table 7.11: Vector Shift Method for Pitch-flap and Pitch-Lag Variation: Case 4

δ_1 δ_3	Flap		Lag	
0°, 0°	0.0089	VLC	0.0146	VLC
-15°,15°	0.0195	VLC	0.0636	LC
-25°, 25°	0.0232	VLC	0.1047	MC
-35°, 35°	0.0258	VLC	0.1719	MC
-45°, 45°	0.0279	VLC	0.3068	MC

Table 7.12:Vector Shift Method for Pitch-Flap and Pitch-Lag Variation: Case 5

δ_1 δ_3	Flap		Lag	
0, 0	0.0089	VLC	0.0146	VLC
-15 -15	0.0644	LC	0.1292	MC
-20 -20	0.1194	MC	0.2284	MC
-25 -25	0.2569	HC	0.4259	HC
-30 -30	0.9303	VHC	0.8197	VHC
-35-35	2.5411	VHC	1.1091	VHC

Table 7.13: Vector Shift Method for Pitch-Flap and Pitch-Lag Variation: Case 6

δ_1 δ_3	Flap		Lag	
0°, 0°	0.0089	VLC	0.0146	VLC
15°,15°	0.0096	VLC	0.0331	VLC
25°, 25°	0.0150	VLC	0.0584	LC
35°, 35°	0.0185	VLC	0.0857	LC
45°, 45°	0.0209	VLC	0.1186	MC

VLC- Very Lightly Coupled; LC- Very Lightly Coupled; MC- Moderately Coupled; HC- Heavily Coupled; VHC- Very Heavily Coupled

7.4 Application of Milne Criterion to the Investigation of Flap-Lag Coupling

Assume that the blade flapping and lead-lag dynamics are well separated and that the lead-lag motion is the slower one, compared to the flapping motion. In order to apply the Milne criterion, the equations of motion (7.1) have to be written in the semi-canonical form:

$$\begin{Bmatrix} \beta' \\ \beta \\ \zeta' \\ \zeta \end{Bmatrix}' - \begin{bmatrix} -C_\beta / M_\beta & -K_\beta / M_\beta & -C_{\beta\zeta} / M_\beta & -K_{\beta\zeta} / M_\beta \\ 1 & 0 & 0 & 0 \\ -C_{\zeta\beta} / M_\zeta & -K_{\zeta\beta} / M_\zeta & -C_\zeta / M_\zeta & -K_\zeta / M_\zeta \\ 0 & 0 & 1 & 0 \end{bmatrix} \begin{Bmatrix} \beta' \\ \beta \\ \zeta' \\ \zeta \end{Bmatrix} = \begin{Bmatrix} 0 \\ 0 \\ 0 \\ 0 \end{Bmatrix} \tag{7.15}$$

The following parameters can be defined:

- radius of the slow motion $r = \max(|s_\zeta|)$;
- radius of the fast motion $R = \min(|s_\beta|)$;
- maximum of the coupling terms in first and third equations of system (7.15):

$$M_1 = \max\left(|-C_{\beta\zeta} / M_\beta| , |-K_{\beta\zeta} / M_\beta| \right)$$
$$M_2 = \max\left(|-C_{\zeta\beta} / M_\zeta| , |-K_{\zeta\beta} / M_\zeta| \right)$$

The Milne criterion described in section 4.5.2 of Chapter 4 (equations (4.52) and (4.53)) for the flap-lag (7.15) states that the flap and lead-lag motion can be considered weakly coupled if and only if:

1. $$\left[\frac{r}{R} \right] << 1 \tag{7.16}$$

2. $$\max(FL) = \left| \frac{M_1 \cdot M_2}{R^2} \right| << 1 \tag{7.17}$$

These two conditions were computed for all pitch-flap and pitch-lag combinations investigated in this chapter. The results are summarized in Table 7.14 to Table 7.19.

Table 7.14 Milne Criteria when only Pitch-Lag Coupling Varies: Case 1

δ_1(deg)	| r/R |	max(FL)
45°	0.4061	.0092
30°	0.3743	.005
0°	0.3258	.00063
-30°	0.2688	.0063
-45°	0.2178	.0105

Table 7.15 Milne Criteria when only Pitch-Flap Coupling Varies: Case 2

δ_3(deg)	| r/R |	max(FL)
45°	0.2231	0.000655
30°	0.2544	0.000539
0°	0.3258	0.000638
-30°	0.5531	0.0025
-45°	2.3211	0.0709

Table 7.16 Milne Criteria when Pitch-Flap and Pitch-Lag Couplings Vary: Case 3

δ_1(deg)	δ_3(deg)	| r/R |	max(FL)
0°	0°	0.3258	0.000638
15°	- 15°	0.4169	0.0028
20°	- 20°	0.4639	0.0048
25°	- 25°	0.5302	0.0081
30°	- 30°	0.6364	0.0141
32°	- 32°	0.702	0.0183

Table 7.17 Milne Criteria when Pitch-Flap and Pitch-Lag Couplings Vary: Case 4

δ_1(deg)	δ_3(deg)	| r/R |	max(FL)
0°	0°	0.3258	0.000638
- 15°	15°	0.2641	0.0026
- 25°	25°	0.2276	0.0036
- 35°	35°	0.1899	0.0045
- 45°	45°	0.1453	0.0055

Table 7.18 Milne Criteria when Pitch-Flap and Pitch-Lag Couplings Vary: Case 5

δ_1(deg)	δ_3(deg)	| r/R |	max(FL)
0°	0°	0.3258	0.000638
- 15°	- 15°	0.3589	0.0048
- 20°	- 20°	0.3778	0.0073
- 25°	- 25°	0.4062	0.0114
- 30°	- 30°	0.4548	0.0192
- 35°	- 35°	1.0205	0.1303

Table 7.19 Milne Criteria when Pitch-Flap and Pitch-Lag Couplings Vary: Case 6

δ_1(deg)	δ_3(deg)	| r/R |	max(FL)
0°	0°	0.3258	0.00063
15°	15°	0.3068	0.0015
25°	25°	0.2971	0.0025
35°	35°	0.2884	0.0034
45°	45°	0.2801	0.0042

Analysing the numerical values of Table 7.14 to Table 7.19 the Milne criterion was quantified in the following statement:

The flapping and lagging motions decouple if and only if:

- $| r / R | < 0.35$
- $| max(FL) | < 0.005$

For $|r/R| \geq 0.35$ the flapping and lagging motions couple. Observe that the second condition concerning the coupling terms has also to be fulfilled in order to decouple the flapping and lead-lag degrees of freedom. For example, see Table 7.14, where, although for negative pitch-lag couplings the ratio |r/R| is smaller than 0.35, the motion must still be regarded as coupled so as to acquire the useful increase in damping in the lead-lag motion induced by the flapping motion in the rotor model.

7.5 The Critical Pole Distance Criterion for the Flap-Lag Coupling

On the basis of the results of the vector shift method and the Milne criterion and of the described characteristics of the pitch-flap and pitch-lag couplings and their physical interpretation, returning to the critical pole distance criterion (7.10), the following quantification of the flap-lag coupling was established:

The strength of the coupling between the flap-lag motion in a rotor blade can be judged as follows in the critical pole distance criterion:

		$\| N_\beta N_\zeta \|$	< 0.05	*Very Heavily Coupled*
0.05	$<$	$\| N_\beta N_\zeta \|$	< 0.3	*Heavily Coupled*
0.3	$<$	$\| N_\beta N_\zeta \|$	< 2	*Moderately Coupled*
2	$<$	$\| N_\beta N_\zeta \|$	< 3	*Lightly Coupled*
		$\| N_\beta N_\zeta \|$	> 3	*Very Lightly Coupled.*

This critical pole distance criterion may be used to judge whether the blade flapping and lead-lag motions may be decoupled when pitch-flap and pitch-lag couplings are included in the rotor blade model.

Chapter 8

Conclusions

"But, to make this dream come true, first we engineers have to strive harder to achieve simplicity. Our technical community is too easily lulled into complacency. In truth, it is much easier to make something more complicated than to make it simpler"

Bartram Kelley [1982]

8.1 Review of the Goals and Limitations

The goal of the present dissertation was to develop a general method which can be used by the design-analyst to pre-determine the necessary degrees of freedom required by a helicopter or a horizontal-axis wind turbine simulation model. To this end, the so-called "critical pole distance method" was developed. The main advantage of this method is that the designer can obtain some indication in advance as to the level of model detail required, before starting the tedious effort of deriving the large system of equations of motion characteristic to rotary wing problems. The critical pole distance method can be used both as a design tool in the preliminary design when different candidate configurations have to be compared, and as an evaluation tool to obtain insight into already-existing simulation models.

As discussed in the present dissertation, the problem of modeling in rotary wing engineering must be seen in a broad context: on the one hand the adequate representation of rotor flexibility and adequate mathematical and aerodynamic modeling and on the other hand the scope, the required accuracy and the case considered, are all important factors in the process determining which degrees of freedom are necessary to be included in simulation models.

The critical pole distance method developed in this work is actually a formalization of the intuitive fact that, in the complex plane representation, regions of agglomeration of eigenvalues represent critical regions in which the corresponding modes couple (in the time-domain this would mean that their time constants are comparable). Specific for this method is that the critical regions are determined by the uncoupled modes of motion. As described in section 4.1, Chapter 4, the critical pole distance method contains the following steps:

1. Assuming the system (helicopter and horizontal axis wind turbine) as a summation of mutually uncoupled subsystems -blades, hub, (air)frame etc.-, the equations of motion for every uncoupled deflection mode are derived.

2. For each subsystem, the thus formulated equations of motion are solved. The

equations of motion associated with the non-rotating subsystems can be directly solved, their solutions represent the eigenvalues (poles) of the modes of motion. The equations of motion associated with the rotating subsystems are first transformed to the non-rotating system through the so called "Coleman transformation" (multiblade coordinate transformation MCT) and then solved in order to obtain the eigenvalues of the modes of the rotating system in the non-rotating system.

3. Using the representation in the complex plane, "critical regions" are defined. A "critical region" is an area of the complex plane where potential couplings between different modes occur- within and between subsystems. The criterion for a critical region is the relative position of the poles in the complex plane, i.e., if the poles in the complex plane associated with the uncoupled motion of different modes of motion are "close" together, one may account for the coupling effects between these modes in the simulation model; if the poles are sufficiently separated, they may be assumed as uncoupled in the simulation model. The crucial point in the critical pole distance method is therefore how to quantify the relative distance of the poles in order to decide which coupling effects are important in the simulation model and which are not.

4. Finally, conclusions concerning the degrees of freedom to be used in the simulation model are drawn, dividing the modes of motion into three classes:

   - modes to be discarded from the model,
   - modes to be kept separate in the model (neglecting the coupling terms between these modes and other degrees of freedom),
   - modes to be kept in the model including the coupling effects that are essential for the model.

As to step 3 of in the critical pole distance method, a criterion was developed in section 4.2 of Chapter 4 able to quantify whether or not two degrees of freedom of an n degree-of-freedom dynamic system which form a critical region in the complex plane may be considered as being uncoupled. Representing by ω_i respectively ω_j the natural frequency of degrees of freedom x_i and x_j, and by ξ_i and ξ_j their critical damping ratio, the critical pole distance criterion can be generally formulated as following:

Two degrees of freedom x_i and x_j of an n degree-of-freedom linearly coupled system may be assumed as uncoupled if the quantity (8.1) may be considered sufficiently large.

$$\left|N_i N_j\right| = \xi_i\omega_i\left\{\left(9\xi_i^2\omega_i^2+16\omega_i^2\right)\left[\xi_i^4\omega_i^4+2\xi_i^2\omega_i^2\left(\omega_i^2+2\xi_j^2\omega_j^2+\omega_j^2\right)+4\xi_i\omega_i\xi_j\omega_j\times\right.\right.$$
$$\left.\left.\times\left(\omega_i^2+\xi_i^2\omega_i^2+\omega_j^2\right)+4\omega_i^2\xi_j^2\omega_j^2+\left(\omega_j^2-\omega_i^2\right)^2\right]\right\}^{1/2} \quad \text{is large} \tag{8.1}$$

Criterion (8.1) was particularized for two cases:

- the degrees of freedom x_i and x_j are situated near or on the imaginary axis:

$$\left|N_i \cdot N_j\right| = \sqrt{16\xi_i^2\xi_j^2\omega_i^6\omega_j^2 + 4\xi_i^2\omega_i^4\left(\omega_j^2 - \omega_i^2\right)^2} \quad \text{is large} \tag{8.2}$$

- the degrees of freedom x_i and x_j are situated near or on the real axis:

$$\left|N_i \cdot N_j\right| = \left\{ \left|\omega_j^4\xi_j^4 + \omega_j^2\xi_j^2\left(\omega_i^2 + \omega_j^2\right) + \omega_i\omega_j\left(\omega_i\omega_j + 4\omega_j^2 sxi_j^3\xi_i\right) - 2\omega_j^3\xi_j^3\left(\omega_i\xi_i + \omega_j\xi_j\right) - 2\omega_i\omega_j^2\xi_j\left(\xi_i + \xi_j\right)\right|\right\}^{1/2} \quad \text{is large} \tag{8.3}$$

Criterion (8.2) is equivalent to the affirmation that two degrees of freedom decouple either if their uncoupled eigenvalues are sufficiently separated in frequency such that the term $\left(\omega_j^2 - \omega_i^2\right)$ is sufficiently large or, if they are close in frequency, they are both sufficiently damped so that their product of critical damping ratio $\xi_i^2 \cdot \xi_j^2$ is sufficiently large.

The term "large" in the critical pole distance criterion (8.1), (8.2) or (8.3) must be quantified by analysing different case-problems which may provide a "feeling" as to the meaning of large and small, for the dynamic system analyzed.

Next, addressing the limitations of the critical pole distance method and its criterion, one should bear in mind that the critical pole distance criterion is actually an engineering approach to the problem and a multitude of case-problems have to be investigated before being able to draw conclusions. Further, the criterion depends on the uncoupled characteristics of the system only for a coupling between two degrees of freedom. If more than two modes of motion seem to couple in the critical region, the critical pole distance criterion must be considered in its general formulation (equation (4.33) in Chapter 4) and some coupling terms must be computed as well. A way to avoid calculating these terms may be to consider the degrees of freedom in the critical region in pairs and apply the critical pole distance criterion to each pair. In this way, only the uncoupled eigenvalues need to be determined. However, if the coupling terms are not difficult to determine, the designer is advised to use the general criterion (4.33) involving both the coupled and uncoupled characteristics of the system. For example, in a 3 degree-of-freedom system, according to criterion (4.35), the ratios $\frac{T_{12}T_{21}}{N_1N_2}$, $\frac{T_{23}T_{32}}{N_2N_3}$, $\frac{T_{13}T_{31}}{N_3N_1}$, $\frac{T_{12}T_{23}T_{31}}{N_1N_2N_3}$, $\frac{T_{21}T_{32}T_{13}}{N_1N_2N_3}$ should be examined, where T_{12}, ...T_{31} are the coupled system's characteristics and N_1, ... N_3 are the uncoupled system's

characteristics, in order to decide whether the degree of freedom x_2 decouples from x_1 and x_3. Finally, it should not be disregarded that investigating eigenvalues in a dynamic system implies working in a linearized system and one is therefore able to investigate linear couplings only. Often, the non-linear terms are the malicious ones in rotary-wing problems. To the above-discussed limitations of the present dissertation, the assumptions listed in section 1.3 of Chapter 1 should be added.

8.2 Specific Cases and Results

The critical pole distance method was applied to the following rotary wing modeling problems:

- in Chapter 5 for a piloted simulation model in order to examine the couplings between the helicopter body modes and rotor disc-tilt modes;

- in Chapter 6 for the investigation of an instability of a two-bladed horizontal-axis wind turbine;

- in Chapter 7 to investigate the conditions under which the blade flapping degree of freedom decouples from the lead-lag motion when pitch-flap and pitch-lag couplings were included in the model.

In each of the problems investigated a large amount of simulations with a coupled model were performed in order to obtain some understanding on how to quantify the term "large" in the critical pole distance criterion. Additionally, the predictions made were compared to those obtained when by the Milne criterion and the Vector Shift Method presented in Chapter 4.

Concerning the effects of disc-tilt dynamics on body dynamics in piloted simulation modeling, the following conclusions were drawn:

- Starting with the simple case of a hypothetical helicopter equipped first with a teetering rotor and then with a semi-rigid rotor, performing a pitch manoeuvre representing the transition from hover to forward flight, it was demonstrated that while the addition of the disc-tilt dynamics to the body dynamics is hardly noticeable in performing the manoeuvre with the teetering rotor, for the semi-rigid rotor, the disc-tilt dynamics does influence the helicopter response rather profoundly. Essentially, using the critical pole distance method, it was observed that for a semi-rigid rotor, the body motion speeds up and the rotor disc-tilt motion slows down, thus coupling with each other.

- Studying the natural behaviour of two helicopters differing through their rotor configurations, the articulated Puma SA-330 and the semi-rigid Bölkow Bö-105, using the critical pole distance method, it was demonstrated that there were two

critical regions of coupling between the body and the rotor disc-tilt motion: first, a critical region in the longitudinal plane of motion, formed by the body short-period mode eigenvalue and the regressing flapping mode eigenvalue, and a second critical region in the lateral plane of motion formed by the body roll-subsidence mode eigenvalue and the regressing flapping mode eigenvalue. In the first critical region, representing the variation of the quantity (8.2) with the helicopter advance ratio, it was found as a rule of thumb that the quantity $|N_{Freg}N_{SP}|$ (as expressed in (5.24)) had to be larger than 0.1, in order to consider the regressing flapping mode decoupled from the body short-period mode. This was the case with the articulated Puma, but not with the semi-rigid Bö-105. In the second critical region, representing the variation of the quantity (8.3) with the helicopter advance ratio, it was found as a rule of thumb that the quantity $|N_{Freg}N_{roll}|$ (as expressed in (5.32)) had to be larger than 0.1, in order to consider the regressing flapping mode decoupled from the body roll-subsidence mode. Again, this was the case for the articulated Puma, but not for the semi-rigid Bö-105.

- Studying the piloted behaviour of the articulated Puma SA-330 and the semi-rigid Bölkow Bö-105 and using the values of the gains as required to fly these two helicopters in a simulated deceleration and side-step manoeuvre, it was found that, in the above-mentioned first critical region, the quantity $|N_{Freg}N_{SP}|$ had to be larger than 0.3 in order to consider the regressing flapping mode decoupled from the body short-period mode. For the articulated Puma helicopter this depended on the manoeuvre performed: for the deceleration manoeuvre the criterion was met, whereas for the side-step manoeuvre it was not. The semi-rigid Bö-105 was characterized by a $|N_{Freg}N_{SP}|$ value always much smaller than 0.3, thus implying coupling of the body short-period mode and the regressing flapping mode.

The critical pole distance criterion for the body-rotor disc-tilt coupling was formulated as follows:

In helicopter piloted simulation modeling, the strength of the coupling between the body modes and the regressing flapping mode can be quantified as follows:

$|N_{body}\ N_{Freg}| < 0.1$ *Heavily Coupled;*
$0.1 < |N_{body}\ N_{Freg}| < 0.3$ *Moderately to Lightly Coupled;*
$0.3 < |N_{body}\ N_{Freg}|$ *Very Lightly Coupled.*

The articulated Puma SA-330 helicopter in this sense was characterized by very light to moderate couplings, whereas the semi-rigid Bö-105 helicopter was characterized by strong couplings between both the body short-period/regressing flapping modes and roll-subsidence/regressing flapping modes.

Concerning the KEWT instability in the chassis second bending mode and rotor lead-lag modes as given by the Coleman transformation for a two-bladed horizontal-axis wind turbine investigated in Chapter 6, the following conclusions were drawn:

- According to the critical pole distance method, the prime factor responsible for this instability is the coupling between the harmonic ω_{DIF+1} of the differential lead-lag mode and the chassis second bending mode. Through this harmonic the differential lead-lag mode feeds energy to the chassis These two modes form the main path through which the gravity excitation is transmitted from the blade to the chassis and back. The quantity $|N_{DIFF+1} \cdot N_T|$ (as expressed in 6.4) in the critical pole distance criterion was formulated as follows:

  If the quantity $|N_{DIFF+1} \cdot N_T| > 0.75$, the instability of the KEWT wind turbine at a rotational speed $\Omega = 1/2\omega_T$ can be eliminated. A value $|N_{DIFF+1} \cdot N_T| < 0.3$ leads to a strong instability in the operating regime considered.

- Concerning the mechanism of instability, it was observed that the tower acts as a dynamic absorber (Frahm damper) whenever alternating forces start to be induced in the rotor, stoping any tendency of the rotor to oscillate. The oscillations of the rotor-chassis system would tend to slow down, but because of the gravity-constant rpm combination, energy is continuously fed into the system. As a result, the rotor oscillations amplify. In response, the tower oscillations increase with the effort to stop the rotor oscillations. Thus, the gravity force action, the system constant rpm and the tower behaviour as a dynamic absorber are three important elements in the KEWT instability.

- It was found that the instability could be eliminated by increasing the tower damping ratio as in case 3, softening the tower as in case 5 or stiffening the blades as in case 6.

Concerning the criteria on the blade flapping/lead-lag coupling of a rotor system including pitch-flap and pitch-lag couplings investigated in Chapter 7, the following conclusions were drawn:

The strength of the coupling between the flap-lag motion in a rotor blade can be categorized as follows in the critical pole distance criterion:

		$\lvert N_\beta N_\zeta \rvert$	< 0.05	*Very Heavily Coupled*
0.05	$<$	$\lvert N_\beta N_\zeta \rvert$	< 0.3	*Heavily Coupled*
0.3	$<$	$\lvert N_\beta N_\zeta \rvert$	< 2	*Moderately Coupled*
2	$<$	$\lvert N_\beta N_\zeta \rvert$	< 3	*Lightly Coupled*
3	$<$	$\lvert N_\beta N_\zeta \rvert$		*Very Lightly Coupled.*

where $|N_\beta N_\zeta|$ was expressed by (7.10).

The above-reviewed results on the necessary degrees of freedom to be considered in simulation models developed for the three problems investigated in this dissertation were collected in Figure 8.1.

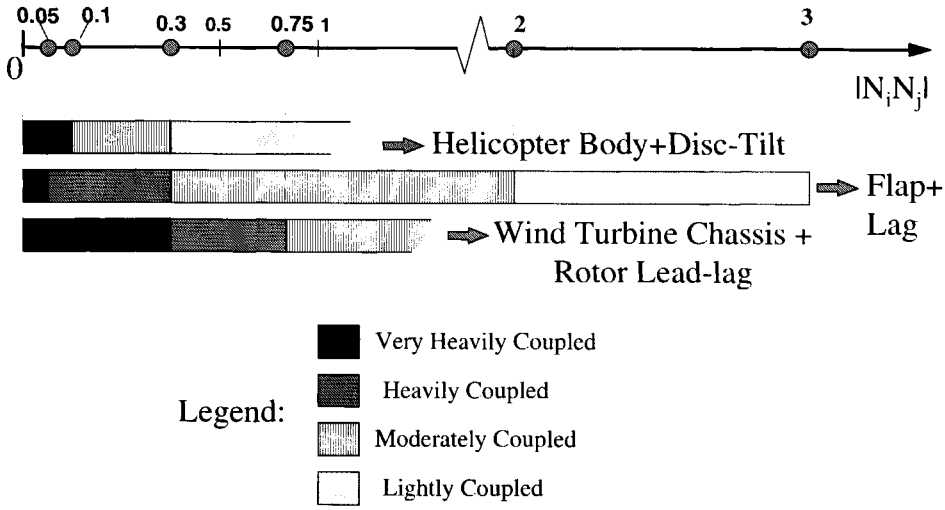

Figure 8.1 Quantification of the Critical Pole Distance Criterion for the Analyzed Problems

It should be underlined that all the cases investigated in the present dissertation in the critical pole distance method needed a pre-knowledge of the coupled system behaviour (this was obtained either from time-domain simulations, either applying the Milne criterion of Vector Shift method). This pre-knowledge is necessary in this stadium of the work because the criteria in critical pole distance method have to be substantiated for different cases. Ones obtained, these criteria can be applied to a class of similar problems without having available information on the behaviour of the coupled system. The criteria derived in this dissertation are consistent with the physics of the case-problems analyzed.

Another important conclusion of the present dissertation was discussed in section 2.7 in Chapter 2 and later in section 3.3.2 of Chapter 3 and refers to the interpretation of Figure 2.10. According to this figure, it appears that modern wind turbines are stiffening in terms of non-dimensional flapping and lead-lag natural frequencies ω_β/Ω and ω_ζ/Ω. This renders them vulnerable to the very complicated dynamic instabilities characteristic for such stiff systems, as known from experiences with early helicopter design. This very problem caused helicopter configurations to evolve towards softer solutions. This observation serves as a warning to wind turbine designers to be aware that the current tendency toward higher power generating designs, with its associated scale increase, may introduce the problem of dynamic instabilities to the wind turbine

community.

Finally, it should be mentioned that the present work attempted to draw a parallel between the problem of helicopter and wind turbine modeling. These two systems are characterized by common and specific parameters. Some of these parameters were reviewed in the present dissertation (see section 2.7 of Chapter 2). In Appendix H special attention was paid to the structural couplings existing in the blade which have a great impact on the level of detail considered in the simulation model. It was underlined that although helicopters and horizontal-axis wind turbines both involve a rotating and a non-rotating structure, the frequency range for which the models are built is different, a difference which it seems will become more accentuated in the future. This may lead to a diverging approach in simulation modeling. The custom of applying helicopter modeling philosophy for wind turbine design, as was practised in the past, may not be feasible in the future.

8.3 Future Work

The present dissertation endeavoured to provide the designer with a new tool to assess the necessary amount of detail needed in a simulation model. As seen in Figure 8.1, all conclusions drawn in this dissertation refer to interactions between specific degrees of freedom for specific problems applied to helicopters and wind turbines. The quantities in the critical pole distance criterion in all cases analyzed were non-dimensionalized in order to give a general form to the problem.

However, to transform the critical pole distance method into a general design tool, the database of problems analyzed must be extended. In this context, one should for example investigate for piloted simulation modeling, the effects of the rotor lead-lag modes on the body modes for a number of different simulated manoeuvres. For wind turbine modeling, the database should be extended with cases of modern wind turbines e.g. such as the STABTOOL-project (see **van Holten et. al.** [1999][48]). Finally, the effects of structural couplings listed in Appendix H involved in a simulation model should be quantified in the critical pole distance criterion (one example of quantification in this sense was given in Chapter 7. An extension of this chapter would be the analysis of hingeless helicopters in forward flight). Also, it would be interesting to determine for which applications the critical pole distance criterion presented in Chapter 4, section 4.2 is both necessary and sufficient in order to decouple system's degrees of freedom.

Concluding, the present dissertation may be considered as a first step in developing a general method which can be used by the design-analyst to determine the necessary degrees of freedom for helicopters and horizontal-axis wind turbines. The method developed in the present dissertation may be used as a simple intuitive tool before deriving a complete model, being an engineering approach to the simulation modeling problem. The validity of the critical pole distance method was evaluated by comparing

it to similar methods. The strength of the critical pole distance method is that it may be used as a simple engineering approach, before a comprehensive model is developed. A condition for the method to become a useful tool is to enhance the fidelity of the quantification of the employed criteria, by means of an elaborate data collection, based on a large quantity of base-studies.

Bibliography

1 Aponso, B.L., et.al., "*Identification of Higher Order Helicopter Dynamics Using Linear Modeling Methods*", J. of the American Helicopter Society, Vol.39, No.4, July 1994, pp.3-11

2 Anderson, W.D., "*Investigation of Reactionless Mode Stability Characteristics of a Stiff Inplane Hingeless Rotor System*", 29th Forum of the American Helicopter Society, May 1973, Paper No.734

3 Anderson, C., et.al., "*The Use of Blade Mounted Dampers to Eliminate Edgewise Stall Vibration*", European Wind Energy Conference, Nice, March 1-5, 1999

4 Azuma, A., Saito, S., Nakamura, F., "*Dynamic Response of Wind turbine to Yawed Wind*", 10th European Rotorcraft Forum, The Hague, Netherlands, Aug. 28-31, 1984, paper no. 55

5 Bennett, J.A.J., "*The Era of the Autogiro*", The First Cierva Memorial Lecture, J. of the Royal Aeronautical Society, Vol. 65, No. 610, October 1961, pp. 649-660

6 Bielawa, R.L., "*Rotary Wing Structural Dynamics and Aeroelasticity*", AIAA Education Series, Copyright by the American Institute of Aeronautics and Astronautics Inc., Washington, D.C., 1992

7 Bir, G.S., Wright, A.D., Butterfield, C.P., "*Stability Analysis of a Variable-Speed Wind Turbine*", AIAA-97-0965, 35th Aerospace Sciences Meeting and Exhibit, Jan. 6-10, 1997, Reno, N.V.

8 Blake, R.B., Burkam, J.E., Loewy, R.G., "*Recent Studies of the Pitch-Lag Instabilities of Articulated Rotors*", J. of the American Helicopter Society, Vol. 6, No. 3, July 1961, pp.13-21

9 Bousman, W.G., Sharpe, D.L., Ormiston, R.A., "*An Experimental Study of Techniques for Increasing the Lead-Lag Damping of Soft-Inplane Hingeless Rotors*", 32nd Annual National V/STOL Forum of the American Helicopter Society, May, 1976, Washington, D.C.

10 Bousman, W.G., "*An Experimental Investigation of the Effects of Aeroelastic Couplings on Aeromechanical Stability of a Hingeless Rotor Helicopter*", J. of the American Helicopter Society, Vol.26, No.1, Jan 1981, pp. 46-54

11 Burkam, J.E., Miao W.-L., "*Exploration of Aeroelastic Stability Boundaries with a Soft-in-Plane Hingeless-Rotor Model*", J. of the American Helicopter Society, Vol. 17, No. 4, October 1972, pp.27-35

12 Cannon, Robert H., Jr., "*Dynamics of Physical Systems*", Published by McGraw-Hill, Inc., 1967

13 Carpenter, P.J., Fridovich, B., *"Effect of Rapid Blade Pitch Increase on the Thrust and Induced Velocity Response of a Full Scale Helicopter Rotor"*, NACA TN-3044, Nov. 1953

14 Chen, R.T.N., Lebacqz, J.V., Aiken, E.W., Tischler, M.B., *"Helicopter Mathematical Models and Control Law Development for Handling Qualities Research"*, NASA CP-2496, Proceedings of a Conference held at Ames Research Centre, Moffett Field, March 17-19, 1987

15 Chen, R.T.N., and Hindson, W.S., *"Influence of High-Order Dynamics on the Helicopter Flight-Control System Bandwidth"*, 11th European Rotorcraft Forum, London, England, Sept.10-13, 1985, paper no. 83

16 Chopra, I., *"Perspectives in Aeromechanical Stability of Helicopter Rotors"*, Vertica Vol. 4, No.4, 1990, pp. 457-508

17 Chopra, I., Dugundji, J., *"Non-linear Dynamic Response of a Wind Turbine Blade"*, J. of Sound and Vibration, Vol 63, No. 2, 1979, pp. 265-286

18 Chou, Pei Chi, "*Pitch-Lag Instability of Helicopter Rotors*", J. of the American Helicopter Society, Vol. 3, No. 3, July 1958, pp. 30-39

19 Coleman, R.P. and Feingold, A.M., "*Theory of Self-Excited Mechanical Oscillation of Helicopter Rotors with Hinged Blades*", NACA TR-1351, 1956

20 Curtiss, H.C. Jr., and Shupe, N.K., *"A Stability and Control Theory for Hingeless Rotors"*, 27th American Helicopter Society Annual Forum, Washington D.C., August 1971

21 Curtiss, H.C. Jr., *"Stability and Control Modelling"*, 12th European Rotorcraft Forum, Garmisch-Partenkirchen, Germany, Sept. 22-25, 1986, paper no. 41

22 Curtiss, H.C. Jr., *"On the Calculation of the Response of Helicopters to Control Inputs"*, 18th European Rotorcraft Forum, Avignon, France, Sept. 14-17, 1992, paper no. F07

23 Deutsch, M.L., *"Ground Vibrations of Helicopters"*, J. of the Aeronautical Sciences, Vol.13. No. 5, May 1946, pp. 223-228

24 Diftler, M.A., *"UH-60A Helicopter Stability Augmentation Study"*, 14th European Rotorcraft Forum, Milano, Italy, Sept. 20-23, 1988, paper no. 74

25 Doman, Spera, David A., "*Wind Turbine Technology-Fundamental Concepts of Wind Turbine Engineering*", Copyright by The American Society of Mechanical Engineering, New York

26 Dugundji, J., *"Some Dynamic Problems of Rotating Windmill Systems"*, NASA CP-2001, 13th Annual Meeting Society of Engineering Science, Hampton V.A.,

Nov. 1-3, 1976, pp. 439-447

27 Eggleston, D.M. and Stoddard, F.S. *"Wind Turbine Engineering Design"*, Copyright Van Nostrand Reinhold, New York, 1987

28 Ellis, C.W., *"Effects of Articulated Rotor Dynamics on Helicopter Control System Requirements"*, Aeronautical Engineering Review, July 1953, pp. 30-38

29 Feitosa, E.A.N., "*Parametric Resonance in Horizontal Axis Wind Turbines*", Ph.D. Dissertation, University of Southampton, England, 1989

30 Fletcher, J.W., Tischler, M.B., "*Improving Helicopter Flight Mechanics Models with Laser Measurements of Blade Flapping*", 53rd American Helicopter Society Annual Forum, Virginia Beach, B.A., April 29-May 1, 1997, pp.1467-1494

31 Friedmann, P.P., *"Recent Developments in Rotary-Wing Aeroelasticity"*, J. of Aircraft, Vol.14, No. 11, Nov. 1977, pp. 1027-1041

32 Friedmann, P., *"Influence of Modeling and Blade Parameters on the Aeroelastic Stability of a Cantilevered Rotor"*, AIAA Journal, Vol. 15, No.2, February 1977, pp.149-158

33 Friedmann, P.P., "*Aeroelastic Modeling of Large Wind Turbines*", J. of the American Helicopter Society, Vol.21, No.4, Oct. 1976, pp. 17-27

34 Fu, K.H., Kaletka, J., "*Frequency-Domain Identification of Bo 105 Derivative Models with Rotor Degrees of Freedom*", 16th European Rotorcraft Forum, Glasgow, England, Sept., 1990, paper no. III.10.3

35 Gaffey, T.M., "*The Effect of Positive Pitch-Flap Coupling (Negative δ_3) on Rotor Blade Motion Stability and Flapping*", J. of the American Helicopter Society, Vol. 14, No. 2, April 1969, pp.49-67

36 Gallot, J., *"Effects Aeroelastique sur les Qualités de Vol d'un Rotor Rigide"*, AGARD 34th Flight Mechanics Panel Meeting, Marseille, France, April 1969, AIAA Paper 69-204

37 Hall, W.E. Jr., Bryson, A.E. Jr., *"Inclusion of Rotor Dynamics in Controller Design for Helicopters"*, J. of Aircraft, Vol.10, No.4, Apr.1973, pp.200-206

38 Heimbold, R.C., and Griffith, D.C., "*Synthesis of an Electromechanical Control System for a Compound Hingeless Rotor Helicopter*", J. of American Helicopter Society, Vol.17, No.2, April 1972, pp.55-65

39 Hodges, D.H., Ormiston, R.A., "*Stability of Elastic Bending and Torsion of Uniform Cantilevered Rotor Blades in Hover with Variable Structural Couplings*", NASA TN D-8192, April 1976

40 Hodges, D.H., Ormiston, R.A., "*Stability of Hingeless Rotor Blades in Hover*

with Pitch-Link Flexibility", AIAA Journal, Vol. 15, No. 4, 1977

41 Hohenemser, K., "*Hingeless Rotorcraft Flight Dynamics*", AGARD-AG-197, 1974

42 Hohenemser, K, "*Dynamic Stability of a Helicopter with Hinged Rotor Blades*", NACA TM-907, September, 1939

43 Hohenemser, K.H., Yin, S.K., "*On the Use of First Order Rotor Dynamics in Multiblade Coordinates*", 30th American Helicopter Society Annual Forum, Washington D.C., May 1974, paper no. 831

44 Hohenemser, K.H., Perischo, C.H., "*Analysis of the Vertical Flight Dynamic Characteristics of the Lifting Rotor with Floating Hub and Off-set Coning Hinges*", J. of the American Helicopter Society, Vol.3 No.4, Oct. 1958, pp.20-33

45 Holley, W.E., Thresher, R.W., Lin, S-R., "*Atmospheric Turbulence Inputs for Horizontal Axis Wind Turbines*", European Wind Energy Conference, Hamburg, Germany, Oct, 22-26, 1984

46 Holten, Th. van, "*KEWT Wind Turbine*", Stork Product Engineering Report, Delft University of Technology, Sept. 1980

47 Holten, Th. van, "*Energy Flow Considerations, an Educational Tool to Clarify Aeroelastic Phenomena*", paper no. 66, 26th European Rotorcraft Forum, The Hague, The Netherlands, Sept. 26-29, 2000

48 Holten, Th. van, et. al. "*Aeroelastic Stability of Modern Wind Turbines*", Memorandum M-880, Delft University of Technology, Sept. 1999, work done within the frame of STABTOOL-project

49 Holten, Th. van, Pavel M.D., Smits, G.N., "*The Influence of Scales Effects on the Aeroelastic Stability of Large Wind Turbines*", paper no. 71, 26th European Rotorcraft Forum, The Hague, The Netherlands, Sept. 26-29, 2000

50 Holten, Th. van, "*Hamiltonian Mechanics as a Possible Alternative for Deriving Aero-elastic Equations*"", paper no. 6-8, 13th European Rotorcraft Forum, Arles, France, Sept. 1987

51 Houston, S.S., Horton, R.I., "*The Identification of Reduced Order Models of Helicopter Behaviour for Handling Qualities Studies*", 13th European Rotorcraft Forum, Arles, France, Sept. 8-11, 1987, paper no.7.9

52 Huber, H.B., "*Effect of Torsion-Flap-Lag Coupling on Hingeless Rotor Stability*", 29th Annual National Forum of the American Helicopter Society, Washington D.C., May 1973, Paper no. 731

53 Johnson, W., "*Recent Developments in the Dynamics of Advanced Rotor Systems- I, II*", Vertica Vol. 10, No.1, pp. 73-107, and No.2, pp. 109-150, 1986

54 Johnston, J.F. and Cook, J.R., "*AH-56A Vehicle Development*", 27th American Helicopter Society Forum, May 1971, Preprint 574

55 Kaletka, J., Gimonet, B., "*Identification of Extended Models from BO 105 Flight Test Data for Hover Flight Condition*", 21st European Rotorcraft Forum, St. Petersburg, Russia, Aug. 30-Sept. 1, 1995, paper no. VII-7

56 Kaza, K.R.V., Hammond, C.E., "*An Investigation of Flap-Lag Stability of Wind Turbine Rotors in the Presence of Velocity Gradients and Helicopter Rotors in Forward Flight*", AIAA/ASME/SAE 17th Structures, Structural Dynamics, and Materials Conference, Pennsylvania, May 5-7, 1976, pp. 421-431 or AIAA CP-76-02, pp.421-431

57 Kaza, K.R.V., Kvaternik, R.G., "*Examination of the Flap-Lag Stability of Rigid Articulated Rotor Blades*", J. of Aircraft, Vol.16, No.12, December 1979, pp. 876-884

58 Kawamato, T., Sakakibara, T., "*Dynamic Responses of an Upside Yawing Wind Turbine to Wind Direction Changes*", European Community Wind Energy Conference, June, 6-10, 1988, Denmark, pp. 314-319

59 Kolwey, H.G., *The new ADS-33 Process: Caution for Implementation Technical Note*", J. of the American Helicopter Society, Vol. 41, No. 1, Jan. 1996, Technical Note, pp.3-6

60 Kothmann, B.D., *"Understanding the Effects of Blade Flexibility on Helicopter Control Response"*, 52nd American Helicopter Society Annual Forum, Washington, DC, June 1996

61 Kuczynski, W.A., et.al., *"The Influence of Engine/Fuel Control Design on Helicopter Dynamics and Handling Qualities"*, J. of the American Helicopter Society, Vol.25, No.2, Apr. 1980, pp.26-34

62 Kuik, G.A.M. van, Dekker, J.W.M., *"The Development of Advanced Rotor Systems- A survey of the Flexhat program, Including Full Scale Results"*, European Community Wind Energy Conference, 10-14 September, 1990

63 Loewy, R.G., *"Review of Rotary-Wing V/STOL Dynamic and Aeroelastic Problems"*, Journal of the American Helicopter Society, Vol. 14, No 3, July, 1969, pp. 3-23

64 Leconte, P., Széchényi, E., *"Aeroelastic Tailoring of Blades: Prospects for Reducing Unsteady Loads and Enhancing Performance"*, Proceedings of the European Wind Energy Conference EWEC '91, Amsterdam, The Netherlands, Oct. 14-18, 1991

65 Lindenburg, C., Snel, H., *"Parameterstudie naar het Gedrag van een Rotor met Pendelnaaf met behulp van Phatas-II"*, 5th Dutch National Wind Energy

Conference, 1990, in Dutch

66 Lobitz, D.W., Veers, P.S., *"Aeroelastic Behaviour of Twist-Coupled HAWT Blades"*, AIAA-98-0029

67 Malcolm, D.J., Wright, A.D., *"The Use of ADAMS to Model the AWT-26 Prototype"*, SED-Vol.15, Wind Energy -1994, ASME 1994

68 Marinescu, A., Anghel, V., "*Aerodinamica si Dinamica Elicopterului*", Academy Press, 1992, in Romanian

69 McKillip, R.M., Jr., and Curtiss, H.C. Jr., *"Approximations for Inclusion of Rotor Lag Dynamics in Helicopter Dynamic Models"*, 17th European Rotorcraft Forum, Berlin, Germany, September 1991

70 Miller, R.H., *"A Method for Improving the Inherent Stability and Control Characteristics of Helicopters"*, J. of Aeronautical Sciences, June 1950, pp. 363-374

71 Miller, R.H. et. al., *"Methods for Design Analysis of Horizontal Axis Wind Turbine"*, ASRL-TR-184-7 to ASRL-TR-184-16, volume 1 to 10 , MIT, Sept. 1978

72 Milne, R.D., *"The Analysis of Weakly Coupled Dynamical Systems"*, International J. of Control, Vol.2, No.2, 1965, pp.171- 199

73 Miyajima, K, "*Analytical Design of a High Performance Stability and Control Augmentation System for a Hingeless Rotor Helicopter*", J. of American Helicopter Society, Vol. 24, No. 4 , 1979, pp. 29-36

74 Morduchow, M., Hinchey, F.G., "*Theoretical Analysis of Oscillations in Hovering of Helicopter Blades with Inclined and Offset Flapping and Lagging Hinge Axes*", NACA TN-2226, Dec. 1950

75 Ormiston, R.A., *"Investigations of Hingeless Rotor Stability"*, Vertica, Vol. 7, No.2, pp. 143-181, 1983, pp. 143-181

76 Ormiston, R.A., Warmbrodt, W.G., Hodges, D.H., Peters, D.A., *"Rotorcraft Aeroelastic Stability"*, NASA CP-2495, Proceedings of NASA/Army Technology Conference, March, 1987

77 Ormiston, Robert A., *"Rotor Dynamic Considerations for Large Wind Power Generator Systems"*, Wind Energy Conversion Systems Workshop Proceedings, National Science Foundation, NSF/RA/W-73-006, Dec 1973

78 Ormiston, R.A., Hodges D.H., "*Linear Flap-Lag Dynamics of Hingeless Helicopter Rotor Blades in Hover*", J. of the American Helicopter Society, 17(2), April 1972, pp.2-14

79 Ormiston, R.A., *"Aeromechanical Stability of Soft-Inplane Hingeless Rotor Helicopters"*, 3rd European Rotorcraft Forum, Sept. 7-9, 1977, Aix-En-Provence, France, Paper No. 25

80 Padfield, G.D., "*On the Use of Approximative Models in Helicopter Flight Mechanics*", 6th European Rotorcraft and Powered Aircraft Forum, Bristol, England, Sept. 16-19, 1980, paper no. 57

81 Padfield, G.D., "*Helicopter Flight Dynamics -The Theory and Application of Flying Qualities and Simulation Modeling*", Blackwell Science LTD, 1996

82 Pass, H.B., Pearce, B.F., and Wolkovitch J., *"Topics On Flexible Airplane Dynamics"*, Part III: Coupling of the Rigid and Elastic Degrees of Freedom of an Airframe, ASD-TDR-63-334, July 1963

83 Pavel, M.D., Schoones, M.M.J., Winkelaar, D. "*Literature Survey on Aeromechanical Instabilities for Helicopters and Wind Turbines*", Mem. M-877, TU Delft, July 1999

84 Pavel, M.D., "*Six Degrees of Freedom Linear Model for Helicopter Trim and Stability Calculations*", Mem. M-756, TU Delft, Dec. 1996

85 Pavel, M.D., "*Prediction of the Necessary Flapping Dynamics for Helicopter Flight Simulation*", Mem. M-757, TU Delft, Dec. 1996

86 Pavel, M.D. and Holten, van. Th., "*On the Prediction of the Necessary Rotor Dynamics for Helicopter Flight Simulation*", 23rd European Rotorcraft Forum, Dresden, Germany, Sept., 16-18, 1997, paper no. 39

87 Pavel, M.D., "*Effects of Rotor Disc-Tilt on Helicopter Piloted Simulation*", 24th European Rotorcraft Forum, Marseilles, France, Sept. 15-17, 1998, paper no. FM.03

88 Pavel, M.D. and Holten, van Th., "*An Rotor-Tower Instability Associated with the Advancing Lead-Lag Mode*", AIAA-2000-0068, Reno, 2000

89 Perkins, F.W., Johnes, R., *"The Effect of δ_3 on a Yawing HAWT Blade and on Yaw Dynamics"*, NASA CP-2185, 1981

90 Peters, D.A., "*Flap-Lag Stability of Helicopter Rotor Blades in Forward Flight*", J.of the American Helicopter Society, Vol.1, No.3, Oct. 1975, pp.2-13

91 Quarton, D.C., et. al. *"Wind Turbine Design Calculations. The State of the Art"*, Proceedings of the European Wind Energy Conference EWEC '91, Amsterdam, The Netherlands, Oct. 14-18, 1991

92 Reichert, G. and Huber, H., *"Influence of Elastic Coupling Effects on the Handling Qualities of a Hingeless Rotor Helicopter"*, 39th AGARD Flight

Mechanics Panel Meeting, Hampton, Va., Sept. 1971, AGARD-CP-121

93 Shapiro, J., "*Principles of Helicopter Engineering*", Published by Loxley Brothers Limited, Letchworth, 1955

94 Sharpe, D.L., "*An Experimental Investigation of the Flap-Lag-Torsion Aeroelastic Stability of a Small-Scale Hingeless Rotor in Hover*", NASA TP-2546, 1986

95 Sissingh, G.J., "*Dynamics of Rotors Operating at High Advance Ratios*", J. of the American Helicopter Society, Vol 13, No.3, July 1968, pp.56-63

96 Sopher, R., Cassarino, S.J., "*Effects of Analytical Modeling Assumptions on the Predicted Stability of a Model Hingeless Rotor*", J. of the American Helicopter Society, Vol. 33, No.4, Oct.1988, pp. 15-27

97 Smith, C.E., et.al., "*A Rigid Body Model for Analysis of Aerogenerator Rotor Dynamics*", 31st Annual National Forum of the American Helicopter Society, May, 1975, preprint 991

98 Steinhardt, E., "*Dynamic and Aeroelastic Characteristics of a Complete Wind Turbine Systems*", 7th European Rotorcraft Forum, Paper No. 10, Sept. 1981, Garmisch-Partenkirchen/Germany

99 Sullivan, T.L., "*A review of Resonance Response in Large, Horizontal-Axis Wind Turbines*", NASA CP-2185, 1981

100 Vegte, J. van de, "*Feedback Control Systems*", Published by Prentice-Hall, Inc., 1994

101 Wright, A.D., Kelley, N.D., Osgood, R.M., "*Validation of A Model for a Two-Bladed Flexible Rotor System:Progress to Date*", AIAA-99-0060

102 Wright, G.P., Lappos, N., *Sikorsky 76 Handling Qualities Design and Development*", 35th Annual National Forum of the American Helicopter Society, May, 1979

103 Yeager, W. T. Jr., Hamouda, M.H., Mantay, W.R., "*Aeromechanical Stability of a Hingeless Rotor in Hover and Forward Flight: analysis and Wind Tunnel Tests*", NASA TM-85683, 1983

104 Young, M.I., "*A Simplified Theory of Hingeless Rotors with Application to Tandem Helicopters*", 8th American Helicopter Society Annual Forum, May 1962, Washington D.C.

Appendix A

Correlation between the Complex Plane and the Time-Domain Response

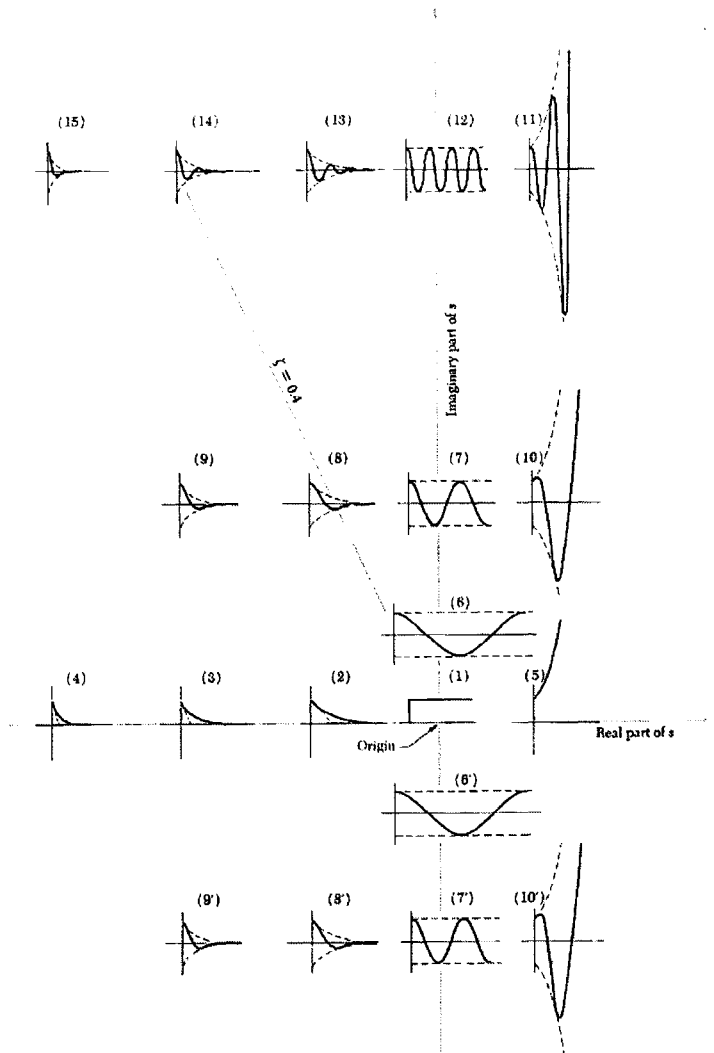

*Figure A.1 Correlation between the natural response and complex plane (**Cannon** [1967][12])*

Figure A.1 (**Cannon** [1967][12]) presents the correlation between the s-plane picture of eigenvalues and the corresponding time-response pictures:

- if the eigenvalues are on the real axis, the response of the system is always pure exponential; the farther from the origin in the left half-plane, the faster the response decreases (see (1), (2), (3), (4)); in the right half-plane the motion is unstable (see (5));
- if the eigenvalues are on the imaginary axis, the response of the system is always an undamped oscillation; the farther up and down from the origin, the higher the frequency (see (1), (6)=(6)', (7)=(7)', (12));
- the eigenvalues on a constant frequency line are damped oscillations (in the left half-plane) and unstable oscillations (in the right half-plane); the farther from the origin in the left half-plane, the quicker they decay time (see (15), (14), (13)); the farther from the origin in the right half-plane, the quicker they grow in time (see 11));
- the eigenvalues on a constant damping have a constant decay time, but variable frequency.
- the eigenvalues on a constant ζ line have the number of cycles to damp constant; the farther from the origin, the faster the whole response (see (8), (14)).

Appendix B

Helicopter and Horizontal-Axis Wind Turbine Blade Flapping Dynamics

Using the assumptions introduced in section 2.6.1, Chapter 2, the present appendix derives the equations of motion of a flapping blade for both helicopter and wind turbine configurations. Consider the blade initially in equilibrium and perturb the blade with a flapping angle β. The dominant forces acting on a blade element dm, at a radius r from the flapping hinge in the flapping plane are the aerodynamic forces and the centrifugal forces (see Figure B.1). The following section determines the moments of each force acting on the blade with respect to the flapping hinge.

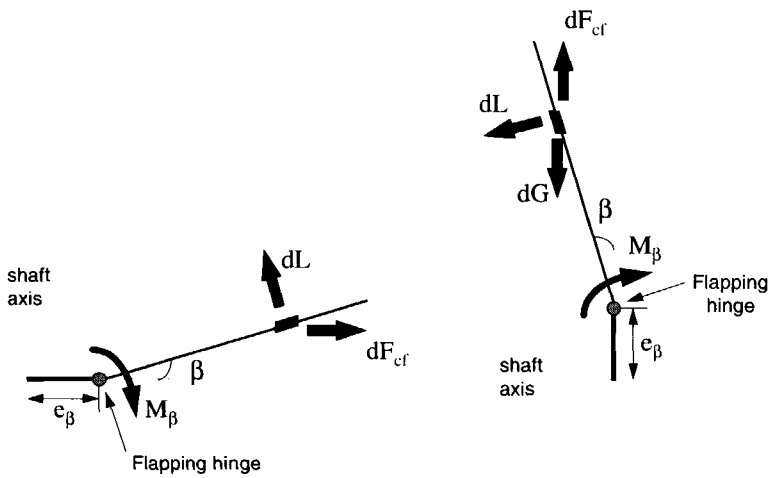

Helicopter Flapping plane Wind Turbine Flapping plane

Figure B.1 Forces on the blade in the flapping motion for a helicopter and a wind turbine

Aerodynamic Flapping Moment

The aerodynamic moment of the flapping blade element is a direct function of the components of the blade velocity. The initial components of the blade velocity in the rotating system for respectively helicopters and wind turbines, before the blade has been perturbed, are presented in Figure B.2 and Figure B.3.

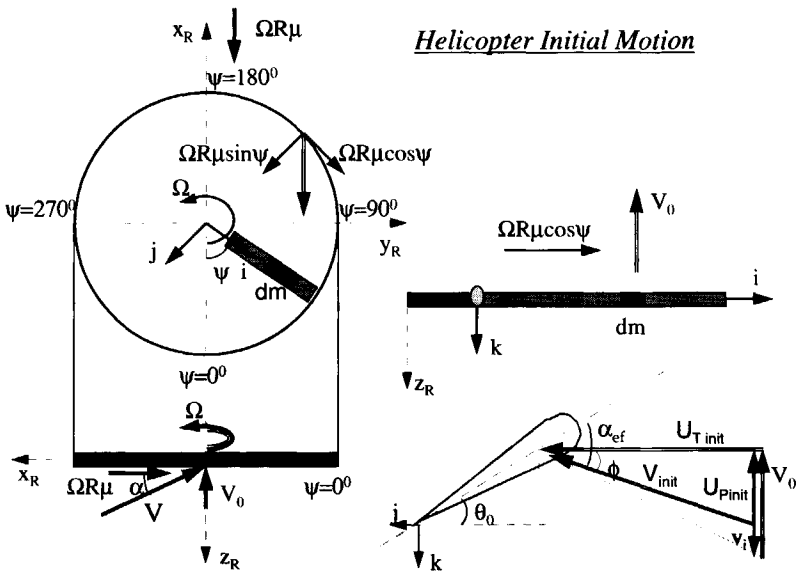

Figure B.2 Initial velocity components on the helicopter blade

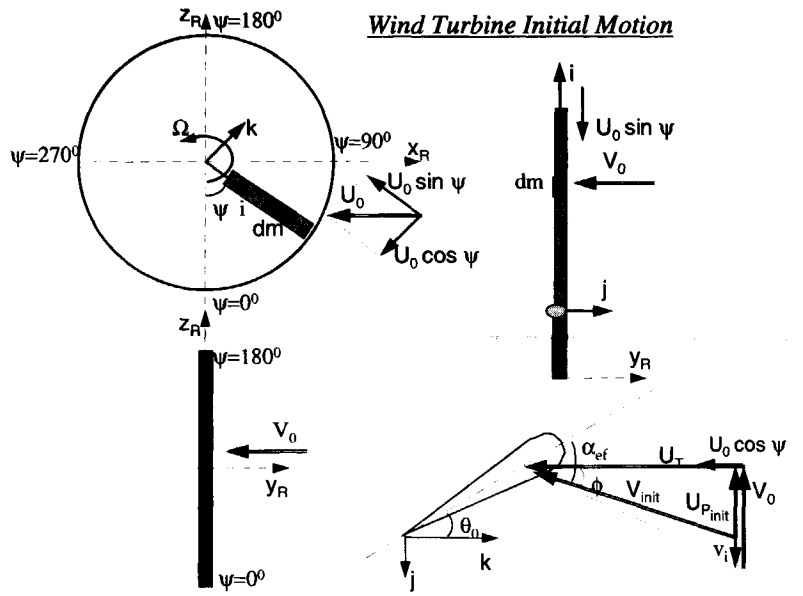

Figure B.3 Initially velocity components on the wind turbine blade

For a helicopter, the initial components (before the blade was perturbed) of the blade

velocity are (see Figure B.2):

- i direction (radial to the blade)

$$U_{R\,init} = V\cos\alpha\cdot\cos\psi = \Omega R\mu\cdot\cos\psi \tag{B.1}$$

- j direction (tangential to the shaft plane)

$$U_{T\,init} = \Omega r + V\cos\alpha\sin\psi = \Omega r + \Omega R\mu\cdot\sin\psi \tag{B.2}$$

- (-k) direction (perpendicular to the shaft plane)

$$U_{P\,init} = V_0 - v_i = \Omega R\left(\bar{V}_0 - \lambda_i\right) = \Omega R\lambda \tag{B.3}$$

For a wind turbine, the initial components of the blade velocity are (see Figure B.3):

- i direction (radial to the blade):

$$U_{R\,init} = -U_0\sin\psi = -\Omega R\bar{U}_0\sin\psi \tag{B.4}$$

- (-k) direction (tangential to the shaft plane):

$$U_{T\,init} = \Omega r + U_0\cos\psi = \Omega r + \Omega R\bar{U}_0\cos\psi \tag{B.5}$$

- (-j) direction (perpendicular to the shaft plane):

$$U_{P\,init} = V_0 - v_i = \Omega R\left(\bar{V}_0 - \lambda_i\right) = \Omega R\lambda \tag{B.6}$$

The initial blade angle of attack can be written as:

$$\alpha_{ef\,init} = \theta_p + \phi_{init} \approx \theta_p + \frac{U_{P\,init}}{U_{T\,init}} \tag{B.7}$$

Consider next the blade being perturbed with a flapping angle β ($\beta>0$ for blade up). The perturbation will be felt by the blade as a change in the components U_R radial to the blade and U_P perpendicular to the shaft plane as illustrated in Figure B.4 and Figure B.5 for respectively the helicopter and the wind turbine.

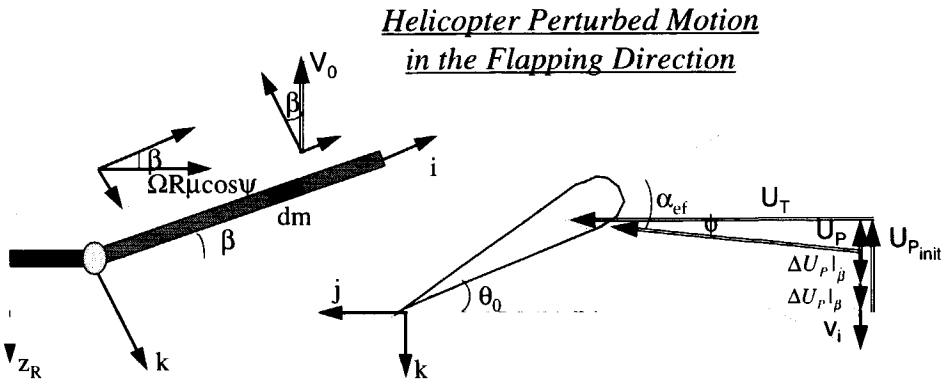

Figure B.4 Perturbed velocity components on the helicopter blade

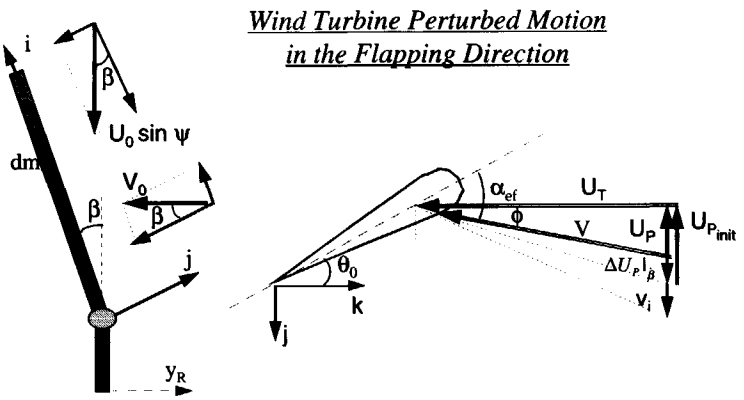

Figure B.5 Perturbed velocity components on the wind turbine blade

Assuming small flapping angles, the perturbed velocity components may be expressed in case of a helicopter as (see Figure B.4):

$$U_R = \Omega R\mu \cdot \cos\psi\cos\beta + V_0 \sin\beta \approx \Omega R\mu \cdot \cos\psi + V_0 \beta \tag{B.8}$$

$$\begin{aligned} U_P &= V_0\cos\beta - v_i - r\dot{\beta} - \Omega R\mu\cos\psi \sin\beta \approx \\ &\approx U_{P\,init} - r\dot{\beta} - \Omega R\mu\cos\psi\,\beta = U_{P\,init} + \Delta U_P|_{\dot{\beta}} + \Delta U_P|_{\beta} \end{aligned} \tag{B.9}$$

where $\Delta U_P|_{\dot{\beta}} = -r\dot{\beta}$ and $\Delta U_P|_{\beta} = -\Omega R\mu\cos\psi\,\beta$.

In the case of a wind turbine, the perturbed velocity components are (see Figure B.5):

$$U_R = -\Omega R \bar{U}_0 \sin\psi \cos\beta + V_0 \sin\beta \approx -\Omega R \bar{U}_0 \sin\psi + V_0 \beta \tag{B.10}$$

$$U_P = \Omega R \bar{U}_0 \sin\psi \sin\beta + V_0 \cos\beta - v_i - r\dot{\beta} \approx \Omega R \bar{U}_0 \sin\psi\beta + V_0 - v_i - r\dot{\beta} = \\ = U_{P\,init} + \Delta U_P|_{\dot{\beta}} + \Delta U_P|_{\beta} \tag{B.11}$$

where $\Delta U_P|_{\dot{\beta}} = -r\dot{\beta}$ and $\Delta U_P|_{\beta} = \Omega R \bar{U}_0 \sin\psi\,\beta$. The change in the U_P component is felt as a change in the blade angle of attack α_{ef} which can be expressed for both configurations as:

$$\alpha_{ef} = \theta_p + \phi \approx \theta_p + \frac{U_P}{U_T} = \alpha_{ef\,init} + \frac{\Delta U_P|_{\dot{\beta}}}{U_T} + \frac{\Delta U_P|_{\beta}}{U_T} = \alpha_{ef\,init} + \Delta\alpha|_{\dot{\beta}} + \Delta\alpha|_{\beta} \tag{B.12}$$

Thus, the angle of attack of a flapping blade changes due to the flapping velocity $\dot{\beta}$ and due to the displacement of the blade (resulting from the change of the initial radial velocity) and can be expressed as:

- in the helicopter case:

$$\Delta\alpha|_{\dot{\beta}} = -\frac{r\dot{\beta}}{U_T} \quad ; \quad \Delta\alpha|_{\beta} = -\frac{\Omega R \mu \beta \cos\psi}{U_T} \tag{B.13}$$

- in the wind turbine case:

$$\Delta\alpha|_{\dot{\beta}} = -\frac{r\dot{\beta}}{U_T} \quad ; \quad \Delta\alpha|_{\beta} = \Omega R \bar{U}_0 \sin\psi \frac{\beta}{U_T} \tag{B.14}$$

The change in angle of attack gives rise to a change of the lift of the blade element which is:

-for the helicopter:

$$\Delta dL|_{\dot{\beta}} = \frac{\rho}{2} c_e C_{l_\alpha} U_T^2 \left(\Delta\alpha|_{\dot{\beta}}\right) dr = -\frac{\rho}{2} c_e C_{l_\alpha} U_T\, r\dot{\beta} \tag{B.15}$$

$$\Delta dL|_{\beta} = \frac{\rho}{2} c_e C_{l_\alpha} U_T^2 \left(\Delta\alpha|_{\beta}\right) dr = -\frac{\rho}{2} c_e C_{l_\alpha} U_T \cdot \Omega R \mu \beta \cos\psi \tag{B.16}$$

- for the wind turbine:

$$\Delta dL|_{\dot\beta} = \frac{\rho}{2} c_e C_{l_\alpha} U_T^2 \left(\Delta\alpha|_{\dot\beta}\right) dr = -\frac{\rho}{2} c_e C_{l_\alpha} U_T r \dot\beta \tag{B.17}$$

$$\Delta dL|_{\beta} = \frac{\rho}{2} c_e C_l^\alpha U_T^2 \left(\Delta\alpha|_{\beta}\right) dr = \frac{\rho}{2} c_e C_l^\alpha U_T \cdot \Omega R \bar U_0 \beta \sin\psi \tag{B.18}$$

where the aerodynamic forces are derived using the classical blade-element theory approach (i.e. by isolating the blade element dm at radius r and assuming $U_P << U_T$ and using linear aerodynamics).

Concerning the elementary drag force, perturbing the blade in the flapping direction will not change the drag component of the aerodynamic force in a first order approximation:

$$dD = \frac{\rho}{2} c_e C_d V^2 dr \approx \frac{\rho}{2} c_e C_d U_T^2 dr \tag{B.19}$$

The lift on the flapping blade element therefore consists of components dependent as well as independent on the flapping angle. The independent components may be considered external excitations for the flapping blade:

$$dL = \frac{\rho}{2} c_e C_{l_\alpha} U_T^2 \alpha_{ef} dr = \frac{\rho}{2} c_e C_{l_\alpha} U_T^2 \left(\alpha_{ef\,init} + \Delta\alpha|_{\dot\beta} + \Delta\alpha|_{\beta}\right) dr = dL_{excit} + \Delta dL|_{\dot\beta} + \Delta dL|_{\beta} \tag{B.20}$$

Finally, the aerodynamic flapping moment of the entire blade about the flapping hinge may be calculated as an integral of the elementary aerodynamic forces acting on the blade element dm (the integration starting from the hinge):

$$M^{\beta}_{aero} = \int_0^{R(1-\varepsilon_\beta)} r\, dF_z \approx \int_0^{R(1-\varepsilon_\beta)} r\, dL \tag{B.21}$$

where dF_z is the resultant of the lift and drag force perpendicular to the blade and dF_y the resultant tangential to the blade (Figure B.6):

$$\begin{aligned} dF_z &= dL\cos\phi + dD\sin\phi \approx dL + \phi\, dD \approx dL \\ dF_y &= dL\sin\phi - dD\cos\phi \approx \phi\, dL - dD \end{aligned} \tag{B.22}$$

Substituting (B.20) into (B.21), the aerodynamic flapping moment can be divided into three components:

- one component that may be interpreted as an aerodynamic excitation:

$$M_{a\,excit} = \int_0^{R(1-\varepsilon_\beta)} dF_{z\,excit}\, r \approx \int_0^{R(1-\varepsilon_\beta)} dL_{excit}\, r = \frac{\rho}{2} c_e C_{l_\alpha} \int_0^{R(1-\varepsilon_\beta)} \left(\theta_p U_T^2 + U_{P\,init} U_T\right) r\, dr \tag{B.23}$$

- two components resulting from the change in lift induced by the flapping motion, which are:

- in case of the helicopter:

$$\Delta M_a|_{\dot\beta} = \int_0^{R(1-\varepsilon_\beta)} \Delta dF_z|_{\dot\beta}\, r \approx \int_0^{R(1-\varepsilon_\beta)} \Delta dL|_{\dot\beta} \cdot r = -\rho C_{l_\alpha} c_e R^4 (1-\varepsilon_\beta)^3 \left[\frac{1}{8} - \frac{\varepsilon_\beta}{8} + \frac{1}{6}\mu\sin\psi\right]\Omega\dot\beta \tag{B.24}$$

$$\begin{aligned} \Delta M_a|_{\beta} = \int_0^{R(1-\varepsilon_\beta)} \Delta dF_z|_{\beta}\, r \approx \int_0^{R(1-\varepsilon_\beta)} \Delta dL|_{\beta}\, r = -\rho C_{l_\alpha} c_e R^4 (1-\varepsilon_\beta)^2 \Big[\frac{1}{6}\mu\cos\psi - \\ - \frac{\varepsilon_\beta}{6}\mu\cos\psi + \frac{1}{8}\mu^2\sin 2\psi\Big]\Omega^2\beta \end{aligned} \tag{B.25}$$

- in case of the wind turbine:

$$\Delta M_a|_{\dot\beta} = \int_0^{R(1-\varepsilon_\beta)} \Delta dF_z|_{\dot\beta}\, r \approx \int_0^{R(1-\varepsilon_\beta)} \Delta dL|_{\dot\beta}\, r = -\rho C_{l_\alpha} c_e R^4 (1-\varepsilon_\beta)^3 \left[\frac{1}{8} - \frac{\varepsilon_\beta}{8} + \frac{1}{6}\bar U_0 \sin\psi\right]\Omega\dot\beta \tag{B.26}$$

$$\begin{aligned} \Delta M_a|_{\beta} = \int_0^{R(1-\varepsilon_\beta)} \Delta dF_z|_{\beta}\, r \approx \int_0^{R(1-\varepsilon_\beta)} \Delta dL|_{\beta}\, r = -\rho C_{l_\alpha} c_e R^4 (1-\varepsilon_\beta)^2 \Big[-\frac{1}{6}\bar U_0 \sin\psi + \\ + \frac{\varepsilon_\beta}{6}\bar U_0 \sin\psi - \frac{1}{8}\bar U_0^2 \sin 2\psi\Big]\Omega^2\beta \end{aligned} \tag{B.27}$$

Summarizing, an upward flapping perturbation β, will be experienced by the aerodynamic moment as a damping-term (B.24) induced by the flapping velocity $\dot\beta$, and a spring-term (B.25) induced by the flapping displacement, with both components

counteracting the motion.

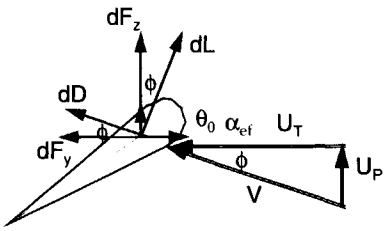

Figure B.6 Elementary aerodynamic forces dF_z and dF_y on the blade element

Centrifugal Moment

The centrifugal force acting on the blade element dm at radius r may be expressed both for helicopter and wind turbine configurations as:

$$dF_{cf} = \Omega^2 (r\cos\beta + e_\beta)dm \approx \Omega^2 (r + e_\beta)dm \tag{B.28}$$

Comparing (B.15) and (B.16) (respectively (B.17) and (B.18)) to (B.28), one may observe that while the aerodynamic excitation tends to move the blade away from the shaft plane, the centrifugal force has an opposite tendency, driving the blade back to the shaft plane. The moment due to the centrifugal force on the whole blade may be determined by integrating along the blade:

$$M_{cf} = -\int_0^{R-e_\beta} dF_{cf} \cdot r\sin\beta = -\Omega^2 (I_\beta + e_\beta \sigma_\beta)\sin\beta \approx -\Omega^2 (I_\beta + e_\beta \sigma_\beta)\beta \tag{B.29}$$

The following definitions are introduced in (B.29):

- the blade static moment around the flapping hinge $\sigma_\beta = \int_0^{R(1-\varepsilon_\beta)} r\,dm$ which for a uniform blade mass becomes:

$$\sigma_{bl} = \int_0^{R(1-\varepsilon_\beta)} r\left(\frac{M_b}{R}dr\right) = M_b \frac{R}{2}\left(1-\varepsilon_\beta\right)^2 = M_b r_g (1-\varepsilon_\beta)^2 = M_b \bar{r}_g R(1-\varepsilon_\beta)^2 \approx M_b \bar{r}_g R \tag{B.30}$$

- the blade moment of inertia around the flapping hinge (sometimes ambiguously called

polar moment of inertia) $I_\beta = \int_0^{R-e_\beta} r^2\,dm$ which for a uniform blade mass becomes:

$$I_{bl} = \int_0^{R(1-\varepsilon_\beta)} r^2\left(\frac{M_b}{R}\,dr\right) = M_b\,\frac{R^2}{3}(1-\varepsilon_\beta)^3 = M_b\,\frac{2}{3}\,R\,r_g\,(1-\varepsilon_\beta)^3 = \frac{2}{3}M_b\bar{r}_g R^2(1-\varepsilon_\beta)^3 \approx \frac{2}{3}M_b\bar{r}_g R^2 \tag{B.31}$$

Concluding, the centrifugal moment for both helicopters and wind turbines is a spring-term, which tends to decrease the flapping angle.

Restraint Moment

For helicopter and wind turbine hingeless rotors, using the rigid-blade concept (defined in section 2.6 in Chapter 2), the bending of the elastic blade in the flapping direction may substituted by the flapping of a rigid blade around a flapping hinge with a hinge offset and a hinge spring of constant K_β. The restraint moment acting on the flapping hinge is then:

$$M_\beta = -K_\beta\,\beta \tag{B.32}$$

Inertial Moment

The moment due to blade inertia may be expressed for both helicopters and wind turbines as:

$$M_i = -\int_0^{R-e_\beta} dF_i \cdot r = -\int_0^{R-e_\beta} r\ddot{\beta}\,dm \cdot r = -I_\beta\ddot{\beta} \tag{B.33}$$

Gravity Moment

In case of the helicopter, the gravity force can be neglected. For the horizontal axis wind turbine however, the gravity force cannot be neglected. The component of this force on the blade element in the flapping plane is:

$$dG = g\cos\psi\,dm \tag{B.34}$$

and its moment on the flapping hinge is:

$$M_G = -\int_0^{R(1-\varepsilon_\beta)} dG \cdot r \sin\beta = -g\,\sigma_\beta \cos\psi \sin\beta \approx -g\,\sigma_\beta\,\beta\cos\psi \tag{B.35}$$

Helicopter Flapping Equation of Motion

Combining (B.23), (B.24), (B.25), (B.29), (B.32), (B.33) and (B.35) and assuming an uniform mass for the blade $I_\beta \approx I_{bl}$, the dynamic motion of a flapping blade can be written as:

$$\begin{aligned} &M_{a\,excit} - \rho C_{l_\alpha} c_e R^4 (1-\varepsilon_\beta)^3 \left[\frac{1}{8} - \frac{\varepsilon}{8} + \frac{1}{6}\mu\sin\psi\right]\Omega\dot{\beta} - \rho C_{l_\alpha} c_e R^4 (1-\varepsilon_\beta)^2 \times \\ &\times\left[\frac{1}{6}\mu\cos\psi - \frac{\varepsilon}{6}\mu\cos\psi + \frac{\mu^2}{8}\sin 2\psi\right]\Omega^2\beta - \left(I_\beta + e_\beta\sigma_\beta\right)\Omega^2\beta - K_\beta\beta = I_{bl}\ddot{\beta} \end{aligned} \tag{B.36}$$

Further, the following definitions are introduced: Lock number defined as $\gamma = \left(\rho C_{l_\alpha} c_e R^4\right)/I_{bl}$; blade flapping non-rotating natural frequency (dimensional as well as non-dimensional) $\omega_\beta = \sqrt{K_\beta / I_\beta}$, $\bar{\omega}_\beta = \omega_\beta/\Omega$; non-dimensional offset term $\dfrac{e_\beta\sigma_\beta}{I_\beta} = \dfrac{3}{2}\dfrac{\varepsilon_\beta}{(1-\varepsilon_\beta)}$ and blade flapping rotating natural frequency (non-dimensional) $\nu_\beta = \sqrt{1 + \bar{\omega}_\beta^2 + \dfrac{3}{2}\dfrac{\varepsilon_\beta}{(1-\varepsilon_\beta)}}$. Dividing equation (B.36) by the moment of inertia I_{bl}, rearranging the terms, and using the above definitions, the blade flapping equation of motion is obtained as:

$$\begin{aligned} &\ddot{\beta} + \gamma\left(\frac{1}{8} - \frac{\varepsilon_\beta}{8} + \frac{1}{6}\mu\sin\psi\right)(1-\varepsilon_\beta)^3\Omega\dot{\beta} + \left[\nu_\beta^2 + \gamma\left(1-\varepsilon_\beta\right)^2 \times\right. \\ &\left.\times\left(\frac{1}{6}\mu\cos\psi - \frac{\varepsilon_\beta}{6}\mu\cos\psi + \frac{\mu^2}{8}\sin 2\psi\right)\right]\Omega^2\beta = \frac{M_{a\,excit}}{I_{bl}} \end{aligned} \tag{B.37}$$

Usually, a change of variable to the azimuth angle is made $\dot{\beta} = \Omega\dfrac{d\beta}{d\psi} = \Omega\beta'$ resulting in an equivalent form of the flapping equation (B.37):

$$\beta'' + \gamma\left(\frac{1}{8} - \frac{\varepsilon_\beta}{8} + \frac{1}{6}\mu\sin\psi\right)(1-\varepsilon_\beta)^3\beta' + \left[\nu_\beta^2 + \gamma\left(1-\varepsilon_\beta\right)^2 \times \right.$$
$$\left. \times\left(\frac{1}{6}\mu\cos\psi - \frac{\varepsilon_\beta}{6}\mu\cos\psi + \frac{\mu^2}{8}\sin 2\psi\right)\right]\beta = \frac{M_{a\,excit}}{I_{bl}} \qquad \text{(B.38)}$$

Horizontal Axis Wind Turbine Flapping Equation

Combining the moments as expressed in (B.23), (B.26), (B.27), (B.29), (B.32), (B.33) and (B.35) and assuming a uniform mass for the blade $I_\beta \approx I_{bl}$, the flapping equation of motion for the wind turbine is obtained as:

$$M_{a\,excit} - \rho C_{l_\alpha} c_e R^4 (1-\varepsilon_\beta)^3\left[\frac{1}{8} - \frac{\varepsilon_\beta}{8} + \frac{1}{6}\bar{U}_0\sin\psi\right]\Omega\dot{\beta} - \rho C_{l_\alpha} c_e R^4 (1-\varepsilon_\beta)^2\left[-\frac{1}{6}\bar{U}_0\sin\psi + \right.$$
$$\left. + \frac{\varepsilon_\beta}{6}\bar{U}_0\sin\psi - \frac{1}{8}\bar{U}_0^2\sin 2\psi\right]\Omega^2\beta - \Omega^2\left(I_\beta + e_\beta\sigma_\beta\right)\beta - g\,\sigma_\beta\,\beta\cos\psi - K_\beta\,\beta = I_{bl}\ddot{\beta} \qquad \text{(B.39)}$$

A gravity term is defined as $G = \frac{g\,\sigma_{bl}}{I_{bl}} = \frac{g\,m_{bl}\,\bar{r}_g\,R}{I_{bl}}$. Dividing equation (B.39) by the blade moment of inertia I_{bl} and using the definition of the Lock number γ, the non-rotating natural flapping frequency ω_β, the rotating natural flapping frequency ν_β and the non-dimensional gravity term G as above, after some algebraic manipulation the flapping equation of motion for a wind turbine becomes:

$$\ddot{\beta} + \gamma\left[\frac{1}{8} - \frac{\varepsilon_\beta}{8} + \frac{1}{6}\bar{U}_0\sin\psi\right](1-\varepsilon_\beta)^3\Omega\dot{\beta} + \left[\nu_\beta^2 + G\cos\psi + \gamma(1-\varepsilon_\beta)^2 \times \right.$$
$$\left. \times\left(-\frac{1}{6}\bar{U}_0\sin\psi + \frac{\varepsilon_\beta}{6}\bar{U}_0\sin\psi - \frac{1}{8}\bar{U}_0^2\sin 2\psi\right)\right]\Omega^2\beta = \frac{M_{a\,excit}}{I_{bl}} \qquad \text{(B.40)}$$

or expressed as a derivative relative to the azimuth angle:

$$\beta'' + \gamma\left[\frac{1}{8} - \frac{\varepsilon_\beta}{8} + \frac{1}{6}\bar{U}_0\sin\psi\right](1-\varepsilon_\beta)^3\beta' + \left[\nu_\beta^2 + G\cos\psi + \gamma(1-\varepsilon_\beta)^2 \times \right.$$
$$\left. \times\left(-\frac{1}{6}\bar{U}_0\sin\psi + \frac{\varepsilon_\beta}{6}\bar{U}_0\sin\psi - \frac{1}{8}\bar{U}_0^2\sin 2\psi\right)\right]\beta = \frac{M_{a\,excit}}{I_{bl}} \qquad \text{(B.41)}$$

Appendix C

Helicopter and Horizontal-Axis Wind Turbine Blade Lead-Lag Dynamics

Using the assumptions introduced in section 2.6.2, Chapter 2, the present appendix derives the equation of motion of a lead-lagging blade for both helicopter and wind turbine configurations. It is assumed that the blade is initially in equilibrium, and subsequently perturbed with a lagging angle ζ at time t = 0. The dominant forces acting on a blade element dm, at a radius r from the lagging hinge are the aerodynamic forces and the centrifugal forces (see Figure C.1).

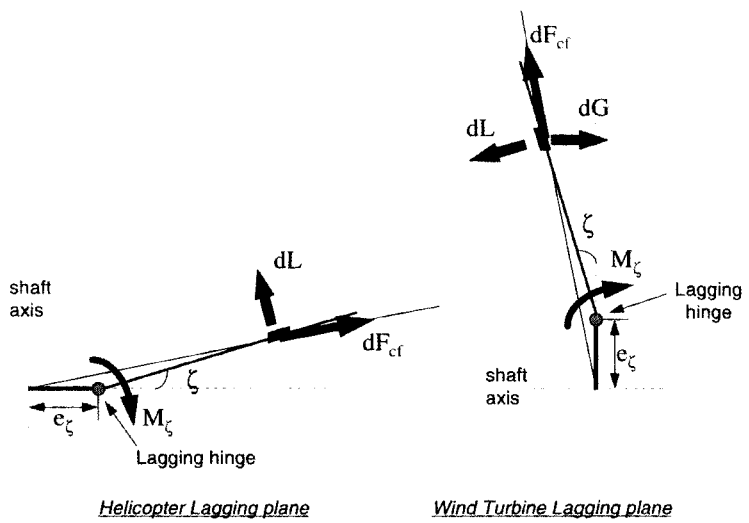

Figure C.1 Forces on the lagging blade for a helicopter and a wind turbine

Aerodynamic Moment

For a helicopter, the initial components of the velocity are given by (B.1), (B.2), and (B.3) in Appendix B. For a wind turbine, the initial components of the velocity are expressed in (B.4), (B.5) and (B.6). Consider the blade perturbed in the lagging plane with a lagging angle ζ (ζ>0 blade back). The blade will feel the perturbation as a change of velocity in the components U_R radial and U_T perpendicular to the shaft plane as illustrated in Figure C.2 for the helicopter and in Figure C.3 for the wind turbine.

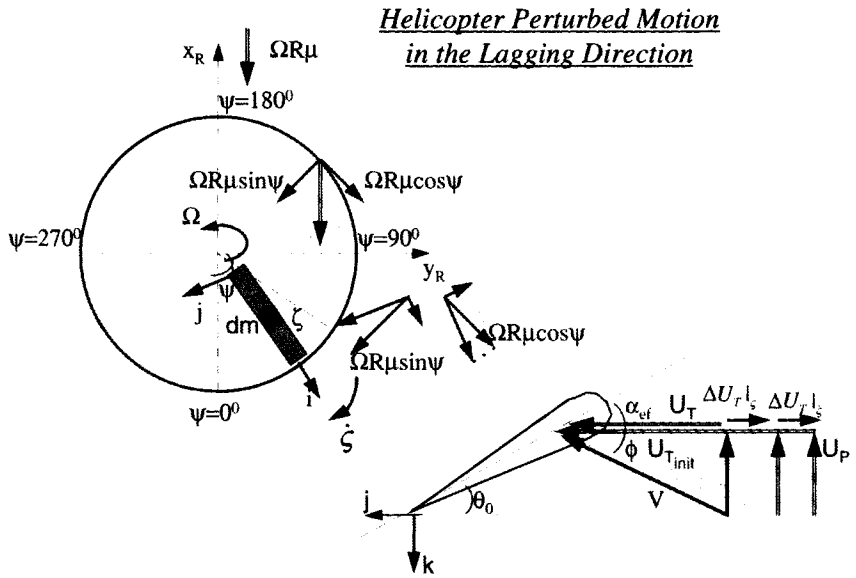

Figure C.2 Velocities on the helicopter blade perturbed in the lagging direction

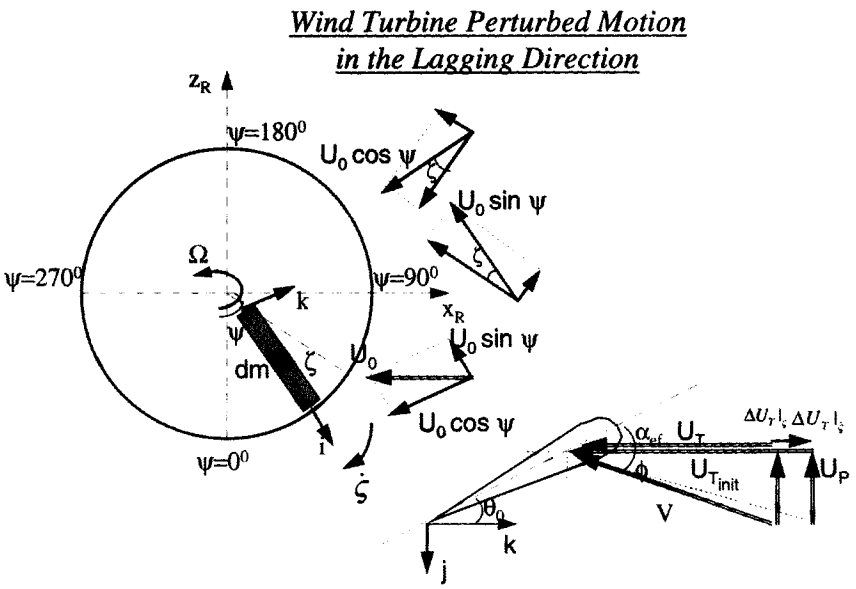

Figure C.3 Velocities on the wind turbine blade perturbed in the lagging direction

For the helicopter, these components can be expressed as (see Figure C.2):

$$U_R = \Omega R\mu \sin\psi \sin\zeta + \Omega R\mu \cos\psi \cos\zeta \approx \Omega R\mu \left(\cos\psi + \zeta \sin\psi\right) \tag{C.1}$$

$$\begin{aligned} U_T &= \Omega r + \Omega R\mu \sin\psi \cos\zeta - r\dot{\zeta} - \Omega R\mu \cos\psi \sin\zeta \approx \left(\Omega r + \Omega R\mu \sin\psi\right) - \\ &- r\dot{\zeta} - \Omega R\mu \cos\psi \zeta = = U_{T\,init} + \Delta U_T|_{\dot{\zeta}} + \Delta U_T|_{\zeta} \end{aligned} \tag{C.2}$$

where $\Delta U_T|_{\dot{\zeta}} = -r\dot{\zeta}$ and $\Delta U_T|_{\zeta} = -\Omega R \mu \cos\psi \zeta$.

For the wind turbine, the change in the velocity components is (see Figure C.3):

$$U_R = -U_0 \cos\psi \sin\zeta - U_0 \sin\psi \cos\zeta \approx -\Omega R \bar{U}_0 \left(\zeta \cos\psi + \sin\psi\right) \tag{C.3}$$

$$\begin{aligned} U_T &= \Omega r - r\dot{\zeta} + U_0 \cos\psi \cos\zeta - U_0 \sin\psi \sin\zeta \approx \\ &\approx \Omega r + U_0 \cos\psi - r\dot{\zeta} - U_0 \zeta \sin\psi = U_{T\,init} + \Delta U_T|_{\dot{\zeta}} + \Delta U_T|_{\zeta} \end{aligned} \tag{C.4}$$

where $\Delta U_T|_{\dot{\zeta}} = -r\dot{\zeta}$; $\Delta U_T|_{\zeta} = -U_0 \zeta \sin\psi$.

The change in the tangential velocity U_T will cause a change in the inflow angle:

$$\phi = \frac{U_P}{U_{T\,init} + \Delta U_T} \cdot \frac{U_{T\,init}}{U_{T\,init}} = \phi_{init} \frac{U_{T\,init}}{U_{T\,init} + \Delta U_T} \tag{C.5}$$

On the other hand $\phi = \phi_{init} + \Delta\phi$, whence it follows that:

$$\Delta\phi = -\phi_{init} \frac{\Delta U_T}{U_{T\,init} + \Delta U_T} \tag{C.6}$$

The initial angle of attack is:

$$\alpha_{ef\,init} = \theta_0 + \phi_{init} \tag{C.7}$$

and after the initial lagging perturbation:

$$\alpha_{ef} = \theta_0 + \phi = \theta_0 + \phi_{init} + \Delta\phi \quad \alpha_{ef\,init} + \Delta\phi \tag{C.8}$$

It follows that the change in angle of attack after the initial lagging perturbation can be

written as:

$$\Delta\alpha = \Delta\phi = -\phi_{init}\frac{\Delta U_T}{U_{T\,init}+\Delta U_T} \tag{C.9}$$

and therefore, the change in the angle of attack is due to the change in the tangential component of the velocity. The initial lift and drag forces on the blade element are:

$$dL_{init} = \frac{\rho}{2} c_e C_{l_\alpha} U_{T\,init}^2 \alpha_{init}\, dr = \frac{\rho}{2} c_e C_{l_\alpha}\left(\theta_p U_{T\,init}^2 + U_P U_{T\,init}\right)dr \tag{C.10}$$

$$dD = \frac{\rho}{2} c_e C_d V_{init}^2\, dr \approx \frac{\rho}{2} c_e C_d U_{T\,init}^2\, dr \tag{C.11}$$

and after the blade is perturbed in the lagging direction, the lift and drag forces are:

$$\begin{aligned}\Delta dL &= \frac{\rho}{2} c_e C_{l_\alpha} U_T^2 \alpha\, dr = \frac{\rho}{2} c_e C_{l_\alpha}\left(\theta_p U_T^2 + U_P U_T\right)dr = \\ &= L_{init} + \frac{\rho}{2} c_e C_{l_\alpha}\Delta U_T\left[2\theta_p U_{T\,init} + \theta_p \Delta U_T + U_P\right]dr\end{aligned} \tag{C.12}$$

$$\Delta dD \approx \frac{\rho}{2} c_e C_d \left(U_{T\,init} + \Delta U_T\right)^2 dr \tag{C.13}$$

where the classical blade-element approach was used in order to express the aerodynamic forces on the blade.

The aerodynamic lagging moment on the whole blade can now be calculated. Referring to Figure B.6 of Appendix B, the general expression for the lagging moment -after integrating along the blade (starting from the lagging hinge)- is:

$$\begin{aligned}M_{aero}^{\zeta} &= \int_0^{R(1-\varepsilon_\zeta)} r\, dF_y = \int_0^{R(1-\varepsilon_\zeta)} r\left(\phi\, dL - dD\right) = \frac{\rho}{2} c_e C_{l_\alpha} \int_0^{R(1-\varepsilon_\zeta)} r\left(\theta_p U_P U_T + U_P^2\right)dr - \\ &- \frac{\rho}{2} c_e C_{l_\alpha}\frac{C_d}{C_{l_\alpha}} \int_0^{R(1-\varepsilon_\zeta)} r\, U_T^2\, dr\end{aligned} \tag{C.14}$$

The initial aerodynamic lagging moment is then:

$$M^{\zeta}_{\text{aero init}} = \frac{\rho}{2} c_e C_{l_\alpha} \int_0^{R(1-\varepsilon_\zeta)} r\left(\theta_p U_P U_{T\,init} + U_P^2\right) dr - \frac{\rho}{2} c_e C_{l_\alpha} \frac{C_d}{C_{l_\alpha}} \int_0^{R(1-\varepsilon_\zeta)} r U^2_{T\,init} dr \tag{C.15}$$

and after the blade was perturbed in the lagging direction:

$$\begin{aligned} M^{\zeta}_{\text{aero}} &= \frac{\rho}{2} c_e C_{l_\alpha} \int_0^{R(1-\varepsilon_\zeta)} r\left(\theta_p U_P \left(U_{T_{init}} + \Delta U_T\right) + U_P^2\right) dr - \\ &- \frac{\rho}{2} c_e C_{l_\alpha} \frac{C_d}{C_{l_\alpha}} \int_0^{R(1-\varepsilon_\zeta)} r\left(U_{T\,init} + \Delta U_T\right)^2 dr = M^{\zeta}_{excit} + \Delta M^{\zeta}_{a} \end{aligned} \tag{C.16}$$

Looking at (C.16), the elementary aerodynamic moment may be divided in two components: one independent of the lagging, which will be considered as an external excitation M^{ζ}_{excit}, and an other representing the change in the aerodynamic lagging moment denoted ΔM^{ζ}_{a}:

$$M^{\zeta}_{excit} = \frac{\rho}{2} c_e C_{l_\alpha} \int_0^{R(1-\varepsilon_\zeta)} r\left(\theta_p U_P U_{T\,init} + U_P^2\right) dr - \frac{\rho}{2} c_e C_{l_\alpha} \frac{C_d}{C_{l_\alpha}} \int_0^{R(1-\varepsilon_\zeta)} r\, U^2_{T\,init}\, dr \tag{C.17}$$

$$\Delta M^{\zeta}_{a} = \frac{\rho}{2} c_e C_{l_\alpha} \int_0^{R(1-\varepsilon_\zeta)} r\,\theta_p U_P \Delta U_T\, dr - \frac{\rho}{2} c_e C_{l_\alpha} \frac{C_d}{C_{l_\alpha}} \int_0^{R(1-\varepsilon_\zeta)} r\left(2\, U_{T\,init} \Delta U_T + \Delta U_T^2\right) dr \tag{C.18}$$

The first component in (C.18) results from the change in the lift force and the second from the change in the damping force. Neglecting ΔU_T^2 in the expression of ΔM^{ζ}_{a}, after some rewriting, one obtains for the helicopter:

$$\Delta M_a|_{\dot\zeta} = \frac{\rho}{2} C_{l_\alpha} c_e \int_0^{R(1-\varepsilon_\zeta)} r\theta_p U_P \Delta U_T|_{\dot\zeta}\, dr = -\rho\, C_{l_\alpha} c_e R^4 \theta_p \lambda \frac{(1-\varepsilon_\zeta)^3}{6} \Omega\, \dot\zeta \tag{C.19}$$

$$\Delta M_a|_{\zeta} = \frac{\rho}{2} C_{l_\alpha} c_e \int_0^{R(1-\varepsilon_\zeta)} r\,\theta_p U_P \Delta U_T|_{\zeta}\, dr = -\rho\, c_e C_{l_\alpha} R^4 \theta_p \lambda \frac{(1-\varepsilon_\zeta)^2}{4} \mu \cos\psi\, \Omega^2 \zeta \tag{C.20}$$

$$\begin{aligned} \Delta M_a|_{\dot\zeta} &= -\frac{\rho}{2} c_e C_{l_\alpha} \frac{C_d}{C_{l_\alpha}} \int_0^{R(1-\varepsilon_\zeta)} 2r\, U_{T\,init} \Delta U_T|_{\dot\zeta}\, dr \\ &= \rho\, c_e C_{l_\alpha} R^4 \frac{C_d}{C_{l_\alpha}} (1-\varepsilon_\zeta)^3 \left(\frac{1-\varepsilon_\zeta}{4} + \frac{\mu \sin\psi}{3}\right) \Omega\, \dot\zeta \end{aligned} \tag{C.21}$$

$$\Delta M_a|_\zeta = -\frac{\rho}{2} c_e C_{l_\alpha} \frac{C_d}{C_{l_\alpha}} \int_0^{R(1-\varepsilon_\zeta)} 2 r U_{T\,init} \Delta U_T|_\zeta \, dr = \rho c_e C_{l_\alpha} R^4 \frac{C_d}{C_{l_\alpha}} (1-\varepsilon_\zeta)^2 \times$$
$$\times \left[\frac{1-\varepsilon_\zeta}{3} \mu \cos\psi + \frac{1}{4} \mu^2 \sin 2\psi \right] \Omega^2 \zeta \qquad \text{(C.22)}$$

Summarizing, the change in the aerodynamic moment due to a lagging perturbation is induced by:

- the lagging velocity $\dot{\zeta}$ leading to a positive damping-term resulting from the change in the lift force (C.19) and a negative damping-term resulting from the change in the drag force (C.21);
- the lagging displacement ζ leading to a positive spring-term resulting from the change in lift (C.20) and a negative spring-term resulting from the change in drag (C.22).

For the wind turbine, the change in the aerodynamic moment about the lagging hinge due to the lagging motion is, according to (C.18):

$$\Delta M_a|_{\dot\zeta} = \frac{\rho}{2} C_{l_\alpha} c_e \int_0^{R(1-\varepsilon_\zeta)} r \theta_p U_P \Delta U_T|_{\dot\zeta} \, dr = -\rho C_{l_\alpha} c_e R^4 \theta_p \lambda \frac{(1-\varepsilon_\zeta)^3}{6} \Omega \dot{\zeta} \qquad \text{(C.23)}$$

$$\Delta M_a|_\zeta = \frac{\rho}{2} C_{l_\alpha} c_e \int_0^{R(1-\varepsilon_\zeta)} r \theta_p U_P \Delta U_T|_\zeta \, dr = -\rho C_{l_\alpha} c_e R^4 \theta_p \lambda \frac{(1-\varepsilon_\zeta)^2}{4} \bar{U}_0 \sin\psi \, \Omega^2 \zeta \qquad \text{(C.24)}$$

$$\Delta M_a|_{\dot\zeta} = -\frac{\rho}{2} c_e C_{l_\alpha} \frac{C_d}{C_{l_\alpha}} \int_0^{R(1-\varepsilon_\zeta)} 2 r U_{T\,init} \Delta U_T|_{\dot\zeta} \, dr = \rho c_e C_l^\alpha R^4 \frac{C_d}{C_{l_\alpha}} (1-\varepsilon_\zeta)^3 \cdot$$
$$\cdot \left(\frac{1-\varepsilon_\zeta}{4} + \frac{\bar{U}_0 \cos\psi}{3} \right) \Omega \dot{\zeta} \qquad \text{(C.25)}$$

$$\Delta M_a|_\zeta = -\frac{\rho}{2} c_e C_{l_\alpha} \frac{C_d}{C_{l_\alpha}} \int_0^{R(1-\varepsilon_\zeta)} 2 r U_{T\,init} \Delta U_T|_\zeta \, dr = -\rho c_e C_{l_\alpha} R^4 \frac{C_d}{C_{l_\alpha}} (1-\varepsilon_\zeta)^2 \times$$
$$\times \left[\frac{1-\varepsilon_\zeta}{3} \bar{U}_0 \sin\psi + \frac{1}{4} \bar{U}_0^2 \sin 2\psi \right] \Omega^2 \zeta \qquad \text{(C.26)}$$

Again, as in the helicopter case, the lagging motion is sensed by the wind turbine blade as having two components: one of a damping nature and the other of a spring nature, resulting from the changes in lift and drag due to the lagging velocity $\dot{\zeta}$ and displacement ζ.

Centrifugal Moment

The centrifugal force acting on the blade element can be expressed for both the helicopter and the wind turbine as:

$$dF_{cf} = \Omega^2 \left(e_\zeta + r \right) dm \tag{C.27}$$

The centrifugal component that produces a moment about the lagging hinge can be expressed as:

$$dF'_{cf} = \Omega^2 \left(r + e_\zeta \right) \sin\delta \, dm \tag{C.28}$$

where δ is the angle between the blade and the centrifugal moment arm (see Figure C.4).

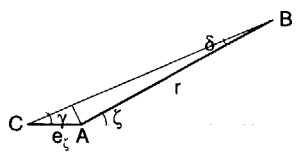

Figure C.4 Definition of δ angle

In ΔABC, using the sine theory, it follows that:

$$\frac{\sin\delta}{e_\zeta} = \frac{\sin\gamma}{r} = \frac{\sin(\zeta - \delta)}{r} \tag{C.29}$$

From (C.29), using small angle approximations, the angle δ can be determined:

$$\sin\delta = \frac{e_\zeta}{r + e_\zeta} \sin\zeta \tag{C.30}$$

Assuming also a blade of uniform mass, the moment due to the centrifugal force on the whole blade may now be calculated by integrating along the blade:

$$M_{cf} = - \int_0^{R - e_\zeta} dF'_{cf} \cdot r = - \int_0^{R - e_\zeta} \Omega^2 e_\zeta \sin\zeta \, dm \cdot r = - \Omega^2 e_\zeta \sigma_{bl} \sin\zeta \approx - \Omega^2 e_\zeta \sigma_{bl} \zeta \tag{C.31}$$

The centrifugal moment attempts to drive the blade back to the initial condition, acting

as a spring-term.

Restraint Moment

The restraint moment on the lagging hinge for both the helicopter and the wind turbine is:

$$M_\zeta = - K_\zeta \zeta \tag{C.32}$$

Inertia Moment

The moment due to the blade inertia is for both the helicopter and the wind turbine:

$$M_i = - \int_0^{R-e_\zeta} dF_i \cdot r = - \int_0^{R-e_\zeta} r \ddot{\zeta} \, dm \cdot r = -I_\zeta \ddot{\zeta} \tag{C.33}$$

Gravity Moment

As explained in Appendix B, for a wind turbine the gravity force on the blade element cannot be neglected. The component of this force in the lagging plane is:

$$dG = g \sin(\psi - \zeta) \, dm \tag{C.34}$$

so that its moment around the lagging hinge becomes:

$$M_G = \int_0^{R(1-e_\zeta)} dG \cdot r = g \sigma_\zeta \sin(\psi - \zeta) \approx g \sigma_\zeta (\sin\psi - \zeta \cos\psi) \tag{C.35}$$

In the lagging plane, the influence of the gravity is equivalent to a restraint-moment as well as an external excitation for the lagging motion.

Helicopter Lagging Equation of Motion

Combining (C.17), (C.19), (C.20), (C.21), (C.22), (C.31), (C.32), and (C.33) and assuming a uniform blade mass $I_\zeta \approx I_{bl}$, the lagging dynamics of a helicopter rotor

blade can be obtained as:

$$M_{a\,excit} - \rho C_{l_\alpha} c_e R^4 \theta_p \lambda \frac{(1-\varepsilon_\zeta)^3}{6} \Omega \dot{\zeta} + \rho c_e C_{l_\alpha} R^4 \frac{C_d}{C_{l_\alpha}} (1-\varepsilon_\zeta)^3 \left(\frac{1-\varepsilon_\zeta}{4} + \frac{\mu \sin\psi}{3} \right) \Omega \dot{\zeta} -$$
$$- \rho C_{l_\alpha} c_e R^4 \theta_p \lambda \frac{(1-\varepsilon_\zeta)^2}{4} \mu \cos\psi \, \Omega^2 \zeta + \rho c_e C_{l_\alpha} R^4 \frac{C_d}{C_{l_\alpha}} (1-\varepsilon_\zeta)^2 \left[\frac{1-\varepsilon_\zeta}{3} \mu \cos\psi + \right. \tag{C.36}$$
$$\left. + \frac{1}{4} \mu^2 \sin 2\psi \right] \Omega^2 \zeta - \Omega^2 e_\zeta \sigma_{bl} \zeta - K_\zeta \zeta = I_{bl} \ddot{\zeta}$$

Dividing (C.36) by the moment of inertia I_{bl}, using the Lock number definition and defining the blade non-rotating lead-lag natural frequency ω_ζ (dimensional and non-dimensional) as $\omega_\zeta = \sqrt{\frac{K_\zeta}{I_{bl}}}$, $\bar{\omega}_\zeta = \frac{\omega_\zeta}{\Omega}$ and the blade rotating lead-lag natural frequency (non-dimensional) $\nu_\zeta = \sqrt{\bar{\omega}_\zeta^2 + \frac{3}{2} \frac{\varepsilon_\zeta}{(1-\varepsilon_\zeta)}}$ the lagging equation of motion (C.36) becomes:

$$\ddot{\zeta} + \gamma \left[\theta_p \lambda \frac{(1-\varepsilon_\zeta)^3}{6} - \frac{C_d}{C_{l_\alpha}} (1-\varepsilon_\zeta)^3 \left(\frac{1-\varepsilon_\zeta}{4} + \frac{\mu \sin\psi}{3} \right) \right] \Omega \dot{\zeta} + \left\{ \nu_\zeta^2 + \gamma \left[\theta_p \lambda \times \right. \right.$$
$$\left. \left. \times \frac{(1-\varepsilon_\zeta)^2}{4} \mu \cos\psi - \frac{C_d}{C_{l_\alpha}} (1-\varepsilon_\zeta)^2 \left(\frac{1-\varepsilon_\zeta}{3} \mu \cos\psi + \frac{1}{4} \mu^2 \sin 2\psi \right) \right] \right\} \Omega^2 \zeta = \frac{M_{a\,excit}}{I_{bl}} \tag{C.37}$$

Usually, a transformation of variable to the azimuth angle is made $\dot{\zeta} = \Omega \frac{d\zeta}{d\psi}$ resulting in an equivalent form of the lead-lag equation (C.37):

$$\zeta'' + \gamma \left[\theta_p \lambda \frac{(1-\varepsilon_\zeta)^3}{6} - \frac{C_d}{C_{l_\alpha}} (1-\varepsilon_\zeta)^3 \left(\frac{1-\varepsilon_\zeta}{4} + \frac{\mu \sin\psi}{3} \right) \right] \zeta' + \left\{ \nu_\zeta^2 + \gamma \left[\theta_p \lambda \times \right. \right.$$
$$\left. \left. \times \frac{(1-\varepsilon_\zeta)^2}{4} \mu \cos\psi - \frac{C_d}{C_{l_\alpha}} (1-\varepsilon_\zeta)^2 \left(\frac{1-\varepsilon_\zeta}{3} \mu \cos\psi + \frac{1}{4} \mu^2 \sin 2\psi \right) \right] \right\} \zeta = \frac{M_{a\,excit}}{I_{bl}} \tag{C.38}$$

Wind Turbine Lagging Equation of Motion

Adding all the moments acting on the lagging hinge as given by (C.17), (C.23), (C.24), (C.25), (C.26), (C.31), (C.32), (C.33) and (C.35) the lead-lag equation of motion is

obtained:

$$M_{a\,excit} - \rho C_{l_\alpha} c_e R^4 \theta_p \lambda \frac{(1-\varepsilon)^3}{6} \Omega \dot{\zeta} + \rho c_e C_{l_\alpha} R^4 \frac{C_d}{C_{l_\alpha}} (1-\varepsilon_\zeta)^3 \left(\frac{1-\varepsilon_\zeta}{4} + \frac{\bar{U}_0 \cos\psi}{3}\right) \Omega \dot{\zeta}$$
$$- \rho C_{l_\alpha} c_e R^4 \theta_p \lambda \frac{(1-\varepsilon)^2}{4} \bar{U}_0 \sin\psi\, \Omega^2 \zeta - \rho c_e C_{l_\alpha} R^4 \frac{C_d}{C_{l_\alpha}} (1-\varepsilon_\zeta)^2 \left[\frac{1-\varepsilon_\zeta}{3} \bar{U}_0 \sin\psi + \right. \tag{C.39}$$
$$\left. + \frac{1}{4} \bar{U}_0^2 \sin 2\psi \right] \Omega^2 \zeta - \Omega^2 e_\zeta \sigma_\zeta \zeta + g \sigma_\zeta (\sin\psi - \zeta \cos\psi) - K_\zeta \zeta = I_\zeta \ddot{\zeta}$$

Approximating I_ζ and σ_ζ by I_{bl} and σ_{bl} respectively, dividing (C.39) by I_{bl}, and using the definition of Lock number, non-rotating natural lead-lag frequency ω_ζ, non-dimensional rotating natural lead-lag frequency ν_ζ and the definition of the gravity term $G = \frac{g\,\sigma_{bl}}{I_{bl}} = \frac{g\,m_{bl}\,\bar{r}_g\,R}{I_{bl}}$, the horizontal axis wind turbine lead-lag equation of motion is obtained in the blade rotating system:

$$\ddot{\zeta} + \gamma \left[\theta_p \lambda \frac{(1-\varepsilon_\zeta)^3}{6} - \frac{C_d}{C_{l_\alpha}} (1-\varepsilon_\zeta)^3 \left(\frac{1-\varepsilon_\zeta}{4} + \frac{\bar{U}_0 \cos\psi}{3}\right)\right] \Omega \dot{\zeta} + \left\{\nu_\zeta^2 + G\cos\psi + \gamma \left[\theta_p \lambda \frac{(1-\varepsilon_\zeta)^2}{4} \times \right.\right. \tag{C.40}$$
$$\left.\left. \times \bar{U}_0 \sin\psi + \frac{C_d}{C_{l_\alpha}} (1-\varepsilon_\zeta)^2 \left(\frac{1-\varepsilon_\zeta}{3} \bar{U}_0 \sin\psi + \frac{1}{4} \bar{U}_0^2 \sin 2\psi\right)\right]\right\} \Omega^2 \zeta = \frac{M_{a\,excit}}{I_{bl}} + G \sin\psi$$

or expressed as a derivative relative to the azimuth angle:

$$\zeta'' + \gamma \left[\theta_p \lambda \frac{(1-\varepsilon_\zeta)^3}{6} - \frac{C_d}{C_{l_\alpha}} (1-\varepsilon_\zeta)^3 \left(\frac{1-\varepsilon_\zeta}{4} + \frac{\bar{U}_0 \cos\psi}{3}\right)\right] \zeta' + \left\{\nu_\zeta^2 + G\cos\psi + \gamma \left[\theta_p \lambda \frac{(1-\varepsilon_\zeta)^2}{4} \times \right.\right. \tag{C.41}$$
$$\left.\left. \times \bar{U}_0 \sin\psi + \frac{C_d}{C_{l_\alpha}} (1-\varepsilon_\zeta)^2 \left(\frac{1-\varepsilon_\zeta}{3} \bar{U}_0 \sin\psi + \frac{1}{4} \bar{U}_0^2 \sin 2\psi\right)\right]\right\} \zeta = \frac{M_{a\,excit}}{I_{bl}} + G \sin\psi$$

Appendix D

Coleman Transformation and Its Interpretation

D.1 Definition of Coleman Transformation

Usually, the degrees of freedom associated with rotating subsystems can be transformed into the non-rotating system by means of the "Coleman transformation" (multiblade coordinate transformation (MCT), Fourier transformation). This transformation was first used by **Coleman** [1958][19] in order to investigate the ground resonance phenomenon for a hinged blade helicopter. In multiblade coordinates, the individual flap motion (or lead-lag motion or any other degree of freedom of the blade, which will be noted as χ) is seen as the motion of the rotor disc.

In general, the motion of the rotor blades may be observed either in the blade rotating system of reference, as N degrees of freedom representing the motion of each blade deflected in a certain direction χ, or in the hub non-rotating system of reference as N degrees of freedom representing the multiblade effect of the motion of all blades deflected in direction χ. The degrees of freedom in the non-rotating system are obtained by means of the Coleman transformation. The Coleman transformation represents a linear transformation between the non-rotating degrees of freedom (denoted a_0, a_1,...,a_n, b_1,...,b_n) and the blade rotating degrees of freedom χ_k defined as:

$$\begin{aligned}
\text{Rotating:} \quad & \chi_k(t) = a_0(t) + (-1)^k \chi_{N/2}(t) + \sum_{n=1}^{K} \left(a_n(t)\cos n\psi_k + b_n(t)\sin n\psi_k \right) \quad \Leftrightarrow \\
\text{Non-rotating:} \quad & a_0(t) = \frac{1}{N}\sum_{k=1}^{N} \chi_k(t) \; ; \; \chi_{N/2}(t) = \frac{1}{N}\sum_{k=1}^{N} (-1)^k \chi_k(t) \\
& a_n(t) = \frac{2}{N}\sum_{k=1}^{N} \chi_k(t)\cos n\psi_k \quad ; \quad n = 1...K \\
& b_n(t) = \frac{2}{N}\sum_{k=1}^{N} \chi_k(t)\sin n\psi_k \quad ; \quad n = 1...K
\end{aligned} \tag{D.1}$$

where:

$$\psi_k = \psi + (k-1)\frac{2\pi}{N} \; ; \; k = 1...N \; ; \; N \geq 3 \; ; \quad K = \frac{N-1}{2}, \; N \text{ odd} \; ; \; K = \frac{N-2}{2}, \; N \text{ even} \tag{D.2}$$

The new degrees of freedom of the rotor in the non-rotating frame as obtained via the

Coleman transformation consist of the so-called "collective" mode a_0, "cyclic" modes a_1 ... a_n and b_1 ... b_n and, for an even-bladed rotor, the "differential or reactionless" mode $\chi_{N/2}$. Sections D.2 and D.5 of the present appendix explain the physical meaning of these new rotor degrees of freedom for the blade flap and lead-lag motions. Observe that the Coleman transformation is defined for a rotor with a number of blades N≥3. For a two-bladed rotor, the non-rotating degrees of freedom are only the coning a_0 and the differential modes $\chi_{N/2}$. Because of the absence of the cyclic modes, two-bladed rotor dynamics are fundamentally different from the dynamics of rotors with three or more blades. Section F.2 of Appendix F presents the Coleman transformation applied to the lead-lag motion of a two-bladed rotor and Chapter 6 the corresponding dynamics of the motion of such a rotor in the case a two-bladed wind turbine.

Defining the rotating coordinates as $\chi_R = \{\chi_1\ \chi_2\ \chi_3\ \cdots\ \chi_N\}^T$ and the corresponding non-rotating coordinates as $\chi_{NR} = \{a_0\ a_1\ b_1\ \chi_{N/2} \cdots\ a_N\ b_N\}^T$, the Coleman transformation (D.1) can be written as:

$$\text{Rotating:} \quad \chi_R = \left[L_R\right]\left\{\chi_{NR}\right\} \quad \Leftrightarrow \quad \text{Non-rotating:} \quad \chi_{NR} = \left[L_{NR}\right]\left\{\chi_R\right\} \tag{D.3}$$

where L_{NR} is the matrix of coefficients in the non-rotating frame and L_R is the matrix of coefficients in the rotating frame. Looking at (D.1), the expression of L_{NR} is:

$$[\ L_{NR}\ ] = [\ L_R\ ]^{-1} = \begin{bmatrix} 1/N & 1/N & \cdots & \cdots & 1/N \\ (2/N)\cos\psi_1 & (2/N)\cos\psi_2 & \cdots & \cdots & (2/N)\cos\psi_N \\ (2/N)\sin\psi_1 & (2/N)\sin\psi_2 & \cdots & \cdots & (2/N)\sin\psi_N \\ \cdots\cdots & \cdots\cdots\cdots & & & \\ (2/N)\cos K\psi_1 & (2/N)\cos K\psi_2 & \cdots & \cdots & (2/N)\cos K\psi_N \\ (2/N)\sin K\psi_1 & (2/N)\sin K\psi_2 & \cdots & \cdots & (2/N)\sin K\psi_N \\ -(1/N) & (1/N) & \cdots & \cdots & (-1)^N(1/N) \end{bmatrix} \tag{D.4}$$

From (D.4), the expression of L_R is obtained as the inverse of matrix L_{NR}: $L_R = \text{inv}\left(L_{NR}\right)$. Knowing the blade equation of motion in the χ_k degree of freedom and writing this equation for each blade (defined by a specific azimuth position), one obtains the system of equations giving the motion of each blade in the rotating system. Chapter 2 demonstrated that for a rotor blade, the motion of each blade in χ_k usually corresponds to a one degree-of-freedom vibrating system. The best way is to conduct

the calculation in the matrix form. For N blades this can be formally written as:

$$\left[M_R \right] \left\{ \chi_R \right\}'' + \left[C_R \right] \left\{ \chi_R \right\}' + \left[K_R \right] \left\{ \chi_R \right\} = \left\{ F_R \right\} \tag{D.5}$$

where M_R, C_R, K_R and F_R are respectively the mass matrix, damping matrix, spring (stiffness) matrix and the vector of external forces. Equation (D.5) is usually brought to the form:

$$\left\{ \chi_R \right\}'' + \left[M_R^{-1} C_R \right] \left\{ \chi_R \right\}' + \left[M_R^{-1} K_R \right] \left\{ \chi_R \right\} = \left\{ M_R^{-1} F_R \right\} \tag{D.6}$$

The derivatives χ'_R and χ''_R can formally be also expressed by deriving (D.5) w.r.t. ψ as:

$$\begin{aligned} \left\{\chi_R\right\}' &= \left(\left[L_R\right]\left\{\chi_{NR}\right\}\right)' = \left[L_R\right]' \left\{\chi_{NR}\right\} + \left[L_R\right]\left\{\chi_{NR}\right\}' \\ \left\{\chi_R\right\}'' &= \left[L_R\right]'' \left\{\chi_{NR}\right\} + 2\left[L_R\right]' \left\{\chi_{NR}\right\}' + \left[L_R\right]\left\{\chi_{NR}\right\}'' \end{aligned} \tag{D.7}$$

Substituting (D.7) into (D.6), after multiplying with the inverse matrix L_R^{-1} one obtains:

$$\begin{aligned} &\left\{\chi_{NR}\right\}'' + \left[L_{NR}\right]\left(2\left[L'_R\right] + \left[M_R^{-1} C_R L_R\right]\right) \left\{\chi_{NR}\right\}' + \left[L_{NR}\right] \times \\ &\times \left(\left[L_R\right]'' + \left[M_R^{-1} C_R L'_R\right] + \left[M_R^{-1} K_R L_R\right]\right) \left\{\chi_{NR}\right\} = \left[L_{NR} M_R^{-1}\right] \left\{F_R\right\} \end{aligned} \tag{D.8}$$

The formal form of the equations of motion (D.5) in the non-rotating frame is therefore:

$$\left\{\chi_{NR}\right\}'' + \left[C_{NR}\right] \left\{\chi_{NR}\right\}' + \left[K_{NR}\right] \left\{\chi_{NR}\right\} = \left\{F_{NR}\right\} \tag{D.9}$$

with respectively C_{NR}, K_{NR}, and F_{NR} as the damping, spring and external forces matrices as expressed in the non-rotating system of reference as:

$$\begin{aligned} C_{NR} &= L_{NR}\left(2L'_R + M_R^{-1} C_R L_R\right) \qquad K_{NR} = L_{NR}\left(L''_R + M_R^{-1} C_R L'_R + M_R^{-1} K_R L_R\right) \\ F_{NR} &= \left[L_{NR} M_R^{-1}\right] \left\{F_R\right\} \end{aligned} \tag{D.10}$$

The present appendix exemplifies how the Coleman transformation can be applied to the flapping and lagging motion and what the physical interpretation of the new degrees of freedom obtained in the non-rotating system is.

D.2 The Flapping Motion in the Non-rotating System

Assuming the χ_k degree of freedom as the blade flapping β_k, the above process of transforming the equations of motion from the rotating to the non-rotating system may be applied to a 4-bladed rotor of equation (B.38) (in case of a helicopter blade) or (B.41) (in case of a wind turbine blade). Assuming a 4-bladed helicopter rotor, the flapping coordinates are respectively $\beta_R = \{\beta_1\ \beta_2\ \beta_3\ \beta_4\}^T$ and $\beta_{NR} = \{a_0\ a_1\ b_1\ \beta_{N/2}\}^T$ in the rotating and non-rotating system. Assuming that the blade has no hinge offset (e_β= 0), the helicopter flapping equations of motion (B.38) were transformed into the non-rotating shaft system, resulting in the following equations:

$$\beta''_{NR} + \begin{bmatrix} \frac{\gamma}{8} & 0 & \gamma\frac{\mu}{12} & 0 \\ 0 & \frac{\gamma}{8} & 2 & -\gamma\frac{\mu}{6}\sin 2\psi \\ \gamma\frac{\mu}{6} & -2 & \frac{\gamma}{8} & \gamma\frac{\mu}{6}\cos 2\psi \\ 0 & -\gamma\frac{\mu}{12}\sin 2\psi & \gamma\frac{\mu}{12}\cos 2\psi & \frac{\gamma}{8} \end{bmatrix} \beta'_{NR} + \tag{D.11}$$

$$+ \begin{bmatrix} \nu_\beta^2 & 0 & 0 & -\gamma\frac{\mu^2}{8}\sin 2\psi \\ \gamma\frac{\mu}{6} & \nu_\beta^2 - 1 + \gamma\frac{\mu^2}{16}\sin 4\psi & \frac{\gamma}{8} + \gamma\frac{\mu^2}{16} - \gamma\frac{\mu}{16}\cos 4\psi & -\gamma\frac{\mu}{6}\cos 2\psi \\ 0 & -\frac{\gamma}{8} + \gamma\frac{\mu^2}{16} - \gamma\frac{\mu^2}{16}\cos 4\psi & \nu_\beta^2 - 1 - \gamma\frac{\mu^2}{16}\sin 4\psi & -\gamma\frac{\mu}{6}\sin 2\psi \\ -\gamma\frac{\mu^2}{8}\sin 2\psi & -\gamma\frac{\mu}{6}\cos 2\psi & -\frac{\gamma}{6}\sin 2\psi & \nu_\beta^2 \end{bmatrix} \beta_{NR} = \left\{F_R\right\}$$

For a detailed derivation of this equation one may also consult **Pavel** [1996][85].

As introduced, the Coleman transformation seems to be more of a purely mathematical skill that enables the designer to handle both rotating and non-rotating coordinates. However, it can be demonstrated that the new coordinates of the flap motion in the non-rotating system correspond to the rotor disc-tilt coordinates.

In the rotor disc-tilt approximation, the flapping motion is expressed by the coning angle, and the longitudinal and lateral disc-tilt angles. The coning angle shows that all blades are coning from a reference plane to the rotor disc plane. The longitudinal disc-tilt angle corresponds to a tilting of the rotor disc in the longitudinal plane whereas the

lateral disc-tilt angle corresponds to a tilting of the rotor disc in the lateral plane (see Figure D.1 and Figure D.2).

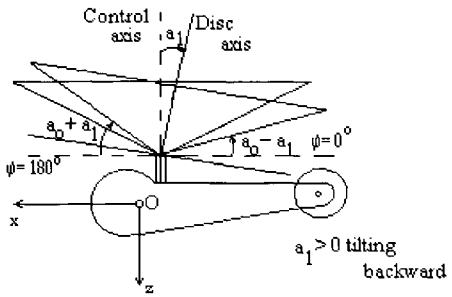

Figure D.1 Longitudinal disc-tilt angle

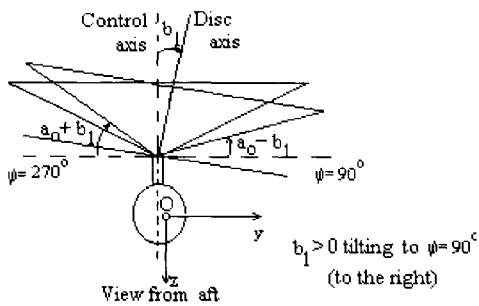

Figure D.2 Lateral disc-tilt angle

By means of the Coleman transformation, the first flapping mode of the rotating blade of a frequency equal to the rotor rotational speed, splits in four rotor modes (for a 4-bladed rotor):

- a "coning" mode where all blades are moving simultaneously in the same direction;
- a "progressive (nutation) tilting" mode corresponding to a high-frequency wobbling of the rotor disc in the same direction as the rotor rotation (the frequency is approximative 1-P higher than the isolated blade flapping frequency);
- a "regressive (precession) tilting" mode corresponding to a low-frequency wobbling of the rotor disc in the same or opposite direction of the rotor rotation, depending on the correlation between the isolated blade flapping frequency ω_β and the rotor speed Ω: when $\omega_\beta < \Omega$ ($\bar{\omega}_\beta < 1$/rev), i.e. the rotor is soft flapwise according to the definition of section 3.3, the disc plane tilts in the same direction as the rotor direction; when $\omega_\beta > \Omega$ ($\bar{\omega}_\beta > 1$/rev), i.e the rotor is stiff flapwise, the disc plane tilts in the opposite direction. In general, articulated rotors have an isolated flapping frequency smaller than 1/rev, so the wobble is in the direction of the rotor rotation, but hingeless rotors have a flapping frequency larger than 1/rev, so that the low-frequency mode is truly a regressive one, the disc plane wobbling opposite to the direction of the rotor rotation.
- a "differential (reactionless) tilting" mode introduced only in an even-bladed rotor in which blades 1 and 3 move up while blades 2 and 4 move down (highly damped).

A five-bladed rotor instead of a differential mode, has a "progressive warping mode" and a "regressive warping mode" which are reactionless.

D.3 Interpretation of the Non-rotating Flapping Characteristics in the Complex Plane

Some characteristics of the flapping eigenvalues in the non-rotating frame can be obtained by analysing the helicopter motion in hover. Equations (D.11) for the case of hovering flight, neglecting the terms varying with the blade azimuth (this is allowed in the domain of normal manoeuvres according to **Hohenemser and Yin** [1974][43]) become:

$$a_0'' + \frac{\gamma}{8}a_0' + a_0 = 0 \quad ; \quad \beta_{N/2}'' + \frac{\gamma}{8}\beta_{N/2}' + \beta_{N/2} = 0$$

$$\begin{Bmatrix} a_1 \\ b_1 \end{Bmatrix}'' + \begin{bmatrix} \gamma/8 & 2 \\ -2 & \gamma/8 \end{bmatrix} \begin{Bmatrix} a_1 \\ b_1 \end{Bmatrix}' + \begin{bmatrix} \nu_\beta^2 - 1 & \gamma/8 \\ -\gamma/8 & \nu_\beta^2 - 1 \end{bmatrix} \begin{Bmatrix} a_1 \\ b_1 \end{Bmatrix} = 0 \qquad \text{(D.14)}$$

According to (D.14), in hovering flight, the coning and differential flapping modes decouple from the progressing and regressing tilting mode equations. For the rotor disc plane equations, the corresponding advancing and regressing poles are:

$$s_{NR\,adv} = -\frac{\gamma}{16} + i\sqrt{\nu_\beta^2 - \left(\frac{\gamma}{16}\right)^2 + 1 \pm 2\sqrt{\nu_\beta^2 - \left(\frac{\gamma}{16}\right)^2}} = -\frac{\gamma}{16} + i\left(\sqrt{\nu_\beta^2 - \left(\frac{\gamma}{16}\right)^2} \pm 1\right) \qquad \text{(D.15)}$$

$$s_{NR\,reg} = -\frac{\gamma}{16} - i\sqrt{\nu_\beta^2 - \left(\frac{\gamma}{16}\right)^2 + 1 \pm 2\sqrt{\nu_\beta^2 - \left(\frac{\gamma}{16}\right)^2}} = -\frac{\gamma}{16} - i\left(\sqrt{\nu_\beta^2 - \left(\frac{\gamma}{16}\right)^2} \pm 1\right)$$

and the coning and the reactionless mode coincide:

$$\left(s_{NR}\right)_{con} = \left(s_{NR}\right)_{\beta_{N/2}} = -\frac{\gamma}{16} \pm i\sqrt{\nu_\beta^2 - \left(\frac{\gamma}{16}\right)^2} \qquad \text{(D.16)}$$

Recalling the flapping equation in the rotating system (B.38), particularised it for the case of hovering flight (μ=0), it is equivalent to a damped oscillation of equation $\frac{d^2\beta_k}{d\psi^2} + \frac{\gamma}{8}\frac{d\beta_k}{d\psi} + \nu^2\beta_k = 0$ with eigenvalues $s_R = -\frac{\gamma}{16} \pm i\sqrt{\nu_\beta^2 - \left(\frac{\gamma}{16}\right)^2}$. It follows that in the non-rotating system the advancing mode shifts frequency as compared to the

rotating frame by a value +1/rev, whereas the regressing mode shifts frequency in the rotating frame by a value -1/rev, with damping remaining the same as in the rotating system (see Figure D.3):

$$s_{NR\,adv} = s_R + i \quad ; \qquad s_{NR\,reg} = s_R - i \tag{D.17}$$

The eigenvalues of the coning and the reactionless mode coincide with the rotating flapping eigenvalues.

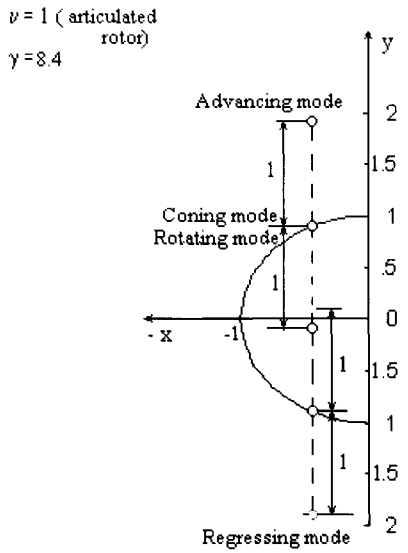

Figure D.3 Interpretation of the Coleman transformation in the complex plane

D.4 Interpretation of the First-Order Flapping Dynamics

In hovering flight, neglecting the flapping accelerations in (D.14), yields for the system of equations:

$$\begin{bmatrix} \gamma/8 & 2 \\ -2 & \gamma/8 \end{bmatrix} \begin{Bmatrix} a_1 \\ b_1 \end{Bmatrix}' + \begin{bmatrix} \nu_\beta^2 - 1 & \gamma/8 \\ -\gamma/8 & \nu_\beta^2 - 1 \end{bmatrix} \begin{Bmatrix} a_1 \\ b_1 \end{Bmatrix} = 0 \tag{D.18}$$

of eigenvalues:

$$s_{1,2} = -\frac{\gamma}{16}\,\frac{\frac{1+\nu_\beta^2}{2}}{1+(\gamma/16)^2} \pm i\,\frac{\left(\frac{\gamma}{16}\right)^2+\frac{1-\nu_\beta^2}{2}}{1+(\gamma/16)^2} \tag{D.19}$$

In vacuum ($\gamma = 0$) and approximating $\frac{1-\nu_\beta^2}{2} \approx 1-\nu_\beta$, which is allowed since the isolated blade flap frequency varies between 1 and 1.15 for helicopters, solution (D.19) becomes:

$$s_{1,2} = \pm i\,(1-\nu_\beta) \tag{D.20}$$

This solution corresponds exactly to the regressing flap mode solution (D.15) in vacuum:

$$s_{NR\ adv} = \pm i\,(1+\nu_\beta) \quad ; \quad s_{NR\ reg} = \pm i\,(1-\nu_\beta) \tag{D.21}$$

Therefore, the eigenvalues obtained by solving the first order differential flapping equations correspond exactly to the regressing flapping mode .

With aerodynamics included ($\gamma \neq 0$), returning to (D.19), one may write:

$$s_{1,2} = \frac{(1+\nu_\beta^2)/2}{1+(\gamma/16)^2}\left[-\frac{\gamma}{16} \pm i\left(\frac{1+(\gamma/16)^2}{(1+\nu_\beta^2)/2}-1\right)\right] \tag{D.22}$$

The eigenvalues (D.22) in this case have to be compared with the regressing flapping mode as given by (D.15):

$$s_{NR\,reg} = -\frac{\gamma}{16} \pm i\left(\sqrt{\nu_\beta^2-\left(\frac{\gamma}{16}\right)^2}-1\right) \tag{D.23}$$

It follows that one has to be able to approximate $\frac{(1+\nu_\beta^2)/2}{1+(\gamma/16)^2}$ to 1 and $\frac{1+(\gamma/16)^2}{(1+\nu_\beta^2)/2}$ to $\sqrt{\nu_\beta^2-\left(\frac{\gamma}{16}\right)^2}$ in order to demonstrate that the first order flapping dynamics solution is close to the regressing flapping solution. For helicopters, the Lock number γ, as

discussed in section 2.6.1 of Chapter 2, varies between 5 and 15 and thus these approximations can be made with an error of maximum 25%. It follows that the solution of the first order differential flapping equation may be approximated by the regressing flapping mode .

In forward flight, the eigenvalue problem of the equations in a_1 and b_1 of (D.11), with the terms periodic in the blade azimuth neglected, is equivalent to the following problem:

$$\begin{Bmatrix} a_1 \\ b_1 \end{Bmatrix}'' + \begin{bmatrix} \gamma/8 & 2 \\ -2 & \gamma/8 \end{bmatrix} \begin{Bmatrix} a_1 \\ b_1 \end{Bmatrix}' + \begin{bmatrix} \nu_\beta^2 - 1 & \gamma/8 + \gamma\mu^2/16 \\ -\gamma/8 + \gamma\mu^2/16 & \nu_\beta^2 - 1 \end{bmatrix} \begin{Bmatrix} a_1 \\ b_1 \end{Bmatrix} = 0 \tag{D.24}$$

Neglecting the flapping accelerations in (D.24) results in solving the system:

$$\begin{bmatrix} \gamma/8 & 2 \\ -2 & \gamma/8 \end{bmatrix} \begin{Bmatrix} a_1 \\ b_1 \end{Bmatrix}' + \begin{bmatrix} \nu_\beta^2 - 1 & \gamma/8 + \gamma\mu^2/16 \\ -\gamma/8 + \gamma\mu^2/16 & \nu_\beta^2 - 1 \end{bmatrix} \begin{Bmatrix} a_1 \\ b_1 \end{Bmatrix} = 0 \tag{D.25}$$

of characteristic equation:

$$\left(4 + \frac{\gamma^2}{64}\right) s^2 + \frac{\gamma}{4}\left(1 + \nu_\beta^2\right) s + \left(1 - \nu_\beta^2\right)^2 + \frac{\gamma^2}{64}\left(1 - \frac{\mu^4}{4}\right) = 0 \tag{D.26}$$

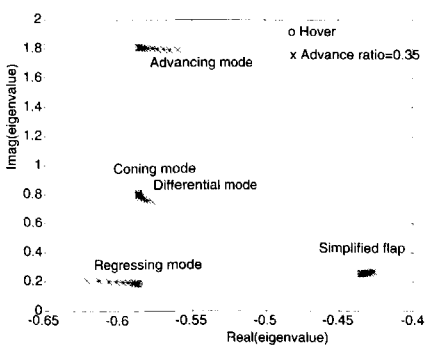

Figure D.4 Puma flapping eigenvalues

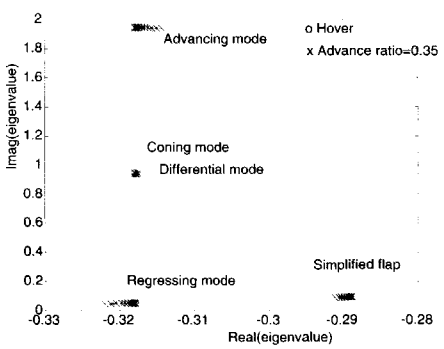

Figure D.5 Bo-105 flapping eigenvalues

Calculating the eigenvalues of the flapping motion represented first by the system of

equations (D.24) and subsequently by the simplified system of equations (D.25), their variation with the advance ratio was represented for two normal helicopter configurations in Figure D.4 and Figure D.5 -one for the Puma SA-330, the other for the Bölkov Bö-105 helicopter-. From these figures it may be observed that the simplified flapping solution corresponding to (D.26) may be approximated by the low frequency regressing mode.

D.5 The Lead-Lag Motion in the Non-rotating System

Assuming the χ_k degree of freedom as the blade lead-lag ζ_k, the lead-lag motion of the blades may also be regarded in the non-rotating system by means of Coleman coordinates. The lead-lag equation of motion as given by Figure C.4 (for a helicopter blade) or Figure C.4 (for a wind turbine blade) can be transposed into the non-rotating system following the above-described procedure. The lead-lag equation first has to be written for each blade (defined by a specific azimuth position) in order to define the damping C_R, spring K_R and external forces F_R matrices in the rotating coordinates $\zeta_R = \left\{\zeta_1\ \zeta_2\ \zeta_3\ \zeta_4\right\}^T$. Next, using (D.10), the same matrices can be calculated, this time in the non-rotating lead-lag coordinates $\zeta_{NR} = \left\{a_0\ a_1\ b_1\ \zeta_{N/2}\right\}^T$. The equations of motion for the lead-lag motion in the non-rotating system are thus obtained. As in the flapping case, the lagging coordinates in the non-rotating system have a physical interpretation. The lead-lag mode transposes from the rotating system to the non-rotating system in (see Figure D.6):

- a "collective (drive train) lead-lag" mode where all the blades move simultaneously in the lead-lag direction;
- a "progressive lead-lag" mode corresponding to a high-frequency whirling of the rotor centre of gravity in the same direction as the rotor rotation (the frequency is approximatively 1-P higher than the isolated blade lead-lag frequency);
- a "regressing lead-lag" mode corresponding to a low-frequency whirling of the rotor centre of gravity in the same or opposite direction as the rotor rotation, depending on the rotor speed: when $\Omega < \omega_\zeta$, i.e. the rotor is stiff-inplane according to the definition of section 3.3 of Chapter 3, the rotor centre of gravity whirls opposite to the rotor rotation and at a frequency 1-P lower than the isolated blade lag frequency. As the rotor speed approaches $\Omega = \omega_\zeta$, the rotor centre of gravity whirl speed reduces and becomes zero at the point $\Omega = \omega_\zeta$ when the centre of gravity is offset from the hub centre and does not rotate with the rotor transition speed; when $\Omega > \omega_\zeta$, i.e. the rotor is soft-inplane, the rotor centre of gravity whirls in the same direction as the rotor and picks up speed as the rotor speed increases (that is why this mode is also called "degenerate regressive lead-lag mode"). This whirl speed, however always stays below the rotor speed.
- a "reactionless" (scissors) lead-lag mode" where blades 1 and 3 move in one direction and blades 2 and 4 in the opposite direction.

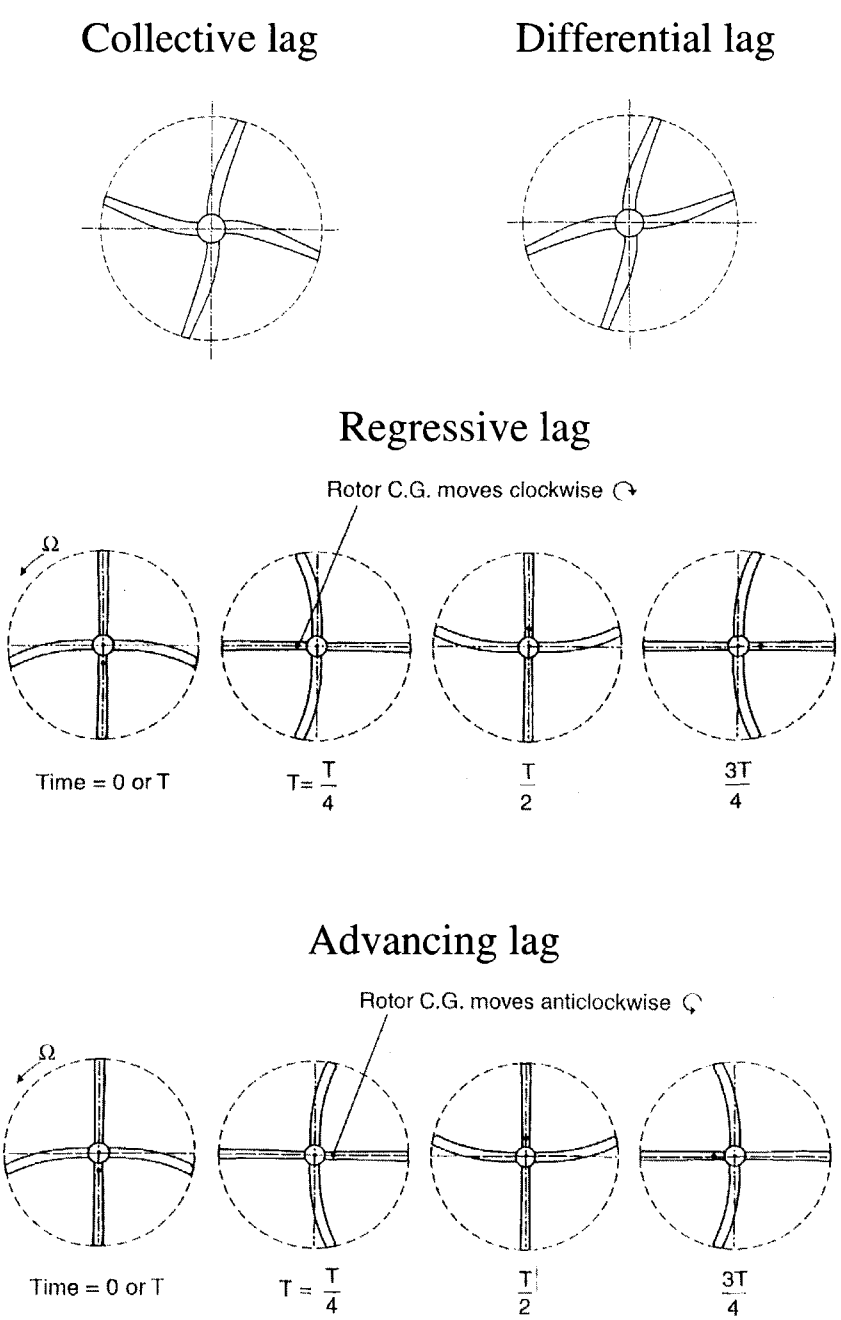

Figure D.6 Lead-lag motion in the non-rotating system [**Bir et. al.** *[1998]*[7])

Appendix E

Six and Eight Degree-of-Freedom Helicopter Flight Dynamics Models

E.1 Six Degree-of-Freedom Non-linear Helicopter Model

The free motion of the helicopter can be described in an inertial system $x_0y_0z_0$ by using a rigid-body dynamic model with six degree-of-freedom {u, v, w, p, q, r} and fourteen state variables {u, v, w, p, q, r, Θ, Φ, Ψ, x, y, z, λ_i, $\lambda_{i\,tr}$ } where u is the horizontal velocity, v the lateral velocity, w the rate of descent, p the roll rate, q the pitch rate, r the yaw rate, Θ the helicopter attitude, Ψ the helicopter yaw, Φ the helicopter lateral inclination, λ_i the main rotor dynamic inflow and $\lambda_{i\,tr}$ the tailrotor dynamic inflow as seen in Figure E.2. The forces and moments exerted on each helicopter component are illustrated in Figure E.1(a) to (c).

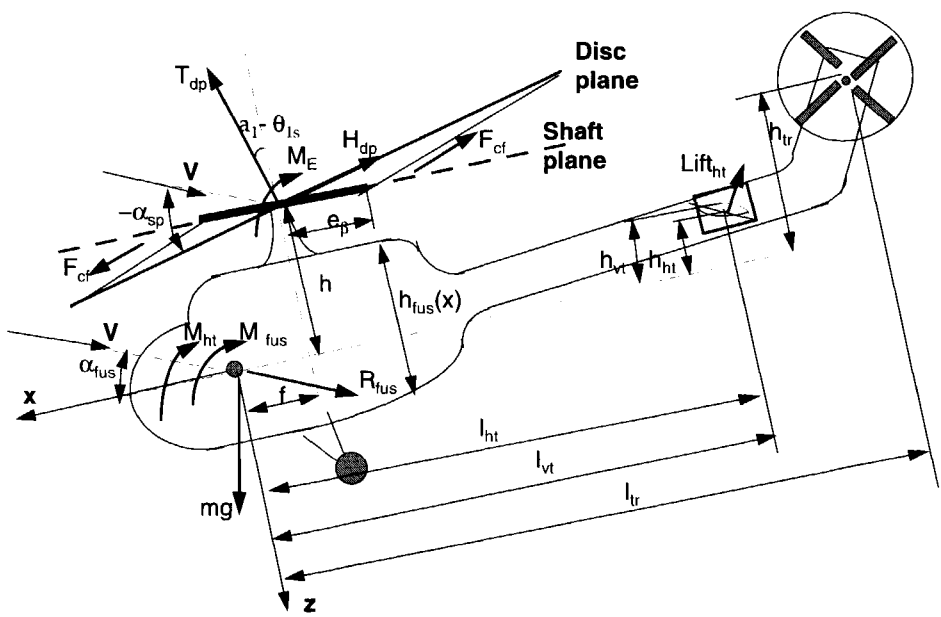

Figure E.1 (a) Helicopter model: Lateral view

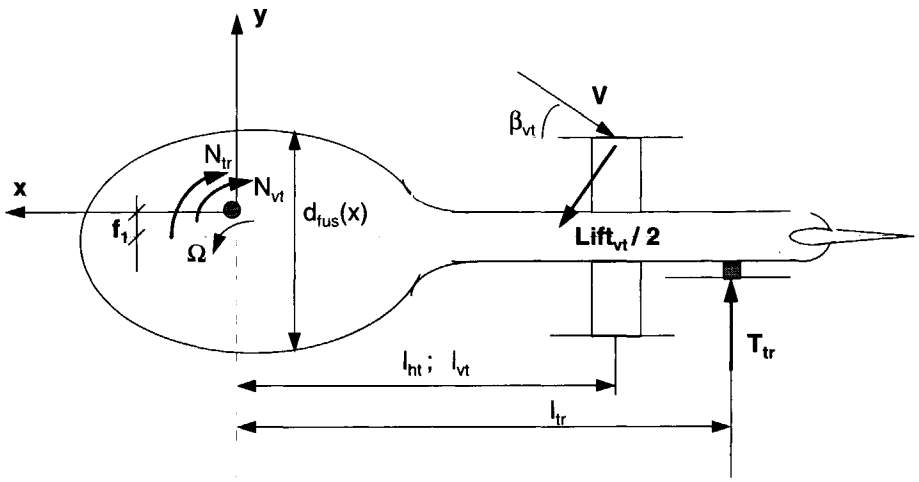

Figure E.1(b) Helicopter model: Top view

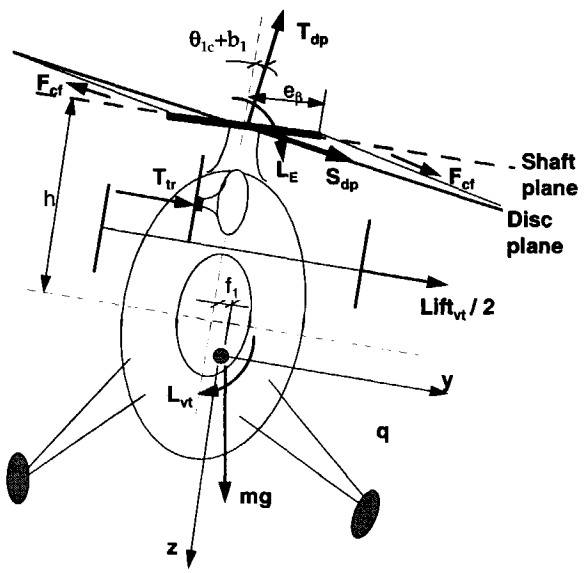

Figure E.1(c) Helicopter model: Aft View

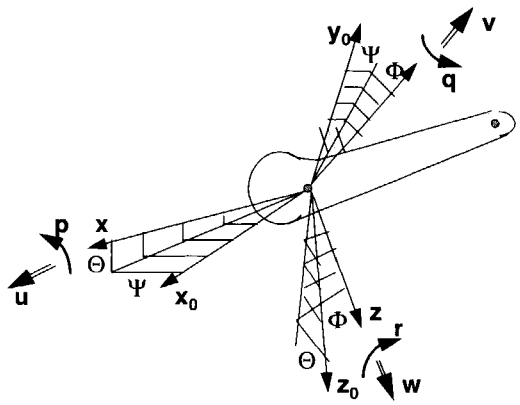

Figure E.2 Helicopter position with respect to a fixed system

E.2 Equations of Motion for the 6-dof Body Model

Using the assumptions introduced on page 101 of Chapter 5, the helicopter equations of motion in a fixed system of reference $\{x_0 y_0 z_0\}$ may be expressed as:

$$\dot{u} = -g\sin\Theta + \frac{X}{m} + r\,v - q\,w \tag{E.1}$$

$$\dot{v} = g\cos\Theta\sin\Phi + \frac{Y}{m} - r\,u + p\,w \tag{E.2}$$

$$\dot{w} = g\cos\Theta\cos\Phi + \frac{Z}{m} - p\,v + q\,u \tag{E.3}$$

$$\dot{p} = \frac{I_z}{I_x I_z - I_{xz}^2} L + \frac{I_{xz}}{I_x I_z - I_{xz}^2} N + \frac{I_y I_z - I_z^2 - I_{xz}^2}{I_x I_z - I_{xz}^2} r\,q + \frac{I_{xz}(I_x - I_y + I_z)}{I_x I_z - I_{xz}^2} p\,q \tag{E.4}$$

$$\dot{q} = \frac{M}{I_y} + \frac{(I_z - I_x)}{I_y} p\,r + \frac{I_{xz}}{I_y}\left(r^2 - p^2\right) \tag{E.5}$$

$$\dot{r} = \frac{I_x}{I_x I_z - I_{xz}^2} N + \frac{I_{xz}}{I_x I_z - I_{xz}^2} L + \frac{I_x^2 - I_x I_y + I_{xz}^2}{I_x I_z - I_{xz}^2} p\,q - \frac{I_{xz}\left(I_x - I_y + I_z\right)}{I_x I_z - I_{xz}^2} r\,q \tag{E.6}$$

$$\dot{\Phi} = p + (\,q \sin\Phi + r \cos\Phi\,) \tan\Theta \tag{E.7}$$

$$\dot{\Theta} = q \cos\Phi - r \sin\Phi \tag{E.8}$$

$$\dot{\Psi} = \frac{q \sin\Psi + r \cos\Phi}{\cos\Theta} \tag{E.9}$$

$$\dot{x} = \left[u \cos\Theta + \left(v \sin\Phi + w \cos\Phi\right) \sin\Theta\right] \cos\Psi - \left(v \cos\Phi - w \sin\Phi\right) \sin\Psi \tag{E.10}$$

$$\dot{y} = \left[u \cos\Theta + \left(v \sin\Phi + w \cos\Phi\right) \sin\Theta\right] \sin\Psi + \left(v \cos\Phi - w \sin\Phi\right) \cos\Psi \tag{E.11}$$

$$\dot{z} = -u \sin\Theta + \left(v \sin\Phi + w \cos\Phi\right) \cos\Theta \tag{E.12}$$

$$\tau_{\lambda\, i}\, \dot{\lambda}_i = C_T^{elem} - C_T^{GI} \tag{E.13}$$

$$\tau_{\lambda\, i\, tr}\, \dot{\lambda}_{i\, tr} = C_{Ttr}^{elem} - C_{Ttr}^{GI} \tag{E.14}$$

As assumed on page 101, observe that the dynamic inflow of both the rotor and the tailrotor system are included in the model as state variables by means of the time constants $\tau_{\lambda\, i}$ and $\tau_{\lambda i\, tr}$.

In equations (E.13) and (E.14) C_T^{elem} represents the thrust coefficient calculated with the blade element theory and $C_T^{GI.}$ represents the thrust coefficient calculated with the Glauert theory. The forces and moments on the helicopter can be calculated as:

$$\begin{aligned} X = & -T_{dp} \sin\left(a_1 - \theta_{1s}\right) \cos\left(b_1 + \theta_{1c}\right) - H_{dp} \cos\left(a_1 - \theta_{1s}\right) + \\ & + S_{dp} \sin\left(a_1 - \theta_{1s}\right) \sin\left(b_1 + \theta_{1c}\right) - R_{fus} \cos\alpha_{fus} \end{aligned} \tag{E.15}$$

$$Y = T_{dp} \sin\left(b_1 + \theta_{1c}\right) + S_{dp} \cos\left(b_1 + \theta_{1c}\right) + T_{tr} F_{tr} - Lift_{vt} + Y_{fus} \tag{E.16}$$

$$Z = -T_{dp}\cos(a_1-\theta_{1s})\cos(b_1+\theta_{1c}) + H_{dp}\sin(a_1-\theta_{1s}) + \\ + S_{dp}\cos(a_1-\theta_{1s})\sin(b_1+\theta_{1c}) - R_{fus}\sin\alpha_{fus} - Lift_{ht} \tag{E.17}$$

$$L = T_{dp}\left[h\sin(b_1+\theta_{1c}) + f_1\cos(a_1-\theta_{1s})\cos(b_1+\theta_{1c})\right] - H_{dp}f_1\sin(a_1-\theta_{1s}) + \\ + S_{dp}\left[h\cos(b_1+\theta_{1c}) - f_1\cos(a_1-\theta_{1s})\sin(b_1+\theta_{1c})\right] + T_{tr}h_{tr}F_{tr} - Lift_{vt}h_{vt} + L_E \tag{E.18}$$

$$M = T_{dp}\left[h\sin(a_1-\theta_{1s})\cos(b_1+\theta_{1c}) + f\cos(a_1-\theta_{1s})\cos(b_1+\theta_{1c})\right] + H_{dp}\left[h\cos(a_1-\theta_{1s}) - \\ - f\cos(a_1-\theta_{1s})\right] - S_{dp}\left[h\sin(a_1-\theta_{1s})\sin(b_1+\theta_{1c}) + f\cos(a_1-\theta_{1s})\sin(b_1+\theta_{1c})\right] + \\ + M_{fus} + M_{ht} + M_E \tag{E.19}$$

$$N = Q - T_{dp}\left[f_1\sin(a_1-\theta_{1s})\cos(b_1+\theta_{1c}) + f\sin(b_1+\theta_{1c})\right] - H_{dp}f_1\cos(a_1-\theta_{1s}) + \\ + S_{dp}\left[f_1\sin(a_1-\theta_{1s})\sin(b_1+\theta_{1c}) - f\cos(b_1+\theta_{1c})\right] - T_{tr}F_{tr}l_{tr} + Lift_{vt}l_{vt} + N_{fus} \tag{E.20}$$

The main rotor action can be expressed by the thrust T_{dp}, horizontal force H_{dp} (equivalent to a drag force), lateral force S_{dp} and a torque Q, all expressed in the disc plane:

$$T_{dp} = \rho(\pi R^2)(\Omega R)^2 C_T^{elem} \tag{E.21}$$

$$H_{dp} = \rho(\pi R^2)(\Omega R)^2 C_H \tag{E.22}$$

$$S_{dp} = \rho(\pi R^2)(\Omega R)^2 C_S \tag{E.23}$$

$$Q = \rho(\pi R^2)(\Omega R)^2 R C_Q \tag{E.24}$$

All these forces are calculated by using the blade-element theory, resulting in the following coefficients:

$$C_T^{elem} = \frac{\sigma C_l^{\alpha}}{2}\left[\left(\frac{1-2\bar{r}}{3}+\frac{\mu_x^2+\mu_y^2}{2}-\mu_x h\bar{q}\right)\theta_0+\left[\frac{1+\mu_x^2+\mu_y^2}{4}-\frac{\bar{r}+\mu_x h\bar{q}}{2}\right]\theta_{tw}+\right.$$
$$+\left[\frac{(1-\bar{r})\mu_y}{2}+\frac{(1-\bar{r})\,h\bar{p}}{2}+\frac{a_0\bar{p}}{3}+\frac{a_1\mu_x\bar{q}-b_1\mu_x\bar{p}}{8}\right]\theta_{1c}+ \qquad (E.25)$$
$$\left.+\left[\frac{(1-\bar{r})\mu_x}{2}-\frac{(1-\bar{r})\,h\bar{p}}{2}+\frac{a_0\bar{q}}{3}+\frac{a_1\mu_y\bar{q}-b_1\mu_y\bar{p}}{8}\right]\theta_{1s}+\frac{\mu_x\bar{p}+\mu_y\bar{q}}{4}-\frac{(1-\bar{r})\lambda}{2}-\frac{a_1\mu_x\bar{r}+b_1\mu_y\bar{r}}{4}\right]$$

$$C_T^{GI} = 2\lambda_i\sqrt{\left[\mu\cos\left(\alpha_{cp}-a_1\right)\right]^2+\left[\mu\sin\left(\alpha_{cp}-a_1\right)+\lambda_i\right]^2} \qquad (E.26)$$

$$C_S = \sigma C_d\left[\frac{-(1-\bar{r})\,\mu_y}{4}+\frac{(-1+\bar{r})\,a_0\bar{p}}{6}+\frac{(\mu_x\bar{p}-\mu_y\bar{q})\,b_1}{16}+\frac{(-\mu_x\bar{q}+3\mu_y\bar{p})\,b_1}{16}\right]+\sigma C_{l_\alpha}\left\{\left[a_0\times\right.\right.$$
$$\times\left[\frac{\bar{p}}{8}(\lambda_i-\mu_z)+\frac{\mu_x}{8}(-1+\bar{r})\right]+b_1\left[-\frac{1}{12}\bar{r}+\frac{1}{8}\mu_x^2+\frac{1}{8}\mu_y^2\right]+\frac{1}{24}a_1pq-\frac{1}{4}\mu_y(-\lambda_i+\mu_z)+\frac{1}{12}\bar{p}(-1+\bar{r})\Big]\theta_0+$$
$$+\left[a_0\left[\frac{1}{12}\bar{p}(-\mu_z+\lambda_i)+\frac{1}{12}\mu_x(-1+\bar{r})\right]+\frac{1}{16}b_1(\mu_x^2+\mu_y^2-\bar{r})+\frac{1}{32}\bar{p}\bar{q}a_1+\frac{1}{16}\bar{q}(-1+\bar{r})+\frac{1}{8}\mu_y(\lambda_i-\mu_z)\right]\theta_{tw}+$$
$$+\left[a_1\left[-\frac{1}{32}\mu_x\bar{r}+\frac{3}{32}\bar{p}(\lambda_i-\mu_z)\right]+b_1\left[\frac{3}{32}\mu_y\bar{r}+\frac{1}{32}\bar{q}(\mu_z-\lambda_i)\right]+\frac{1}{24}a_0\bar{p}\bar{q}+\frac{1}{16}\bar{q}a_0a_1+\frac{1}{48}\bar{p}a_0b_1+\right. \qquad (E.27)$$
$$+\frac{1}{8}(\mu_z-\lambda_i)(1-\bar{r})+\frac{1}{32}(\bar{p}\mu_x+3\bar{q}\mu_y)\Big]\theta_{1c}+\left[a_0\left[\frac{1}{12}+\frac{1}{8}(\mu_x^2+\mu_y^2)-\frac{1}{6}\bar{r}\right]+b_1\left[\frac{1}{32}\bar{p}(\lambda_i-\mu_z)-\frac{1}{8}\mu_x+\right.\right.$$
$$\left.+\frac{5}{32}\mu_x\bar{r}\right]+a_1\left[\frac{1}{32}\bar{q}(\mu_z-\lambda_i)-\frac{1}{8}\mu_y+\frac{3}{32}\mu_y\bar{r}\right]+\frac{1}{32}(\bar{q}\mu_x+\bar{p}\mu_y)-\frac{1}{16}\bar{p}a_0b_1+\frac{5}{48}\bar{q}a_0a_1\Big]\theta_{1s}+$$
$$+\frac{1}{8}\bar{q}(-\mu_z+\lambda_i)-\frac{1}{16}\mu_xa_1b_1+\frac{1}{4}a_0a_1(\mu_x^2+\mu_y^2)+\frac{1}{12}a_0a_1(1-\bar{r})+\frac{1}{16}a_1(\mu_y\bar{p}-\mu_x\bar{q})+$$
$$\left.+a_0\left[\frac{1}{12}\bar{p}(-1+\bar{r})+\frac{1}{4}\mu_x(\mu_z-\lambda_i)\right]+b_1\left[\frac{1}{16}(\mu_y\bar{q}+\mu_x\bar{p})+\frac{1}{8}\bar{r}(-\mu_z+\lambda_i)\right]\right\}$$

$$
\begin{aligned}
C_Q &= \sigma C_d\left[\frac{1}{8}b_1\bar{q}(1-\bar{r})+\frac{1}{8}a_1\bar{p}(-1+\bar{r})+\frac{1}{6}a_0(\mu_x\bar{q}+\mu_y\bar{p})+\frac{1}{8}(\mu_x^2+\mu_y^2)+\frac{1}{8}(1-\bar{r}^2)-\frac{1}{4}\bar{r}\right]+\\
&+\sigma C_{l_\alpha}\left\{\left[\frac{1}{6}(\mu_z-\lambda_i)(1-\bar{r})+\frac{1}{12}(\bar{p}\mu_x+\bar{q}\mu_y)+\frac{1}{12}\bar{p}a_1(-\mu_z+\lambda_i)+\frac{1}{12}\bar{q}b_1(\mu_z-\lambda_i)+\frac{1}{16}(\bar{p}b_1+\bar{q}a_1)+\right.\right.\\
&+\left.\frac{1}{12}\bar{r}(\mu_y b_1-\mu_x a_1)\right]\theta_0+\left[\frac{1}{16}a_1\left[\bar{p}(-\mu_z+\lambda_i)-\mu_x\bar{r}\right]+\frac{1}{16}b_1\left[\bar{q}(\mu_z-\lambda_i)+\mu_y\bar{r}\right]+\frac{1}{16}(\bar{p}\mu_x+\bar{q}\mu_y)+\right.\\
&+\left.\frac{1}{20}a_0(a_1\bar{q}+b_1\bar{p})+\frac{1}{8}(\mu_z-\lambda_0)(1-\bar{r})\right]\theta_{tw}+\left[a_0\left[\frac{1}{12}\bar{p}(-\mu_z+\lambda_i)+\frac{1}{12}\mu_x(1-\bar{r})\right]+a_1\left(-\frac{1}{16}\mu_x\mu_y+\right.\right. \qquad \text{(E.28)}\\
&\left.\frac{1}{32}\bar{p}\bar{q}\right)+b_1\left[\frac{1}{32}\mu_y^2-\frac{1}{32}\mu_x^2+\frac{1}{16}(-1+\bar{r})\right]+\frac{1}{32}\bar{p}a_1b_1+\frac{1}{16}\bar{q}(-1+\bar{r})+\frac{1}{8}\lambda_i\mu_y\Big]\theta_{1c}+\left[a_0\left[\frac{1}{12}\bar{q}(\mu_z-\lambda_i)+\right.\right.\\
&+\left.\frac{1}{12}\mu_y(-1+\bar{r})\right]+b_1\left(\frac{1}{16}\mu_x\mu_y-\frac{1}{32}\bar{p}\bar{q}\right)+a_1\left[\frac{1}{32}\mu_y^2-\frac{1}{32}\mu_x^2+\frac{1}{16}(1-\bar{r})\right]+\frac{1}{32}\bar{q}a_1b_1+\frac{1}{16}\bar{p}(-1+\bar{r})+\\
&+\left.\frac{1}{8}\mu_x(-\mu_z+\lambda_i)\right]\theta_{1s}+\frac{1}{12}a_0(\mu_x\bar{q}-\mu_y\bar{p})+a_1\left[\frac{1}{4}\mu_x(-\mu_z+\lambda_i)+\frac{1}{8}\bar{p}\right]+b_1\left[\frac{1}{4}\mu_y(\mu_z-\lambda_i)-\frac{1}{8}\bar{q}\right]+\\
&+\left.\frac{1}{2}\mu_z\lambda_0+\frac{1}{12}a_0(\mu_y a_1+\mu_x b_1)\right\}
\end{aligned}
$$

$$
\begin{aligned}
C_H &= \sigma C_d\left[\frac{(1-\bar{r})\,\mu_x}{4}+\frac{(-1+r)\,a_0\bar{q}}{6}+\frac{(\mu_y\bar{q}-\mu_x\bar{p})\,a_1}{16}+\frac{(-\mu_y\bar{p}+3\mu_x\bar{q})\,b_1}{16}\right]+\sigma C_{l_\alpha}\left\{\left[a_0\left[\frac{\bar{q}}{8}(\lambda_i-\mu_z)+\right.\right.\right.\\
&+\left.\frac{\mu_y}{8}(-1+\bar{r})\right]+a_1\left[-\frac{1}{12}\bar{r}+\frac{1}{8}\mu_x^2+\frac{1}{8}\mu_y^2\right]+\frac{1}{24}b_1pq-\frac{1}{4}\mu_x(\lambda_i-\mu_z)+\frac{1}{12}\bar{p}(1-\bar{r})\Big]\theta_0+\\
&+\left[a_0\left[\frac{1}{12}\bar{q}(-\mu_z+\lambda_i)+\frac{1}{12}\mu_y(-1+\bar{r})\right]+\frac{1}{16}a_1(\mu_x^2+\mu_y^2-\bar{r})+\frac{1}{32}\bar{p}\bar{q}b_1+\frac{1}{16}\bar{p}(1-\bar{r})-\frac{1}{8}\mu_x(\lambda_0-\mu_z)\right]\theta_{tw}+\\
&+\left[b_1\left[-\frac{1}{32}\mu_y\bar{r}+\frac{3}{32}\bar{q}(\lambda_i-\mu_z)\right]+a_1\left[\frac{3}{32}\mu_x\bar{r}+\frac{1}{32}\bar{p}(\mu_z-\lambda_i)\right]+\frac{1}{24}a_0\bar{p}\bar{q}-\frac{1}{16}\bar{p}a_0b_1-\frac{1}{48}\bar{q}a_0a_1+\right. \qquad \text{(E.29)}\\
&+\left.\frac{1}{8}(-\mu_z+\lambda_i)(1-\bar{r})-\frac{1}{32}(\bar{q}\mu_y+3\bar{p}\mu_x)\right]\theta_{1s}+\left[a_0\left[\frac{1}{12}+\frac{1}{8}(\mu_x^2+\mu_y^2)-\frac{1}{6}\bar{r}\right]+a_1\left[\frac{1}{32}\bar{q}(\lambda_i-\mu_z)-\frac{1}{8}\mu_y+\right.\right.\\
&+\left.\frac{5}{32}\mu_y\bar{r}\right]+b_1\left[\frac{1}{32}\bar{p}(\mu_z-\lambda_i)-\frac{1}{8}\mu_x+\frac{3}{32}\mu_x\bar{r}\right]-\frac{1}{32}(\bar{p}\mu_y+\bar{q}\mu_x)+\frac{1}{16}\bar{q}a_0b_1-\frac{5}{48}\bar{p}a_0a_1\Big]\theta_{1c}+\\
&+\frac{1}{8}\bar{p}(\mu_z-\lambda_i)+\frac{1}{16}\mu_y a_1b_1-\frac{1}{4}a_0b_1(\mu_x^2+\mu_y^2)+\frac{1}{12}a_0b_1(-1+\bar{r})+\frac{1}{16}b_1(\mu_x\bar{q}-\mu_y\bar{p})+a_0\left[\frac{1}{12}\bar{q}(-1+\bar{r})+\right.\\
&+\left.\left.\frac{1}{4}\mu_y(\mu_z-\lambda_i)\right]+a_1\left[\frac{1}{16}(\mu_x\bar{p}+\mu_y\bar{q})+\frac{1}{8}\bar{r}(-\mu_z+\lambda_i)\right]\right\}
\end{aligned}
$$

The steady-state disc-tilt angles can be calculated as:

$$\begin{cases} \left(\nu_\beta^2 - 2\bar{r}\right)a_0 = \frac{\gamma}{8}\left(1+\mu_x^2-2\bar{r}\right)\theta_0 - \frac{\gamma}{6}\mu_y\,\theta_{1c} - \frac{\gamma}{6}\mu_x\,\theta_{1s} + \frac{\gamma}{8}\left(\frac{4}{5} - \frac{8}{5}\bar{r} + \frac{2}{3}\mu_x^2\right)\theta_{tw} - \\ \qquad - \frac{\gamma}{6}\left(-\mu_z + \lambda_i\right) + \frac{\gamma}{12}\mu_x\bar{p} + \frac{\gamma}{12}\mu_y\bar{q} \\ \frac{\gamma}{8}\left(1-\bar{r} - \frac{\mu_x^2}{2} + \frac{\mu_y^2}{2}\right)a_1 = \frac{\gamma}{6}\mu_y a_0 + \left(\nu_\beta^2 - 1 - 2\bar{r}\right)b_1 + \frac{\gamma}{3}\mu_x\theta_0 - \frac{\gamma}{8}\mu_x\mu_y\theta_{1c} - \frac{\gamma}{8}\left(1 - 2\bar{r} + \frac{3}{2}\mu_x^2\right)\theta_{1s} + \\ \qquad + \frac{\gamma}{4}\mu_x\,\theta_{tw} - \frac{\gamma}{4}\mu_x\left(-\mu_z + \lambda_i\right) + \frac{\gamma}{8}\bar{p} - 2\,\bar{q} \\ \frac{\gamma}{8}\left(-1+\bar{r} - \frac{\mu_x^2}{2} + \frac{\mu_y^2}{2}\right)b_1 = -\frac{\gamma}{6}\mu_x a_0 + \left(\nu_\beta^2 - 1 - 2\bar{r}\right)a_1 + \frac{\gamma}{3}\mu_y\theta_0 - \frac{\gamma}{8}\left(1 - 2\bar{r} + \frac{\mu_x^2}{2}\right)\theta_{1c} - \frac{\gamma}{8}\mu_x\mu_y\theta_{1s} + \\ \qquad + \frac{\gamma}{4}\mu_y\theta_{tw} - \frac{\gamma}{8}\mu_y\left(-\mu_z + \lambda_i\right) + 2\bar{p} + \frac{\gamma}{8}\bar{q} \end{cases} \tag{E.30}$$

Due to the blade hinge eccentricity, the centrifugal force induces a supplementary roll and pitch moment on the rotor (see Figure E.1a and c) :

$$L_E = 2\,e_\beta \sin\left(b_1 + \theta_{1c}\right)F_{cf} = \rho\left(\pi R^2\right)\left(\Omega R\right)^2 R \sin\left(b_1 + \theta_{1c}\right)C_{mE} \tag{E.31}$$

$$M_E = 2\,e_\beta \sin\left(a_1 - \theta_{1s}\right)F_{cf} = \rho\left(\pi R^2\right)\left(\Omega R\right)^2 R \sin\left(a_1 - \theta_{1s}\right)C_{mE} \tag{E.32}$$

where the C_{mE} coefficient is defined as:

$$C_{mE} = \frac{2\,e_\beta F_{cf}}{\rho\left(\pi R^2\right)\Omega^2 R^3} = \frac{2\,\varepsilon_\beta R\left(m_{bl}\,\Omega^2\,\bar{r}_g\right)}{\rho\left(\pi R^2\right)\Omega^2 R^3} = \frac{\varepsilon_\beta\, m_{bl}}{\rho\left(\pi R^2\right)R} \tag{E.33}$$

The tailrotor is represented by its thrust force T_{tr} and may be calculated using the blade-element or the Glauert theory. The tail rotor thrust force is defined as:

$$T_{tr} = \rho\left(\pi R_{tr}^2\right)\left(\Omega_{tr} R_{tr}\right)^2 C_{T\,tr} \tag{E.34}$$

The tailrotor thrust coefficient may be calculated with the blade element theory or with the Glauert theory:

$$C_{T\,tr}^{elem} = \frac{\sigma_{tr} C_{l\,tr_\alpha}}{2}\left[\left(\frac{1}{3}+\frac{1}{2}\mu_{x\,tr}^2\right)\theta_{0\,tr} - \frac{-\mu_{z\,tr}+\lambda_{i\,tr}}{2}\right] \tag{E.35}$$

$$C_{T\,tr}^{GI} = 2\lambda_{i\,tr}\sqrt{\mu_{x\,tr}^2+\left(-\mu_{z\,tr}+\lambda_{i\,tr}\right)^2} \tag{E.36}$$

where the advance ratio μ_{xtr} and μ_{ztr} are defined as:

$$\mu_{xtr} = \frac{\sqrt{u^2+\left(w+K_{tr}\,\Omega\,R\,\lambda_i+q\,l_{tr}\right)^2}}{\Omega_{tr}\,R_{tr}} \quad ; \quad \mu_{ztr} = -\frac{v-r\,l_{tr}+p\,h_{tr}}{\Omega_{tr}\,R_{tr}} \tag{E.37}$$

K_{tr} is main rotor downwash factor at tailrotor and is assumed that K_{tr}=1

The tailrotor thrust introduced in the component Y of the helicopter total force, equation (E.16) by a fin blockage factor which can be taken according to Padfield [1996][81] as:

$$F_{tr} = 1 - 3\,S_{vt}/\left(4\,\pi\,R_{tr}^2\right) \tag{E.38}$$

The fuselage is represented by the force R_{fus} and a pitch moment M_{fus} which are calculated according to linear aerodynamics:

$$R_{fus} = \frac{\rho}{2} V^2 F_0 \tag{E.39}$$

$$M_{fus} = \rho\,A\left(\Omega\,R\right)^3 C_{m\,fus} \tag{E.40}$$

where F_0 is the parasite drag area and for helicopters in current production represents 1.1 to 1.4 from the maximum fuselage frontal surface S_{fus}, or 0.01 to 0.015 from rotor area A. Statistically, F_0 depends on the helicopter mass and angle of attack (see **Marinescu and Anghel** [1992][68]). The angle of attack of the fuselage is denoted as α_{fus} and is represented in Figure E.1 (a).

The fuselage pitch moment coefficient can be calculated as:

$$C_{m\,fus} = \mu^2 K_{fus}\left(Vol_{fus}\right)_m\left(\alpha_{sp}-\alpha_{sp\,|M_{fus}=0}-\varepsilon_0\right) \tag{E.41}$$

where K_{fus} is a correction coefficient and can be determined from Figure E.3 as a function of the ratio between the fuselage length l_{fus} and the equivalent diameter of the fuselage D_{fus} defined as the diameter of a circle of area equal to the area of the

maximum fuselage front view.

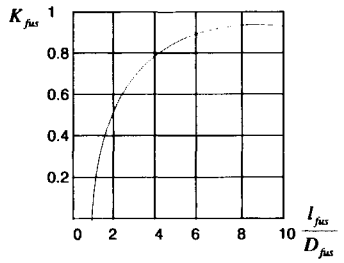

*Figure E.3 Correction coefficient K_{fus} (**Marinescu and Anghel** [1992][68])*

$(Vol_{fus})_m$ is the volume of a body equivalent to the fuselage having only circular sections of diameter d_{fus} (s) $(Vol_{fus})_m = \frac{\pi}{4}\int_0^{l_f} d_{fus}^2(x)\,dx$, $\alpha_{sflM\ fus=0}$ is the rotor incidence corresponding to zero fuselage pitching moment and ε_0 is the average downwash angle which at high velocities can be approximated as:

$$\varepsilon_0 = v_i / V \approx \lambda_i / \mu \tag{E.42}$$

In sideslip flight under an angle β_s ($\beta_s \approx v/V$) the fuselage introduces a lateral force Y_{fus} and a yaw moment N_{fus} defined as:

$$Y_{fus} = \rho\left(\pi R^2\right)\left(\Omega R\right)^2 C_{Y\,fus} \tag{E.43}$$

$$N_{fus} = \rho A\left(\Omega R\right)^3 C_{n\,fus} \tag{E.44}$$

The coefficient C_{Yfus} may be defined as:

$$C_{Y\,fus} = C_H \sin\beta_s \approx C_H \frac{\mu_y}{\mu} \tag{E.45}$$

The fuselage yaw moment coefficient can be calculated as:

$$C_{n\,fus} = \mu^2 K_{fus}\left(Vol_{fus}\right)_n \beta_s \tag{E.46}$$

where $(Vol_{fus})_n$ is the volume of a body equivalent to the fuselage, with the same form

in lateral view and having only circular sections $(Vol_{fus})_n = \frac{\pi}{4}\int_0^{l_t} h_{fus}^2(x)\,dx$.

The horizontal tail will be considered only by its lift force $Lift_{ht}$ and pitch moment produced by the lift force on the horizontal tail M_{ht} relative to the centre of gravity:

$$Lift_{ht} = \frac{\rho}{2} S_{ht} V_{ht}^2 C_{l\,ht_\alpha} \alpha_{ht} \tag{E.47}$$

$$M_{ht} = \rho\left(\pi R^2\right)\left(\Omega R\right)^2 R\, C_{m\,ht} \tag{E.48}$$

with the local velocity given by the components u, w and q of the helicopter:

$$V_{ht}^2 = u^2 + \left(w + q\, l_{ht}\right)^2 \tag{E.49}$$

The horizontal tail incidence α_{ht} is defined as:

$$\alpha_{ht} = \alpha_{sp} + \alpha_{0ht} - \varepsilon_{ht} + \frac{\bar{q}\bar{l}_{ht}}{\mu} + \frac{\bar{l}_{ht} R}{V}\dot{\alpha}_{sp}\frac{d\varepsilon_{ht}}{d\alpha_{sp}} \tag{E.50}$$

in which α_{0ht} represents the built-in horizontal stabilizer incidence, ε_{ht} is the medium downwash angle calculated in the area of horizontal tail and can be approximated as $\varepsilon_{ht} = \varepsilon_0 K_{ht}$ according to **Marinescu and Anghel** [1992][68], where ε_0 is the medium downwash angle approximated as (E.42) and K_{ht} is a correction coefficient determined graphically as a function of $\bar{f}_{ht}$ and $\bar{\zeta}_{ht} = \left[\bar{f}_{ht}\left(\lambda_i/\mu - \alpha_{dp}\right) - \left(\bar{h}_{ht} - \bar{h}\right)\right]$ and can be seen in Figure E.4.

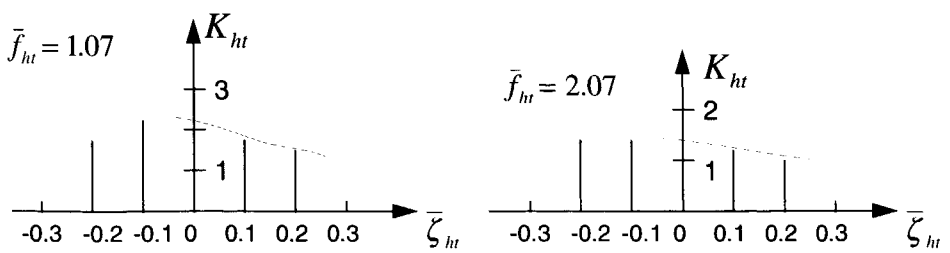

*Figure E.4 Correction coefficient K_{ht} (**Marinescu and Anghel** [1992][68])*

Relation (E.50) includes the effects of pitch rate and the variation of blade angle of

attack $\dot{\alpha}_{sp}$.

The horizontal tail pitch coefficient $C_{m\,ht}$ is defined as follows:

$$C_{m\,ht} = -\frac{1}{2}\left(\bar{Vol}_{ht}\right)\mu^2 C_{l\,ht_\alpha}\,\alpha_{ht} \tag{E.51}$$

where $(Vol)_{ht}$ is defined as $(Vol)_{ht} = (S_{ht} l_{ht})$.

The vertical tail will be considered by its lift force $Lift_{vt}$ and its roll L_{vt} and yaw N_{vt} moments produced by the lift force $Lift_{vt}$ relative to the centre of gravity:

$$Lift_{vt} = \frac{\rho}{2} S_{vt} V_{vt}^2 C_{l\,vt_\beta}\,\beta_s \tag{E.52}$$

$$L_{vt} = -\rho\left(\pi R^2\right)\left(\Omega R\right)^2 R\, C_{L\,vt} \tag{E.53}$$

$$N_{vt} = \rho\left(\pi R^2\right)\left(\Omega R\right)^2 R\, C_{N\,vt} \tag{E.54}$$

The local velocity is given by the components u and v combined with a yaw and roll rate component:

$$V_{vt}^2 = u^2 + \left(v - r\,l_{vt} + p\,h_{vt}\right)^2 \tag{E.55}$$

and the angle of attack of the vertical tail is:

$$\beta_{vt} \approx \beta_{0\,vt} + \left(v - r\,l_{vt} + p\,h_{vt}\right)/u \tag{E.56}$$

with β_{0vt} the built-in incidence of vertical tail. The roll and yaw vertical tail coefficients are defined as:

$$C_{L\,vt} = \frac{1}{2}\bar{S}_{vt}\mu^2 C_{l\,vt_\beta}\,\beta_{vt}\,\bar{h}_{vt} \tag{E.57}$$

$$C_{N\,vt} = \frac{1}{2}\bar{S}_{vt}\mu^2 C_{l\,vt_\beta}\,\beta_{vt}\,\bar{l}_{vt} \tag{E.58}$$

E.3 Pilot Model

The control variables used by the pilot to control the helicopter are the collective pitch θ_0, longitudinal cyclic pitch θ_{1s}, lateral cyclic pitch θ_{1c} and tailrotor collective θ_{0tr}. To fly the helicopter, four stabilization functions are developed, one for each control:

Collective controls vertical speed

$$\theta_0 = \theta_{0\,gen} + K_c (c_{des} - c) + K_{corrc} \int_0^t (c_{des} - c) \, d\tau \tag{E.59}$$

The desired vertical speed is controlled by an "altitude hold" controller, feeding back the height to the vertical speed:

$$c_{des} = K_h (h_{des} - h) \tag{E.60}$$

Longitudinal cyclic controls pitch attitude

$$\theta_{1s} = K_\Theta (\Theta - \Theta_{des}) + K_q q + K_{\Theta corr} \int_0^t (\Theta - \Theta_{des}) \, d\tau \tag{E.61}$$

The desired pitch attitude is controlled by a "longitudinal position hold" controller:

$$\Theta_{des} = K_x (x_{des} - x) + K_u u + K_{x\,corr} \int_0^t (x_{des} - x) \, d\tau \tag{E.62}$$

Lateral cyclic controls roll attitude

$$\theta_{1c} = K_\Phi (\Phi_{des} - \Phi) + K_p p + K_{\Phi corr} \int_0^t (\Phi_{des} - \Phi) \, d\tau \tag{E.63}$$

The desired roll angle is controlled by a "lateral position hold" controller:

$$\Phi_{des} = K_y (y_{des} - y) + K_v v + K_{y\,corr} \int_0^t (y_{des} - y) \, d\tau \tag{E.64}$$

Tailrotor collective controls heading angle

$$\theta_{0tr} = K_\Psi (\Psi_{des} - \Psi) + K_r r + K_{\Psi\,corr} \int_0^t (\Psi_{des} - \Psi) \, d\tau \tag{E.65}$$

The desired yaw angle is controlled fast and smooth and does not need any proportional-integration-differentiation (PID) controller.

Initial Parameters - helicopter M_{hel}, I_x, I_y, I_z, I_{xz}
- fuselage F_0, S_{fus}, K_{fus} $(Vol_{fus})_m$
-rotor M_{bl}, N, σ, C_{l_α}, C_d, Ω, R, c_e, $A=\pi R^2$, CG (h, f, f_1), γ, I_β, e_β, θ_{tw}, K_β,v, $\tau_{\lambda i}$
- tailrotor R_{tr}, Ω_{tr}, c_{tr} , N_{tr}, σ_{tr}, $C_{l\,tr_\alpha}$, K_{tr}, $\tau_{\lambda tr}$, CG(l_{tr}, f_{tr}), α_{0tr}, $\tau_{\lambda itr}$
- horizontal tail Vol_{ht}, S_{ht}, $C_{l\,ht_\alpha}$, K_{ht} CG(l_{ht}, h_{ht})
- vertical tail S_{vt}, $\beta_{0\,vt}$, $C_{l\,vt_\beta}$, CG(l_{vt}, h_{vt})

Initial Trim Controls θ_0 , θ_{1s} θ_{1c} $\theta_{0\,tr}$

Flight condition u, v, w, p, q, r, Θ, Ψ, Φ

$$V = \sqrt{\left(u^2+v^2+w^2\right)} \qquad \alpha_{cp} = -\arctan\frac{w}{u}+\theta_{1s} \qquad \alpha_{dp} = \alpha_{cp}+a_1$$

$$\mu_x = \frac{u}{\Omega R} \qquad \mu_y = \frac{v}{\Omega R} \qquad \mu_z = \frac{w}{\Omega R}$$

$$\lambda = -\mu_z+\lambda_i$$

Tailrotor

$$\mu_{x\,tr} = \frac{\sqrt{u^2+\left(w+K_{tr}\Omega R\lambda_i+q\,l_{tr}\right)^2}}{\Omega_{tr}R_{tr}} \qquad \mu_{z\,tr} = -\frac{v-r\,l_{tr}+p\,h_{tr}}{\Omega_{tr}R_{tr}}$$

$$\lambda_{tr} = -\mu_{z\,tr}+\lambda_{i\,tr}$$

Horizontal tail

$$V_{ht} = \sqrt{u^2+\left(w+q\,l_{ht}\right)^2} \qquad \alpha_{ht} = \alpha_{0ht}+\arctan\left(\frac{w+q\,l_{ht}}{u}\right)$$

Vertical tail

$$V_{vt} = \sqrt{u^2+\left(v-r\,l_{vt}+p\,h_{vt}\right)^2} \qquad \beta_{vt} = \beta_{0vt}+\arctan\left(\frac{v-r\,l_{vt}+p\,h_{vt}}{u}\right)$$

Calculate main rotor inflow λ_i using the expressions of C_T^{elem} (E.25) and C_T^{GI} (E.26)

Calculate tailrotor inflow λ_{itr} using the expressions of C_{Ttr}^{elem} (E.35) and C_{Ttr}^{GI} (E.36)

Known are now for main rotor λ_i, λ, a_0 a_1 b_1 C_T, $\lambda_{i\,tr}$, λ_{tr}, $C_{T\,tr}$
Calculate C_H C_S C_Q, $C_{D\,fus}$, $C_{m\,fus}$, α_{ht}, $C_{m\,ht}$, $C_{l\,vt}$, $C_{n\,vt}$
Evaluate all parameters and let integration routine operate on the system of the equations of motion (E.1) to (E.14)

E.4 Six Degree-of-Freedom Linear Helicopter Model

To be able to determine the body modes, the nonlinear six degree-of-freedom model developed above has to be linearized about a suitable trim condition. Assuming as a basic motion a uniform forward flight:

$$\begin{aligned} &\dot{u}_0 = \dot{v}_0 = \dot{w}_0 = \dot{p}_0 = \dot{q}_0 = \dot{r}_0 = 0 \\ &v_0 = p_0 = q_0 = r_0 = 0 \\ &\Psi_0 = 0 \ , \ \Theta_0 = \tau_u + \alpha_{sp} \\ &\dot{\Theta}_0 = \dot{\Phi}_0 = \dot{\Psi}_0 = 0 \end{aligned} \tag{E.66}$$

Substituting (E.66) into (E.1) to (E.9), the parameters in the basic motion can be derived. As in the case of the airplane, assume that the longitudinal helicopter motion decouples from the lateral motion. The longitudinal motion is characterized by the state variables {u, w, q, Θ} and the control variables θ_0 and θ_{1s}. The lateral motion is described by the state variables {v, p, r, Φ, Ψ} and the control variables θ_{1c} and θ_{0tr}. Perturbing the longitudinal motion around the trim condition and linearizing, the longitudinal perturbed equations of motion can be written as:

$$\begin{cases} \dot{u} = -g\sin\Theta + \dfrac{1}{M_{hel}}\left[X_u u + X_w w + X_q q + X_{\theta 1s}\Delta\theta_{1s} + X_{\theta 0}\Delta\theta_0\right] \\ \dot{w} = -g\cos\Theta + V q + \dfrac{1}{M_{hel}}\left[Z_u u + Z_w w + Z_q q + Z_{\theta 1s}\Delta\theta_{1s} + Z_{\theta 0}\Delta\theta_0\right] \\ \dot{\Theta} = q \\ \dot{q} = \dfrac{1}{I_y}\left[M_u u + M_w w + M_{\dot{w}}\dot{w} + M_q q + M_{\theta 1s}\Delta\theta_{1s} + M_{\theta 0}\Delta\theta_0\right] \end{cases} \tag{E.67}$$

where X_u, ..$X_{\theta 0}$., Z_u, ...$Z_{\theta 0}$, M_u,....$M_{\theta 0}$ are defined as the derivatives of the X-force, Z-force and pitch moment M with respect to u, w, ... θ_0:

$$X_u = \frac{\delta X}{\delta u} \ , \ X_w = \frac{\delta X}{\delta w} \ , \ .... \ , \ M_{\theta 0} = \frac{\delta M}{\delta \theta_0} \tag{E.68}$$

In the lateral motion, the helicopter equations of motion are (neglecting Y_p and Y_r as

being very small):

$$\begin{cases} \dot{v} = g\Phi + g\Psi - rV + \dfrac{1}{M_{hel}}\left[Y_v v + Y_{\theta 1c}\Delta\theta_{1c} + Y_{\theta 0tr}\Delta\theta_{0tr} \right] \\ \dot{\Phi} = p \\ \dot{p} = \dfrac{I_z}{I_x I_z - I_{xz}^2}\left[L_v v + L_p p + L_r r + L_{\theta 1c}\Delta\theta_{1c} + L_{\theta 0tr}\Delta\theta_{0tr} \right] \\ \quad + \dfrac{I_{xz}}{I_x I_z - I_{xz}^2}\left[N_v v + N_p p + N_r r + N_{\theta 1c}\Delta\theta_{1c} + N_{\theta 0tr}\Delta\theta_{0tr} \right] \\ \dot{\Psi} = r \\ \dot{r} = \dfrac{I_x}{I_x I_z - I_{xz}^2}\left[N_v v + N_p p + N_r r + N_{\theta 1c}\Delta\theta_{1c} + N_{\theta 0tr}\Delta\theta_{0tr} \right] + \\ \quad + \dfrac{I_{xz}}{I_x I_z - I_{xz}^2}\left[L_v v + L_p p + L_r r + L_{\theta 1c}\Delta\theta_{1c} + L_{\theta 0tr}\Delta\theta_{0tr} \right] \end{cases} \tag{E.69}$$

The force derivatives can be calculated by deriving the helicopter forces and moments with respect to the state and control variables. Using the matrix notation, the linearized equations in the longitudinal and lateral plane can be formally written as:

$$\dot{X} = A \cdot X + B \cdot U \tag{E.70}$$

where A is the matrix of motion derivatives, B is the matrix of control derivatives, X the motion states and U the control states. In the 6-dof linear model the equations (E.67) and (E.69) are non-dimensionalized according to the table presented in the beginning of the dissertation in the chapter Notations. By doing so, in the longitudinal plane, the matrices A and B are:

$$\bar{A}_{long} = \begin{bmatrix} x_u & x_w & -C_G\cos\tau_u & x_q \\ z_u & z_w & -C_G\sin\tau_u & \mu + z_q \\ 0 & 0 & 0 & 1 \\ m_u + z_u m_{\dot{w}} & m_w + z_w m_{\dot{w}} & -m_{\dot{w}} C_G \sin\tau_u & m_q + m_{\dot{w}}(\mu + z_q) \end{bmatrix} \tag{E.71}$$

$$\bar{B}_{long} = \begin{bmatrix} x_{\theta 1s} & z_{\theta 1s} & 0 & m_{\theta 1s} + m_{\dot{w}} z_{\theta 1s} \\ x_{\theta 0} & z_{\theta 0} & 0 & m_{\theta 0} + m_{\dot{w}} z_{\theta 0} \end{bmatrix}^T$$

and the states are $X = \left\{u, w, q, \Theta\right\}^T$ and $U = \left\{\theta_0, \theta_{1s}\right\}^T$. C_G is the helicopter weight coefficient defined as $C_G = \dfrac{M_{hel}\, g}{\rho\, A\, \Omega^2 R^2}$ and τ_u is the helicopter climb angle. In the lateral plane, the matrices A and B are:

$$\bar{A}_{lat} = \begin{bmatrix} y_v & C_G \cos\tau_u & 0 & C_G \sin\tau_u & -\mu \\ 0 & 0 & 1 & 0 & 0 \\ \dfrac{l_v + \bar{I}_1 n_v}{\bar{I}_0} & 0 & \dfrac{l_p + \bar{I}_1 n_p}{\bar{I}_0} & 0 & \dfrac{l_r + \bar{I}_1 n_r}{\bar{I}_0} \\ 0 & 0 & 0 & 0 & 1 \\ \dfrac{n_v + \bar{I}_3 l_v}{\bar{I}_0} & 0 & \dfrac{n_p + \bar{I}_3 l_p}{\bar{I}_0} & 0 & \dfrac{n_r + \bar{I}_3 l_r}{\bar{I}_0} \end{bmatrix} \tag{E.72}$$

$$\bar{B}_{lat} = \begin{bmatrix} y_{\theta 1c} & 0 & \dfrac{l_{\theta 1c} + \bar{I}_1 n_{\theta 1c}}{\bar{I}_0} & 0 & \dfrac{n_{\theta 1c} + \bar{I}_3 l_{\theta 1c}}{\bar{I}_0} \\ y_{\theta 0tr} & 0 & \dfrac{l_{\theta 0tr} + \bar{I}_1 n_{\theta 0tr}}{\bar{I}_0} & 0 & \dfrac{n_{\theta 0tr} + \bar{I}_3 l_{\theta 0tr}}{\bar{I}_0} \end{bmatrix}^T$$

where $\bar{I}_0 = 1 - \dfrac{\bar{I}_{xz}^2}{\bar{I}_x \bar{I}_z}$, $\bar{I}_1 = \dfrac{\bar{I}_{xz}}{\bar{I}_x}$, $\bar{I}_3 = \dfrac{\bar{I}_{xz}^2}{\bar{I}_z}$. The helicopter states in helicopter lateral plane are $X = \left\{v, \Phi, p, \Psi, r\right\}^T$ and the corresponding control states $U = \left\{\theta_{1c}, \theta_{0tr}\right\}^T$. The complete derivation of the all listed helicopter derivatives and the final linear equations of motion is done in **Marinescu and Anghel** [1992][68] and **Pavel** [1996][84].

Considering the developed pilot model as presented in the previous section, the matrix U of controls can be written as (assuming no I-action):

$$U = K \cdot X \tag{E.73}$$

where K is the matrix containing the gains used to stabilize the motion in the longitudinal and lateral plane. Substituting (E.73) into (E.70), the linear equations of motion describing the helicopter motion become:

$$\dot{X} = \left(A + B \cdot K\right) \cdot X \tag{E.74}$$

In the longitudinal plane, matrix K can be written as:

$$\bar{K}_{long} = \begin{bmatrix} 0 & 0 & K_{\Theta} & \frac{K_q}{\bar{t}} \\ 0 & 0 & 0 & 0 \end{bmatrix} \tag{E.75}$$

$$\bar{K}_{lat} = \begin{bmatrix} 0 & K_{\Phi} & \frac{K_p}{\bar{t}} & 0 & 0 \\ 0 & 0 & 0 & K_{\Psi} & \frac{K_r}{\bar{t}} \end{bmatrix} \tag{E.76}$$

E.5 Eight Degree-of-Freedom Nonlinear Model

In order to investigate the importance of modeling the rotor degrees of freedom for flight dynamics purposes, the 6-dof non-linear model presented in section E.1 was extended to an 8-dof model including the first order disc-tilt dynamics of the rotor $\dot{a}_0$, $\dot{a}_1$, $\dot{b}_1$. The degrees of freedom of the extended model are $\{u, v, w, p, q, r, a_1, b_1\}$ and there are seventeen state variables $\{u, v, w, p, q, r, \Theta, \Phi, \Psi, x, y, z, \lambda_0, \lambda_{0ir}, a_0, a_1, b_1\}$. Appendix D demonstrated that neglecting the disc-tilt accelerations $\ddot{a}_0 = \ddot{a}_1 = \ddot{b}_1 = 0$ and retaining only the first-order rotor disc-tilt dynamics in the helicopter piloted simulation model is equivalent to retaining the low frequency regressing flapping mode in the model on top of the steady-state disc-tilt solution. The extended 6-dof model can be formally represented as the following system:

$$\left[\begin{array}{c|c} I & Body\text{-}Rotor^I \\ \hline Rotor^I\text{-}Body & Rotor^I\text{-}Rotor^I \end{array}\right] \begin{bmatrix} \dot{u} \\ \dot{r} \\ \dot{a}_0 \\ \dot{b}_1 \end{bmatrix} = \left[\begin{array}{c|c} Body\text{-}Body & Body\text{-}Rotor^I \\ \hline Rotor^I\text{-}Body & Rotor^I\text{-}Rotor^{s.s} \end{array}\right] \begin{bmatrix} u \\ r \\ a_0 \\ b_1 \end{bmatrix} \tag{E.77}$$

where index I is for the first order rotor disc-tilt dynamics and s.s for the steady-state disc-tilt. Relation (E.77) shows that the 8-dof model includes a body-to-rotor first-order disc-tilt dynamics coupling as well as a rotor-to-body first-order disc-tilt dynamics coupling. The simulations performed in Chapter 5 contain only a partially extended 6-dof model, in the sense that the body-to-rotor first-order disc-tilt dynamics (matrix Body-Rotor^I of system (E.77)) was assumed to be zero. With this, the 6-dof model given by the system of equations from (E.1) to (E.14) was extended to a 8-dof model by adding three more equations representing the first order disc-tilt dynamics:

$$
\begin{cases}
\frac{\gamma}{8}(1-\bar{r})\frac{\dot{a}_0}{\Omega}-\frac{\gamma}{12}\mu_x\frac{\dot{b}_1}{\Omega}-\frac{\gamma}{12}\mu_y\frac{\dot{a}_1}{\Omega}+\left(\nu_\beta^2-2\bar{r}\right)a_0 = \frac{\gamma}{8}\left(1+\mu_x^2-2\bar{r}\right)\theta_0-\frac{\gamma}{6}\mu_y\theta_{1c}-\frac{\gamma}{6}\mu_x\theta_{1s}+ \\
+\frac{\gamma}{8}\left(\frac{4}{5}-\frac{8}{5}\bar{r}+\frac{2}{3}\mu_x^2\right)\theta_{tw}-\frac{\gamma}{6}(-\mu_z+\lambda_0)+\frac{\gamma}{12}\mu_x\bar{p}+\frac{\gamma}{12}\mu_y\bar{q} \\
-\frac{\gamma}{8}(1-\bar{r})\frac{\dot{a}_1}{\Omega}+\frac{\gamma}{6}\mu_y\frac{\dot{a}_0}{\Omega}-2\frac{\dot{b}_1}{\Omega}+\frac{\gamma}{6}\mu_x a_0+\left(1-\nu^2+2\bar{r}\right)a_1+\frac{\gamma}{8}\left(-1+\bar{r}-\frac{\mu_x^2}{2}+\frac{\mu_y^2}{2}\right)b_1 = \\
=\frac{\gamma}{3}\mu_x\theta_0-\frac{\gamma}{8}\left(1-2\bar{r}+\frac{\mu_x^2}{2}\right)\theta_{1c}-\frac{\gamma}{8}\mu_x\mu_y\theta_{1s}+\frac{\gamma}{4}\mu_y\theta_{tw}-\frac{\gamma}{8}\mu_y(-\mu_z+\lambda_0)+2\bar{p}+\frac{\gamma}{8}\bar{q} \\
\gamma\frac{\mu_x}{6}\frac{\dot{a}_0}{\Omega}+2\frac{\dot{a}_1}{\Omega}-\frac{\gamma}{8}(1-\bar{r})\frac{\dot{b}_1}{\Omega}+\frac{\gamma}{6}\mu_y a_0-\frac{\gamma}{8}\left(1-\bar{r}-\frac{\mu_x^2}{2}+\frac{\mu_y^2}{2}\right)a_1-\left(1-\nu^2+2\bar{r}\right)b_1 = \\
=-\frac{\gamma}{3}\mu_x\theta_0+\frac{\gamma}{8}\mu_x\mu_y\theta_{1c}+\frac{\gamma}{8}\left(1-2\bar{r}+\frac{3}{2}\mu_x^2\right)\theta_{1s}-\frac{\gamma}{4}\mu_x\theta_{tw}+\frac{\gamma}{4}\mu_x(-\mu_z+\lambda_0)-\frac{\gamma}{8}\bar{p}+2\bar{q}
\end{cases}
\tag{E.78}
$$

The 8-dof nonlinear model is represented by equations (E.1) to (E.14) plus equations (E.78).

E.6 Data for Puma SA-330 and Bö-105

Parameter	*Puma Sa-330*	*Bölkow Bö-105*
M_{hel}	*5805 kg*	*2096 kg*
m_{bl}	*68 kg*	*27.3 kg*
$\bar{f}$	*0.015*	*-0.00155*
$\bar{h}$	*0.25*	*0.1924*
$\bar{f}_1$	*0*	*0.0061*
N	*4*	*4*
R	*7.5 m*	*4.91 m*
c_e	*0.5401 m*	*0.27 m*
e_β	*0.3 m*	*0 m*
C_l^α	*5.73 rad $^{-1}$*	*5.73 rad $^{-1}$*
Ω	*270 rot/min*	*424 rot/min*
I_γ	*9638 kg m^2*	*1803 kg m^2*

I_y	33240 kg m^2	4892 kg m^2
I_z	25889 kg m^2	4428 kg m^2
I_{xz}	2226 kg m^2	0 kg m^2
I_{bl}	1280 kg m^2	219.5 kg m^2
N_{tr}	5	2
R_{tr}	1.5 m	0.95 m
c_{tr}	0.18 m	0.18 m
l_{tr}-f	9 m	6. 01726 m
h_{tr}-h	1.2 m	0.1095 m
C_{ltr}^{α}	5.7 rad^{-1}	5.7 rad^{-1}
Ω_{tr}	1350 rot/min	1350 rot/min
S_{ht}	1.4 m^2	0.809 m^2
$C_{l\,ht}^{\alpha}$	4 rad^{-1}	4 rad^{-1}
$\alpha_{0\,ht}$	3 deg	0 deg
l_{ht}-f	7 m	4.556 m
h_{ht}-h	1.5 m	0.898144 m
F_0	1.8 m^2	1.3 m^2
K_{ht}	1.5	1.5
K_{fus}	0.83	0.83
S_{fus}	F_0 / 0.2	F_0 / 0.2
l_{fus}	14.82 m	8.509 m
$(Vol_{fus})_n$	$(\pi/4)\times 45.29$ (AR)	$(\pi/4)\times 25$ (AR)
$(Vol_{fus})_m$	$(\pi/4)\times 22$ (AR)	$(\pi/4)\times 6$ (AR)
S_{vt}	0	0
$\tau_{\lambda i}$	0.1	0.1
$\tau_{\lambda i\,tr}$	0.1	0.1
$\bar{t} = \frac{M_{hel}}{\rho A \Omega R}$	0.12645	0.103625

Appendix F

Modeling the Coupled Rotor-Chassis Motion for the KEWT Two-Bladed Wind Turbine

Consider a 2-bladed wind turbine, modelled as in Figure F.1 in which the blades can lead-lag with an angle ζ_k and the tower can bend fore and aft in the second bending mode. By the vertical displacement of the chassis x is meant the vertical motion of the chassis as a result of the inclination of the nacelle when the tower bends fore and aft in the second bending mode (this motion will be shortly called during this work the chassis second bending mode). Assume that the chassis cannot yaw and that the rotor blades are connected to the hub with a zero offset. The present appendix will derive the equations of the coupled rotor-chassis system in the degrees of freedom mentioned above.

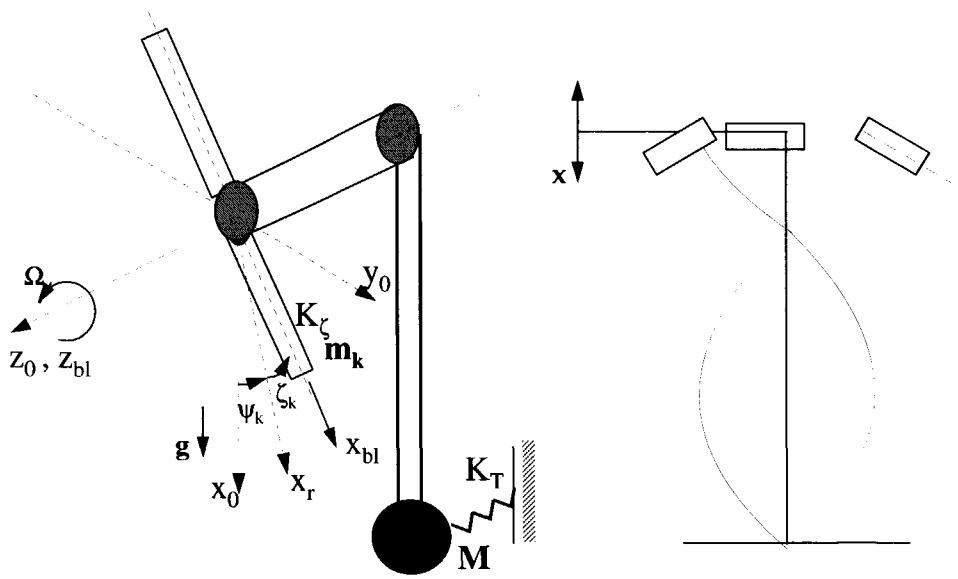

Figure F.1 Rotor-Chassis System

F.1 Rotor-Chassis Equations of Motion in the Rotating System

Figure F.1 defines the systems of reference $\{x_0,y_0,z_0\}$ (rotor head system of reference), $\{x_r,y_r,z_r\}$ (rotating system of reference), and $\{x_{bl},y_{bl},z_{bl}\}$ (blade system of reference) related through the following transformations:

$$x_0y_0z_0 \xrightarrow{\psi_k(z_0)} Ox_ry_rz_r \xrightarrow{\zeta_k\,(z_r)} Ox_{bl}y_{bl}z_{bl}$$

$$\left\{\bar{E}_r\right\} = \begin{bmatrix} \cos\psi_k & \sin\psi_k & 0 \\ -\sin\psi_k & \cos\psi_k & 0 \\ 0 & 0 & 1 \end{bmatrix} \left\{\bar{E}_0\right\} = \left[\psi_k\right]\left\{\bar{E}_0\right\} \; ; \; \left\{\bar{E}_{bl}\right\} = \begin{bmatrix} \cos\zeta_k & \sin\zeta_k & 0 \\ -\sin\zeta_k & \cos\zeta_k & 0 \\ 0 & 0 & 1 \end{bmatrix} \left\{\bar{E}_r\right\} = \left[\zeta_k\right]\left\{\bar{E}_r\right\} \quad \text{(F.1)}$$

where $\psi_k = \Omega t + 2\pi(k-1)/N$. The blade system of reference can thus be characterized by the vector $\{ E_{bl} \}$ expressed in the chassis system of reference as:

$$\left\{\bar{E}_{bl}\right\} = \left[\zeta_k\right]\left[\psi_k\right]\left\{\bar{E}_0\right\} = \begin{bmatrix} \cos(\psi_k+\zeta_k) & \sin(\psi_k+\zeta_k) & 0 \\ -\sin(\psi_k+\zeta_k) & \cos(\psi_k+\zeta_k) & 0 \\ 0 & 0 & 1 \end{bmatrix} \left\{\bar{E}_0\right\} \quad \text{(F.2)}$$

Consider a point P on blade k situated at a distance r from the hub. The position of the blade w.r.t. the rotor head is:

$$\bar{\rho}_{bl} = r\left(1,0,0\right)\left\{\bar{E}_{bl}\right\} = r\left(1,0,0\right)\left[\zeta_k\right]\left[\psi_k\right]\left\{\bar{E}_0\right\} = \\ = \left(r\cos(\psi_k+\zeta_k), r\sin(\psi_k+\zeta_k), 0\right)\left\{\bar{E}_0\right\} \quad \text{(F.3)}$$

and the angular velocity of the blade is:

$$\bar{\omega}_{bl} = \left(0,0,\Omega+\dot{\zeta}_k\right)\left\{\bar{E}_{bl}\right\} \quad \text{(F.4)}$$

Consider a displacement of the chassis in the vertical direction:

$$\bar{\rho}_0 = \left(x,0,0\right)\left\{\bar{E}_0\right\} \quad \text{(F.5)}$$

The displacement of point P of the k-th blade w.r.t. the chassis will be:

$$\bar{r}_{bl} = \bar{\rho}_0 + \bar{\rho}_{bl} = \left(x + r\cos(\psi_k + \zeta_k), r\sin(\psi_k + \zeta_k), 0\right)\left\{\bar{E}_0\right\} \tag{F.6}$$

and the corresponding velocity:

$$\begin{aligned}\dot{r}_{bl} &= \dot{x}\left(1,0,0\right)\left\{\bar{E}_0\right\} + r\left(1,0,0\right)\left\{\dot{E}_{bl}\right\} = \left\{\left(\dot{x},0,0\right) + r\left(1,0,0\right)\left[\omega_b\right]\left[\zeta_k\right]\left[\psi_k\right]\right\}\left\{\bar{E}_0\right\} = \\ &= \left(-r\left(\Omega + \dot{\zeta}_k\right)\sin(\psi_k + \zeta_k), r\left(\Omega + \dot{\zeta}_k\right)\cos(\psi_k + \zeta_k), 0\right)\left\{\bar{E}_0\right\}\end{aligned} \tag{F.7}$$

The kinetic energy T_k of the k-th blade is:

$$T_k = \frac{1}{2}\int_B m\left[\dot{x}_k^2 + \dot{y}_k^2\right]dr = \frac{1}{2}m_k\dot{x}^2 + \frac{1}{2}I_k\left(\Omega + \dot{\zeta}_k\right)^2 + \sigma_k\dot{x}\left(\Omega + \dot{\zeta}_k\right)\sin\left(\psi_k + \zeta_k\right) \tag{F.8}$$

where $m_k = \int_B m\,dr$, $\sigma_k = \int_B m r\,dr$, $I_k = \int_B m r^2\,dr$.
The kinetic energy of the entire system is then:

$$T_{tot} = \frac{1}{2}M_{tot}\dot{x}^2 + \sum_{k=1}^{N}\left\{\frac{1}{2}I_k\left(\Omega + \dot{\zeta}_k\right)^2 + \sigma_k\dot{x}\left(\Omega + \dot{\zeta}_k\right)\sin\left(\psi_k + \zeta_k\right)\right\} \tag{F.9}$$

where the total mass of the rotor+tower system is $M_{tot} = M_{ch} + N\,m_k$. The potential energy of the system is:

$$V = \frac{1}{2}K_x x^2 + \sum_{k=1}^{N}\frac{1}{2}K_\zeta\zeta_k^2 + \sum_{k=1}^{N}\int_B mg\left(x + r\cos\left(\psi_k + \zeta_k\right)\right)dr \tag{F.10}$$

The Lagrange equations are:

$$\frac{d}{dt}\left(\frac{\partial T}{\partial\dot{q}_k}\right) - \frac{\partial T}{\partial q_k} + \frac{\partial V}{\partial q_k} = Q_k^{noncons} \quad ; \quad Q_k^{noncons} = 0 \tag{F.11}$$

where $Q^{noncons}$ is the sum of generalized forces acting on the system. Substituting (F.9), (F.10) into (F.11) N+1 equations are obtained. Linearizing and assuming the lead-lag angle of the blade small so that $\cos\zeta_k = 1$ and $\sin\psi_k = \psi_k$ and adding artificial damping

to the chassis and lead-lag motion through damping coefficients C_T and C_ζ, the final rotor-tower equations of motion in the rotating system are:

$$\begin{cases} M_{tot}\ddot{x} + C_T\dot{x} + K_T x + \sum_{k=1}^{N} \sigma_k \frac{d^2}{dt^2}\left(\zeta_k \sin\psi_k\right) = -\Omega^2 \sum_{k=1}^{N} \sigma_k \cos\psi_k - \sum_{k=1}^{N} m_k g \\ \sigma_k \ddot{x} \sin\psi_k + I_k\ddot{\zeta}_k + C_\zeta \dot{\zeta}_k + K_\zeta \zeta_k = g\sigma_k\left(\sin\psi_k + \zeta_k \cos\psi_k\right) \qquad k = 1 \ldots N \end{cases} \tag{F.12}$$

where $\frac{d^2}{dt^2}\left(\zeta_k \sin\psi_k\right) = \ddot{\zeta}_k \sin\psi_k + 2\Omega\dot{\zeta}_k \cos\psi_k - \Omega^2 \zeta_k \sin\psi_k$.

Small Perturbation Equations

Assuming solutions in the form:

$$\begin{cases} x = x_0 + \Delta x \\ \zeta = \Delta\zeta \end{cases} \tag{F.13}$$

representing small perturbations about large static positions, the static solution x_0 (to not be confounded with the axis x_0) can be obtained by substituting (F.13) into equations (F.12) and imposing $\Delta x = \Delta\zeta = 0$. By doing so, the static solution becomes:

$$K_T x_0 = -\Omega^2 \sum_{k=1}^{N} \sigma_k \cos\psi_k - \sum_{k=1}^{N} m_k g \tag{F.14}$$

The coupled tower bending-blade lead-lag small perturbation equations of motion in the rotating system can be obtained by substituting the static solution (F.14) into (F.12):

$$\begin{cases} M_{tot}\ddot{x} + C_T\dot{x} + K_T x + \sum_{k=1}^{N} \sigma_k \frac{d^2}{dt^2}\left(\zeta_k \sin\psi_k\right) = 0 \\ \sigma_k \ddot{x} \sin\psi_k + I_k\ddot{\zeta}_k + C_\zeta\dot{\zeta}_k + \left(K_\zeta - g\sigma_k \cos\psi_k\right)\zeta_k = g\sigma_k \sin\psi_k \qquad k = 1 \ldots N \end{cases} \tag{F.15}$$

where, to simplify the expression, the perturbations were denoted as $\Delta x = x$; $\Delta\zeta = \zeta$. Equations (F.15) are a set of N+1 coupled, linear second-order differential equations with periodic coefficients, representing the tower-blade motion in the rotating system of reference of the blade. Assuming that the mass, inertia and static blade properties are identical $I_1 = I_2 = I_{bl}$; $\sigma_1 = \sigma_2 = \sigma_{bl}$; $m_1 = m_2 = m_{bl}$, these equations are non-dimensionalized by dividing the first equation in (F.15) by $M_{tot}R$ and

the second equation by I_{bl}. Using the non-dimensional notation for the tower displacement $\eta = \frac{x}{R}$ and defining the chassis damping ratio $\xi_T = C_T / C_{T\,crit}$, the blade damping ratio $\xi_\zeta = C_\zeta / C_{\zeta\,crit}$, the chassis natural frequency $\omega_T = \sqrt{K_T / M_{tot}}$ and the blade lead-lag natural frequency $\omega_\zeta = \sqrt{K_\zeta / I_{bl}}$ it results:

$$\begin{cases} \ddot{\eta} + 2\xi_T \omega_T \dot{\eta} + \omega_T^2 \eta + \sum_{k=1}^{N} \frac{\sigma_{bl}}{M_{tot} R} \frac{d^2}{dt^2}\left(\zeta_k \sin\psi_k\right) = 0 \\ \frac{\sigma_{bl} R}{I_{bl}} \ddot{\eta} \sin\psi_k + \ddot{\zeta}_k + 2\xi_\zeta \omega_\zeta \dot{\zeta}_k + \left(\omega_\zeta^2 - \frac{g\,\sigma_{bl}}{I_{bl}} \cos\psi_k\right)\zeta_k = \frac{g\,\sigma_{bl}}{I_{bl}} \sin\psi_k \; ; \quad k = 1 \ldots N \end{cases} \tag{F.16}$$

For a 2-bladed rotor, additionally presuming that the blades are uniform, the blade static moment and the moment of inertia equal $\sigma_{bl} = m_{bl} R/2$; $I_{bl} = m_{bl} R^2/3$. A parameter α_m may be defined as $\alpha_m = \frac{1}{2 + M_{ch} / m_{bl}}$, such that the ratios $\sigma_{bl}/(M_{tot} R)$; $(\sigma_{bl} R)/I_{bl}$; $(g\sigma_{bl})/I_{bl}$ respectively may be approximated as $\alpha_m/2$; 1 and g/R. Notating $g\sigma_{bl} / I_{bl} = g/R = \varepsilon$ and with the transformation to the azimuth angle $\frac{d}{dt} = \Omega \frac{d}{d\psi} = \Omega(\,)'$, the equations of motion (F.16) for a 2-bladed rotor become:

$$\begin{cases} \eta'' + 2\xi_T \bar{\omega}_T \eta' + \bar{\omega}_T^2 \eta + \sum_{k=1}^{2} \frac{\alpha_m}{2} \frac{d^2}{d\psi^2}\left(\zeta_k \sin\psi_k\right) = 0 \\ \eta'' \sin\psi_k + \zeta_k'' + 2\xi_\zeta \bar{\omega}_\zeta \zeta_k' + \left(\bar{\omega}_\zeta^2 - \varepsilon \cos\psi_k\right)\zeta_k = \varepsilon \sin\psi_k \; ; \; k = 1,2 \quad \psi_1 = \psi \; , \; \psi_2 = \psi + \pi \end{cases} \tag{F.17}$$

In the coupled rotor-chassis equations of motion (F.17) the gravity force contributes both as an external and as a parametric excitation to the lead-lag motion.

F.2 Rotor-Chassis Equations of Motion in Non-rotating System

The periodic coefficients in (F.17) arise because the tower motion is written with respect to a fixed reference system while the blade equations are in the rotating system. For an N≥3 bladed rotor, the Coleman transformation from Appendix D can be used in order to eliminate the periodic coefficients. For a two-bladed rotor, the Coleman transformation does not eliminate the periodicity. As discussed in this appendix, for this type of rotor, the non-rotating degrees of freedom are only the coning and differential modes and the rotor has no cyclic modes. For the blade lead-lag motion, the non-

rotating coordinates are:

$$\begin{cases} a_0 = \frac{1}{2}(\zeta_2 + \zeta_1) \\ \zeta_{N/2} = \frac{1}{2}(\zeta_2 - \zeta_1) \end{cases} \tag{F.18}$$

Actually, the differential mode $\zeta_{N/2}$ replaces the cyclic modes a_1 and b_1 as defined by (D.1) and therefore couples to the fixed system. The Coleman transformation as defined by (F.18) will be applied to the coupled rotor-chassis equations of motion (F.17). The calculation is best way conducted in matrix form. The vector of coordinates in the rotating and the non-rotating system can be defined as:

$$\{\chi_R\} = \begin{Bmatrix} \eta \\ \zeta_1 \\ \zeta_2 \end{Bmatrix} \quad ; \quad \{\chi_{NR}\} = \begin{Bmatrix} \eta \\ a_0 \\ \zeta_{N/2} \end{Bmatrix} \tag{F.19}$$

According to (D.5) and looking at (F.17), the matrices defining the rotor-chassis equations of motion in the rotating system can be written as:

$$[M_R] = \begin{bmatrix} 1 & \frac{\alpha_m}{2}\sin\psi & -\frac{\alpha_m}{2}\sin\psi \\ \sin\psi & 1 & 0 \\ -\sin\psi & 1 & 0 \end{bmatrix} \quad ; \quad [C_R] = \begin{bmatrix} 2\xi_T\bar{\omega}_T & \alpha_m\cos\psi & -\alpha_m\cos\psi \\ 0 & 2\xi_\zeta\bar{\omega}_\zeta & 0 \\ 0 & 0 & 2\xi_\zeta\bar{\omega}_\zeta \end{bmatrix}$$

$$[K_R] = \begin{bmatrix} \bar{\omega}_T^2 & -\frac{\alpha_m}{2}\sin\psi & \frac{\alpha_m}{2}\sin\psi \\ 0 & \bar{\omega}_\xi^2 - \varepsilon\cos\psi & 0 \\ 0 & \bar{\omega}_\zeta^2 + \varepsilon\cos\psi & 0 \end{bmatrix} \quad ; \quad \{F_R\} = \begin{Bmatrix} 0 \\ \varepsilon\sin\psi \\ -\varepsilon\sin\psi \end{Bmatrix} \tag{F.20}$$

The matrices characteristic to the Coleman transformation for the coupled rotor-chassis system are according to (D.3) and looking at (F.18):

$$[L_{NR}] = \begin{bmatrix} 1 & 0 & 0 \\ 0 & 1/2 & 1/2 \\ 0 & -1/2 & 1/2 \end{bmatrix} \quad ; \quad [L_R] = [L_R]^{-1} = \begin{bmatrix} 1 & 0 & 0 \\ 0 & 1 & -1 \\ 0 & 1 & 1 \end{bmatrix} \tag{F.21}$$

The Coleman transformation applied to the system of equations (F.17) can now be

performed according to the algorithm given in section D.1 of Appendix D. The new matrices, expressing the rotor-chassis matrices in the non-rotating system of reference of the chassis, were calculated according to equation D.1 and their final expressions are:

$$[C_{NR}] = \frac{1}{1-\frac{\alpha_m}{2}+\frac{\alpha_m}{2}\cos 2\psi}\begin{bmatrix} 2\xi_\tau\bar{\omega}_\tau & 0 & -2\alpha_m(\cos\psi-\xi_\zeta\bar{\omega}_\zeta\sin\psi) \\ 0 & 2\xi_\zeta\bar{\omega}_\zeta\left(1-\frac{\alpha_m}{2}+\frac{\alpha_m}{2}\cos 2\psi\right) & 0 \\ 2\xi_\tau\bar{\omega}_\tau\sin\psi & 0 & 2\xi_\zeta\bar{\omega}_\zeta-\alpha_m\sin 2\psi \end{bmatrix}$$

$$[K_{NR}] = \frac{1}{1-\frac{\alpha_m}{2}+\frac{\alpha_m}{2}\cos 2\psi}\begin{bmatrix} \bar{\omega}_\tau^2 & \frac{\alpha_m}{2}\varepsilon\sin 2\psi & \alpha_m(1+\bar{\omega}_\zeta^2)\sin\psi \\ 0 & \bar{\omega}_\zeta^2\left(1-\frac{\alpha_m}{2}+\frac{\alpha_m}{2}\cos 2\psi\right) & \varepsilon\left(1-\frac{\alpha_m}{4}\right)\cos\psi+\frac{\alpha_m\varepsilon}{4}\cos 3\psi \\ \bar{\omega}_\tau^2\sin\psi & \varepsilon\cos\psi & \bar{\omega}_\zeta^2+\frac{\alpha_m}{2}(1-\cos 2\psi) \end{bmatrix}$$

$$\{F_{NR}\} = \frac{1}{1-\frac{\alpha_m}{2}+\frac{\alpha_m}{2}\cos 2\psi}\begin{Bmatrix} \frac{\alpha_m}{4}\varepsilon(-1+\cos 2\psi-\sin 2\psi) \\ \frac{\varepsilon}{2}\left(1-\frac{3\alpha_m}{4}\right)\sin\psi+\frac{\varepsilon}{2}\left(-1+\frac{\alpha_m}{4}\right)\cos\psi+\frac{\alpha_m\varepsilon}{8}\sin 3\psi-\frac{\alpha_m\varepsilon}{8}\cos 3\psi \\ -\frac{\varepsilon}{2}(\sin\psi+\cos\psi) \end{Bmatrix} \quad \text{(F.22)}$$

The equations of motion of the rotor-chassis system are given by:

$$\begin{Bmatrix} \eta \\ a_0 \\ \zeta_{N/2} \end{Bmatrix}'' + [C_{NR}]\begin{Bmatrix} \eta \\ a_0 \\ \zeta_{N/2} \end{Bmatrix}' + [K_{NR}]\begin{Bmatrix} \eta \\ a_0 \\ \zeta_{N/2} \end{Bmatrix} = \{F_{NR}\} \quad \text{(F.23)}$$

with the matrices expressed as in (F.22).

F.3 Solutions of the Rotor-Chassis Equations of Motion in an Asymptotic Expansion

Although the equations of motion (F.17) of the rotor-chassis system were transformed to the non-rotating system using the Coleman transformation, the new equations (F.23) still contain the sine and cosine functions periodic in the blade azimuth ψ. The stability of a linear system of equations with periodic coefficients may be investigated by

applying the Floquet theory as presented in Appendix G. Nevertheless, the response of the system (F.23) can also be determined assuming solutions in an asymptotic expansion. The present section will determine the response of the system in the asymptotic expansion. Consider the equations of motion (F.23) in the expanded form:

$$
\begin{cases}
\left(1-\frac{\alpha_m}{2}+\frac{\alpha_m}{2}\cos 2\psi\right)\eta'' + 2\xi_T\bar{\omega}_T\eta' + \bar{\omega}_T^2\eta + \alpha_m\left[2\left(\xi_\zeta\bar{\omega}_\zeta\sin\psi-\cos\psi\right)\zeta'_{N/2} + \left(1+\bar{\omega}_\zeta^2\right)\times\right. \\
\left.\times\sin\psi\,\zeta_{N/2} + \frac{\varepsilon}{2}a_0\sin 2\psi\right] = \frac{\alpha_m\varepsilon}{4}\left(-1+\cos 2\psi-\sin 2\psi\right) \\
\left(1-\frac{\alpha_m}{2}+\frac{\alpha_m}{2}\cos 2\psi\right)a_0'' + 2\xi_\zeta\bar{\omega}_\zeta\left(1-\frac{\alpha_m}{2}+\frac{\alpha_m}{2}\cos 2\psi\right)a_0' + \bar{\omega}_\zeta^2\left(1-\frac{\alpha_m}{2}+\frac{\alpha_m}{2}\cos 2\psi\right)a_0 \\
+\left[\varepsilon\cos\psi\left(1-\frac{\alpha_m}{4}\right)+\frac{\alpha_m\varepsilon}{4}\cos 3\psi\right]\zeta_{N/2} = \frac{\varepsilon}{2}\left(1-\frac{3\alpha_m}{4}\right)\sin\psi + \frac{\varepsilon}{2}\left(-1+\frac{\alpha_m}{4}\right)\cos\psi + \frac{\alpha_m\varepsilon}{8}\sin 3\psi \\
-\frac{\alpha_m\varepsilon}{8}\cos 3\psi\left(1-\frac{\alpha_m}{2}+\frac{\alpha_m}{2}\cos 2\psi\right)\zeta''_{N/2} + \left(2\xi_\zeta\bar{\omega}_\zeta-\alpha_m\sin 2\psi\right)\zeta'_{N/2} + \left[\bar{\omega}_\zeta^2+\right. \\
\left.+\frac{\alpha_m}{2}\left(1-\cos 2\psi\right)\right]\zeta_{N/2} + 2\xi_T\bar{\omega}_T\sin\psi\,\eta' + \bar{\omega}_T^2\sin\psi\,\eta + \varepsilon\cos\psi\,a_0 = -\frac{\varepsilon}{2}\left(\sin\psi+\cos\psi\right)
\end{cases}
\tag{F.24}
$$

and assume solutions for the system (F.24) in the form:

$$
\begin{cases}
\eta = \eta_0 + \alpha_m\eta_1 + \ldots \\
a_0 = d_0 + \alpha_m d_1 + \ldots \\
\zeta_{N/2} = b_0 + \alpha_m b_1 + \ldots
\end{cases}
\tag{F.25}
$$

Solutions in the Approximation of order $O(\alpha_m{}^0)$

Substituting (F.25) into (F.24), the equations of motion (F.24) in the approximation $O(\alpha_m{}^0)$ become:

$$\begin{cases} \eta_0'' + 2\xi_T\bar{\omega}_T\eta_0' + \bar{\omega}_T^2\eta_0 = 0 \\ d_0'' + 2\xi_\zeta\bar{\omega}_\zeta d_0' + \bar{\omega}_\zeta^2 d_0 + \varepsilon\cos\psi b_0 = \dfrac{\varepsilon}{2}\left(\sin\psi - \cos\psi\right) \\ b_0'' + 2\xi_\zeta\bar{\omega}_\zeta b_0' + \bar{\omega}_\zeta^2 b_0 + 2\xi_T\bar{\omega}_T\sin\psi\eta_0 + \bar{\omega}_T^2\sin\psi\eta_0 + \varepsilon\cos\psi d_0 = -\dfrac{\varepsilon}{2}\left(\sin\psi + \cos\psi\right) \end{cases} \quad \text{(F.26)}$$

In system (F.26), the chassis motion decouples from the collective lead-lag but is still coupled to the differential lead-lag mode. Solving the first equation of system (F.26), the tower steady-state solution is:

$$\eta_0 = 0 \quad \text{(F.27)}$$

The rotor collective and differential lead-lag response in d_0 and b_0 remain coupled via parameter ε containing the gravity force. Also assume the solution of the rotor motion as an asymptotic expansion in ε, that is:

$$\begin{cases} d_0 = d_{00} + \varepsilon\, d_{01} + \ldots \\ b_0 = b_{00} + \varepsilon\, b_{01} + \ldots \end{cases} \quad \text{(F.28)}$$

Substituting (F.28) into (F.26) and taking into account (F.27) leads to the following equations of motion for the lead-lag modes in a first approximation:

$$\begin{cases} d_{00}'' + 2\xi_\zeta\bar{\omega}_\zeta d_{00}' + \bar{\omega}_\zeta^2 d_{00} + \varepsilon\left[d_{01}'' + 2\xi_\zeta\bar{\omega}_\zeta d_{01}' + \bar{\omega}_\zeta^2 d_{01} + \cos\psi b_{00} - \dfrac{1}{2}\left(\sin\psi - \cos\psi\right)\right] = 0 \\ b_{00}'' + 2\xi_\zeta\bar{\omega}_\zeta b_{00}' + \bar{\omega}_\zeta^2 b_{00} + \varepsilon\left[b_{01}'' + 2\xi_\zeta\bar{\omega}_\zeta b_{01}' + \bar{\omega}_\zeta^2 b_{01} + \cos\psi d_{00} + \dfrac{1}{2}\left(\sin\psi + \cos\psi\right)\right] = 0 \end{cases} \quad \text{(F.29)}$$

The solutions of system (F.29) in the approximation of order $O(\varepsilon^0)$ are therefore:

$$\begin{cases} d_{00} = 0 \\ b_{00} = 0 \end{cases} \quad \text{(F.30)}$$

The solutions d_{01} and b_{01} in the approximation of order $O(\varepsilon^1)$ are according to (F.29) of form:

$$\begin{cases} d_{0i} = e_{c0}\cos\psi + e_{s0}\sin\psi \\ b_{0i} = f_{c0}\cos\psi + f_{s0}\sin\psi \end{cases} \tag{F.31}$$

Substituting (F.31) into (F.29) and equating to zero, the coefficients e_{c0}, e_{s0} and f_{c0}, f_{s0} are obtained as:

$$\begin{aligned} e_{c0} &= -\frac{A}{\left[\left(\bar{\omega}_\zeta - 1\right)^2 + 4\xi_\zeta^2\bar{\omega}_\zeta^2\right]} \quad ; \quad e_{s0} = \frac{B}{\left[\left(\bar{\omega}_\zeta - 1\right)^2 + 4\xi_\zeta^2\bar{\omega}_\zeta^2\right]} \\ f_{c0} &= -\frac{B}{\left[\left(\bar{\omega}_\zeta - 1\right)^2 + 4\xi_\zeta^2\bar{\omega}_\zeta^2\right]} \quad ; \quad f_{s0} = -\frac{A}{\left[\left(\bar{\omega}_\zeta - 1\right)^2 + 4\xi_\zeta^2\bar{\omega}_\zeta^2\right]} \end{aligned} \tag{F.32}$$

where A and B are notations for the following expressions:

$$A = \frac{\left[\left(\bar{\omega}_\zeta - 1\right) + 2\xi_\zeta\bar{\omega}_\zeta\right]}{2} \quad ; \quad B = \frac{\left[\left(\bar{\omega}_\zeta - 1\right) - 2\xi_\zeta\bar{\omega}_\zeta\right]}{2} \tag{F.33}$$

The solution of the chassis-rotor motion in the approximation of order $O(\alpha_m^0)$ is now completely determined by looking at (F.32), (F.31), (F.30) (F.28) and (F.27):

$$\begin{cases} \eta_0 = 0 \\ d_0 = \dfrac{\varepsilon}{\left[\left(\bar{\omega}_\zeta - 1\right)^2 + 4\xi_\zeta^2\bar{\omega}_\zeta^2\right]}\left(-A\cos\psi + B\sin\psi\right) \\ b_0 = \dfrac{\varepsilon}{\left[\left(\bar{\omega}_\zeta - 1\right)^2 + 4\xi_\zeta^2\bar{\omega}_\zeta^2\right]}\left(B\cos\psi - A\sin\psi\right) \end{cases} \tag{F.34}$$

with A and B given by (F.33).

Solution in the Approximation of order $O(\alpha_m^1)$

The solution of the chassis-rotor motion in the approximation of order $O(\alpha_m^1)$ are

derived by substituting (F.25) into (F.24) and considering only the terms in α_m:

$$\begin{cases} \eta_1'' + 2\xi_T\bar{\omega}_T\eta_1' + \bar{\omega}_T^2\eta_1 + \frac{1}{2}\left(-1+\cos 2\psi\right)\eta_0'' + \left(2\xi_\zeta\bar{\omega}_\zeta\sin\psi - \cos\psi\right)b_0' + \left(1+\bar{\omega}_\zeta^2\right)\sin\psi\, b_0 + \\ + \frac{\varepsilon}{2}\, d_0 \sin 2\psi \;=\; \frac{\varepsilon}{4}\left(-1+\cos 2\psi - \sin 2\psi\right) \\ d_1'' + 2\xi_\zeta\bar{\omega}_\zeta\, d_1' + \bar{\omega}_\zeta^2\, d_1 + \frac{1}{2}\left(-1+\cos 2\psi\right)d_0'' + \frac{1}{2}\left(-1+\cos 2\psi\right)d_0' + \frac{1}{2}\left(-1+\cos 2\psi\right)d_0 + \\ + \varepsilon\cos\psi\, b_1 - \frac{\varepsilon}{4}\cos\psi\, b_0 + \frac{\varepsilon}{4}\cos 3\psi\, b_0 \;=\; -\frac{3\varepsilon}{8}\sin\psi + \frac{\varepsilon}{8}\cos\psi + \frac{\varepsilon}{8}\sin 3\psi - \frac{\varepsilon}{8}\cos 3\psi \\ b_1'' + 2\xi_\zeta\bar{\omega}_\zeta b_1' + \bar{\omega}_\zeta^2\, b_1 + \frac{1}{2}\left(-1+\cos 2\psi\right)b_0'' - \sin 2\psi\, b_0' + \frac{1}{2}\left(1-\cos 2\psi\right)b_0 + \\ + 2\xi_T\bar{\omega}_T\sin\psi\,\eta_1' + \bar{\omega}_T^2\sin\psi\,\eta_1 + \varepsilon\cos\psi\, d_1 \;=\; 0 \end{cases} \tag{F.35}$$

Substituting the solutions (F.34) of b_0 and d_0 into the first equation of system (F.35), the chassis equation becomes:

$$\begin{aligned} \eta_1'' + 2\xi_T\bar{\omega}_T\eta_1' + \bar{\omega}_T^2\eta_1 \;&=\; \varepsilon\left[-\frac{1}{4} + \frac{A}{2}\bar{\omega}_\zeta^2 - \xi_\zeta\bar{\omega}_\zeta B\right] + \varepsilon\left[\xi_\zeta\bar{\omega}_\zeta B - \frac{A}{2} - \frac{A}{2}\left(1+\bar{\omega}_\zeta^2\right) + \frac{1}{4}\right]\cos 2\psi + \\ + \varepsilon\left[\xi_\zeta\bar{\omega}_\zeta A + \frac{B}{2} + \frac{B}{2}\left(1+\bar{\omega}_\zeta^2\right) - \frac{1}{4}\right]&\sin 2\psi + \frac{\varepsilon^2}{4}\left[-B\cos\psi + A\sin\psi + B\cos 3\psi + A\sin 3\psi\right] \end{aligned} \tag{F.36}$$

Again, assuming the solution in η_1 as an asymptotic expansion in ε:

$$\eta_1 = \eta_{10} + \varepsilon\eta_{11} + \ldots \tag{F.37}$$

and substituting this into (F.36), one obtains:

$$\eta_{10} = 0 \tag{F.38}$$

For η_{11} one may assume for the chassis a solution in the form:

$$\eta_{11} = g_{c1}\cos 2\psi + g_{s1}\sin 2\psi \tag{F.39}$$

Substituting (F.39) into (F.36) and equating to zero the terms in $\sin 2\psi$ and $\cos 2\psi$, it

results:

$$g_{c1} = \frac{C}{\left[\left(\bar{\omega}_\zeta^2 - 1\right)^2 + 4\xi_\zeta^2\bar{\omega}_\zeta^2\right]\left[\left(\bar{\omega}_T^2 - 4\right)^2 + 16\xi_T^2\bar{\omega}_T^2\right]}$$
$$g_{s1} = \frac{D}{\left[\left(\bar{\omega}_\zeta^2 - 1\right)^2 + 4\xi_\zeta^2\bar{\omega}_\zeta^2\right]\left[\left(\bar{\omega}_T^2 - 4\right)^2 + 16\xi_T^2\bar{\omega}_T^2\right]} \qquad \text{(F.40)}$$

where A and B are of form (F.33) and C, D are the following expressions:

$$C = \left(-\frac{3}{2}\xi_\zeta\bar{\omega}_\zeta - \frac{3}{4}\bar{\omega}_\zeta^2 + \frac{3}{4}\right)\bar{\omega}_T^2 + \left(3 + 6\xi_\zeta\bar{\omega}_\zeta - 3\bar{\omega}_\zeta^2\right)\xi_T\bar{\omega}_T + 3\bar{\omega}_T^2 + 6\xi_T\bar{\omega}_T - 3$$
$$D = \left(-\frac{3}{2}\xi_\zeta\bar{\omega}_\zeta + \frac{3}{4}\bar{\omega}_\zeta^2 - \frac{3}{4}\right)\bar{\omega}_T^2 + \left(3 - 6\xi_\zeta\bar{\omega}_\zeta - 3\bar{\omega}_\zeta^2\right)\xi_T\bar{\omega}_T - 3\bar{\omega}_T^2 + 6\xi_T\bar{\omega}_T + 3 \qquad \text{(F.41)}$$

The solution of the chassis motion in the approximation of order $O(\alpha_m^{\,1})$ is thus:

$$\eta_1 = \frac{\varepsilon}{\left[\left(\bar{\omega}_\zeta^2 - 1\right)^2 + 4\xi_\zeta^2\bar{\omega}_\zeta^2\right]\left[\left(\bar{\omega}_T^2 - 4\right)^2 + 16\xi_T^2\bar{\omega}_T^2\right]}\left(C\cos 2\psi + D\sin 2\psi\right) \qquad \text{(F.42)}$$

Looking at the second and third equations of motion of system (F.35) it follows that the chassis motion does not contribute to the collective lead-lag motion but it does to the differential lead-lag mode. Substituting (F.34) and (F.40) into these equations one obtains:

$$\begin{cases} d_1'' + 2\xi_\zeta\bar{\omega}_\zeta d_1' + \bar{\omega}_\zeta^2 d_1 + \varepsilon\cos\psi b_1 = \dfrac{\varepsilon}{4\left[\left(\bar{\omega}_\zeta^2 - 1\right)^2 + 4\xi_\zeta^2\bar{\omega}_\zeta^2\right]}\left[\dfrac{2B+1}{8}\cos\psi + 3\dfrac{2A-1}{8}\sin\psi + \right. \\ \left. + \dfrac{2B+1}{8}\cos 3\psi - \dfrac{2A-1}{8}\sin 3\psi\right] - \dfrac{\varepsilon^2\left[B\cos 2\psi + A\sin 2\psi - B\cos 4\psi - A\sin 4\psi\right]}{8\left[\left(\bar{\omega}_\zeta^2 - 1\right)^2 + 4\xi_\zeta^2\bar{\omega}_\zeta^2\right]} \\ b_1'' + 2\xi_\zeta\bar{\omega}_\zeta b_1' + \bar{\omega}_\zeta^2 b_1 + \varepsilon\cos\psi d_1 = \dfrac{\varepsilon\left[B\cos\psi + A\sin\psi - B\cos 3\psi - A\sin 3\psi\right]}{\left[\left(\bar{\omega}_\zeta^2 - 1\right)^2 + 4\xi_\zeta^2\bar{\omega}_\zeta^2\right]} - \\ - \dfrac{\varepsilon}{\left[\left(\bar{\omega}_\zeta^2 - 1\right)^2 + 4\xi_\zeta^2\bar{\omega}_\zeta^2\right]\left[\left(\bar{\omega}_T^2 - 4\right)^2 + 16\xi_T^2\bar{\omega}_T^2\right]}\left[\left(-2\xi_T\bar{\omega}_T C + \dfrac{\bar{\omega}_T^2}{2}D\right)\cos\psi + \right. \\ \left. + \left(-2\xi_T\bar{\omega}_T D + \dfrac{\omega_T^2}{2}C\right)\sin\psi + \left(2\xi_T\bar{\omega}_T C - \dfrac{\omega_T^2}{2}D\right)\cos 3\psi + \left(2\xi_T\bar{\omega}_1 D + \dfrac{\bar{\omega}_T^2}{2}C\right)\sin 3\psi\right] \end{cases} \qquad \text{(F.43)}$$

Assuming the solution as an asymptotic expansion in ε, that is:

$$\begin{cases} d_1 = d_{01} + \varepsilon\, d_{11} + \dots \\ b_1 = b_{01} + \varepsilon\, b_{11} + \dots \end{cases} \tag{F.44}$$

and neglecting the terms in ε^2 and substituting this into (F.43) yields:

$$\begin{cases} d_{01} = 0 \\ b_{01} = 0 \end{cases} \tag{F.45}$$

and respectively:

$$\begin{cases} d_{11}'' + 2\xi_\zeta \bar{\omega}_\zeta\, d_{11}' + \bar{\omega}_\zeta^2\, d_{11} = \dfrac{1}{4\left[\left(\bar{\omega}_\zeta^2 - 1\right)^2 + 4\xi_\zeta^2\, \bar{\omega}_\zeta^2\right]} \left[\dfrac{2B+1}{8}\cos\psi + 3\dfrac{2A-1}{8}\sin\psi + \right. \\ \left. + \dfrac{2B+1}{8}\cos 3\psi - \dfrac{2A-1}{8}\sin 3\psi\right] \\ b_{11}'' + 2\xi_\zeta \bar{\omega}_\zeta b_{11}' + \bar{\omega}_\zeta^2 b_{11} = \dfrac{1}{\left[\left(\bar{\omega}_\zeta^2 - 1\right)^2 + 4\xi_\zeta^2 \bar{\omega}_\zeta^2\right]} \left[B\cos\psi + A\sin\psi - B\cos 3\psi - \right. \\ \left. - A\sin 3\psi\right] - \dfrac{1}{\left[\left(\bar{\omega}_\zeta^2 - 1\right)^2 + 4\xi_\zeta^2 \bar{\omega}_\zeta^2\right]\left[\left(\bar{\omega}_T^2 - 4\right)^2 + 16\xi_T^2 \bar{\omega}_T^2\right]} \left[\left(-2\xi_T \bar{\omega}_T C + \dfrac{\omega_T^2}{2} D\right)\cos\psi + \right. \\ \left. + \left(-2\xi_T \bar{\omega}_T D + \dfrac{\bar{\omega}_T^2}{2} C\right)\sin\psi + \left(2\xi_T \bar{\omega}_T C - \dfrac{\bar{\omega}_T^2}{2} D\right)\cos 3\psi + \left(2\xi_T \bar{\omega}_T D + \dfrac{\bar{\omega}_T^2}{2} C\right)\sin 3\psi \right] \end{cases} \tag{F.46}$$

The solution in d_{11} and b_{11} can now be determined assuming modes of form:

$$\begin{cases} d_{11} = e_{c1}\cos\psi + e_{s1}\sin\psi + e_{c3}\cos 3\psi + e_{s3}\sin 3\psi \\ b_{11} = f_{c1}\cos\psi + f_{s1}\sin\psi + f_{c3}\cos 3\psi + f_{s3}\sin 3\psi \end{cases} \tag{F.47}$$

Substituting (F.47) into (F.46) and equating to zero the terms in $\sin\psi$, $\cos\psi$, $\sin 3\psi$ and

cos 3ψ, the coefficients e_{c1}, e_{s1}, e_{c3}, e_{s3}, f_{c1}, f_{s1}, f_{c3}, f_{s3} are obtained as:

$$e_{c1} = \frac{B_2\left(\bar{\omega}_\zeta^2 - 1\right) - 2\xi_\zeta\bar{\omega}_\zeta A_2}{\left[\left(\bar{\omega}_\zeta - 1\right)^2 + 4\xi_\zeta^2\bar{\omega}_\zeta^2\right]^2} \quad ; \quad e_{s1} = \frac{A_2\left(\bar{\omega}_\zeta^2 - 1\right) + 2\xi_\zeta\bar{\omega}_\zeta B_2}{\left[\left(\bar{\omega}_\zeta - 1\right)^2 + 4\xi_\zeta^2\bar{\omega}_\zeta^2\right]^2} \tag{F.48}$$

$$e_{c3} = \frac{B_3\left(\bar{\omega}_\zeta^2 - 9\right) - 6\xi_\zeta\bar{\omega}_\zeta A_3}{\left[\left(\bar{\omega}_\zeta - 1\right)^2 + 4\xi_\zeta^2\bar{\omega}_\zeta^2\right]\left[\left(\bar{\omega}_\zeta - 9\right)^2 + 36\xi_\zeta^2\bar{\omega}_\zeta^2\right]} \; ; \; e_{c3} = \frac{A_3\left(\bar{\omega}_\zeta^2 - 9\right) + 6\xi_\zeta\bar{\omega}_\zeta B_3}{\left[\left(\bar{\omega}_\zeta - 1\right)^2 + 4\xi_\zeta^2\bar{\omega}_\zeta^2\right]\left[\left(\bar{\omega}_\zeta - 9\right)^2 + 36\xi_\zeta^2\bar{\omega}_\zeta^2\right]}$$

$$f_{c1} = \frac{B_4\left(\bar{\omega}_\zeta^2 - 1\right) - 2\xi_\zeta\bar{\omega}_\zeta A_4}{\left[\left(\bar{\omega}_\zeta - 1\right)^2 + 4\xi_\zeta^2\bar{\omega}_\zeta^2\right]\left[\left(\bar{\omega}_T^2 - 4\right)^2 + 16\xi_T^2\bar{\omega}_T^2\right]} \; ; \; f_{s1} = \frac{A_4\left(\bar{\omega}_\zeta^2 - 1\right) + 2\xi_\zeta\bar{\omega}_\zeta B_4}{\left[\left(\bar{\omega}_\zeta - 1\right)^2 + 4\xi_\zeta^2\bar{\omega}_\zeta^2\right]\left[\left(\bar{\omega}_T^2 - 4\right)^2 + 16\xi_T^2\bar{\omega}_T^2\right]}$$

$$f_{c3} = \frac{B_5\left(\bar{\omega}_\zeta^2 - 9\right) - 6\xi_\zeta\bar{\omega}_\zeta A_5}{\left[\left(\bar{\omega}_\zeta - 1\right)^2 + 4\xi_\zeta^2\bar{\omega}_\zeta^2\right]\left[\left(\bar{\omega}_T^2 - 4\right)^2 + 16\xi_T^2\bar{\omega}_T^2\right]\left[\left(\bar{\omega}_\zeta - 9\right)^2 + 36\xi_\zeta^2\bar{\omega}_\zeta^2\right]} \tag{F.49}$$

$$f_{s3} = \frac{A_5\left(\bar{\omega}_\zeta^2 - 9\right) + 6\xi_\zeta\bar{\omega}_\zeta B_5}{\left[\left(\bar{\omega}_\zeta - 1\right)^2 + 4\xi_\zeta^2\bar{\omega}_\zeta^2\right]\left[\left(\bar{\omega}_T^2 - 4\right)^2 + 16\xi_T^2\bar{\omega}_T^2\right]\left[\left(\bar{\omega}_\zeta - 9\right)^2 + 36\xi_\zeta^2\bar{\omega}_\zeta^2\right]}$$

where:

$$A_2 = \frac{2A - 1}{8} \quad ; \quad B_2 = \frac{2B + 1}{8} \quad ; \quad A_3 = -\frac{2A - 1}{8} \quad ; \quad B_3 = -\frac{2B + 1}{8} \tag{F.50}$$

$$\begin{aligned}
B_4 &= B\left[\left(\bar{\omega}_T^2 - 4\right)^2 + 16\xi_T^2\bar{\omega}_T^2\right] + \left(2\xi_T\bar{\omega}_T C - \frac{\bar{\omega}_T^2}{2}D\right) \\
A_4 &= A\left[\left(\bar{\omega}_T^2 - 4\right)^2 + 16\xi_T^2\bar{\omega}_T^2\right] + \left(2\xi_1\bar{\omega}_T D + \frac{\omega_T^2}{2}C\right) \\
B_5 &= -B\left[\left(\bar{\omega}_T^2 - 4\right)^2 + 16\xi_T^2\bar{\omega}_T^2\right] + \left(-2\xi_T\bar{\omega}_T D + \frac{\bar{\omega}_T^2}{2}C\right) \\
A_5 &= -A\left[\left(\bar{\omega}_T^2 - 4\right)^2 + 16\xi_T^2\bar{\omega}_T^2\right] + \left(-2\xi_T\bar{\omega}_T D - \frac{\bar{\omega}_T^2}{2}C\right)
\end{aligned} \tag{F.51}$$

Adding the solutions for the first approximation of order $O(\alpha_m^{\,1})$ (F.47), (F.45), (F.44), (F.39) one obtains:

$$
\begin{cases}
\eta_1 = \dfrac{\varepsilon}{\left[\left(\bar{\omega}_\zeta^2-1\right)^2+4\xi_\zeta^2\bar{\omega}_\zeta^2\right]\left[\left(\bar{\omega}_T^2-4\right)^2+16\xi_T^2\bar{\omega}_T^2\right]}\left(C\cos 2\psi + D\sin 2\psi\right) \\
d_{11} = \dfrac{\varepsilon}{\left[\left(\bar{\omega}_\zeta-1\right)^2+4\xi_\zeta^2\bar{\omega}_\zeta^2\right]}\left\{\left[B_2\left(\bar{\omega}_\zeta^2-1\right)-2\xi_\zeta\bar{\omega}_\zeta A_2\right]\cos\psi+\left[A_2\left(\bar{\omega}_\zeta^2-1\right)+2\xi_\zeta\bar{\omega}_\zeta B_2\right]\sin\psi\right\}+ \\
\quad+\dfrac{\varepsilon}{\left[\left(\bar{\omega}_\zeta-1\right)^2+4\xi_\zeta^2\bar{\omega}_\zeta^2\right]\left[\left(\bar{\omega}_\zeta-9\right)^2+36\xi_\zeta^2\bar{\omega}_\zeta^2\right]}\left\{\left[B_3\left(\bar{\omega}_\zeta^2-9\right)-6\xi_\zeta\bar{\omega}_\zeta A_3\right]\cos 3\psi+\right. \\
\quad\left.+\left[A_3\left(\bar{\omega}_\zeta^2-9\right)+6\xi_\zeta\bar{\omega}_\zeta B_3\right]\sin 3\psi\right\} \\
b_{11} = \dfrac{\varepsilon}{\left[\left(\bar{\omega}_\zeta-1\right)^2+4\xi_\zeta^2\bar{\omega}_\zeta^2\right]\left[\left(\bar{\omega}_T^2-4\right)^2+16\xi_T^2\bar{\omega}_T^2\right]}\left\{\left[B_4\left(\bar{\omega}_\zeta^2-1\right)-2\xi_\zeta\bar{\omega}_\zeta A_4\right]\cos\psi+\left[A_4\left(\bar{\omega}_\zeta^2-1\right)+\right.\right. \\
\quad\left.+2\xi_\zeta\bar{\omega}_\zeta B_4\right]\sin\psi\Big\}+\dfrac{\varepsilon}{\left[\left(\bar{\omega}_\zeta-1\right)^2+4\xi_\zeta^2\bar{\omega}_\zeta^2\right]\left[\left(\bar{\omega}_T^2-4\right)^2+16\xi_T^2\bar{\omega}_T^2\right]\left[\left(\bar{\omega}_\zeta-9\right)^2+36\xi_\zeta^2\bar{\omega}_\zeta^2\right]}\times \\
\quad\times\left\{\left[B_5\left(\bar{\omega}_\zeta^2-9\right)-6\xi_\zeta\bar{\omega}_\zeta A_5\right]\cos 3\psi+\left[A_5\left(\bar{\omega}_\zeta^2-9\right)+6\xi_\zeta\bar{\omega}_\zeta B_5\right]\sin 3\psi\right\}
\end{cases}
\tag{F.52}
$$

Recalling the solution (F.34) for the $O(\alpha_m^0)$ solution, the final solution for the equations of motion (F.24) using the asymptotic expansion (F.52) are:

$$
\begin{cases}
\eta = \dfrac{\alpha_m\varepsilon}{\left[\left(\bar{\omega}_\zeta^2-1\right)+4\xi_\zeta^2\bar{\omega}_\zeta^2\right]\left[\left(\bar{\omega}_T^2-4\right)+16\xi_T^2\bar{\omega}_T^2\right]}\left(C\cos 2\psi + D\sin 2\psi\right) \\
a_0 = \dfrac{\varepsilon}{\left[\left(\bar{\omega}_\zeta-1\right)^2+4\xi_\zeta^2\bar{\omega}_\zeta^2\right]}\left[\left(-A+\alpha_m A_2^*\right)\cos\psi+\left(B+\alpha_m B_2^*\right)\sin\psi\right]+ \\
\quad+\dfrac{\alpha_m\varepsilon\left[A_3^*\cos 3\psi+B_3^*\sin 3\psi\right]}{\left[\left(\bar{\omega}_\zeta-1\right)^2+4\xi_\zeta^2\bar{\omega}_\zeta^2\right]\left[\left(\bar{\omega}_\zeta-9\right)^2+36\xi_\zeta^2\bar{\omega}_\zeta^2\right]} \\
\zeta_{N/2} = \dfrac{\varepsilon}{\left[\left(\bar{\omega}_\zeta-1\right)^2+4\xi_\zeta^2\bar{\omega}_\zeta^2\right]}\left[B\cos\psi-A\sin\psi\right]+\dfrac{\alpha_m\varepsilon}{\left[\left(\bar{\omega}_\zeta-1\right)^2+4\xi_\zeta^2\bar{\omega}_\zeta^2\right]\left[\left(\bar{\omega}_T^2-4\right)+16\xi_T^2\bar{\omega}_T^2\right]}\times \\
\quad\times\left[B_4^*\cos\psi+A_4^*\sin\psi\right]+\dfrac{\alpha_m\varepsilon\left[B_5^*\cos 3\psi+A_5^*\sin 3\psi\right]}{\left[\left(\bar{\omega}_\zeta-1\right)^2+4\xi_\zeta^2\bar{\omega}_\zeta^2\right]\left[\left(\bar{\omega}_T^2-4\right)+16\xi_T^2\bar{\omega}_T^2\right]\left[\left(\bar{\omega}_\zeta-9\right)^2+36\xi_\zeta^2\bar{\omega}_\zeta^2\right]}
\end{cases}
\tag{F.53}
$$

where:

$$A_2^* = \frac{2B+1}{8}\left(\bar{\omega}_\zeta^2 - 1\right) - 6\xi_\zeta\bar{\omega}_\zeta\frac{2A-1}{8} \quad ; \quad B_2^* = 3\frac{2A-1}{8}\left(\bar{\omega}_\zeta^2 - 1\right) + 2\xi_\zeta\bar{\omega}_\zeta\frac{2B+1}{8}$$
$$A_3^* = -\frac{2B+1}{8}\left(\bar{\omega}_\zeta^2 - 9\right) + 6\xi_\zeta\bar{\omega}_\zeta\frac{2A-1}{8} \quad ; \quad B_3^* = -\frac{2A-1}{8}\left(\bar{\omega}_\zeta^2 - 9\right) - 6\xi_\zeta\bar{\omega}_\zeta\frac{2B+1}{8} \tag{F.54}$$

$$B_4^* = \left[B\left[\left(\bar{\omega}_T^2 - 4\right)^2 + 16\xi_T^2\bar{\omega}_T^2\right] + \left(2\xi_T\bar{\omega}_T C - \frac{\bar{\omega}_T^2}{2}D\right)\right]\left(\bar{\omega}_\zeta^2 - 1\right) -$$
$$- 2\xi_\zeta\bar{\omega}_\zeta\left[A\left[\left(\bar{\omega}_T^2 - 4\right)^2 + 16\xi_T^2\bar{\omega}_T^2\right] + \left(2\xi_T\bar{\omega}_T D + \frac{\bar{\omega}_T^2}{2}C\right)\right]$$
$$A_4^* = \left[A\left[\left(\bar{\omega}_T^2 - 4\right)^2 + 16\xi_T^2\bar{\omega}_T^2\right] + \left(2\xi_T\bar{\omega}_T D + \frac{\bar{\omega}_T^2}{2}C\right)\right]\left(\bar{\omega}_\zeta^2 - 1\right) +$$
$$+ 2\xi_\zeta\bar{\omega}_\zeta\left[B\left[\left(\bar{\omega}_T^2 - 4\right)^2 + 16\xi_T^2\bar{\omega}_T^2\right] + \left(2\xi_T\bar{\omega}_T C - \frac{\bar{\omega}_T^2}{2}D\right)\right] \tag{F.55}$$

$$B_5^* = \left[-B\left[\left(\bar{\omega}_T^2 - 4\right)^2 + 16\xi_T^2\bar{\omega}_T^2\right] + \left(-2\xi_T\bar{\omega}_T D + \frac{\bar{\omega}_T^2}{2}C\right)\right]\left(\bar{\omega}_\zeta^2 - 9\right) - 6\xi_\zeta\bar{\omega}_\zeta \times$$
$$\times\left[-A\left[\left(\bar{\omega}_T^2 - 4\right)^2 + 16\xi_T^2\bar{\omega}_T^2\right] + \left(-2\xi_T\bar{\omega}_T D - \frac{\bar{\omega}_T^2}{2}C\right)\right]$$
$$A_5^* = \left[-A\left[\left(\bar{\omega}_T^2 - 4\right)^2 + 16\xi_T^2\bar{\omega}_T^2\right] + \left(-2\xi_T\bar{\omega}_T D - \frac{\bar{\omega}_T^2}{2}C\right)\right]''\left(\bar{\omega}_\zeta^2 - 9\right) + 6\xi_\zeta\bar{\omega}_\zeta \times$$
$$\times\left[-B\left[\left(\bar{\omega}_T^2 - 4\right)^2 + 16\xi_T^2\bar{\omega}_T^2\right] + \left(-2\xi_T\bar{\omega}_T D + \frac{\bar{\omega}_T^2}{2}C\right)\right] \tag{F.56}$$

and the coefficients A and B are given by (F.33) and C and D by (F.41).

F.4 Effects of Higher-Order Terms in the Expansion

The question arises what the effect of higher-order terms than $O(\alpha_m^1)$ of the expansion is on the system response. Considering the expansion (F.25) in higher-order terms it follows that:

$$\begin{cases} \eta = \eta_0 + \alpha_m\eta_1 + \alpha_m^2\eta_2 + \ldots \\ a_0 = d_0 + \alpha_m d_1 + \alpha_m^2 d_2 + \ldots \\ \zeta_{N/2} = b_0 + \alpha_m b_1 + \alpha_m^2 b_2 + \ldots \end{cases} \tag{F.57}$$

The chassis equation will contain terms proportional to $\alpha_m^2\, b'_1 \cos\psi$, $\alpha_m^2\, b'_1 \sin\psi$ and $\alpha_m^2\, b_1 \sin\psi$ (see (F.35)) resulting from the differential mode, Since the differential lead-lag response b_1 contains the harmonics $\cos\psi$, $\sin\psi$, $\cos 3\psi$, $\sin 3\psi$, it follows that these terms will contain the harmonics $\cos 2\psi$, $\sin 2\psi$, $\cos 4\psi$, $\sin 4\psi$. By analogy with the chassis response in the order $O(\alpha_m^1)$ investigated above (F.53), it can be demonstrated that the response of the chassis in the approximation up to $O(\alpha_m^2)$ will contain a term proportional (~) to:

$$\sim \alpha_m^2 \varepsilon \cos 4\psi \frac{1}{\left[\left(\bar{\omega}_\zeta^2-1\right)^2+4\xi_\zeta^2\bar{\omega}_\zeta^2\right]} \cdot \frac{1}{\left[\left(\bar{\omega}_T^2-4\right)^2+16\xi_T^2\bar{\omega}_T^2\right]} \cdot \frac{1}{\left[\left(\bar{\omega}_\zeta^2-9\right)^2+36\xi_\zeta^2\bar{\omega}_\zeta^2\right]} \cdot \frac{1}{\left[\left(\bar{\omega}_T^2-16\right)^2+64\xi_T^2\bar{\omega}_T^2\right]} \tag{F.58}$$

and respectively the same term in $\sin 4\psi$. Therefore, the chassis response further contains a resonance region situated in the vicinity of the frequency $\bar{\omega}_T = 4 \Leftrightarrow \Omega = \omega_T / 4$. Additionally, in the approximation $O(\alpha_m^3)$, there will be a term proportional (~) to:

$$\sim \alpha_m^3 \varepsilon \cos 6\psi \frac{1}{\left[\left(\bar{\omega}_\zeta^2-1\right)^2+4\xi_\zeta^2\bar{\omega}_\zeta^2\right]} \frac{1}{\left[\left(\bar{\omega}_T^2-4\right)^2+16\xi_T^2\bar{\omega}_T^2\right]} \frac{1}{\left[\left(\bar{\omega}_\zeta^2-9\right)^2+36\xi_\zeta^2\bar{\omega}_\zeta^2\right]} \cdot \frac{1}{\left[\left(\bar{\omega}_T^2-16\right)^2+64\xi_T^2\bar{\omega}_T^2\right]} \frac{1}{\left[\left(\bar{\omega}_\zeta^2-25\right)^2+100\xi_\zeta^2\bar{\omega}_\zeta^2\right]} \frac{1}{\left[\left(\bar{\omega}_T^2-36\right)^2+144\xi_T^2\bar{\omega}_T^2\right]} \tag{F.59}$$

and also a similar term in $\sin 6\psi$ which reveals a resonance of the chassis nearby $\bar{\omega}_T = 6 \Leftrightarrow \Omega = \omega_T / 6$.

Finally, the question arises to the effect of higher-order terms in the expansions to ε. Assuming for example an expansion for the lead-lag modes of form:

$$\begin{cases} d_0 = d_{00} + \varepsilon d_{01} + \varepsilon^2 d_{02} + \ldots \\ b_0 = b_{00} + \varepsilon b_{01} + \varepsilon^2 b_{02} + \ldots \end{cases} \tag{F.60}$$

in the approximation $O(\alpha_m^0)$ instead of the expansion (F.28), it can be demonstrated that the lead-lag equations of motion (F.26) extended to include the terms d_{02} and b_{02} in the approximation $O(\varepsilon^2)$ respectively contain the terms $\varepsilon^2 \cos\psi b_{01}$ and $\varepsilon^2 \cos\psi d_{01}$. Since the response in b_{01} and d_{01} include the harmonics $\cos\psi$ and $\sin\psi$, the above mentioned terms will comprise the harmonics $\cos 2\psi$ and $\sin 2\psi$. Thus the lead-lag response (F.26) in the approximation $O(\varepsilon^2)$ in b_0 and d_0 will contain terms proportional to $\varepsilon^2 \cos 2\psi$ and $\varepsilon^2 \sin 2\psi$. These harmonics will be transmitted to the chassis equation of motion in the

expansion of order $O(\alpha_m{}^1)$ via the differential lead-lag mode in terms proportional to $\alpha_m b'_0 \sin\psi$, $-\alpha_m b'_0 \cos\psi$, $-\alpha_m b_0 \sin\psi$ and via the collective in a term proportional to $\alpha_m \varepsilon d_0 \sin 2\psi$ as seen in equation (F.35). It follows that the chassis equation of motion will contain terms in $\alpha_m \varepsilon^2 \cos\psi$, $\alpha_m \varepsilon^2 \sin\psi$, $\alpha_m \varepsilon^2 \cos 3\psi$, $\alpha_m \varepsilon^2 \sin 3\psi$ and, also considering the terms in ε^2 in the chassis equation (F.36), it can be demonstrated that the chassis response η_1 will also contain the harmonics $\cos\psi$, $\sin\psi$, $\cos 3\psi$ and $\sin 3\psi$. Therefore, the approximation $O(\varepsilon^2)$ introduces the harmonics $\cos\psi$, $\sin\psi$, $\cos 3\psi$ and $\sin 3\psi$ in the chassis response (F.53):

$$\eta \quad \sim \alpha\varepsilon^2 \sin\psi \ , \quad \sim \alpha\varepsilon^2 \cos\psi \ , \quad \sim \alpha\varepsilon^2 \sin 3\psi \ , \quad \sim \alpha\varepsilon^2 \cos 3\psi \tag{F.61}$$

Concluding, extending the expansion in α_m, introduces higher even harmonics $\cos 4\psi$, $\sin 4\psi$, $\cos 6\psi$, $\sin\psi$, $\cos 8\psi$, ... and resonances in the vicinity of rotational velocities $\Omega=\omega_T/4$; $\Omega=\omega_T/6$....in the chassis response (F.53). Extending the expansion in ε introduces odd harmonics $\cos\psi$, $\sin\psi$, $\cos 3\psi$, $\sin 3\psi$, ... in the chassis response (F.53) but it does not introduce new resonance regions.

Appendix G

Floquet Transition Matrix Method

The stability of a system of ordinary linear differential equations having periodic coefficients may be determined by applying the theory of **Floquet** [1923]. The technique consists basically of finding the eigenvalues of the so-called "Floquet transition matrix". The Floquet transition matrix relates the values of the state variables at the beginning and the end of the period.

Consider the system of linear equations with periodic coefficients:

$$\left[M(\psi) \right] \left\{ \chi \right\}'' + \left[C(\psi) \right] \left\{ \chi \right\}' + \left[K(\psi) \right] \left\{ \chi \right\} = \left\{ F(\psi) \right\} \tag{G.1}$$

where the coefficient matrices $M(\psi)$, $C(\psi)$, $K(\psi)$ and $F(\psi)$ are periodic with period $\psi_T = 2\pi$ (this is the most general case for helicopter and wind turbine rotor dynamics). To find the general solutions, one needs first to transform the system (G.1) into the equivalent homogenous system:

$$\left\{ x \right\}' = \left[S(\psi) \right] \left\{ x \right\} \tag{G.2}$$

in which:

$$\left\{ x \right\}' = \begin{Bmatrix} \chi \\ \chi' \end{Bmatrix} \; ; \; \left[S(\psi) \right] = \begin{bmatrix} [0] & [I] \\ -[M]^{-1}[K] & -[M]^{-1}[C] \end{bmatrix} \tag{G.3}$$

The Floquet transition matrix [Q] of system (G.2) is defined by the matrix equation:

$$\left\{ x(\psi_T) \right\} = \left[Q \right] \left\{ x(0) \right\} \tag{G.4}$$

Relation (G.4) can be extended to the form:

$$\left\{x(\psi_T)\right\} = \begin{Bmatrix} Q_{11} \\ \dots \\ Q_{N1} \end{Bmatrix} x_1(0) + \begin{Bmatrix} Q_{12} \\ \dots \\ Q_{N2} \end{Bmatrix} x_2(0) + \dots + \begin{Bmatrix} Q_{1N} \\ \dots \\ Q_{NN} \end{Bmatrix} x_N(0) \tag{G.5}$$

The column $\{x(\psi_T)\}$ corresponding to the initial conditions

$$x_k(0) = \begin{cases} 1 & k=i \\ 0 & k\neq i \end{cases} \tag{G.6}$$

is identical to the i-th column of [Q]. By numerically integrating the equations of motion (G.2) through one period for N sets of initial conditions defined by (G.6) for i=1..N, it is possible to generate the N columns of the transition matrix . Then, the eigenvalues Λ_k of the [Q] matrix can be found (they are usually complex eigenvalues). These eigenvalues are related to the eigenvalues of matrix $S(\psi)$ in the various modes, through the equation:

$$\Lambda_k = e^{(\sigma_k + i\bar{\omega}_k)T} \tag{G.7}$$

Thus, the real and imaginary components of the system eigenvalues may be determined from:

$$\sigma_k = \frac{1}{2\psi_T}\ln\left(\Re(\Lambda_k) + \Im(\Lambda_k)\right) \quad ; \quad \bar{\omega}_k = \frac{1}{\psi_T}\text{atan}\left(\frac{\Im(\Lambda_k)}{\Re(\Lambda_k)}\right) \tag{G.8}$$

Since atan is a multivalued function, each frequency ω_k may only be determined for a basic frequency plus or minus an integer multiple of Ω.

Concluding, the main task in the Floquet theory is to determine the transition matrix [Q]. This is not an easy task, realizing that for N equations, N integration passes are required and for large systems this may require excessive computing time. To overcome this inefficiency, **Kaza and Hammond** [1976][56] developed an algorithm which allows to determine the Floquet transition matrix with a single integration pass only. The algorithm makes use of the Runge-Kutta method and gives the response as:

$$\left\{ x_{i+1} \right\} = \left[H(\psi_i) \right] \left\{ x_i \right\} \tag{G.9}$$

The matrix $H(\psi_i)$ can be determined as:

$$\left[H(\psi_i) \right] = \left[I \right] - \frac{h}{6}\left[S(\psi_i) \right] - \frac{h}{3}\left(1 - \frac{1}{\sqrt{2}}\right)\left[E(\psi_i) \right] - \frac{h}{3}\left(1 + \frac{1}{\sqrt{2}}\right)\left[F(\psi_i) \right] - \frac{h}{6}\left[G(\psi_i) \right] \quad \text{(G.10)}$$

$$\left[E(\psi_i) \right] = \left[S\left(\psi_i + \frac{h}{2}\right) \right] \left\{ \left[I \right] - \frac{h}{2}\left[S(\psi_i) \right] \right\} \quad \text{(G.11)}$$

$$\left[F(\psi_i) \right] = \left[S\left(\psi_i + \frac{h}{2}\right) \right] \left\{ \left[I \right] - \left(-\frac{1}{2} + \frac{1}{\sqrt{2}} \right) h \left[S(\psi_i) \right] - \left(1 - \frac{1}{\sqrt{2}}\right) h \left[E(\psi_i) \right] \right\} \quad \text{(G.12)}$$

$$\left[G(\psi_i) \right] = \left[S\left(\psi_i + \frac{h}{2}\right) \right] \left\{ \left[I \right] + \frac{1}{\sqrt{2}} h \left[E(\psi_i) \right] - \left(1 + \frac{1}{\sqrt{2}}\right) h \left[F(\psi_i) \right] \right\} \quad \text{(G.13)}$$

The Floquet transition matrix can be then easily determined by writing:

$$\left[Q \right] = \left[H(T-h) \right] \left[H(T-2h) \right] \ldots \left[H(h) \right] \left[H(0) \right] \quad \text{(G.14)}$$

Appendix H

An Outline Survey on Helicopter Rotor Blade Structural Couplings

The present appendix presents the effects of structural couplings as defined in section 3.4 of chapter 3 on the couplings between the rotor and rotor-body degrees of freedom.

H.1 Flap-Lag Coupling (Elastic Coupling)

Ormiston and Hodges [1972][78] defined for a rigid blade a so-called "degree of elastic coupling parameter R" by dividing the flap and lead-lag hinge springs into two separate spring systems, one inboard and one outboard from the pitch-axis:

- R = 0 corresponds to a soft hub with all the bending flexibility concentrated in the hub (bending inboard the pitch);
- R = 1 corresponds to a stiff hub with all the bending flexibility distributed in the blade (bending outboard the pitch);
- combinations of a soft hub and flexible blades are characterized by values of flap-lag coupling between 0 and 1.

They observed that according to the value of R, there are essential dynamic differences between rotors with the feathering hinge attached to the hub and rotors for which part of the bending deflections occur inboard of the feathering hinge. For example, in helicopter design, Westland, Bell and Lockheed generally choose for a soft flapwise hub, whereas Bölkow/Vertol choose for a stiff flapwise hub in soft flapwise rotors. The effects of the elastic coupling on the stability characteristics depend on the blade natural lagging frequency. In this respect, Ormiston and Hodges demonstrated that in hovering flight the soft- and stiff-inplane rotors show a different behaviour as to elastic coupling: while for the soft-inplane configurations distinction between a soft or a stiff hub is of little concern, for stiff-inplane configurations flap-lag coupling effects are larger and more varied. A small flap-lag coupling may produce lead-lag mode instabilities while a large elastic coupling is usually highly stabilizing (see Figure H.1). Looking at this figure it appears that the stiff-inplane rotors are very sensitive to flap-lag coupling variation, and therefore, in these systems, the designer must carefully choose the flap-lag coupling.

Peters [1975][90] extended the previous analysis from hovering to forward flight showing that as the advance ratio is increasing, the inflow decreases, and hence, both the soft- and stiff-inplane rotors with low flap-lag coupling are destabilized. Although the advance ratio introduces periodic coefficients in the flap and lag equations of motion, no parametric instabilities were found.

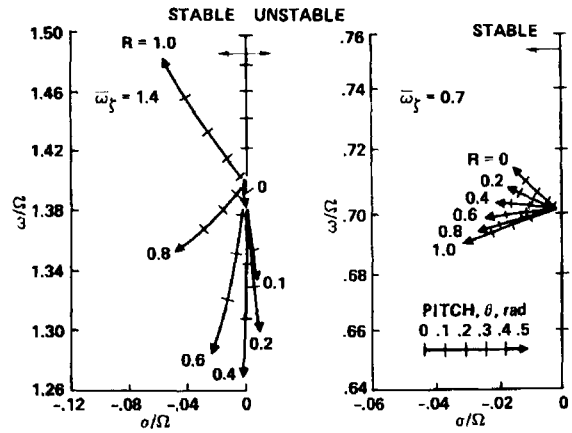

*Figure H.1 Effect of Flap-Lag Coupling in a Soft- and Stiff-Inplane Rotor (**Ormiston and Hodges** [1972][78])*

Burkam and Miao [1972][11] extended the previous analysis from an isolated rotor to coupled rotor-body air resonance characteristics in a soft-inplane hingeless rotor model. The placement of the pitch hinge is a critical parameter for the stability characteristics: with the pitch hinge inboard of the flap flexure (stiff hub), a favourable pitch-flap coupling (see section H.2) occurred, which increased the stability with collective pitch until the steady induced-drag term became dominant at high collective; with the pitch bearing outboard of the flap flexure (soft hub), the favourable couplings available within the practical helicopter manoeuvre range were eliminated. Therefore, from a design trade-off standpoint, inboard pitch hinge placement is favoured over the outboard position for a soft-inplane case. The authors only investigated thrusts of 1g, but underlined that thrusts other than 1g should be examined because, with thrust changes, the collective pitch and coning angles change, leading to important changes in the structural couplings, particularly with the hinge sequence of feathering-flap-lag.

H.2 Pitch-Flap Coupling

Section 3.4 of Chapter 3 defined the way in which the pitch-flap coupling may be introduced in an articulated and a hingeless rotor. In hingeless rotors, the pitch-flap coupling is characterized by a pitch-flap coupling parameter $K_{P\beta}$ defined as the slope of pitch versus flap curve $K_{P\beta} = \frac{\partial\theta}{\partial\beta}$; in articulated rotors the pitch-flap coupling is introduced by an inclination of the flapping hinge with an angle δ_3 (see Figure 3.6) from where the name of "δ_3 hinge" for the pitch-flap coupling in articulated rotors and is defined as $K_{P\beta} = -\tan\delta_3$. The present section reveals the way in which the pitch-flap coupling affects the rotor and rotor/body characteristics. Remember that a positive pitch-flap coupling (negative δ_3) in this dissertation corresponds to flap up with pitch

up or flap down with pitch down. This sign convention is not standard used in the literature and therefore can result in ambiguous interpretations.
Morduchow and Hinchey [1950][74] presented for an articulated rotor helicopter early design criteria on the pitch-flap coupling for a hovering helicopter. The effects of the pitch-flap coupling on the flapping and lagging degrees of freedom concern primarily the blade flapping frequency, and secondarily the damping of the lead-lag mode: as δ_3 decreases to negative values (i.e. flap down with pitch down), the flapping frequency decreases and the damping in lagging increases. For very small negative values of δ_3, the flapping motion diverges. Therefore, the designer, is advised to adjust δ_3 to positive values (flap up with pitch down) in order to avoid flapping divergence but, to not forget that by doing this, the damping in lead-lag decreases.

While the criteria of Morduchow and Hinchey were derived in a steady-state flying condition, **Shapiro** [1955][93] investigated the effect of pitch-flap coupling in two transient helicopter conditions: a sudden application of the collective pitch and a power failure. During the transient response to a sudden application of collective pitch, due to the increasing lift on the blades, the blades coned upwards and transmitted an increased thrust force to the rotor. The presence of a pitch-flap coupling reduced the transient increase of lift because upward coning is associated with an automatic reduction in pitch. The pitch-flap coupling therefore acted as a "lift equaliser". With regard to the design criteria on pitch-flap coupling, Shapiro recommended to use a negative but small pitch-flap coupling (for instance 0.4 corresponding to pitch up with flap down). Large pitch-flap coupling prevent the application of transient thrust and, therefore reduce the manoeuvrability of the helicopter. In the case of a power failure, Shapiro demonstrated that the pitch-flap coupling had a favourable influence as well. The transient behaviour of the rotor in the first two to three seconds after the power failure are of great importance. To continue in autorotational flight, the collective pitch of the rotor had to be adjusted to the requirements of such flight, and in most helicopter rotors a considerable reduction was required. Before this reduction takes place, the rotor slowed down and the resultant diminished coning caused an automatic reduction of pitch.

Because pitch-flap coupling affects primarily the flapping characteristics, it follows that the flying qualities will also be strongly affected by this parameter. Some of the positive effects on the helicopter's flying qualities introduced by a well-chosen pitch-flap coupling are: *control and gust sensitivity** are reduced, the rotor *angle-of-attack instability** is diminished, the *control cross-coupling** is changed. **Wright and Lappos [1979]**[102] reported that the integration of a positive δ_3 in the design of the articulated Sikorsky S-76, was of great importance. The use of the pitch-flap coupling suppressed the gust response (with a minimum horizontal stabilizer area) and reduced the pitch-to-roll coupling, improving the helicopter's control response and stability.

For a hingeless rotor, one of the first investigations on the effects of pitch-flap coupling was given by **Ormiston and Hodges** [1972][78]. Looking for favourable pitch-flap couplings in soft- and stiff-inplane hingeless configurations in hover, they concluded

that while soft-inplane configurations are almost insensitive to the variation of the pitch-flap coupling, stiff-inplane rotors are very sensitive to this parameter. For a soft-inplane rotor, a negative pitch-flap coupling is desirable (i.e. flap up with pitch down); for a stiff-inplane rotor, a variety of different kinds of behaviour exists, depending on the flap-lag coupling R (see Figure H.2). The most critical configurations are the combinations of a stiff-inplane rotor with a soft hub (for R = 0.2, positive and negative pitch-flap couplings should be used). For these rotors, care should be taken to prevent the flap and lag blade frequencies from becoming too close, leading to resonance. For elastic couplings R ≥ 0.4 (configurations of stiff-inplane rotor and stiff hub combinations), positive pitch-flap couplings (i.e. pitch down with flap up) are stabilizing.

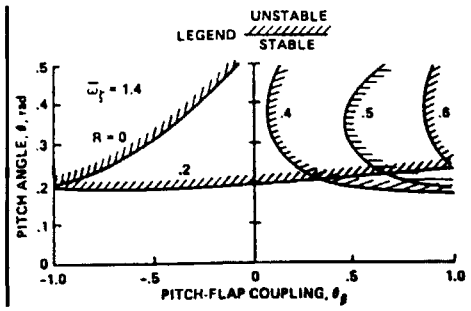

*Figure H.2 Flap-lag Stability Boundaries Dependence on the Pitch-Flap Coupling for a Stiff-Inplane Rotor (**Ormiston** [1977][79])*

Peters [1975][90] extended Ormiston's conclusions for a stiff-inplane rotor, investigating the effect of advance ratio on pitch-flap coupling. When in hover, the effect of pitch-flap coupling on the flapping and lagging modes is strongly dependent on the elastic coupling; in forward flight, negative pitch-flap coupling (i.e flap up with pitch down) is generally destabilizing. At advance ratios of around 0.4, an instability appeared (this was demonstrated even for an articulated rotor), but, this instability was mild and a moderate amount of lead-lag damping was still sufficient to stabilize the motion.

The combination of pitch-flap coupling and hub flexibility not only reflects in the isolated rotor characteristics, but it also has consequences for the coupled rotor-body motion. This is especially the case with stiff-inplane rotors, where the pitch-flap coupling is very sensitive to the variation of other parameters in the system. Two examples from the literature will be mentioned, one reporting a lead-lag blade instability, the other a coupled rotor-body instability, both in stiff-inplane/soft hub configurations:

Johnston [1971][54] described the "half-P-hop" lead-lag blade instability of the stiff-inplane/soft hub Lockheed AH-56A Cheyenne that occurred during high-speed forward flight. The adverse positive pitch-flap coupling used in the beginning of the design contributed to the intensity of the instability. The instability was partly eliminated by

changing the positive pitch-flap coupling of 0.22 to about zero.
The second example, described by **Anderson** [1973][2], refers to the rotor-body instability of the reactionless lead-lag mode in the stiff-inplane/soft hub rotor of the Lockheed AH-56A encountered at low speed and high lift. This instability was actually caused by the increased adverse pitch-lag coupling, but, the pitch-flap coupling was also contributing to the instability. In this case, changing the pitch-flap coupling from zero to negative values had a destabilizing effect.

For stiff-inplane/stiff hub configurations, positive pitch-flap coupling (i.e. flap up with pitch down) should be used to stabilize the motion. But, one should not forget that, by doing this, there is a danger that the flap and lead-lag blade frequencies become too close to each other, leading to resonance. This was the case reported by **Gaffey** [1963][35] for a proprotor in axial flight. Proprotors are stiff-inplane/stiff hub configurations and therefore, at first, a positive pitch-flap coupling (flap up with pitch down) was incorporated in the design, in the belief that this was favourable for this type of system. The result obtained was opposite. This instability could only be explained by realizing that the amount of positive pitch-flap used was too high, inducing static flap divergence. The proprotor requires large pitch settings in axial flight, and this led to a strong reduction of the blade lead-lag frequency to a value which nearly coincided with the flap frequency.

Pitch-flap coupling in a hingeless rotor may be adjusted by modifying the blade geometry. In practice, the designer may use so-called "geometric parameters" which, although small in magnitude, have a strong influence on the degree of coupling between the blade flap-lag-and-torsion degrees of freedom. As to pitch-flap coupling, **Huber** [1973][52] described how this coupling may be adjusted by two geometric parameters: sweep and precone (see also sections H.4.1 and H.4.3) . This practical technique was used for the Bölkow Bö-105 in order to change the dynamic flight behaviour. It was demonstrated that even as small a change as 15° in equivalent δ_3 angle for the Bö-105 helicopter flying at 100 knots reduced the angle-of-attack instability by 40%. This technique is very important, because by properly combining the structural couplings via the design parameters, the design may be adapted exactly to the customer's requirements and more freedom can be gained in the design process. Also, although the selection of the flap frequency is normally subject to certain limitations and is often impractical beyond a certain point, a higher margin may be gained by using the aeroelastic coupling effects.

H.3 Pitch-Lag Coupling (Pitch-Lead Coupling)

Section 3.4 of Chapter 3 defined the way in which the pitch-lag coupling may be introduced in an articulated and a hingeless rotor. In hingeless rotors, the pitch-lag coupling is characterized by the pitch-lag coupling parameter $K_{P\zeta}$ defined as defined as the slope of pitch versus lag curve $K_{P\zeta} = \frac{\partial\theta}{\partial\zeta}$; in articulated rotor the pitch-lag coupling

is introduced by an inclination of the lagging hinge with an angle α_2 or δ_1 (see Figure 3.7) from where the name of "α_2 hinge" or "δ_1 hinge" for the pitch-lag coupling in articulated rotors and is defined as $K_{P\zeta} = + \tan\alpha_2$ or $K_{P\zeta} = + \tan\delta_1$. It is assumed that a positive pitch-lag coupling (i.e. positive α_2 or δ_1 hinge) corresponds to a pitch down with lag or pitch up with lead. The effects of the pitch-lag coupling on the aeroelastic and flight mechanics helicopter stability characteristics are summarized below.

For an articulated rotor, **Morduchow and Hinchey** [1950][74], investigating the influence of pitch-lag coupling on the flapping and lagging characteristics of an articulated rotor in hover, showed that pitch-lag coupling primarily affects the blade lead-lag damping and secondly the flapping damping: by decreasing δ_1 to negative values (i.e pitch up with lag), the damping in lead-lag increases, but the damping in flap decreases. In answer to the question on how the designer should use the pitch-lag coupling, their recommendation was to adjust δ_1 to negative values (i.e lag back with pitch up) but not to forget that by doing this, the damping in lead-lag is increased and the damping in flap is decreased.

The lead-lag mode is characterized by small damping and therefore, in case of an instability, this mode very quickly becomes unstable. Probably the first reported case of instability caused by the adverse pitch-lag coupling was a flap-lag instability reported by **Chou** [1958][18] for an articulated rotor. The instability was due to the adverse control-linkage mechanism which induced an adverse pitch-lag coupling in the system (the flap-lag instability is also called pitch-lag instability because it appears due to the adverse pitch-lag coupling in the system). **Chou** [1958][18] developed a stability criterion with respect to the minimum lead-lag damping required for stability. The lead-lag damping was derived as a function of pitch-lag coupling and coning angle. It was demonstrated that the damping in lagging decreases as the coning angle increases and that negative pitch-lag coupling is stabilizing (i.e pitch up with lag). **Blake et. al.** [1961][8] demonstrated that Chou's stability criterion is unconservative if - besides the pitch-lag coupling - negative pitch-flap coupling is included in the model.

Note that pitch-lag coupling mainly affects the damping in lead-lag motion, thus being important for the helicopter's aeroelastic stability. Once such instabilities are avoided, the effect of pitch-lag coupling on the flying qualities is usually not substantial. In contrast, pitch-flap coupling always affects significantly the flying qualities. Commenting on the influence of the pitch-lag instability on the flying characteristics, **Blake et al.** [1961][8] considered that it takes a reasonable amount of time before the pilot reacts to a flap-lag instability and, therefore, this instability is not likely to cause flight failures (in fully articulated rotors). The strong dependency of this instability on the coning angle suggests that, once he recognizes the situation, the pilot could get into a stable regime by quickly dropping collective pitch. The authors also drew attention to the fact that the lead-lag dampers frequently have non-linear characteristics (with regards to the damping force for a given lagging velocity) and therefore, a prior

knowledge of the steady or transient lagging velocity should be available in order to predict the instability in forward flight.

Hohenemser and Perisho [1958][44] presented a test case of an articulated rotor in which the use of a positive pitch-lag coupling was destabilizing. This behaviour opposite to the previous cases resulted from the different value of the blade lead-lag frequency. Usually, an articulated rotor is soft-inplane, but the test rotor used in this paper was a stiff-inplane rotor. Also in this case, Chou's criterion was unconservative. **Kaza and Kwatemik** [1979][57] demonstrated that the pitch-lag coupling depends not only on the lead-lag frequency, pitch-flap coupling or coning angle, but the order in which the flap and lag hinge are situated is a critical parameter as well.

For a hingeless rotor, **Ormiston and Hodges** [1972][78] and later **Hodges and Ormiston** [1976][40] developed criteria concerning the pitch-lag coupling $K_{p\zeta}$ to be applied in a hingeless rotor in hover. As with articulated rotors, pitch-lag coupling in the first place affects the blade lead-lag damping and in the second place, the flapping damping (see Figure H.3). However, compared to an articulated configuration, a hingeless rotor presents a variety of behaviours, depending primarily on the lead-lag frequency (soft/stiff distinction) and secondly on the elastic coupling (soft/stiff hub). For soft-inplane rotors, negative pitch-lag coupling (lag back with pitch up) stabilizes the motion. For stiff-inplane rotors, depending on the flap-lag coupling parameter, a variety in behaviour is observed, as seen in Figure H.3: in a stiff-inplane/soft hub rotor, positive pitch-lag coupling should be used, in a stiff-inplane/stiff hub rotor, negative pitch-lag coupling should be used, in a stiff-inplane rotor with elastic coupling between [0.1; 0.3] either positive or negative pitch-lag coupling may be used.

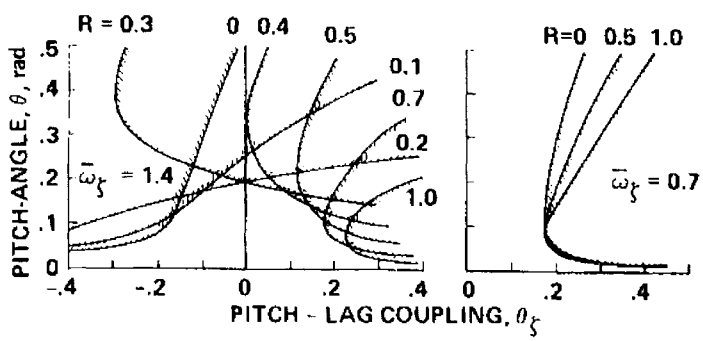

*Figure H.3 Flap-Lag Stability Dependence on the Pitch-Lag Coupling for Soft and Stiff-Inplane Parameters (**Ormiston and Hodges** [1972][78])*

Peters [1975][90] extended the conclusions of Ormiston and Hodges [1972][78] from hovering to forward flight. For a stiff-inplane rotor, the qualitative trends in pitch-lag

coupling are not affected by the advance ratio, but, for a soft-inplane rotor, the effects of pitch-lag coupling can be reversed from hover to forward flight. Hence, for a soft-inplane rotor, the criterion on the pitch-lag coupling should not be generalized from hovering to forward flight, neither for the isolated rotor nor for the coupled rotor-body motion. At advance ratios of 0.4 instabilities were encountered for negative pitch-lag coupling. The level of lead-lag damping for a soft or stiff-inplane hingeless helicopter may be augmented by using the pitch-flap and pitch-lag couplings. In turn, the pitch-flap and pitch-lag couplings may be augmented by adjusting the different geometrical parameters, as witnessed for the pitch-flap coupling. It has already been shown in this literature survey that stiff-inplane rotors are very sensitive to the different structural couplings which may lead to different rotor instabilities in these rotors. The soft-inplane rotors, although not so much exposed to structural couplings variation, are dangerously sensitive to rotor-body instabilities such as ground and air resonance. Therefore, adjusting the flap-lag, pitch-flap and pitch-flap couplings in the system through the blade geometric parameters is a valuable technique for the designer. As a result, the rotor and rotor-body instabilities are counteracted and helicopter flying qualities may be improved.

Huber [1973][52] and **Hodges and Ormiston** [1977][40] used this technique for the isolated rotor, adjusting the pitch-lag coupling by using droop, precone and pre-sweep (see section H.4). **Bousman et al** [1976][9] used the pitch-lag and elastic coupling to augment the low level of lead-lag damping for a soft-inplane rotor, first for an isolated blade and next for the rotor-body motion. **Ormiston** [1977][79] used the same technique to counteract the air resonance of a soft-inplane rotor. He demonstrated that - although some couplings were very effective at zero-pitch-angle for the isolated blade - for the rotor-body case, they were destabilizing. These conflicting trends in the pitch-flap and pitch-lag couplings were also reported by **Bousman** [1981][10] who simulated the air resonance condition for low and high pitch angles (0^o and 9^o): at zero-pitch-angle, pitch-lag coupling was actually destabilizing; at high pitch angle, the combination pitch-lag and pitch-flap coupling was stabilizing, although not sufficient to eliminate the roll mode instability.

Hence, the designer should bear in mind that the effects of structural couplings on the isolated rotor are not necessarily a valid indication on how they will affect the coupled rotor-body motion. This was the problem with the stiff-inplane/soft hub rotor of the Lockheed AH-56A. **Anderson** [1973][2] reported a rotor-body instability of the scissors mode (inplane reactionless mode) caused by the increased adverse pitch-lag coupling due to the large coning angle at the high lift condition. For the isolated blade, a positive pitch-lag coupling was used in order to stabilize the motion caused by the negative droop, but in the coupled rotor-body motion, this pitch-lag coupling became overcompensated by a high coning angle at high lift. As a general recommendation for a soft-inplane rotor, one should always use some degree of negative pitch-lag coupling to avoid ground and air resonance.

Hodges and Ormiston [1977][40] derived an analytical expression for the blade pitch-lag coupling including precone β_{pc}, droop β_d, blade pitch-link flexibility f and blade torsional stiffness K_Θ distribution of torsion stiffness between the blade K_ϕ and the pitch control system K_Φ:

$$K_{P\zeta} = \frac{1}{K_\Theta}\left\{-\frac{\gamma}{8\nu_\beta^2}\left(K_\zeta - K_\beta\right)\left(\theta_0 - \phi_i\right) + \frac{\left(K_\zeta - K_\beta\right)}{\nu_\beta^2}\beta_{pc} - \left(\frac{K_\zeta - K_\beta}{\nu_\beta^2} - \frac{K_\zeta}{1+f}\right)\beta_d\right\} \qquad \text{(H.1)}$$

where K_ϕ is the rigid blade torsional spring stiffness, K_Φ is the rigid blade pitch-link spring stiffness, $K_\Theta = \dfrac{K_\Phi K_\phi}{K_\Phi + K_\phi}$ is the rigid blade total torsion equivalent spring stiffness, $f = \dfrac{K_\Phi}{K_\phi}$ is the pitch-link flexibility defined as the ratio of pitch-link stiffness to blade elastic torsion stiffness, K_ζ the lead-lag bending stiffness, K_β the flapping bending stiffness, θ_0 blade root pitch angle , ϕ_i rigid blade induced inflow angle, ν_β the flapping frequency, β_{pc} the precone angle , β_d the droop angle.

H.4 Geometric Parameters of Hingeless Rotor Blade

The main geometric parameters in a hingeless rotor through which the blade frequency and damping characteristics may be varied may be seen in Figure 3.8 of Chapter 3.

H.4.1 Precone angle

In a hingeless configuration, the precone angle is a fixed angle built into the blade roots of hingeless rotor blades to place them in a fixed coning position independent of lift or centrifugal forces. Introducing precone, the values of blade coning angle will change. Since the precone influences the equilibrium blade coning angle, it strongly affects the structural couplings in the system, especially the pitch-lag coupling. In practice, precone angle has been used to reduce blade stress. In general, precone controls:

- pitch-lag coupling According to (H.1), the effect of precone on the pitch-lag coupling are given by a term $K_{P\zeta}|_{\beta_{pc}} = \dfrac{1}{K_\Theta}\cdot\dfrac{\left(K_\zeta - K_\beta\right)}{\nu_\beta^2}\beta_{pc}$. Also, from (H.1) one should observe that the effect of pitch and precone on the pitch-lag coupling are of opposite sign. At low pitch angles, a high precone angle thus causes a positive pitch-lag coupling which is usually adverse, favouring instability as demonstrated above. These instabilities appearing at low pitch angles and caused by precone is called "precone instability". In contrast, low precone angle causes a negative pitch-lag coupling, thus favourable for the blade which increases the blade inplane stability and air resonance characteristics. For example, for the Bö-105, a 5° precone is less stable than a 2.5° precone configuration and the 0° precone case is even better. For different manoeuvre levels, high precone

degrades the favourable pitch-flap coupling. For the Bö-105, for example, a 0° precone rotor adds about 5% damping ratio as compared to a 2.5° precone. For *matched stiffness blade configurations** ($K_\zeta=K_\beta$), looking at (H.1), neither pitch nor precone generate pitch-lag coupling. This explains the virtual absence of instabilities for matched hingeless rotors.

- pitch-flap coupling **Burkam and Miao** [1972][11] demonstrated that precone controls directly the Coriolis coupling of the blade (that is if a flapping-up velocity produces a nose-up or nose-down pitch moment) by controlling the aerodynamic coning angle. In a soft-inplane configuration, precone less than the total cone angle relieves the blade root from the flapping moment and gives a positive aerodynamic coning angle which consequently produces a favourable pitch-flap coupling (flap-up pitch-down moment). Using a too high precone (built-in pitch axis above equilibrium coning angle) in a soft-inplane configuration results in an adverse pitch-flap coupling (this is because with overprecone, the aerodynamic coning angle resulted is negative producing consequently an adverse pitch-flap coupling (see section H.2).

Hence, too high precone (built-in pitch axis above equilibrium coning angle) introduces both unfavourable pitch-flap and pitch-lag coupling. Low or negative precone (built-in pitch axis below equilibrium coning angle) is in general recommended for improved air resonance stability. This conclusion was also confirmed during the beginning of hingeless rotor design at Aerospatiale. **Gallot** [1969][36] reported that the use of excessive precone in Aerospatiale soft-inplane hingeless rotor experiments created a lot of difficulties for the designer. Accordingly, he recommended the designer to use precone in soft-inplane rotors with caution.

Huber [1973][52], searching for changing the pitch-flap coupling in the soft-inplane Bölkow Bö-105, demonstrated that precone and pre-sweep have equal effect on the pitch-flap coupling (called δ_3-change). However, blade precone is not as δ_3- active as blade pre-sweep. For the Bö-105 a δ_3-change of 12° per degree sweep angle was equivalent to a δ_3- change of only 6° per degree precone angle. Since the total coning angle (given by summing precone and aerodynamic coning) is fixed for a certain thrust condition, the influences of precone and thrust are supplementary: low precone acts like high thrust and vice versa. **Hodges and Ormiston** [1977][40] this time compared the effects of precone to the droop and found that, depending on pitch-link flexibility, precone and droop had either identical or very different effects on the flap-lag-torsion stability boundaries. **Sharpe** [1986][94] also illustrated both theoretically and experimentally how combining the precone and droop parameters may be used to augment the level of lead-lag damping in a stiff-inplane/stiff hub rotor. **Yeager et. al.** [1983][103] conducted a wind-tunnel test of a soft-inplane hingeless rotor with body and pitch motion. The measurements showed the favourable influence of either precone or negative droop on the stability. **Peters** [1975][90] demonstrated that, qualitatively, precone has the same effect in forward flight as in hover.

H.4.2 Droop (Pre-flap) Angle

Droop angle can be defined as a constant built-in angle in the same plane as the precone angle (see Figure 3.8). The effect of droop angle on the general stability characteristics was investigated by **Hodges and Ormiston** [1977][40] in a stiff-inplane configuration. Droop, just as precone may be used to control the pitch-lag coupling. Looking at (H.1), the effect of precone on the pitch-lag coupling is given by a term $K_{p\zeta}|_{\beta_d} = -\frac{1}{K_\Theta} \cdot \left(\frac{K_\zeta - K_\beta}{\nu_\beta^2} - \frac{K_\zeta}{1+f}\right) \beta_d$. The effect of droop on the pitch-lag coupling is more complex that the effect of pitch or precone. There are two droop terms, one similar to the precone term and one depending only on the lead-lag bending stiffness K_ζ and the pitch-control flexibility f (see also section H.5). Droop angle alone is not as effective as precone:

- when the pitch-link is rigid ($f = \infty$), the effect of droop is similar to negative precone;
- as pitch-link flexibility is introduced, the contribution of droop to pitch-lag coupling depends strongly on the pitch-link flexibility: the effect of droop decreases with increasing pitch-link flexibility. For very low values of f, the sign of the pitch-lag coupling due to droop will change and result in instability at negative blade pitch angles. In the case of the stiff-inplane rotor used by Hodges and Ormiston, negative droop generated a destabilizing positive pitch-lag coupling.

Even for *matched stiffness configurations**, the blade droop generates a pitch-lag coupling and therefore according to section H.3, a lead-lag instability can result for a positive droop angle.

H.4.3 Sweep (Prelag) Angle (forward sweep=pre-sweep)

Sweep angle can be defined as a fixed built-in angle in the disc plane (see Figure 3.8). Investigating the effect of blade pre-sweep on a soft-inplane rotor, **Huber** [1973][52] represented the effect of blade sweep on elastic pitch-flap-lag coupling as seen in Figure H.4. The sweep angle can be used to control:

- pitch-flap coupling. Using forward blade sweep, the pitch is increased when the blade flaps up (see Figure H.4) which is equivalent to a positive pitch-flap coupling (according to the sign convention of section H.2). Using rearward blade sweep, due to the relief of the centrifugal force moment, the mean lead-lag moment is nearly nullified and the total coupling is influenced by the alternating flap and lead-lag terms. As both blade motions are 180° out of phase, the pitching motion is in phase with flapping motion, as opposed to the previous case, indicating a negative pitch-flap coupling (positive δ_3-effect). Therefore,

forward sweep results in negative δ_3 angles, rearward sweep in positive δ_3 angle. The author demonstrated that pre-sweep angle had a great impact on flight dynamics behaviour: only small rearward blade sweep is sufficient to make the aircraft stable at a speed of 100 knots.

- pitch-lag coupling. In the case of a forward swept blade, the pitch is reduced when the blade lags back and increased when the blade moves forward. This type of pitch-lag coupling is unfavourable and has a destabilizing influence on the blade lead-lag motion. In contrast, the aft swept blade shows an elastic pitch increase when the blade lags back and a pitch decrease when the blade moves forward. This is a favourable pitch-lag coupling.

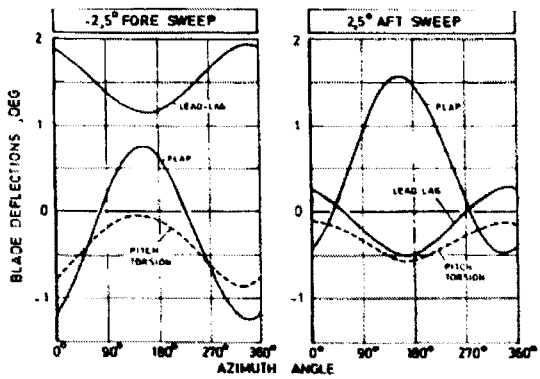

*Figure H.4 Effect of Blade Sweep on Elastic Pitch-Flap-Lag Coupling (**Huber** [1973][52])*

The effect of blade pre-sweep on air resonance for a soft-inplane rotor was investigated by **Burkam and Miao** [1972][11]. Blade sweep both forward and rearward on the critical 4° precone hub had a significant effect on the high collective instability: forward 5° sweep raised the stability region, but lowered the high collective instability boundary; aft 5 degree sweep lowered the stability region but raised and almost eliminated the high collective or fast roll instability. Roll damping was increased by the sweptback blades, giving a δ_3 effect when pitch link flexibility .

H.4.4 Twist Angle

Hodges and Ormiston [1977][40] demonstrated that the twist angle introduces an increment in flap-lag coupling (see section H.1) that varies along the blade and is independent of the blade pitch angle. Pre-twist also influences the distribution of aerodynamic forces along the blade. When blade pre-twist is included in the configuration, the use of structural coupling parameter R becomes ambiguous. (for example R=0 implies that the bending flexibility of the blade outboard pitch bearing is zero, in which case the twist could have no significance in a structural sense). Therefore, it is advisable to eliminate R from the equations by putting R=1. For a stiff-

inplane rotor, blade pre-twist increases flap-lag structural coupling in the region of the blade where most of the bending takes place (because it increases the inclination of the principal flexible axes of the blade cross section at the blade root). Increasing flap-lag coupling significantly increases the lead-lag damping, especially at low blade pitch angles. For a soft- inplane rotor, the effect of pre-twist is less important since the difference between flap and lead-lag mode bending stiffness is smaller.

H.5 Control-System Flexibility

Control-system flexibility increases the couplings in the rotor, and creates the possibility to use the flexibility of the blade to counteract the instabilities. On the isolated blade, the adverse control-system flexibility was responsible for the instability reported by **Hohenemser and Perisho** [1958][44] in the case of an articulated rotor. The adverse control-system flexibility resulted in their case in a pitch-lag instability. **Gaffey** [1969][35] also reported in the case of a tilting prop-rotor, that, when control system flexibility was introduced, the phasing between the flapping and inplane motion changed such that the Coriolis force from the blade flapping tended to increase the inplane motion.

On the coupled rotor-body, the effect of control-system flexibility on air resonance was investigated by **Huber** [1973][52] for the soft-inplane rotor of the Bö-105. The typical influence of control flexibility must be seen in connection with rotor thrust and the resulting aerodynamic coning angle. At low thrust, the blade experiences slightly unfavourable pitch-lag coupling, which results in reduced damping. An extremely soft control system could introduce an instability into this region. Conversely, pitch-lag coupling acts stabilizing in the normal and high thrust region, which results in a considerable damping increase with reduced stiffness. Therefore, a completely rigid control system - even if it would be achievable- is not optimal. It is advisable to introduce some control-system flexibility within the practical helicopter manoeuvre g-range. The effects of control-system flexibility are even more outstanding when other parameters have been optimized: a zero precone rotor, for instance, will take advantage from control-system flexibility. **Burkam and Miao** [1972][11] also investigated the effects of control-system flexibility on the air resonance characteristics, concluding that a stiff control-system minimizes the blade pitch response and improves overall stability. They explained the mechanism of deterioration of air resonance stability at high collective pitch: a steady aerodynamic drag force acting through the blade perturbation flap displacement above the feathering axis produces a destabilizing nose-up pitch moment. An increase in collective pitch increases the steady aerodynamic drag force, consequently increasing the unfavourable coupling. This unfavourable aerodynamic coupling may be minimized by increasing control stiffness, making the blade less responsive in pitch; conversely, a soft control system would degrade stability.

To characterize the distribution of torsion flexibility between the pitch link and the blade the so-called "pitch-link flexibility" f is defined yielding the ratio between blade

pitch-link stiffness and blade torsional stiffness:

$$f = \frac{k_\phi R}{G J} \tag{H.2}$$

where k_ϕ is the pitch-link stiffness, GJ blade elastic torsion rigidity, R blade radius. f = 0 corresponds to pure root torsion (torsionally rigid blade) and f = ∞ to pure elastic torsion (configurations without pitch-link flexibility).

The effects of adding pitch-link flexibility on a stiff-inplane rotor were investigated by **Hodges and Ormiston** [1977][40] . From equation (H.1) it follows that effects of pitch-link flexibility on the rotor characteristics depend firstly on the droop angle and secondly on the torsional stiffness:

- when no droop angle is present, in a blade with torsional frequency ω_ϕ=8, the effect of adding pitch-link flexibility (f decreasing from ∞ to 0) is to reduce the pitch angle at which the lead-lag instability occurred (slightly destabilizing the stiff inplane instability); in a blade with torsional frequency ω_ϕ=5, similar results are observed, except that, for configurations with large pitch-link flexibility (small f), the lead-lag mode instability is eliminated at high pitch angles and a *flap divergence** occurs.
- when droop is present, the effect of pitch-link flexibility is quantitatively different from that of elastic blade torsional flexibility. Blade droop and pitch-link flexibility together can strongly influence blade stability. Without pitch-link flexibility, the effect of negative droop is equivalent to precone. With pitch-link flexibility, droop produces additional effects that can generate instability in *matched-stiffness blade configurations**.

H.6 Chordwise Blade Balance

Miller [1950][70] demonstrated how the designer may tune the rotorcraft's flight dynamics by modifying the chordwise blade balance for an articulated rotor in conjunction with control flexibility. The main parameter that influences elastic blade torsion is the offset between the aerodynamic centre of the blade and its centre of gravity. If the centre of gravity is ahead of the aerodynamic centre, an elastic feathering feedback is introduced which tends to alleviate aerodynamic disturbances- for example, an increase in rotor angle of attack normally increases the lift on the advancing blade and decreases the lift on the retreating blade, resulting in aft tilt of the tip-path-plane. The reaction to the lift increase is mainly observed in the inertial forces centred in the blade centre of gravity. Thus, the advancing blade, because of flexibility, is elastically feathered with the leading edge down and the retreating blade is feathered with the leading edge up, which introduces an elastic forward cyclic pitch that alleviates the aft lift of the tip- path-plane. This process is the same for both articulated and hingeless rotors, but for a hingeless rotor - because of its flap stiffness - the hub moment caused by elastic

feathering is much greater.

Reichert and Huber [1971][92] showed for example that a 3% forward shift of the centre of gravity of the Bö-105 blade would reduce the rotor angle-of-attack instability by 30% at 100 knots and would increase the time to double the amplitude of the phugoid mode from 6 to 40 sec. The Bö-105 blade is relatively soft with a blade torsional frequency 3.4Ω. For blades that are torsionally stiffer (such as those of Lynx) the effects of elastic cyclic pitch feedback are smaller. For soft-flapwise blades, the lift is transferred to the hub mainly via centrifugal forces centred in the centre of gravity; for stiff flapwise blades, this transfer is mainly elastic and centred in the shear axis of the blade cross section. For stiff flapwise blades, the location of the shear axis is more important than that of the chordwise centre of gravity. Chordwise overbalance:

- destabilizes the flap motion and should be used with caution at high advance ratio (because it is a proportional tilting feedback with a phase angle near zero-see feedback systems)
- provides an elastic negative pitch-flap coupling that is beneficial for all aspects of flight dynamics.

Friedmann [1977][32] studied also the effect of aerodynamic centre offset for an elastic blade. The coupled flap-lag-torsional blade stability seems to be insensitive to small amounts of offset (1-2% of the chord) between the aerodynamic centre and the elastic axis. However values of 5% of the chord or more may lead to severe deterioration of both flutter and divergence boundaries. *"Chordwise overbalance is a means of reducing angle of attack instability. To be effective, the control system must be relatively soft. This may introduce other problems in the reversed-flow region at high advance ratio, such as blade flutter or blade torsional divergence, quite apart from the blade weight penalty."(Friedmann [1977][32]).*

Glossary of Helicopter and Wind Turbine-Related Terms

ADS-33 specifications = Aeronautical-Design-Standard handling quality specifications of helicopters elaborated in 1980's

Air resonance = instability caused by the interaction of low-frequency blade flapping and lead-lag modes and rigid-body modes of the airframe (generally the body pitch and roll modes).

Angle-of-attack instability = instability characterized by an increase of the rotor angle-of-attack of major concern in hingeless rotors. To minimize the angle-of-attack instability it is desirable to keep the flap-bending stiffness of the blades, particularly in the root section, as low as possible.

Advancing lead-lag mode instability = instability involving the coupling of the rotating and fixed structure of the wind turbine in the advancing lead-lag mode and the chassis bending modes

Blade kinematic couplings = Couplings between the blade degrees of freedom resulting from the blade kinematics, usually encountered in articulated rotors

Blade structural (elastic) couplings = Couplings between the blade degrees of freedom resulting from the blade flexibility

Chassis = the tower + nacelle system in a wind turbine

Complex plane (s-plane) = The plane in which the abscissa gives the damping in the system and the ordinate the damped frequency

Crosswind = a superimposed wind component that appears in the plane of the rotor (it can be seen as a gust that causes a change in the relative wind direction and magnitude or yaw misalignment)

Control cross-coupling effects = There are three types of cross-coupling: 1) direct control cross coupling effects where a longitudinal control input also produces a rolling moment, and a lateral control input also produces a pitch moment 2) indirect control couplings where changes in angle of attack produce both pitching and rolling moments and 3) a pitch rate produces not only pitch damping but also a pitching moment. All three types of cross coupling depend on the blade flapping frequency and advance ratio

Control sensitivity = the asymptotic pitch or roll rate per unit step control input (values of 14 to 20 deg/sec/inch are specific for helicopters)

Degree of freedom = a mechanical system is said to have one degree of freedom if its

geometrical position can be expressed at any instant by one variable only. Generally if it takes n variables to specify the position in space of a mechanical system, that system is said to have n degrees of freedom.

Divergence = a blade static instability in the pitch direction depending on the distance between the section's centre of gravity and aerodynamic centre, in which the dynamic forces do not play any role

Downwind / Upwind = wind turbine with the rotor placed behind respectively in front of the tower as seen from the main wind direction

Droop = constant built-in angle in the blade flapping plane (see Figure 3.8)

Dynamic instability = a system which possesses a multiplicity of vicious circles through which two or more degrees of freedom mutually "pump" energy into each other. These vicious circles are created by destabilizing forces acting on the system that have components in phase with velocity. In a dynamic instability problem the mechanism of couplings between the system's degrees of freedom is important.

Free (natural) response = the free response of a differential equation is the solution of the equation for an input identical to zero (also called natural response)

Forced response = the forced response of a differential equation is the part of the solution of the differential equation depending on the input only

Flutter = blade instability primarily caused by the coupling of the blade bending and torsion degrees of freedom. For helicopters it can be avoided by mass balancing the blade such that the chordwise position of the centre of gravity is forward of the aerodynamic centre

Flapwise instability = instability of the transient flapping motion of the blade sometimes appearing in helicopters at hight advance ratios and frequently in wind turbines in stall conditions

Flapping divergence = instability of the blade flapping motion in which the dynamic aerodynamic forces play no role: a deflection in the flapping angle always results in large deflections in the flapping direction

Flap-lag instability = rotor instability of a weakly damped lead-lag mode caused primarily by coupling of the blade flapping and lead-lag degrees of freedom

Ground resonance = for helicopters this instability is caused by the coupling between the blade lead-lag motion and the in-plane hub motion. It can be eliminated by placing mechanical lag dampers on the blade. For wind turbines this instability is caused by a

coupling between the asymmetric lead-lag mode and the lateral bending of the tower

Gust sensitivity = the asymptotic pitch or roll rate per unit gust input

Loading problem = problem in which the designer concentrates on the response of the system to different external excitation sources

Lumped flexibility = Assumption in which the flexibility of the blade is assumed as being concentrated in flexible lumps (virtual hinges characterized by a specific offset and spring constant), with the rest of the blade being considered as rigid. This assumption is also called rigid-blade concept.

MIL specifications = handling quality specifications of helicopters elaborated in 1950's

Matched stiffness = blade configuration in which the bending-torsion couplings are minimized as much as possible (torsional deflections resulting from the combined flap and lead-lag bending are minimal). This is achieved by designing a blade with a flapping stiffness equal to the lead-lag stiffness $K_\beta=K_\zeta$.

Natural modes of motion (Eigenmotions) = characteristic motions of the system which change in time but stay directed along their corresponding eigenvectors (the motion variables change but their mutual relation does not change during the motion)

Nap-of-the-Earth (NOE) flight = flight using the terrain to the maximum extent possible to avoid detection. In NOE-flight speed requirement is subordinate to the visual cues.

Operational flight envelope = refers to any envelope within which care-free operation is guaranteed (e.g. n-V diagram)

Pitch-flap coupling = coupling of the blade (of kinematic or structural nature) in which the flapping motion of the blade produces a change in pitch. In an articulated rotor, pitch-flap coupling is introduced by inclining the flapping hinge by a δ_3 angle (from whence originates the name of δ_3-hinge)

Pitch-lag coupling = coupling of the blade (of kinematic or structural nature) in which the lead-lag motion of the blade produces a change in pitch. In an articulated rotor, pitch-lag coupling is introduced by inclining the hinge with an α_2 or δ_1 angle (from whence originates the name of α_2-hinge or δ_1-hinge)

Pitch-flap-lag instability = a coupling between blade flapping, lead-lag and pitch degrees of freedom characteristic to hingeless and bearingless rotors (also called flap-edgewise-torsional flutter)

Poles of motion = solutions of the system characteristic equation (which is equivalent with putting the denominator of the transfer function equal to zero)

Primary (ordinary) resonance = resonance of a dynamic system appearing when the frequency of the external excitation is the same as one of the system's natural frequencies

Pendular (parametric) resonance = resonance of a dynamic system in which the external excitation is acting on the system through the coefficients of the system differential equation

1-P excitation = excitation reaching its maximum once per rotor revolution

Precone angle = constant angle built into the blade roots of a hingeless rotor blade to place the blades in a fixed coning position independent of lift or centrifugal forces (see Figure 3.8)

Twist = difference between root and tip angle of incidence

Rotational sampling = fluctuations of the wind excitation frequencies as seen by a rotating blade caused by the cyclically passing of the blade throughout a wind velocity field that varies over the rotor disc

Speed of decay = the speed at which a transient motion of the system dies out

SAS system = Stability-Augmentation-System

SCAS system = Stability-and-Control Augmentation-System

Sweep = built-in angle in the rotor lagging plane (see Figure 3.8)

Stall flutter = in the classical form, stall flutter only involves torsional oscillations of the blade appearing at large blade angles of attack and non-linear, unsteady aerodynamic

Steady-state response = the response of the system after the transient response has died out

Torsional oscillations = Torsional oscillations of the rotor disc and shaft system as observed in wind turbines, which may occur if the shaft system is sufficiently soft

Transient response = the response of the system which approaches zero as time approaches infinity

Teetering rotor = two-bladed rotor mounted on a single horizontal hinge (the so-called teetering hinge) that allows flapping that is always equal and opposite on the two blades. The teetering hinge is a rigid interconnection between the two blades in the hub, allowing a free teeter of the rotor with respect to the shaft

Time constant = the time constant of a transient motion represents the time in seconds needed for the system to reduce that transient to $e^{-1} = 0.368$ of its initial value

Transfer function = the ratio of the Laplace transformation of the output and input of a dynamic system with initial condition zero

Tower shadow = the wake created by the tower of a wind turbine

Unsymmetrical rotor instability = instability in unsymmetrical rotors (rotors with non-uniform properties around the rotor disc) caused by the gyroscopic coupling between the rotor and the elastic support of the rotor

Wind shear = the variation with height of the undisturbed wind velocity

Whirl flutter = self-sustained or divergent precessional motion or "whirl" of the propeller about its unperturbed position. This may occur in a flexibly mounted propeller/nacelle installation in which the nacelle degrees of freedom allow the propeller plane to precess in response to the gyroscopic moments associated with the rotating propeller

Weaving = instability of semi-rigid and teetering rotors primarily described as a rotation of the entire rotor about the universal joint hinge. It is caused by the coupling between the pitching motion and the blade flapping dynamics

Zero of motion = solution of the transfer function numerator put equal to zero

Samenvatting

Tijdens het ontwerp van helikopters of horizontale-as windturbines, worden simulatiemodellen ontwikkeld voor verschillende doeleinden, zoals het bepalen van de prestaties, het zorgen voor aëro-elastische stabiliteit, het bepalen van de responsie van het systeem op verschillende externe excitaties, het bepalen van de vermoeiingseigenschappen en extreme belastingen van kritische componenten alsmede het ontwerp van besturingssystemen. Een van de primaire vragen die beantwoord moeten worden voordat begonnen wordt met het daadwerkelijk afleiden van een simulatiemodel, is hoeveel detail moet worden meegenomen in termen van het aantal en type mechanische vrijheidsgraden en het niveau van aërodynamische modellering. Voor toestellen met roterende bladen is deze vraag nog niet beantwoord. In de literatuur vindt men tegenstrijdige opmerkingen ten aanzien van de vraag welke eigenbewegingen een aanzienlijk invloed hebben op de laag-frequentie karakteristieken die belangrijk zijn voor besturingsmodellen van helikopters en het constructief modelleren van windturbines. Het doel van dit proefschrift is het ontwikkelen van een algemene methode die door de ontwerper-analist kan worden gebruikt voor het bepalen van de noodzakelijke vrijheidsgraden die in aanmerking moeten worden genomen in een lage-frequentie simulatiemodel voor helikopters en horizontale-as windturbines, voordat een compleet model wordt afgeleid.

Een nieuwe methode -de zogenaamde kritieke pool afstands methode- werd afgeleid, die zowel als een ontwerp als een evaluatie tool kan worden gebruikt, en die in staat is de significante vrijheidsgraden in het simulatiemodel te bepalen. De kritieke pool afstands methode bestaat er in principe uit dat de eigenwaarden behorend bij de ongekoppelde eigenbewegingen in het complexe vlak worden gerepresenteerd, waarna "kritieke gebieden" worden gedefinieerd waar potentiële koppelingen tussen verschillende eigenbewegingen zouden kunnen optreden. Een kritiek gebied wordt gevormd door eigenwaarden die als "voldoende dicht bij elkaar" kunnen worden beschouwd in het complexe vlak. Teneinde de onderlinge afstand tussen de eigenwaarden in het complexe vlak te kunnen kwantificeren, is een criterium ontwikkeld dat in staat is voor het geanalyseerde systeem een schatting te geven van wat moet worden verstaan onder "voldoende dicht bij elkaar".

Gebruik makend van de kritieke pool afstands methode werden in drie gevallen richtlijnen uitgewerkt voor de noodzakelijk modelstruktuur: 1) een onderzoek naar de significante rotor *disc-tilt modes* in een besturingssimulatiemodel; 2) een onderzoek naar het instabiliteitsmechanisme van de KEWT tweebladige horizontale-as windturbine; 3) een onderzoek naar de effecten van kinematische *pitch-flap* en *pitch-lag* koppelingen van het blad op diens *flap-lag* bewegingen voor een scharnierende rotor in *hover*. Voor elk geanalyseerd probleem werden criteria en vuistregels voor de kritieke pool afstands methode ontwikkeld om te kunnen beoordelen of eigenwaarden voldoende ver van elkaar verwijderd zijn, dan wel dicht bij elkaar liggen.

Wat betreft de effecten van de *disc-tilt* dynamica op de rompdynamica werden, bij het bestuderen van het natuurlijke zowel als het bestuurde gedrag van de met volledig gescharnierde Puma SA-330 en de semi-stijve Bölkow Bö-105, met behulp van de

kritieke pool afstands methode tijdens het simuleren van een deceleratie manoeuvre en een *side-step* manoeuvre, twee kritieke gebieden ontdekt waar de romp en de *disc-tilt* beweging koppelen: ten eerste een kritiek gebied in het longitudinale bewegingsvlak, gevormd door de eigenwaarde van de korte-periode rompbeweging en die van de *regressing flapping mode* en een tweede kritiek gebied in het laterale bewegingsvlak gevormd door de eigenwaarde van de *roll-subsidence mode* van de romp en die van de *regressing flapping mode.* Een criterium om de koppeling tussen de romp eigenbewegingen en de *regressing flapping* mode te kwantificeren werd vastgesteld. De romp/rotor *disc-tilt* koppeling hangt in het geval van de gescharnierde Puma helikopter af van de uitgevoerde manoeuvre: voor de deceleratiemanoeuvre konden de koppelingen worden verwaarloosd terwijl dit voor de *side-step* manoeuvre niet het geval was. Voor de semi-stijve Bö-105 is de romp/rotor koppeling altijd sterk, onafhankelijk van de uitgevoerde manoeuvre.

Wat betreft de instabiliteit van de tweede buiging-eigenbeweging van het chassis met de *lead-lag* van de rotor in het geval van de KEWT windturbine, is volgens de kritieke pool afstands methode de hoofdoorzaak de koppeling tussen de harmonische ω_{DIF+1} van de *differential lead-lag mode* en de tweede buiging-eigenbeweging van het chassis. Deze twee eigenbewegingen vormen het voornaamste traject waarlangs de excitatie van de zwaartekracht wordt doorgegeven van het blad naar het chassis en omgekeerd. Door de eigenschappen van het blad en het chassis te variëren, werd een criterium ontwikkeld voor de kritieke pool afstands methode. Door dit criterium toe te passen werd ontdekt dat de instabiliteit kon worden opgeheven door hetzij de dempingsverhouding van de toren te verhogen, hetzij de toren flexibeler of de bladen stijver te maken.

Met betrekking tot de sterkte van de koppeling tussen de *flap* en *lag* beweging in een rotor werd een kwantitatief criterium voor de kritieke pool afstands methode afgeleid op basis van verschillende kinematische *pitch-flap* en *pitch-lag* koppelingen in het systeem.

Het kritieke pool afstands criterium moet worden gekwantificeerd door een veelvoud aan *cases* te bestuderen, voordat conclusies kunnen worden getrokken. In die zin moet de methode worden beschouwd als een ingenieursbenadering van het simulatiemodelleringsprobleem. De geldigheid van de methode werd geëvalueerd door vergelijking met soortgelijke methodes (methodes die in staat zijn een indicatie te geven van het detailniveau van het simulatiemodel, zoals het Campbell diagram, het Milne criterium en de *Vector Shift* methode of methodes die worden gebruikt om het mechanisme achter de instabiliteit in een roterend systeem te bepalen, zoals de *Force-Phasing Matrix* techniek of de *Energy-Flow* methode). De kracht van de kritieke pool afstands methode ligt erin dat deze kan worden toegepast voordat met de daadwerkelijke afleiding van de gekoppelde dynamische bewegingsvergelijkingen wordt begonnen.

Tijdens het parallel onderzoeken van de problematiek van helikopter en windturbine modellering, bleek er een misverstand tussen de beide gemeenschappen te bestaan met betrekking tot de definitie van flexibele/stijve configuraties. Het blijkt dat moderne windturbines flexibeler worden in termen van de dimensionale *flapping* en *lead*-lag

frequenties, maar dat zij in termen van de niet-dimensionale frequenties stijver worden. Deze waarneming dient als een waarschuwing aan windturbine ontwerpers om zich bewust te zijn van het feit dat moderne windturbine configuraties een nieuw gebied betreden van rotor- en rotor/toren aëro-elastische instabiliteiten die karakteristiek zijn voor stijve systemen en die mogelijk moeilijk onder controle te houden of te elimineren zijn.

Afsluitend kan dit proefschrift worden beschouwd als een eerste stap in de ontwikkeling van een algemene methode die door de ontwerper-analist kan worden gebruikt om de noodzakelijke vrijheidsgraden voor helikopters en windturbines te kunnen bepalen. Om algemene richtlijnen met betrekking tot de noodzakelijke modelstructuur te verkrijgen, moet de kritieke pool afstands methode worden toegepast op een database van problemen specifiek voor lage-frequentie simulatie modellering van helikopters en windturbines. De genoemde richtlijnen dienen rekening te houden met de gewenste nauwkeurigheid en het toepassingsgebied van het dynamische model.

Sumar

În proiectarea elicopterelor şi a turbinelor eoliene cu ax orizontal, modele dinamice de simulare sunt dezvoltate în diferite scopuri cum ar fi: pentru a asigura performanţa acestor sisteme; pentru a asigura echilibrul aeroelastic; pentru a determina răspunsul sistemului la diferite perturbaţii externe; pentru a determina caractersticile de oboseală sau sarcinile extreme în componentele critice sau pentru a proiecta sisteme de control. Una din primele întrebari ce trebuiesc rezolvate înainte de a începe derivarea efectivă a unui model de simulaţie este legată de nivelul de detaliu ce trebuie considerat în model (mai exact numărul şi tipul gradelor de libertate ce trebuiesc considerate în model precum şi nivelul de aproximare al modelării aeroelastice). Afirmaţii contradictorii sunt întâlnite în literatura de specialitate referitor la întrebarea câte moduri au un efect substanţial asupra caracteristicilor dinamice în domeniul de joasă frecvenţă important pentru simularea comportării pilotate a elicopterelor sau a modelării structurale a turbinelor eoliene. Scopul acestei dizertaţii este de a elabora o metoda generală care să poate fi folosită de proiectantul analist, înainte de începerea derivării unui model complet, în determinarea gradelor necesare de libertate ce trebuiesc luate in considerare în modelarea dinamicii elicopterelor şi a turbinelor eoliene cu ax orizontal in domeniul frecvenţelor joase.

O noua metodă -aşa numita "metoda distanţelor polilor critici"- a fost dezvoltată capabilă să determine gradele de libertate importante în modelul de simulaţie Acestă metodă poate fi folosită ca instrument de proiectare şi evaluare. Metoda distanţelor polilor critici constă în principiu în reprezentarea în planul complex a valorilor proprii ale modurilor decuplate ale sistemului şi definirea "regiunilor critice" unde potenţiale cuplaje între diferite moduri de mişcare sunt posibile. O regiune critică este formată din valori proprii ce pot fi considerate "suficient de apropiate" una de alta în planul complex. Pentru a cuantifica pozitia relativă a valorilor proprii în planul complex, un criteriu capabil să estimeze sensul termenului "suficient de aproape" a fost dezvoltat pentru sistemul dinamic analizat.

Folosind metoda distanţelor polilor critici, direcţii referitoare la structura modelului necesar au fost elaborate în trei cazuri: 1) investigarea modurilor semnificative ale mişcării de bătaie a rotorului in modelele de dinamica zborului; 2) investigarea mecanismului de instabilitate a turbinei eoliene KEWT cu două pale; 3) investigarea efectelor cuplajelor cinematice de pas-bătaie şi pas-baleiaj asupra mişcării simultane de bătaie-baliaj a rotorului articulat de elicopter în zborul la punct fix. Criterii şi reguli practice referitoare la cum trebuiesc interpretate valorilor proprii aflate în apropiere au fost dezvoltate în metoda distanţelor polilor critici în fiecare din problemele analizate.

Referitor la efectele dinamicii mişcării de bătaie a rotorului asupra dinamicii corpului elicopterului, studiind comportarea naturală şi pilotată a elicopterului articulat Puma SA-330 şi a elicopterului semi-rigid Bölkow Bö-105 în metoda distan ţelor polilor critici şi simulând o manevră de deceleratie şi una de pas-lateral, două regiuni critice de cuplaj între mişcarea corpului elicopterului şi mişcarea de bătaie a rotorului au fost descoperite: în primul rând, o regiune critică în planul longitudinal de mişcare, regiune formată din valoarea proprie a modului de scurtă-perioadă şi modul regresiv de bătaie;

în al doilea rând o regiune critică în planul lateral de mişcare format din valoarea proprie a modului de ruliu şi modul regresiv de bătaie. Un criteriu de cuantificare a cuplajului dintre modurile de miscare ale elicopterului şi modul regresiv de bătaie a fost stabilit. Cuplajul dintre modurile de mişcare ale elicopterului şi mişcarea discului rotorului în cazul elicopterului articulat Puma depinde de manevra executată, şi anume: pe când în manevra de deceleratie acest cuplaj poate fi neglijat, în manevra de pas-lateral acest cuplaj trebuie considerat. Cuplajul dintre corpul rigid de elicopter şi mişcarea discului rotorului în cazul elicopterului semi-rigid Bö-105 este întotdeauna puternic, independent de manevra executată.

Relativ la instabilitatea tubinei eoliene KEWT, instabilitate între modul secundar de încovoiere a saşiului şi baleiajul rotorului, conform metodei distanţelor polilor critici, factorul primar responsabil de această instabilitate este cuplajul dintre armonica ω_{DIF+1} a modului diferenţial de baleiaj şi modul secundar de încovoiere a saşiului. Aceste două moduri formează calea principală prin care forţa de excitatie gravitatională se transmite de la pala rotorului la saşiu şi înapoi. Variind caracteristicile dinamice de frecventă şi amortizare ale palelor turbinei eoliene şi ale saşiului, un criteriu în metoda distanţelor polilor critici a fost dezvoltat. Folosind acest criteriu, a fost descoperit că instabilitatea turbinei eoline analizate a putut fi eliminată prin mărirea raportului critic de amortizare a saşiului sau prin creşterea flexibilităţii saşiului sau prin creşterea rigidităţii palelor.

Referitor la gradul de cuplaj dintre mişcarea de bătaie şi de baleiaj al palei rotorului, un criteriu cantitativ a fost stabilit pe baza a diferite cuplaje cinematice de pas-bătaie şi pas-baleiaj considerate în sistemul dinamic.

Criteriul distanţelor polilor critici trebuie să fie cuantificat prin investigarea a unei multitudini de cazuri practice. De aceea, aceasta metodă trebuie să fie considerată de fapt ca o soluţie inginerească în rezolvarea problemei modelării unui system dinamic. Validitatea metodei distanţelor polilor critici a fost evaluată prin compararea acesteia cu metode similare (metode capabile să ofere o indicaţie asupra nivelului de detaliu în modelul de simulare cum ar Diagrama Campbell, Criteriul lui Milne şi Metoda Deplasării Vectoriale sau metode folosite pentru determinarea mecanismului de instabilitate intr-un sistem rotativ cum ar fi Tehnica Matricei de Defazaj al Fortelor sau Metoda Diagramei de Energie). Capacitatea metodei distanţelor polilor critici constă în faptul de a putea fi aplicată înainte de începerea derivării complete a ecuaţiilor de mişcare cuplate ale sistemului.

Examinând simultan problema modelării elicopterului şi a turbinei eoliene a fost constatat că există un dezacord între cele doua comunităti referitor la definirea noţiunii de flexibil/rigid. S-a constatat că turbinele eoliene moderne devin mai flexibile vorbind în termeni dimensionali de frecvenţe naturale ale modurilor de bătaie şi baleiaj, dar în termeni de frecvente adimensionale (adimensionalizate în raport cu viteza unghiulară a rotorului), aceste configuraţii devin din ce în ce mai rigide. Acestă observatie este făcută pentru a atenţiona proiectanţii de turbine eoliene de a deveni conştienţi asupra faptului că evoluţia turbinelor eoliene actuale se îndreaptă în viitor spre un nou regim unde instabilităţi ale rotorului şi ale rotorului/turnului sunt posibile, instabilităti atât de caracteristice sistemelor rigide care sunt greu de controlat şi eliminat.

În concluzie, lucrarea de fată poate fi considerată ca un prim pas în dezvoltarea unei metode generale ce poate fi folosită de analistul proiectant pentru a determina gradele necesare de libertate în modelarea comportării dinamice a elicopterelor şi a turbinelor eoliene cu ax orizontal. Pentru a obţine criterii generale relativ la structura necesară a modelului de simulaţie, metoda distanţelor polilor critici va trebui aplicată pe o baza de date conţinând probleme specifice pentru modelarea simulatorie în domeniul modurilor de joasă frecvenţă a elicopterelor şi a turbinelor eoliene. Criteriile menţionate vor trebui să ia in considerare gradul de aproximare şi scopul în care modelul dinamic va fi folosit.

About the author

Marilena Domnica Pavel was born on July, 23rd, 1967, in Braşov, a city situated in the Transylvanian Carpathians in Romania. After completing primary, secondary and high school in Braşov, she was admitted in 1985 at the "Politehnica" University of Bucharest, Faculty of Aerospace Engineering (at that time Faculty of Aeronautical Engineering). After a general study of three years she specialized in "Aerospace Constructions", in 1990 receiving the title of *"inginer aeronave"* on a final graduation project dealing with the *"Application of the Control Configured Vehicle Concept (CCV Concept) to Improve the Performances of the RomBAC1.11"*.

After graduation she joined the National Institute of Aviation in Bucharest, Department of Theoretical and Experimental Analysis of Aeronautical Structures, as a research engineer. There she first came into contact with helicopters, working in projects related to the aeroelastic modeling of helicopters. From 1992 she became a part- time associate professor for the course of "Mechanical Vibrations" given at the Faculty of Mechanics at the "Politehnica" University of Bucharest.

From 1994 she continued research in the Department of Flight Mechanics of the National Institute of Aviation in Bucharest, familiarizing with helicopter piloted simulation modeling problems.

In 1995 she received a Nuffic scholarship at the Faculty of Aerospace Engineering, Delft University of Technology. Here, she joined the Department of Flight Mechanics and Propulsion (then Department of Design and Flight Mechanics), participating at the off-line modeling of helicopter piloted simulation for the general purpose simulator SIMONA (Simulation Motion and Navigation Technology).

In 1996 she began her Ph.D. study in an interdisciplinary project between different faculties of the Delft University of Technology in the field of wind turbine modeling. This dissertation is the result of her research of the last four years.